Fracture propagation in cementitious materials

Multi-scale approach: measurements and modeling

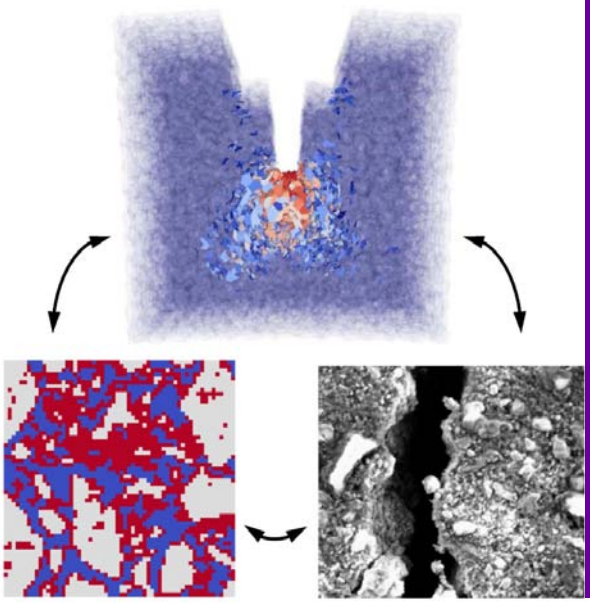

Jan Skocek

PhD Thesis

Department of Civil Engineering

2010

DTU Civil Engineering Report R-232 (UK)
March 2011

DTU Civil Engineering
Department of Civil Engineering

Fracture propagation in cementitious materials

Multi-scale approach: measurements and modeling

Jan Skoček

Ph.D. Thesis

Department of Civil Engineering
Technical University of Denmark

2010

Fracture propagation in cementitious materials
Multi-scale approach: measurements and modeling

Printed by Printed by Rosendahls-Schultz Grafisk
Department of Civil Engineering
Technical University of Denmark
ISBN: 9788778773111
ISSN: 1601-2917

Preface

This thesis is submitted as a partial fulfillment of the requirements for the Danish Ph.d. degree. The thesis is divided into two parts. The first part introduces the background and motivation of the undertaken research and concludes the major findings. Description of the investigated material and experimental techniques is appended. The second part is a collection of five papers focused on the most important topics of the research undertaken.

Preface to the published version

The thesis was defended at a public defense on Friday the 15$^{\text{th}}$ October 2010. Official opponents were Lecturer John Forbes Olesen, Technical University of Denmark, Professor Bhushan Karihaloo, Cardiff University and Professor Eugen Brühwiler, École Polytechnique Fédérale de Lausanne. Subsequently the Ph.D. degree was awarded from the Technical University of Denmark.

Compared to the the original submitted version of the thesis, several minor editorial corrections have been made and the status of some of the appended papers has been updated.

Acknowledgements

The presented work would not have been achieved without the help and support of a range of people and I would like to take the opportunity to express them my gratitude.

First of all, I would like to acknowledge the supervision of Professor Henrik Stang. He was the one who guided me all my way through and provided me numerous useful advices and feedbacks. Next, I would like to name several of my colleagues that contributed significantly to the presented work. They are Jan Eliáš, Denis Davydov, Ružena Chamrová, Professor Milan Jirásek and Professor Petr Kabele.

Secondly, I would like to thank to my wife Ilona for her support and understanding she has had for me all the time and for the partly sacrifice of her career in favor of mine. It was our daughter Adélka who charged me with energy whenever I needed it and who caused that all troubles to disappear with her smile.

Further, I need to express my gratitude to my colleagues and friends from the NanoCem network for the great and motivating atmosphere they created on the courses and meetings. This would not be possible without people coordinating the network - Professor Karen Scrivener, Mette Geiker and Marie-Alix Dalang-Secrétan.

The support and hospitality of people at Lafarge Centre de Recherche and Laboratory of Construction Materials, Ecole Polytechnique Fédérale de Lausanne, who made my stays pleasant and fruitful is acknowledged. A special thanks goes to Fabienne Begaud and Mariette Moevus for their help with the experimental part of the work at LCR.

Finally, I would like to thank to my family and friends who encouraged me throughout the entire project. Even though they were in another country, I could feel their support every day.

This thesis is dedicated to Tomáš Rieger and Petr Vik who left before being able to see it.

Abstract

Mechanical behavior of structures made from cementitious materials has been successfully modeled using non-linear fracture mechanics in recent decades. On the structural scale, an assumption of homogeneity of the material is valid and well established theories can be applied. However, if focus is put on phenomena of a similar scale as is the characteristic size of inhomogeneities of the material, a model which reflects the heterogeneous nature of the material needs to be applied. This is, indeed, the case for prediction of mechanical properties of a material based on the knowledge of properties of its constituents and composition or when focus is put on a single crack and an accurate estimation of its width.

Similarly, in the case of ordinary portland cement paste, a simple relationship linking the strength of the cement paste with its porosity was proposed and widely used for a long time. However, in today's blended cements, systems with higher porosity and higher strength at the same time are often found. Thus, the arrangement of the phases in microstructures plays an important role. These microstructures are highly heterogeneous and a model for prediction of mechanical properties of the materials needs to be able to take this complexity into account.

In this thesis, two frameworks for prediction of strengths of cementitious materials are developed. The first one relates the strength of materials with aggregates with the properties of the matrix and distribution of aggregates. The second one relates the strength of cement paste with the properties of cement phases and its microstructure. The frameworks consist of an experimental part, an identification of material properties from the experiments and a modeling part based on an approximative discrete particle model.

In the case of mortar and concrete, it is demonstrated that the measured mode-I fracture properties of the matrix together with fitted ratios of mode-I to mode-II properties are sufficient to provide estimations of mode-I, mixed-mode and compressive experiments matching favorably experimental records.

In the case of pure cement paste, it is experimentally observed and numerically verified that the cracking plays an important role in mode-I as well as compressive experiments. The approximative particle model extended for materials with heterogeneous matrices predicts strengths matching favorably experimental records in a qualitative way.

Resumé

Mekanisk opførsel af konstruktioner lavet af cementbaserede materialer har kunnet modelleres ved anvendelse af ikke-lineær revnemekanik i de seneste årtier. På den strukturelle skala kan materialet antages homogent, og vel dokumenterede teorier kan anvendes. Hvis der imidlertid fokuseres på fænomener af en skala sammenlignelig med den karakteristiske størrelse af materialets inhomogeniteter, er det nødvendigt at anvende den heterogene natur af materialet. Det er tilfældet når den mekaniske opførsel ønskes forudsagt med udgangspunkt i materialets komponenter og deres sammensætning, eller når fokus er på en enkelt revne og dens åbning.

Tilsvarende for almindelig portlandcementpasta, et simpelt forhold sammenkæder styrken af cement pastaen med dens porøsitet, og har været accepteret og brugt i lang tid. Imidlertid findes der ved anvendelse af nutidens blandede cement produkter, højere porøsitet og højere styrke på samme tid. Det er derfor oplagt at opbygningen af faserne i mikrostrukturen har en afgørende indflydelse. Disse mikrostrukture er meget heterogene, og en model for forudsigelse af de mekaniske egenskaber af et sådant materiale, kræver at denne kompleksitet tages i regning.

I denne afhandling udvikles to metoder til forudsigelse af styrken af cement baserede materialer. Den første metode relaterer styrken af de anvendte aggregater med egenskaberne af matrixmaterialet, samt fordelingen af aggregaterne. Den anden metode relaterer styrken af cement pastaen med dens mikrostruktur og egenskaberne af cement komponenterne. Metoderne består hver af tre dele; en eksperimentel del, en identifikation af materiale egenskaber fra eksperimenterne, og en modellerings del baseret på en approksimativ diskret partikel model.

For de to materialer mørtel og beton, er det demonstreret at de målte mode-I brudegenskaber af matrix materialet sammen med et forhold mellem mode-I og mode-II egenskaber er tilstrækkelig til at leverer estimater af mode-I, mixed-mode and tryk eksperimenter, som matcher eksperimentelle resultater overbevisende. I tilfældet med rent cementpasta, er det eksperimentelt observeret, og numerisk verificeret, at dannelsen af revner spiller en afgørende rolle i mode-I lige som for tryk eksperimenterne. Den approksimative partikel model udvidet for materialer med heterogene matricer, forudsiger styrker som overbevisende stemmer over ens med eksperimentelle resultater på en kvalitativ måde.

Table of Contents

Part I

Introduction and Summary

Chapter 1

Introduction

Nowadays, concrete is the material produced in the largest amount worldwide. With its world annual production of over 10 000 million tonnes, concrete is produced in higher quantity than other materials all together. That is caused by its outstanding properties and low prize. The concrete is an easy accessible material since raw materials for its manufacturing can be found almost everywhere and can be processed with reasonable energy consumption which makes concrete the cheapest structural material available. Further advantage of concrete lies in its transportability and constructibility, when all necessary compounds can be moved using the most common means of transport and mixed together with water to build the final material at the construction or prefabrication site. Concrete is able to fill forms of nearly any shapes and sets and hardens at room temperature. In addition, if well built, concrete structures can survive for centuries. Though the cement production is responsible for approximately 5-7% of man made CO_2, concrete is, compared to other construction materials, sustainable as well. Energy consumption for production of one tonne of concrete based on a common portland cement is about 600 MJ, while for the same amount of steel is, even if production from the scrap is considered, about 11 000 MJ/t. One can object to different strength of steel and concrete, but still several times lower amount of energy is consumed to build a structural member with the same load bearing capacity from the concrete than from the steel.

Concrete consists of two basic compounds: an aggregate skeleton and cement paste acting as a binder. The aggregates present in concrete vary in size from fine sands to coarse gravels to achieve optimal space filling and resulting mechanical performance. The cement paste is formed by cement, water, air and optionally by admixtures and additives. Even though concrete has been the most widely used material for long period of time and its composition is not so complicated, at least at the first sight, mechanisms taking place during setting, hardening and life-time of the material and their influence on mechanical properties are still insufficiently explored.

Two major obstacles against intensification of the knowledge about concrete can be identified: The first one results from a characteristic of the building industry itself. Since

every major structure is unique - build from different (local) materials, located in a different climate, built under different standards etc.- there is not enough resources for a deep research and design for every single structure as is the case e.g. in the car industry where a huge number of identical products is made. In structural engineering, more emphasis is given on experience and consequently heavily simplified relationships are often used in the design of structures. Such an approach proved to be sufficient and correct for most structures built in the past. However, during the last decades, limits of such an approach has been reached. With the development of new materials and more advanced structures where the experience is missing, material research and modeling start to play an important role. The second major obstacle is the complexity of the material. As already mentioned, concrete is a mixture of aggregates, water and cement. Properties of all these compounds influence the final properties. All of these compounds differ from one place to another. To make things even more complex, the properties of the cement paste depend on the way the hydration took place - moisture, temperature, mixing conditions etc. Even after the setting and hardening the material properties keep developing, depending on the chemical composition of the cement paste and conditions of the environment. Mechanical properties also varies in time - same loading for a short period of time gives a different response compared to the longer one. All these effects complicate significantly the exchange of knowledge between different research teams as well as between the research and industry.

Due to the complex nature of cementitious materials, everyday practical design covered by codes is heavily simplified and only a few material parameters - usually compressive strength and elastic modulus - are needed for the design. Codes provide simple analytical relationships between the measured properties and other important properties based mostly on the experience with "simple" systems containing Ordinary Portland Cement (OPC). However, recent cements are mostly blended and contain often various Supplementary Cementitious Materials (SCMs) that have significant effect on the hydration process as well as on the formation of the microstructure of the material. The simple empirical, analytical relationships cannot cover such a wide variety of materials and mixtures. Thus, numerical models that can capture the complex heterogeneous nature of the cementitious materials are therefore needed.

The importance of the microstructure on the properties of cementitious materials is demonstrated in the following example: The compressive strength of mortars with OPC, f_c, is assumed to be indirectly proportional to the porosity, p, and

$$f_c = f_c(1-p)^3$$

is assumed (Powers & Brownyards 1948). However, such a relationship cannot be used for cements with SCMs. Many materials with higher porosity compared to the OPC and with higher strength at the same time are reported in literature (Ramezanianpour & Malhotra 1995, Hossain & Lachemi 2007). Figure

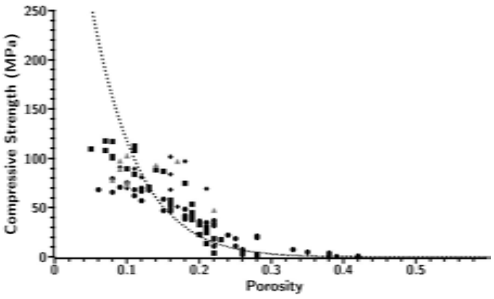

Figure 1.1: Relation between compressive strength and overall porosity for different systems. From (Bishnoi 2008).

, Similar discrepancies can be found when the time-related performance is investigated. For the case of OPC, the longer time and higher degree of hydration, the better mechanical properties. Opposite trends in long-term properties evolution were observed for some blended cements (Khatri, et al. 1995). Durability of the systems with SCMs is very sensitive to the dosage and the type of the SCM used and the relationship between the compressive strength, dosage, porosity etc. is much more complex compared to the systems with OPC (Toutanji, et al. 2004). Micro-structural modeling and models capable of incorporating the actual microstructure and the phase arrangement are keys to understand the differences between the materials.

The thesis focuses on the fracture mechanical properties since the crack formation and propagation in cementitious materials are one of the major mechanisms influencing the strength as well as the durability of the material and structures, respectively. Models for fracture propagation on the structural scale where concrete can be considered homogeneous are well established. However, once the focus is put on phenomena on a scale similar to the size of aggregates or structural details, the heterogeneity of the material starts to play an important role and cannot be neglected anymore. The crack formation at the scale of aggregates is directly linked with the durability of the material since it influences transport properties. Therefore, models capable of predicting the fracture process at this scale are of an utmost importance.

Similarly, limits of the models formulated for homogeneous materials are reached once cement paste is studied. At the level of cement paste phases, the material is highly heterogeneous with phases ranging from a significant amount of porosity to stiff unhydrated grains of clinker. It is self-evident that the arrangement of the phases will play a crucial role and models capable of incorporating of the geometrically explicit heterogeneity of the

material are therefore necessary.

This Chapter is organized in the following way: Section

1.1 Fracture Mechanics - Theories and models for concrete

In the current codes for the design of concrete structures, the load bearing capacity of a structure is governed by a strength criterion. The compressive strength of concrete is measured in a force-driven compression test and the value is then used according to codes. Consequently, the materials shown in Figure

In real-life applications of the structural concrete, however, the deterioration of the material due to an internal or external environment (e.g. delayed ettringite formation, sulfate attack or corrosion of reinforcement, alkali-silica reaction etc.) are often more severe limiting factors for the structural use than the load bearing capacity itself. Such phenomena are caused or accompanied by cracking. Thus, having a better estimation of crack widths, shapes and connectivity potentially improves the design and reduces both primary costs related to the construction as well as secondary costs related to the maintenance of the structure. Fracture mechanics can provide much useful information on the crack formation and propagation.

Last but not the least, strength of a heterogeneous material like concrete depends on processes and properties of materials on various scales. Fracture mechanics provides a solid background for multiscale models bridging the different scales.

1.1.1 Linear elastic fracture mechanics

It is well known that a large discrepancy exists between the theoretically predicted and measured tensile strength of brittle materials. The first satisfactory description the behavior off brittle materials was given as long ago as 1920 by Griffith (Griffith 1920). Based on the analysis of a thin plate with a sharp crack loaded by a remotely applied stress, Griffith found that the tensile strength of brittle materials is determined by presence of flaws. He pointed out that stresses tend to infinity near the crack tips regardless how small the applied stress is. Therefore, the fracture process of brittle materials cannot be governed by any strength criterion. He showed that a certain amount of potential energy needs to be accumulated in the system and consequently released to crack tips to create a new cracked area. From this energetical equilibrium, the formula for the remotely applied constant stress, σ_c, needed for the further crack propagation was derived as:

$$\sigma_c = \sqrt{\frac{EG_c}{\pi a}} \,, \tag{1.1}$$

where E is the Young's modulus, a is the initial crack length and the critical energy release rate, G_c, is a new material parameter. This parameter is called the toughness of the material, and stands for the energy required to create a unit area of the new cracked

surface. The Eq.(provides the criterion for the crack growth. If the remotely applied stress, σ, is lower than σ_c, the potential energy accumulated in the system is too low and no cracking occurs. However, if $\sigma \geq \sigma_c$ cracking propagates in catastrophic manner, until $\sigma < \sigma_c$ is reached again.

In the fifties, Irwin (Irwin 1957) discovered that the singular stress field near sharp crack tips always exhibits the same asymptotic behavior for all components of the stress independent on the shape of the elastic body, boundary conditions or loading. The stress state near the crack tip is called $r^{-\frac{1}{2}}$ asymptotic field with r being a distance from the crack tip. This solution is valid for $r << a$ only. An arbitrarily loading state can be decomposed into three basic states introduced by Irwin based on the deformation state at the crack tip; mode-I, mode-II and mode-III, see Figure

By inserting of the Eq.(to the Eq.(, one can easily find that the Griffith's global energy criterion and Irwin's local stress criterion at the crack tip are essentially identical and that

$$K_{Ic}^2 = E' G_c \ .$$

with $E' = E$ for plane stress and $E' = E/(1 - \nu^2)$ for plane strain. However, since it is much easier to determine critical stress intensity factor from experiments, Irwin's approach is usually preferred over Griffith's one and hand books for the stress intensity factor determination can be found, see e.g. (Tada, et al. 1985). Similar equations and relations for remaining two modes, mode-II and mode-III, can be found in the original work of Irwin (Irwin 1957).

1.1.2 Nonlinear fracture mechanics

The Linear Elastic Fracture Mechanics (LEFM) presented by Griffith and Irwin is capable of predicting the behavior of brittle materials very well. However, this theory, with stresses tending to infinity near the cracks tips, is in discrepancy with natural condition of stress limitations given by the tensile strength of the material. The infinite stresses also violate assumptions of small strains assumed by the linear theory of elasticity. Further, the proposed theory assumes that the energy is dissipated at one point while the bulk of the body remains elastic. For many materials, however, the dissipation takes place in a zone comparable to the size of the structure and the assumption of the dissipation at the single point needs to be abandoned. This problem might be overcome allowing smooth crack faces closure, as proposed by Griffith (Griffith 1920). The first attempt to include cohesive forces closing the crack smoothly was done by Barenblatt (Barenblatt 1959, Barenblatt 1962) who assumed that large cohesive forces of unknown distribution act in a small region, the so-called cohesive zone, near the crack tip. Later, Dugdale (Dugdale 1960) suggested a similar approach with cohesive forces acting in a narrow cohesive zone for elasto-plastic materials. Due to the yield limit and high ductility of such materials the distribution of cohesive forces could be determined. The cohesive forces were distributed uniformly and equal to the yielding stress. Irwin (Irwin 1957) drafted a rough estimation

of the zone where the dissipative processes takes place, the so-called Fracture Process Zone (FPZ), L_p. The maximum stress was assumed limited by the tensile strength, f_t, and L_p was derived as

$$L_p = \frac{1}{\pi}\frac{K_{Ic}^2}{f_t^2} = \frac{1}{\pi}\frac{E'G_c}{f_t^2} \ .$$

When the length of the FPZ, L_p, is small compared to the characteristic dimension of the structure, the assumptions of the LEFM are not violated and the LEFM can be used. In other cases, however, more general nonlinear theories need to be employed. Figure

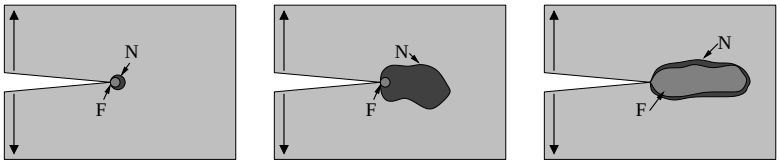

Figure 1.2: Evolution of nonlinear and fracture process zones in different materials: a) brittle material, b) elasto-plastic material and c) quasi-brittle material. After (Karihaloo 1995).

1.1.3 Fracture mechanics for concrete and mortar

As pointed out in the last paragraph, the size of fracture process zone, L_p, compared to a characteristic dimension of the sample or structure determines whether the linear or nonlinear theory should be used to obtain accurate predictions of the behavior. If all the energy dissipated in cracking takes place in a small FPZ which can be considered as a material point, LEFM is applicable. This is, unfortunately, the case only for very large concrete structures such as gravity dams. For the majority of concrete or mortar applications, the aforementioned assumption is not valid and nonlinear fracture mechanics has to be used instead.

In Figure

The first nonlinear fracture theory suitable for concrete was developed by Hillerborg (Hillerborg, et al. 1976). His model, the fictitious crack model, as well as those of Barenblatt and Dugdale, relies upon the smooth crack closure eliminating the energy dissipation at the crack tip. The term fictitious is used to underline the fact that ahead of the real, stress free crack, an artificial crack is supposed to be present and to transfer certain stresses causing the smooth crack closure. Unlike the Dugdale's model, the bridging stresses are not constant. The magnitude of the closing stress depends on the crack opening, w, and increase from zero at $w = w_c$ to f_t at $w = 0$. Moreover, unlike the Barenblatt's model, the size of fracture process, L_p, does not need to be small compared to the crack length and

the specimen size. As was previously pointed out, the crack propagation in the fictitious crack model is governed by the relation between the crack opening, w, and the magnitude of the bridging stress, $\sigma(w)$. This relationship, see Figure

Typically, at the structural scale, concrete is consedered as a homogeneous material and the TSL does not distinguish whether the bridging stress originates from microcracking in pure cement paste, aggregates debonding, crack branching or fiber cross-bridging or other effects; the TSL describes its averaged resulting actions on the current material scale only. The assumption of homogeneity determines both advantages and limitationsiof this approach. Figure

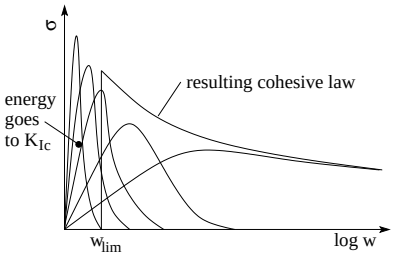

Figure 1.3: Traction separation law as an average of multiscale processes.

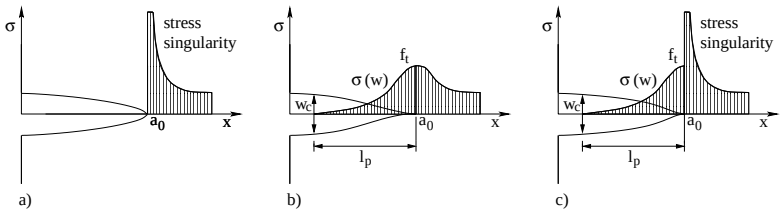

Figure 1.4: Stress distribution in the vicinity of the crack tip for : a) linear elastic fracture mechanics, b) fictitious crack model and c) general bridged crack model. After (Karihaloo 1995).

1.1.4 Models for heterogeneous materials

The nonlinear models for fracture propagation in concrete based on the fictitious crack model assume homogeneous and elastic effective material properties for the bulk behavior and averaged relationships between the crack width and the bridging stress. Utilization of such models is well established and the models are available in many commercial numerical

computer codes for structural analysis. Such models, however, have several limitations resulting from their assumptions. Models based on the averaged elastic and non-elastic properties cannot simulate effects on scales similar to the size of heterogeneities of the material such as micro-cracking prior to the formation of the main crack, crack branching or aggregates bridging. Similarly, if simulations of complex loadings are of interest, for example non-proportional, mixed-mode experiments (Jacobsen, et al. to be published), complicated material laws introducing mode-I and mode-II coupling, shear dilatancy and related sensitivity to confining stresses etc. are needed. These parameters, however, often lack sound physical background and are used as fitting parameters of such models.

Several models going beyond the assumption of homogeneity of the material and at the same time capable of simulating the global behavior of real-sized concrete specimens have been proposed. Since the heterogeneous microstructure responsible for most of the complexity of the concrete behavior is already modeled in such models, simpler material laws can be used and the models are more robust. In contrary to the models assuming homogeneous material, the heterogeneous models are capable of providing more reliable information about processes on the scale similar to the scale of heterogeneities. This can be used with advantages in up-scaling of the fracture propagation. Down-scaling, i.e. focusing on the meso-scale processes in a global simulation can lead to better estimation of the local crack propagation which is of a special importance for coupled transport-mechanical models (Idiart, et al. 2007, Idiart, et al. 2009) where the crack widths predicted by a homogeneous model will be overestimated compared to a heterogeneous model capable of predicting the crack branching and microcracking.

Assuming concrete to be a two phase composite material consisting of aggregate inclusions in mortar matrix and applying the frameworks of the fictitious crack model and Finite Elements Method (FEM) to the phases reaches the limit of the computational power very soon, since one dm^3 of an ordinary concrete contains several thousands of aggregates larger than 4 mm. Therefore, some simplifications have to be made. One of the ways to reduce the computational demands while still maintaining the framework of continuum mechanics and FEM is based on considering the largest aggregates only (Caballero, et al. 2006). Another possibility is a discretization of the material and interactions of its phases (Schlangen & van Mier 1992, Bolander & Saito 1998, Rots, et al. 2008, Karihaloo, et al. 2003, Zubelewicz & Bazant 1987, Adley & Sadd 1992, Cusatis, et al. 2006). The models for fracture propagation in heterogeneous materials are discussed in Chapter

1.2 Objectives

As discussed in the introductory part of this Chapter, the heterogeneity of cementitious materials influences significantly fracture propagation and therefore plays an important role once processes on the scale similar to the size of heterogeneities are studied. However, once the heterogeneities are explicitly modeled, the computational demands rise rapidly. Several models based on various simplifying assumptions can be found in the literature for

modeling of the effect of aggregates in concrete. However, applicability of the models to practical tasks and the way of retrieving input parameters from experimental data needs to be investigated. Further, it is necessary to develop a similar framework of testing and modeling at the scale of cement paste that would provide a tool to predict strength properties of the cement paste based on its microstructure and measured properties of the phases.

Thus, the objectives of the present work are the following:

- Critical review of models for fracture propagation in heterogeneous materials on the scale of concrete and mortar with respect to their practical applicability (measuring of material properties, possibility to simulate real-sized specimens etc.).
- Development and verification of a framework for the prediction of crack propagation in concrete and mortar from experimental work and material parameters identification to the simulations of fracture propagation in real-sized specimens.
- Verification of the developed framework against experimental data.
- Extension of the developed framework to the scale of cement paste and predicting the compressive and tensile limit of the cement paste based on its microstructure and measured properties of phases.

1.3 Outline

The thesis is organized in the following way:

- Material models for fracture propagation in homogeneous materials and applications of such models in the identification of material properties from experiments are discussed in Chapter

Chapter 2

Cohesive Zone Models

2.1 Introduction

As mentioned previously, crack propagation in heterogeneous materials such as cementitious materials is a very complex process. In front of the stress-free crack, a region when nonlinear mechanisms occur is located. Due to cracks presented in concrete even before the external mechanical load is applied and due to stress concentrations resulting from the heterogeneity of the material, the microcracking occurs ahead of the crack tip even before the *macroscopic* tensile strength is reached. The microcracks join in the most loaded region and form a macrocrack. The consequent gradual loss of the load bearing capacity is then a result of aggregates bridging, crack branching, crack tortuosity and shearing. Hillerborg (Hillerborg et al. 1976) made the first attempt to describe such a behavior. His model, the Fictitious Crack Model (FCM), projects all aforementioned effect into a single fictitious crack and postulates the relationship between the *average* bridging stress and the *average* crack opening, the TSL. The material is assumed to behave linearly elastically until the *macroscopic* tensile strength is reach. Then the response is governed by the TSL, see Figure

2.2 FEM Implementation

This Section describes briefly the most common numerical implementations of the FCM.

2.2.1 Cohesive interface elements

The most straightforward finite elements implementation of the FCM are interface cohesive elements. The cohesive interface elements are placed at the region (a line

in 2D or a plane in 3D for mode-I) where the crack propagation is expected. The simplest implementation based on a penalty stiffness approach is described e.g. in (Xie & Waas 2006). A one dimensional cohesive zero thickness interface element connecting nodes i and j of a finite element mesh is assumed (see Figure

Advantages of the interface elements are readily observed. Since the crack path is defined a priory, the re-meshing is not necessary. The interface cohesive element is very simple and can be easily added to an existing FE code. Further, the simple interface element can be easily extended to account for shear or coupled normal-shear softening (see (Walter & Olesen 2008)). Since the crack path is predefined and the bulk of the structure or specimen is modeled using linear elements, there is no risk of localization problems and the model allows modeling of materials with strain hardening - for example fiber reinforces concrete.

The main disadvantage, beside numerical issues related to the rapid change in stiffness of elements requiring small increments, is the predetermination of the crack path. Since the crack path is known (in the scope of the presented model) for mode-I or cracking at the interface of different materials only, this model cannot be used for general crack propagation under mixed mode conditions.

2.2.2 Crack band model

The necessity of the definition of the crack path a priory and the fact that the real fracture process takes places in a zone of a certain width rather than a plane led to the creation of the crack band model by Bažant (Bažant 1976) and to further improvements by Bažant and Cedolin (Bažant & Cedolin 1979) and Bažant and Oh (Bažant & Oh 1983). The width of the band, h in Figure

The crack band model has the advantage that the crack pattern does not need to be defined a priory. The cracking starts at the element which reaches the tensile strength first and further propagation is governed by the state of the stress and mesh orientation. The mesh dependency is significantly reduced in the rotating crack model (K.Gupta & Akbar 1984) and even more in the rotating crack model with transition to scalar damage (see (Jirásek 2006b, Jirásek 1998) for comparison of the models). Since the mesh path is not know a priory, re-meshing is often used during the computation to increase the accuracy of the solution. This leads to increased computational demands, especially in 3D.

2.2.3 Mesh independent implementations

The necessity of the re-meshing needed for a general crack path and accurate FEM discretization was overcome by the eXtended Finite Element Method (XFEM) (Belytschko

& Black 1999). In the XFEM implementation of the cohesive zone models, the enrichment of basis functions of elements for the a jump in the displacement field representing the crack ensures that the direction of the crack propagation is independent on the FE mesh (Mougaard, et al. 2010). The strength of the XFEM implementation of the FCM is demonstrated e.g. in (Unger, et al. 2007) where a simple mesh is used for the simulation of a complex crack path in a mixed-mode experiment.

Another application of the XFEM is demonstrated in (Xiao & Karihaloo 2007). The finite elements at the crack tip were enriched with functions relating displacements to the asymptotic analytical of the displacements around the crack tip of a cohesive crack which led to improvements in the accuracy of simulations.

2.3 Identification of material properties of the fictitious crack model

The mode-I material parameters of the FCM and its variants are usually obtained by finding a combination of the parameters giving a simulation matching favorably an experimental record. In order to make both the simulation as well as the experiment as simple as possible, the position of the crack is usually predefined by a notch. In a structure or specimen with a large enough notch, all the non-elastic behavior can be considered to take place at the plane of the notch and can be easily modeled using the interface element approach within the scope of the FEM. However, in such an approach the entire structure is modeled relatively detailedly (finite elements outside the plane of the notch) which increases the computational time. The computational demands can be decreased by the static condensation of some DOFs outside the FPZ, see (Carpinteri 1989). An alternative approach reducing the computational costs lies in modeling of the parts outside the FPZ analytically. This allows formulations of simple and computationally inexpensive models delivering accuracies comparable to the full FEA (Østergaard 2003).

In Sections

The semi-analytical method for mode-I fracture propagation is based on the hinge model developed by Ulfkjær et al. (Ulfkjær, et al. 1995) and improved by Olesen (Olesen 2001) for elements loaded with a combination of the bending moment and the normal force. The advantage of the original hinge model is that it provides a closed-form analytical solution for the Crack Opening Displacement (COD) for a given load of the hinge, assuming linear elastic material behavior with a multi-linear TSL. The hinge model is based on the assumption that the presence of the crack changes the stress and the strain field only locally while the rest of the structure remains unaffected. Using the closed-form formula instead of the FE discretization

is reflected by the reduction of the computational costs. Even though the hinge model is capable of providing a closed-form analytical solution for any piece-wise linear TSL, derivation of an analytical solution for a more than bi-linear TSL and its implementation would be very complicated. Therefore a semi-analytical approach, with iterative neutral axis position assessment is employed in the work described in Paper I. This modification allows us to involve both the multi-linear TSL and the multi-linear elastic behavior of the undamaged material in the computation with only a tiny increase in the computation costs in the global iterative scheme. The hinge model is suitable for simulation of a mode-I fracture test where the cracked cross-section is loaded by a combination of bending and normal load. Figure

The crack propagation is modeled through incremental layers of spring elements within the rigid element boundary allowed to rotate and translate to ensure compatibility with the bulk of the structure modeled with classical elastic beam theory, see Figure

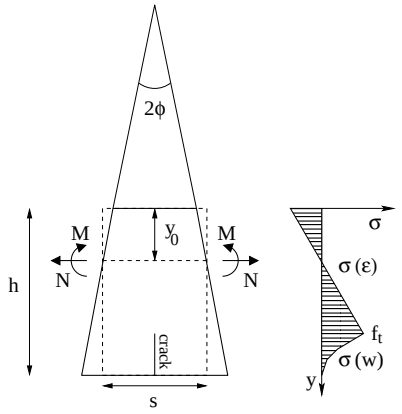

Figure 2.1: The hinge model geometry and assumed stress distribution.

2.3.1 Back analysis approach

An alternative type of a semi-analytical model for mode-I fracture propagation in cross-sections loaded by the combination of bending moment and normal force, called "back analysis" (Casanova 1995) is used at Lafarge Centre de Recherche for evaluation of common fracture tests. The back analysis approach assumes that the material behaves elastically with Young's modulus E up to the tensile strength, f_t. Then the TSL governs the response of the material. The TSL is assumed as a set

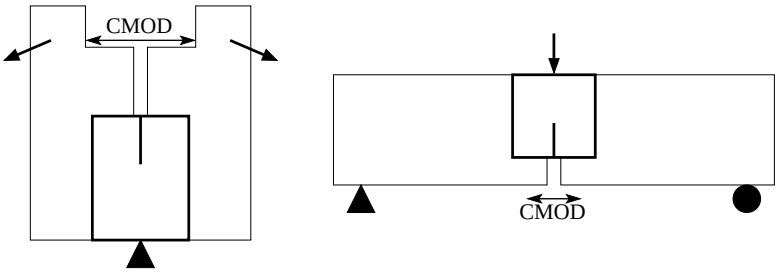

Figure 2.2: The hinge model for wedge splitting test and three point bending test.

of stress-COD pairs, $\sigma^{BA}(w)$. The shape of the TSL can be arbitrary, including hardening or even compressive stresses. Triangular crack shape is assumed, see Figure

For a given CMOD, the stress in the cracked cross-section can be divided into two parts. The first part is the elastic stress

$$\sigma_x^{el}(y) = E\chi_m(\alpha_n h - y),$$

where χ_m stands for the curvature of the cross-section, α_n is the relative height of the neutral axis, h height of the cross-section and y denotes the vertical coordinate, see Figure

In the case of the Three Point Bending Test (TPBT), the following equilibrium equations have to be satisfied in the step i:

$$\begin{aligned} N^{el,i} + N^{w_i,i} &= 0 \\ M^{el,i} + M^{w_i,i} - M^i &= 0 \end{aligned} \tag{2.1}$$

For a given set of $i = 1, 2, \ldots, K$ prescribed or recored CMODs and for given TSL, $\sigma^{BA}(w)$, the bending moment M^i is found in the following way:

$i = 1$
$w_i = 0$
$M^{w,i} = 0$
$Nw, i = 0$
$\sigma_x^w(0) = f_t$
$\alpha^1 = 0$
`for` $i = 2 : K$

```
        find σ_x^w(w_i) as interpolation of σ^BA(w)
        find such M^i and α^i minimizing Eqs. (
    end
```

The found set of M^i is the simulated load and the set of α^i describes the evolution of the crack length.

2.4 Identification of material parameters

Since the material models based on the FCM are capable of providing generally a good simulation of global responses of simple mode-I fracture tests and since the numerical models utilizing the FCM have reasonable computational demands, such models are suitable for the identification of the material properties from experimental records. The semi-analytical hinge model and the back analysis, see Sections

The attached Paper I describes the application of the hinge model for the material parameters identification and addresses the amount of information that it is possible to get from a single test in details. The main conclusion is that the traditionally used bi-linear traction separation law can be substituted by a tri-linear or quad-linear law increasing the accuracy of simulation while still keeping the optimization well constrained and solutions unique. Further, it is verified that the identified parameters can be used as the input for FEA while providing results matching favorably the experimental record used for the identification. The identified material parameters are thus independent on the model used for the identification.

However, even though the hinge-model is a very efficient model with very low computational demands (one simulation takes roughly 10 seconds), the entire inverse analysis procedure can be time consuming. The reason is that, especially for cases when high precision and dense point spacing are desired, a huge number of iterations is needed to fulfill the convergence criteria and the entire inverse analysis can easily take several hours. Thus, searching for an even simpler tool with similar accuracy is of interest.

The inverse analysis based on the back analysis approach introduced in Section

2.4.1 LCR back-analysis

Section

Assume that the experimental record for the inverse analysis consists of a set of $CMOD^i - M^i$ pairs and that E and f_t is known. In every step of the inverse analysis, a solution of Eqs. (is found. In contrary to the forward analysis, the M^i is known and the $\sigma^{BA}(w)$ needs to be found. $N^{w,i}$ and $M^{w,i}$ in Eqs. (depend on $\sigma^{BA}(w)$ for $w \leq w_i$, where $\sigma^{BA}(w)$ for $w < w_i$ has been already identified in previous

steps and the bridging stress corresponding to w_i is the only parameter needed to be found in step i.

The algorithm for the back analysis is very straightforward:

$i = 1$
$w_i = 0$
$M^{w,i} = 0$
$Nw, i = 0$
$\sigma_x^w(0) = f_t$
$\alpha^1 = 0$
`for` $i = 2 : K$
    `set` $w_i = CMOD_i$
    `find such` $\sigma_x^w(w_i)$ `and` α^i `minimizing Eqs. (`
`end`

The values of $\sigma_x^w(w_i)$ are saved and constructs the TSL, thus the set of $\sigma_x^w(w_i) \equiv \sigma^{BA}(w)$.

Since the TSL is identified by fitting Eq.

In step $i = 2$, the value of the bridging stress is found to minimize Eqs. (, where the external moment $M^{(i=2)}$ is measured and thus contains noise. In step $i = 3$, the bridging stress is found again by minimizing Eqs. (dependent on the previously identified bridging stress containing noise. The bridging stress in the step $i = 3$ therefore depends on the structural response containing noise, $M^{(i=3)}$, and on the previously determined bridging stress that also contains noise. This obviously leads to the accumulation of noise and scattered TSL, respectively. Moreover, the recorded experimental response is the response of a heterogeneous material, while the model assumes the homogeneous material. Fitting of the record containing the natural material-noise increases further the scatter in the TSL.

A possibility of smoothing of the TSL was therefore investigated. To suppress the noise, the TSL was filtered using the floating average filter. Values of the bridging stress, $\sigma_x^w(w_i)$, were substituted by $\tilde{\sigma}_x^w(w_i)$, where

$$\tilde{\sigma}_x^w(w_i) = \sum_{j=-I}^{I} \sigma_x^w(w_{i+j})/(2I+1), \tag{2.2}$$

where $2I + 1$ values were used for the averaging. Figure

Figure

Results of the smoothening using Hamming window are shown in Figure

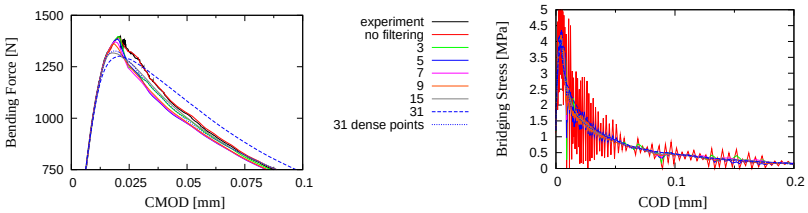

Figure 2.3: Comparison of simulations, a), and traction separation laws, b), identified by the back analysis for different level of filtering using the floating average.

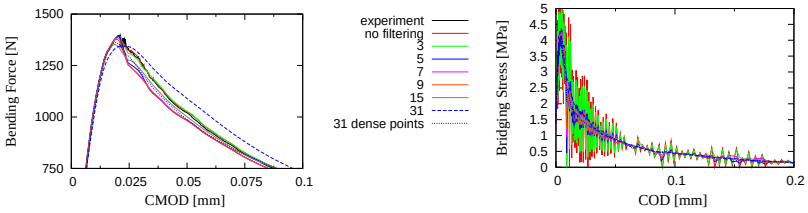

Figure 2.4: Comparison of simulations, a), and traction separation laws, b), identified by the back analysis for different level of filtering using Hamming window.

Figure

2.4.2 Comparison of back analysis and hinge model-based inverse analysis

The hinge model-based inverse analysis, see Section

In this Section the two methods are compared on a set of TPBT records and their applicability is discussed. An utilization of the back analysis as a tool for estimating the initial material properties for the hinge model-based inverse analysis is introduced.

Test setup and investigated materials

Cementitious materials of three different materials scales - concrete, mortar and micro-mortar - were prepared. The materials differed in the size of the largest aggregates used and in Water to Cement ratio (W/C). The concrete contained aggregates up to 8 mm, mortar up to 2 mm and micro-mortar up to 0.8 mm. Washed sea gravel and sand were used. The W/C varied between 0.47 in the case

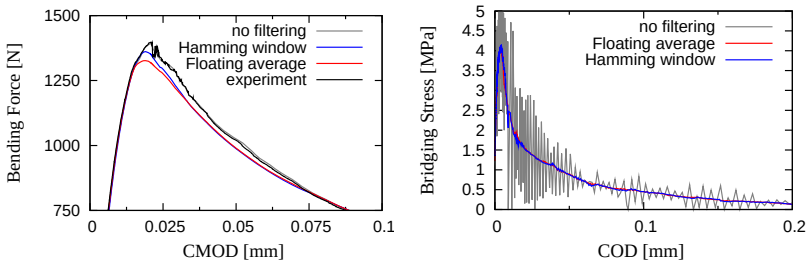

a) b)

Figure 2.5: Comparison of the effect of smoothening using the floating average or the Hamming window on the simulation of the experimental record, a), and the identified TSL, b).

of concrete and 0.43 in the case of micro-mortar. The differences were assumed to compensate for the effect of the increased volume of the ITZ changing the apparent W/C in the bulk material. Two different types of binder - Aalborg Basis cement (AB) and Aalborg White cement (AW) - were used for the preparation. Details about the composition, PSD, mixing and curing are provided in Appendix

Six TPBT were performed and averaged for every material. The samples were identical across the materials and their geometries, dimensions and test setups are depicted in Figure

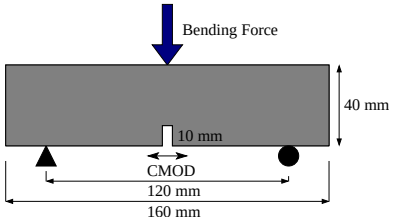

Figure 2.6: Scheme and dimensions of the TPBT.

Results and discussion

The hinge model-based inverse analysis had the following settings (see Paper I for details and nomenclature): the number of lines in the TSL was set to $N = 3$, the convergence criterion was set to 0.02 and the point spacing to 0.05. The identified material properties are summarized in Table

Since the back analysis requires the Young's modulus and tensile strength of the material as the input parameters, values identified by the hinge model-based inverse analyses were considered in this comparison. The same density of the points interpolating the experimental record as in the case of the hinge model-based analysis was considered. The Hamming window filtering algorithm described in Eq. (with width $2I + 1 = 9$ was used for the filtering of the identified TSL.

Simulations of the TPBT test using the back analysis and the hinge model-based analysis are compared in Figure

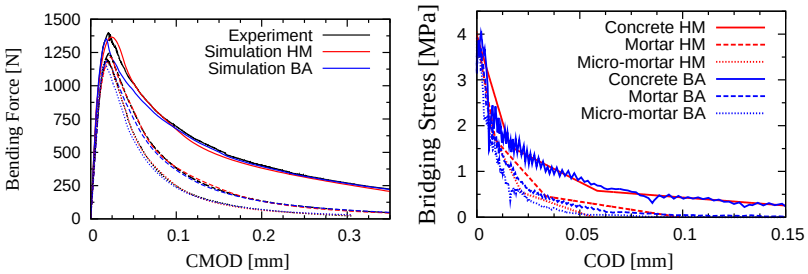

Figure 2.7: Comparison of inverse analysis based on the hinge model and the back analysis for Aalborg Basis binder.

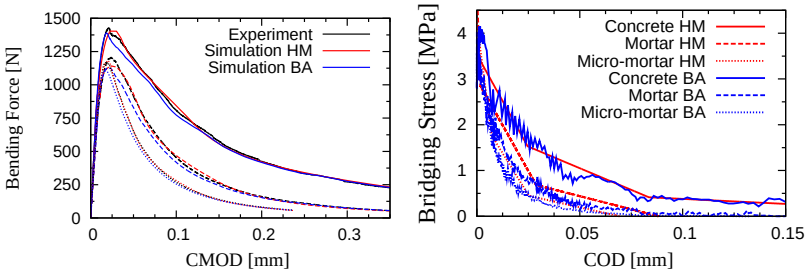

Figure 2.8: Comparison of inverse analysis based on the hinge model and the back analysis for Aalborg White binder.

The fracture energies listed in Table

Binder	Material	E	f_t	G_f [Jm^{-2}]	
		[GPa]	[MPa]	Hinge Analysis	Back Analysis
AB	Concrete	37.1	3.970	136.5	139.8
AB	Mortar	27.2	4.146	66.65	58.76
AB	Micro-mortar	29.1	4.231	48.68	39.50
AW	Concrete	38.3	4.160	158.0	155.7
AW	Mortar	29.0	5.225	75.68	62.64
AW	Micro-mortar	31.1	4.173	51.39	43.23

Table 2.1: Material properties identified by the hinge model-based inverse analysis and by the back analysis. Note that E and f_t was not identified by the back analysis.

2.4.3 Improvements of the hinge model-based inverse analysis with the back analysis initial material estimation

The time needed to perform the hinge model-based inverse analysis is very sensitive to the initial estimation of the material parameters, especially the shape of the TSL is important. Since in every global iteration, see Paper I, the material properties are changed one by one in local iterations and since the shape of the TSL has to meet some constraints (e.g. the first kink-point has to be at smaller crack opening than the second one, etc.), several global iterations are necessary to completely change the shape of TSL e.g. from the TSL of cement paste to the TSL of mortar. Therefore it is desirable to start with the best initial estimation available. Here the back analysis comes into play. Since the shapes of the TSLs identified by the back analysis are similar to those identified by the hinge model, see Figures

The initial estimation of the shape of the TSL of the investigated material is constructed in the following way: Young's modulus and tensile strength are guessed and the back analysis is run and the TSL is found and smoothen (red line in Figure

$$Err(\sigma^{ML}(w)) = \sum_{j=0}^{K} \left(\sigma^{ML}(w_j) - \sigma^{BA}(w_j)\right)^2 \tag{2.3}$$

with the constraints

$$\sigma^{ML}(0) = f_t \quad \text{and} \quad 0 < w_I < w_{II} < ... < w_c, \tag{2.4}$$

$$\tag{2.5}$$

where $\sigma^{ML}(w)$ stands for the multi-linear TSL, $\sigma^{BA}(w)$ is the TSL identified by the back analysis in K discrete crack openings w_j; $w_{I,II,...,N}$ stand for the COD corresponding to the kink points, see Figure

Figure

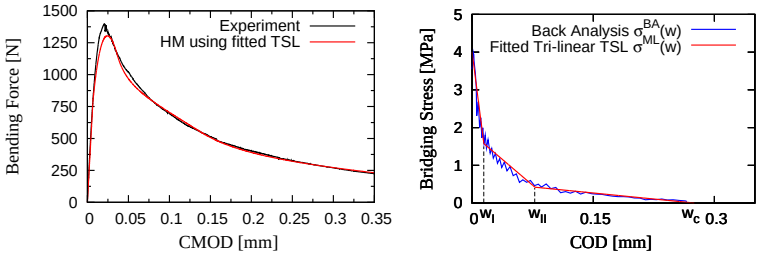

a) b)

Figure 2.9: a) Comparison of the experimental record with the hinge model simulation using the TSL (red in b)) fitted on the TSL identified by the back analysis (blue in b)).

2.4.4 Data acquisition

Deformations in the aforementioned experimental records were measured with a clip-gauge at a single point. However, this approach of displacement measurement has several limitations. First of all, the point where the displacement measurement takes place needs to be specified a priory. Secondly, as the fracture process is investigated on still smaller and smaller scale, sensors also need to be smaller. In certain cases, e.g. for experiments carried out in the chamber of an Environmental Scanning Electron Microscope (ESEM), the space is highly constrained and the transducer cannot be used without shielding the specimen. The measurement of the complete crack propagation in terms of crack opening profile and crack tip position is clearly much more attractive than the single point measurement. Hence, optical measurement of the displacement presents a promising possibility avoiding the aforementioned disadvantages.

Optical measurement systems are typically capable of measuring displacements on the surface of the whole specimen or the part of the specimen where the cracking is supposed to occur. Specific points where the displacement is measured are defined after the test in data post processing. In principle, the only limitation in the number of points where displacement is recorded is the resolution of the digital imaging device and a virtually continuous displacement field can be obtained. The post processing is similar for experiments on all scales and the same software can be used for specimens differing for several orders of magnitude in size. Since any digital image sequence can be used as the input for the post processing, the approach is suitable for evaluation of displacement fields in specimens loaded in an chamber of an ESEM .

The disadvantage of this approach lies in its restrictions to surface deformations only. This implies that this approach is suitable only for cases where cracking can

be considered uniform across the thickness of the specimen. This is fortunately the case for most of commonly used mode I fracture tests and an implicit assumption of Hillerborg's fictitious crack model. The assumption was verified e.g. in (Østergaard, et al. 2002) where two- and three-dimensional analyses of the Wedge Splitting Test (WST) were compared.

The optical measurement of the deformation and crack propagation in a specimen during a fracture test can be used in two basic ways. The displacements of similar points that would be measured with a clip gauge can be recorded and these records used in the same way as data from a transducer. Optical measurements, however, open up other, new possibilities of fracture process analysis. Instead of measuring the deformation in discrete points a displacement field can be recorded and continuous features such as the crack profile evolution or crack tip position can be measured. Measurement of such processes traditionally presents significant difficulties. The crack profile is traditionally obtained by impregnation techniques which however is unable to provide its evolution during loading for a single specimen due to its destructiveness. The approximate crack tip position can be determined by acoustic emission which provides good three dimensional estimation of the dissipated energy. However, the crack profile and dissipation free opening of the crack cannot be characterized by such a technique. When optical deformation analysis is employed, the evolution of crack tip position and crack profile can be easily measured.

A framework developed for inverse analysis of the WST based on the optically acquired data is discussed in Paper II. First of all, extensions of the inverse analysis described in (Skoček & Stang 2008) supporting crack profile data is introduced. The extended inverse analysis is applied to data from the WST of ordinary concrete. The identified parameters of the fictitious crack model are then compared to those obtained by inverse analysis based on global response measured by clip gauge. The parameters are subsequently used as input parameters for simulations of the test by the Finite Element (FE) model and the non-linear semi-analytical hinge model (Ulfkjær et al. 1995, Olesen 2001, Østergaard 2003, Skoček & Stang 2008). Crack profiles and crack tip positions are computed and compared with those measured by the optical deformation analysis system. It is shown that the inverse analysis based on the optical measurement can provide material parameters of the fictitious crack model matching favorably those obtained by classical inverse analysis based on the clip gauge data. It is demonstrated that further advantages of using the optical deformation analysis lie in discovering of such effects as aggregates bridging and crack branching. These effects would remain hidden if the deformation would be measured by the clip gauge and the experiment simulated by the fictitious crack model. The ability of the non-linear hinge model and cohesive finite elements model to represent the crack profile and the crack tip position is investigated. It is

found that the finite elements model performs better in the pre-peak regime whereas the hinge-model performs better in later stages of the crack propagation. Non of these models, however, are capable of modeling the aforementioned effects identified by the optical deformation analysis.

2.5 Advantages and limitations

The FCM and its modifications are very robust models for simulation of global responses of a structure with limited number of localized cracks. Since the FCM assumes homogeneous material and lumps all the processes related to the fracture propagation into one single crack, the implementation of the FCM to a FEM is very straightforward especially for situations when the crack position is known a priory. For cases when only one crack forms in a simple structure or test specimen, the FEA can be substituted with even simpler semi-analytical models. Such models are highly suitable for identification of the material properties of the FCM due to their low computational demands.

However, once the focus is put on the processes at the scale close to the characteristic size of inhomogeneities in concrete, the FCM cannot be used anymore. Unfortunately, this is the case for many crucial industry relevant problems:

- The assumption of homogeneity does not allow distinguishing between various sources of the bridging mechanisms which is necessary for bridging between different material scales and thus for prediction of strength properties and fracture behavior of cementitious materials.
- In the homogeneous material, widths, shapes and locations of cracks cannot be predicted reliably which would be necessary for realistic estimation of transport properties of the material relevant for predictions of corrosion, sulfate attack, leaking of structure etc.
- Creation of a universal robust model for simulation of concrete behavior under complex loadings.

Chapter 3

Fracture Models for Heterogeneous Materials

3.1 Introduction

The cohesive zone model and its modifications discussed in Chapter

Assuming the concrete to be a two phase composite material consisted of aggregates and mortar, application of the frameworks of the CZM and FEM to the phases reaches the limit of the computational power very soon, since one dm^3 of an ordinary concrete contains several thousands of aggregates larger than 4 mm. Therefore some simplifications have to be made. One of the way to reduce the computational demands is based considering the largest aggregates only. Such an approach is briefly describe in Section

3.2 Continuum mechanics approach

A straightforward approach to the modeling of the fracture propagation in heterogeneous materials is the explicit modeling of the materials within the framework of the common FEM. As an example, the approach of Carol et al. (Caballero et al. 2006, Caballero, et al. 2008) is based on the classical 3D finite element method with non-linear interfaces between aggregates-mortar and selected mortar-mortar connections. The advantage of such an approach lies in its accuracy resulting from the utilization of the well established framework of the finite elements method with common types of elements and material laws.

However, such an approach has several disadvantages. Since the aggregates, mortar and ITZ are modeled explicitly, it is necessary to determine their material properties, which is especially for the case of ITZ, extremely difficult since the ITZ properties are

highly sensitive to the type and size of aggregates used (Tasong, et al. 1998, Elsharief, et al. 2003, Aquino, et al. 1995, Zimbelmann 1985, Alexander 1993), age (Elsharief et al. 2003), binder (Elsharief et al. 2003, Aquino et al. 1995, Zimbelmann 1985) and the test used for the identification (Aquino et al. 1995, Zimbelmann 1985, Alexander 1993).

The validation of the model against the experimental data presents a further complication. Since only very limited amount of aggregates can be modeled explicitly due to the high computational demands, the effect of the remaining not explicitely modeled aggregates is included in the properties of the matrix. For example, if a concrete cube with edge of 100 mm made from concrete with spherical aggregates up to 8 mm, the relative volume fraction of aggregates of 0.65 and the PSD shown in Figure

3.3 Lattice models

The lattice models are based on the assumption that it is not necessary to model accurately all the links and interactions in the material, but that the interactions can be approximated e.g. by the normal interactions only. This simplification dates back to Alexander Hrennikoff[1] who showed that problems of elasticity can be solved or approximated by a discretization of a continuum by trusses. An example of such a solution is shown in Figure

The Voronoi-type of the lattice model was extended for heterogeneous materials and simulations of non-linear problems. Figures

Due to the elasto-brittle or elasto-piece-wise-brittle material law, the solution of the macroscopically non-linear problem breaks into a sequence of linear solutions. In every step, the beam with the highest stress to strain ratio is found and its stiffness is reduced according to the considered material law. For a uniform loading such an approach provides a unique solution. However, for a non-proportional loading an algorithm proposed in (Eliáš & Frantík 2009) needs to be considered. Application of the lattice model for non-proportional loading is discussed in Paper III.

The elasto-brittle lattice models provide, despite their simplicity, a robust tool for simulation of the fracture propagation in concrete. The amount of aggregates that can be considered in the simulation can be significantly higher compared to the approach based on the continuum mechanics and detailed discretization of the entire volume. However, the complication with the properties of the ITZ introduced in Section

[1] `http://en.wikipedia.org/wiki/Alexander_Hrennikoff`

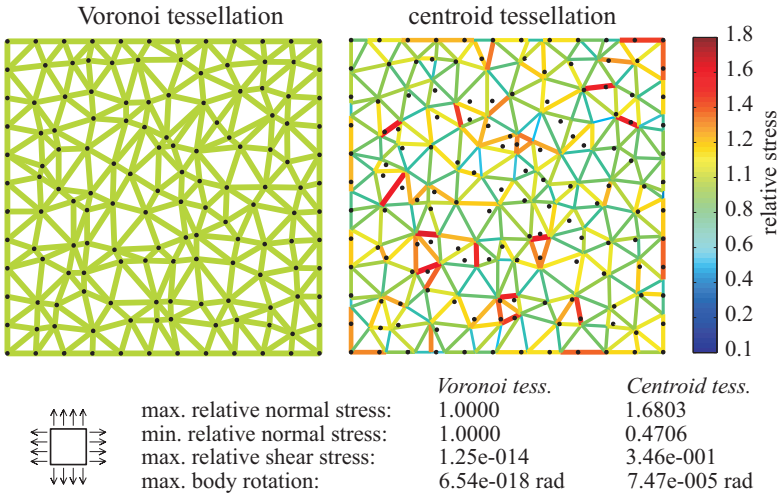

Figure 3.1: Comparison of lattice models with Voronoi and centroid tessellation. Courtesy Jan Eliáš.

3.4 Particle models

In contrary to the lattice models, where the material structure is mapped (Figure

The blue lines in Figures

The way the meshes are created in the particles models allows considering a significantly higher number of aggregates in the simulations compared to lattice models and the continuum mechanics-based models and makes it possible to separate experimentally the investigated material scales.

3.5 Advantages and limitations

In this Chapter, three groups of models for simulation of fracture propagation in heterogeneous materials were presented and their main advantages and limitations were discussed. Here the groups of models are summarized and compared:

Continuum Mechanics approach Section

Since the main focus of the undertaken researched was put on the upscaling of the fracture properties from one material scale to another, the particle model

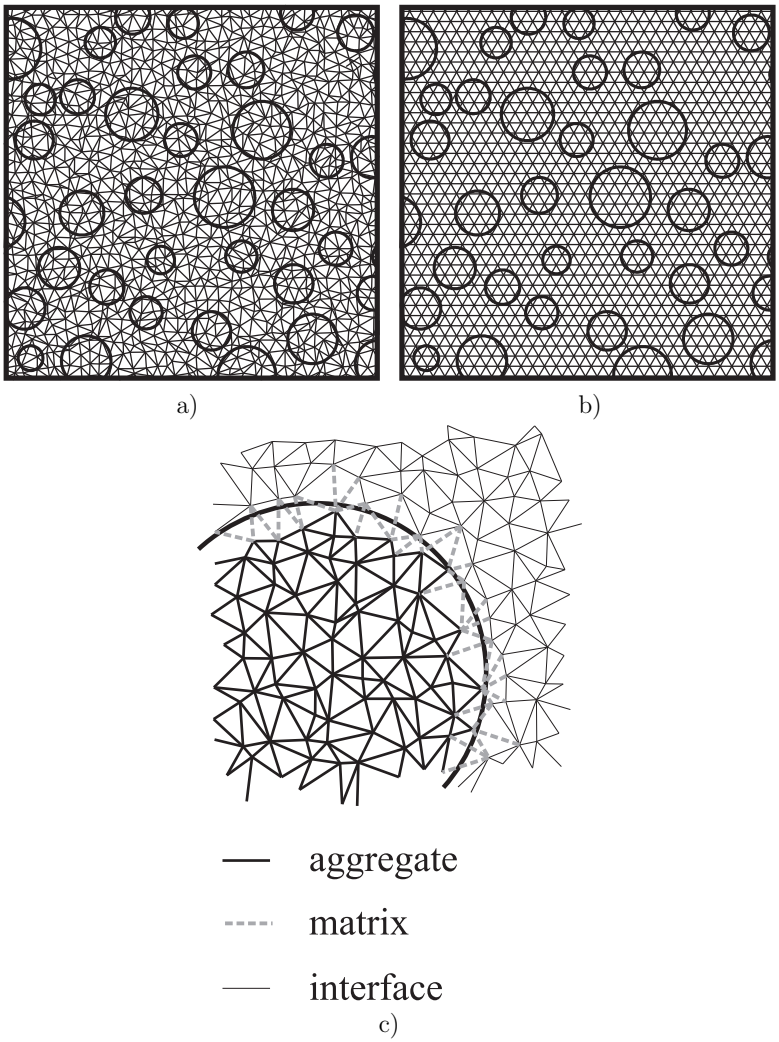

Figure 3.2: a) discretization of concrete mesostructure by random lattice model and regular lattice model; b) assignment of material properties to lattice elements. Courtesy Jan Eliáš.

was chosen because of its lowest computational demands allowing the experi-

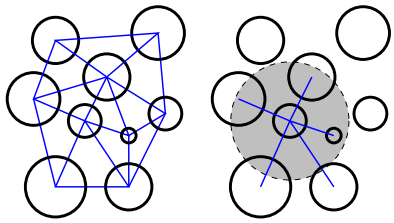

Figure 3.3: Particle models - mesh defined by the particle stack, a), and by the maximum interacting distance, b).

mental scale separation. Particle model of Cusatis (Cusatis, et al. 2003, Cusatis et al. 2006, Cusatis & Cedolin 2007) was taken as the underlying model. The particle model, its modifications and applications are summarized in Chapter

Chapter 4

Particle Model

Simulation of the fracture propagation in heterogeneous materials is a challenging task. Due to computational demands, it is not generally possible to simulate all particles and their mutual interactions with the matrix and some simplifications are needed. In the case of particle models, it is assumed that the fracture propagates in the matrix between the particles only and the behavior can be approximately modeled by links connecting the particles.

This Chapter introduces in a detailed way the particle model developed from the model of Cusatis (Cusatis et al. 2003, Cusatis et al. 2006, Cusatis & Cedolin 2007), its enrichments, applied solution strategies, implementation of the model and its applications for simulations of the fracture process in concrete. Applications of the particle model for upscaling of the fracture properties are discussed in Chapter

$$D_{\text{next}} = D_i + \frac{(D_{i-1} - D_i)(1 - \frac{\alpha_c}{\alpha_{agg}} - f_i)}{f_{i-1} - f_i}, \tag{4.1}$$

where D_i is the diameter of the first sieve that the previous particle does not pass, D_{i-1} denotes the diameter of the last sieve that was passed by the previous particle and f_i and f_{i-1} stand for the corresponding volume fractions of aggregates passed. Symbol α_c denotes the relative volume occupied by particles generated so far and α_{agg} denotes the relative volume which would be occupied when all the particles described by the PSD would be generated. ii) Coordinates of the particle are randomly generated and the particle is checked for overlapping with boundaries of the specimen and with previously placed particles. This last step is repeated until the particle is successfully placed without any overlapping.

The geometrical discretization of the idealized geometry as well as the material model were taken from (Cusatis & Cedolin 2007). The following paragraphs

briefly describe the most important aspects of the model necessary for understanding of the presented applications and stress the improvements done. Readers are referred to the original works for detailed explanations.

The adopted particle model lumps the behavior of the modeled material into a contact between two cells containing always one and only one particle. The cells are created based on tessellation of the mesostructure and determine geometrical properties - position and area - of the contacts. The contacts are created and discretized in the following way. First, the idealized geometry is triangulated using 3D Delaunay triangulation of particles centers (second image of Figure

4.0.1 Kinematics of the model

The overall response of the strut is localized into zero-thickness contact element at the point C. Displacement of a point x of the strut can be expressed from the rigid movements of the two parts as

$$\mathsf{u}(\mathsf{x}) = \mathsf{u}_i + \theta_i \times (\mathsf{x} - \mathsf{x}_i) = \mathsf{A}_i(\mathsf{x})\mathsf{Q}_i, \tag{4.2}$$

where

$$\mathsf{A}_i(\mathsf{x}) = \begin{bmatrix} 1 & 0 & 0 & 0 & z - z_i & y_i - y \\ 0 & 1 & 0 & z_i - z & 0 & x - x_i \\ 0 & 0 & 1 & y - y_i & x_i - x & 0 \end{bmatrix}. \tag{4.3}$$

The vector $\mathsf{x} = [x\ y\ z]^{\mathrm{T}}$ collects spatial coordinates and vectors $\mathsf{u}_i = [u_x\ u_y\ u_z]^{\mathrm{T}}$ and $\theta_i = [\theta_x\ \theta_y\ \theta_z]^{\mathrm{T}}$ collect displacement and rotations of the node of the strut corresponding to the center of the $i-th$ particle. The vector $\mathsf{Q}_i = \left[\mathsf{u}_i^{\mathrm{T}} \theta_i^{\mathrm{T}}\right]^{\mathrm{T}}$ collects all DOFs of the node i. The displacement jump at the contact of two cells belonging to particles i and j can be expressed as

$$[[\mathsf{u}_C]] = \mathsf{u}(\mathsf{x}_C^+) - \mathsf{u}(\mathsf{x}_C^-) = \mathsf{A}_j(\mathsf{x}_C)\mathsf{Q}_j - \mathsf{A}_i(\mathsf{x}_C)\mathsf{Q}_i \tag{4.4}$$

Normal and shear strains can be computed by projecting the displacement jump from Eq. (to given directions and normalizing with respect to the length of the strut, l. This leads to

$$\begin{array}{rclcrclcl} \varepsilon_{\mathrm{N}} & = & \mathsf{n}^{\mathrm{T}}\left[[\mathsf{u}_C]\right]/l & = & \mathsf{n}^{\mathrm{T}}\mathsf{A}_j(\mathsf{u}_C)\mathsf{Q}_j/l - \mathsf{n}^{\mathrm{T}}\mathsf{A}_i(\mathsf{u}_C)\mathsf{Q}_i/l & = & \mathsf{B}_{\mathrm{N}j}\mathsf{Q}_j - \mathsf{B}_{\mathrm{N}i}\mathsf{Q}_i, \\ \varepsilon_{\mathrm{L}} & = & \mathsf{l}^{\mathrm{T}}\left[[\mathsf{u}_C]\right]/l & = & \mathsf{l}^{\mathrm{T}}\mathsf{A}_j(\mathsf{u}_C)\mathsf{Q}_j/l - \mathsf{l}^{\mathrm{T}}\mathsf{A}_i(\mathsf{u}_C)\mathsf{Q}_i/l & = & \mathsf{B}_{\mathrm{L}j}\mathsf{Q}_j - \mathsf{B}_{\mathrm{L}i}\mathsf{Q}_i, \\ \varepsilon_{\mathrm{M}} & = & \mathsf{m}^{\mathrm{T}}\left[[\mathsf{u}_C]\right]/l & = & \mathsf{m}^{\mathrm{T}}\mathsf{A}_j(\mathsf{u}_C)\mathsf{Q}_j/l - \mathsf{m}^{\mathrm{T}}\mathsf{A}_i(\mathsf{u}_C)\mathsf{Q}_i/l & = & \mathsf{B}_{\mathrm{M}j}\mathsf{Q}_j - \mathsf{B}_{\mathrm{M}i}\mathsf{Q}_i, \end{array} \tag{4.5}$$

where $\mathsf{n} = (\mathsf{x}_j - \mathsf{x}_i)/l$ is the unit vector orthogonal to the projected contact area and vectors l and m are mutually orthogonal unit vectors both laying at

the plane of the projected contact area. Consistently, the total elastic stress transfered by the contact area can be split into three components:

$$\begin{aligned} \sigma_{\mathrm{N}} &= E\varepsilon_{\mathrm{N}}, \\ \sigma_{\mathrm{L}} &= E_{\mathrm{T}}\varepsilon_{\mathrm{L}}, \\ \sigma_{\mathrm{M}} &= E_{\mathrm{T}}\varepsilon_{\mathrm{M}}, \end{aligned} \tag{4.6}$$

where E is the elastic normal stiffness and E_{T} is elastic shear stiffness of the contact. Corresponding forces can be obtained by multiplication of the stresses by the projected contract area, A_p. Having formulated relationships between nodal displacements and rotations and forces, the local stiffness matrix of the strut can be expressed. Nodal forces of the strut can be computed as

$$\mathsf{f}^{ij} = \mathsf{K}^{ij}\mathsf{d}^{ij}, \tag{4.7}$$

where $\mathsf{d}^{ij} = [\mathsf{Q}_i^{\mathrm{T}}\ \mathsf{Q}_j^{\mathrm{T}}]^{\mathrm{T}}$ is a vector collecting nodal displacements and rotations in the global coordinate system; vector f^{ij} collects corresponding nodal forces and moments and $\mathsf{K}^{ij} = \boldsymbol{K}_{ab}^{ij}$ with $a, b = 0, 1 \ldots 11$ is the elastic stiffness matrix of the strut in the global coordinate system. The stiffness matrix can be expressed as

$$\begin{aligned} \boldsymbol{K}_{ab}^{ij} &= A_p l \left[E B_a^{\mathrm{N}i} B_b^{\mathrm{N}i} + E_{\mathrm{T}} \left(B_a^{\mathrm{L}i} B_b^{\mathrm{L}i} + B_a^{\mathrm{M}i} B_b^{\mathrm{M}i} \right) \right] && \text{if } a \leq 5 \text{ and } b \leq 5, \\ \boldsymbol{K}_{ab}^{ij} &= A_p l \left[E B_{a-6}^{\mathrm{N}j} B_{b-6}^{\mathrm{N}j} + E_{\mathrm{T}} \left(B_{a-6}^{\mathrm{M}j} B_{b-6}^{\mathrm{L}j} + B_{a-6}^{\mathrm{M}j} B_{b-6}^{\mathrm{M}j} \right) \right] && \text{if } a \geq 6 \text{ and } b \geq 6, \\ \boldsymbol{K}_{ab}^{ij} &= -A_p l \left[E B_{b-6}^{\mathrm{N}j} B_a^{\mathrm{N}i} + E_{\mathrm{T}} \left(B_{b-6}^{\mathrm{M}j} B_a^{\mathrm{L}i} + B_{b-6}^{\mathrm{M}j} B_a^{\mathrm{M}i} \right) \right] && \text{if } a \leq 5 \text{ and } b \geq 6, \\ \boldsymbol{K}_{ab}^{ij} &= -A_p l \left[E B_b^{\mathrm{N}i} B_{a-6}^{\mathrm{N}j} + E_{\mathrm{T}} \left(B_b^{\mathrm{L}i} B_{a-6}^{\mathrm{L}j} + B_b^{\mathrm{M}i} B_{a-6}^{\mathrm{M}j} \right) \right] && \text{if } a \geq 6 \text{ and } b \leq 5 \end{aligned} \tag{4.8}$$

with $\mathsf{B}_{\mathrm{N}i}$, $\mathsf{B}_{\mathrm{L}i}$ etc. defined by Eq. (. Note that Einstein index notation is not used in the above Equations as well as in the remaining part of this Chapter.

4.0.2 Constitutive model

The constitutive model originally introduced in (Cusatis et al. 2003) and further improved in (Cusatis et al. 2006) was taken for the most part. In the following part, its main features and improvements are presented with emphasis given to the particular implementation used.

Elastic behavior

Linear relationships from Eq. (are used. The elastic normal stiffness, E, corresponds to the averaged stiffness of materials laying between nodes i and j of the strut. The average can be approximated by serial coupling and

$$E = l/(l_a/E_a + l_m/E_m), \tag{4.9}$$

where E_a and E_m are Young's moduli of aggregates and matrix, respectively. Length l_a corresponds to segments of the strut laying inside particles i and j, $l_a = \frac{1}{2}(D_i + D_j)$, and $l_m = l - l_a$ denotes the remaining part of the strut belonging to the matrix. The elastic normal stiffness can be expressed as a fraction of the normal stiffness, $E_{\mathrm{T}} = \alpha E$, where α is a coupling parameter controlling the Poisson's ratio.

Inelastic behavior

The mesoscopical damage-like constitutive model is formulated in terms of effective stress, σ, effective strain, ε, and coupling strain, ω. The effective stress is computed by

$$\sigma = \sqrt{\sigma_{\mathrm{N}}^2 + \frac{\sigma_{\mathrm{T}}^2}{\alpha}} \quad \text{where} \quad \sigma_{\mathrm{T}} = \sqrt{\sigma_{\mathrm{L}}^2 + \sigma_{\mathrm{M}}^2}.$$

Accordingly, the effective strain can be expressed as

$$\varepsilon = \sqrt{\varepsilon_{\mathrm{N}}^2 + \alpha\varepsilon_{\mathrm{T}}^2} \quad \text{with} \quad \varepsilon_{\mathrm{T}} = \sqrt{\varepsilon_{\mathrm{L}}^2 + \varepsilon_{\mathrm{M}}^2}.$$

The coupling strain, ω, reflecting the direction of loading, can be expressed as

$$\tan\omega = \frac{\varepsilon_{\mathrm{N}}}{\sqrt{\alpha}\varepsilon_{\mathrm{T}}}. \tag{4.10}$$

See (Cusatis et al. 2003) for all the details. The effective stress, σ, needs to satisfy inequality $0 \leq \sigma \leq \sigma_b(\varepsilon, \omega)$ and the effective stress boundary, $\sigma_b(\varepsilon, \omega)$, can be expressed as

$$\sigma_b(\varepsilon, \omega) = \sigma_{b,0}(\omega)\exp\left[\frac{K(\omega)}{\sigma_{b,0}(\omega)}\left\langle\chi(\varepsilon, \omega) - \varepsilon_0(\omega)\right\rangle\right], \tag{4.11}$$

where $\langle\bullet\rangle = \max\{0, \bullet\}$. Function $\sigma_{b,0}(\omega)$ denotes the initial boundary of the elastic domain, see Figure

The initial elastic domain is a hyperbola in the $\sigma_{\mathrm{N}} - \sigma_{\mathrm{T}}$ space with an ellipsoidal cup in the compression. The hyperbola is described as

$$\sigma_{b,01}(\omega) = \frac{-(f_t + \sigma_a)s + \sqrt{[(f_t + \sigma_a)s]^2 + [\alpha(c/\mu)^2 - s^2](f_t + 2\sigma_a)f_t}}{\alpha(c/\mu)^2 - s^2}, \tag{4.12}$$

where f_t corresponds to the mesoscopical tensile strength, $c = \cos\omega$, $s = \sin\omega$, μ is an asymptote of the hyperbola and $\sigma_a = 0.5 f_t[f_s^2/(\mu f_t)^2 - 1]$ with f_s

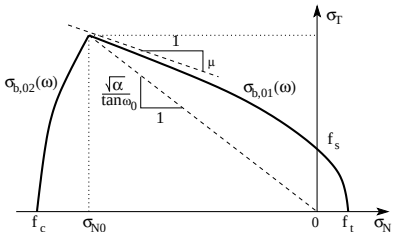

Figure 4.1: Initial boundary of the elastic domain.

denoting the shear strength at the meso-level. The ellipsoidal cup has equation

$$\sigma_{b,02}(\omega) = \frac{f_c}{\sqrt{s^2 + \alpha c^2/\beta}}, \tag{4.13}$$

where f_c is the mesoscopical compressive strength and β is a shape parameter of the ellipse. The strain decay function in Eq. (, $\chi(\varepsilon, \omega)$, is defined as

$$\chi(\varepsilon, \omega) = \begin{cases} \varepsilon & \text{for } \omega \leq \omega_0 \\ \varepsilon_{\max} & \text{for } \omega > \omega_0 \end{cases} \tag{4.14}$$

with ω_0 denoting the intersection of $\sigma_{b,01}(\omega)$ and $\sigma_{b,02}(\omega)$ and $\varepsilon_{\max} = \sqrt{\max\varepsilon_{\mathrm{N}}^2 + \max\varepsilon_{\mathrm{T}}^2}$; $\max\varepsilon_{\mathrm{N}}$ is the maximal positive normal strain reached in the loading history and $\max\varepsilon_{\mathrm{T}}$ is the maximal total shear strain reached. The initial slope function in Eq. (, $K(\omega)$, is defined as

$$K(\omega) = \begin{cases} K_c - K_c \left(\frac{\omega + \pi/2}{\omega_0 + \pi/2} \right)^{n_c} & \text{for } \omega \leq \omega_0 \\ K_t - K_t \left(\frac{\omega - \pi/2}{\omega_0 - \pi/2} \right)^{n_t} & \text{for } \omega > \omega_0 \end{cases} \tag{4.15}$$

The initial slope is positive for $\omega \leq \omega_0$ resulting in a hardening behavior in compression and negative for $\omega > \omega_0$ leading to a strain softening. For $\omega = \pi/2$ corresponding to the pure tension, parameters K_t and n_t can be identified. Since the energy dissipated in a unit volume has to be equal to the mesoscopical mode-I fracture energy, G_t, one can write

$$\int_0^\infty \sigma_{\mathrm{N}}(\varepsilon_{\mathrm{N}})\, \mathrm{d}\varepsilon_{\mathrm{N}} = G_t/l. \tag{4.16}$$

Substituting Eq.

In the very original version of the material model (Cusatis et al. 2003), an effect of confining stresses on the mesoscale was introduced. The confining stresses

modify the post-peak response of a strut due to the improved properties of bonds between the matrix and small particles not considered in the simulation, but present between the simulated particles in reality. The confinement improves the pull-out resistance of the particles out of matrix and promotes bridging. In (Cusatis et al. 2006), the effect of confining stresses is substituted by the effect of confining strains, which makes the formulation completely explicit and the numerical algorithm more robust. However, the original physical justification is partly lost since the strains are not linear function of stresses after the initial elastic boundary is reached. In the strain-based formulation, the highest confining effect, giving the highest bond strength, is reached in very late steps of a simulation when very high strains, but very small stresses, are reached.

Due to the aforementioned discrepancies in the strain-based formulation, increased computational demands of the stress-based formulation and due to only a negligible effect of the confining stresses on the experiments considered, the effect of the confinement was completely excluded from the applied material model. Figure

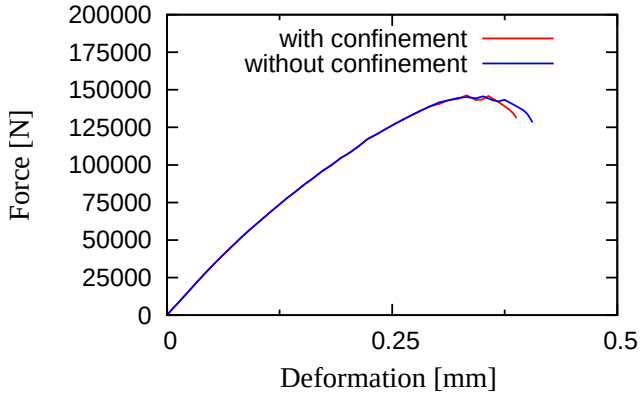

Figure 4.2: Effect of the confining stress on the response of the compressive test on cylinders.

As already mentioned, the material model was implemented as the scalar damage model. The material response is elastic, governed by Eq. (, until the initial boundary of the elastic domain was reached. Then the response was governed by

$$\mathsf{f}^{ij} = (1 - D)\mathsf{K}^{ij}\mathsf{d}^{ij}, \tag{4.17}$$

where $D \in < 0, 1 >$ is the damage parameter.

Nonuniform loading

Since nonuniform loading paths were of interest for certain applications of the particle model, see Paper III, it was necessary to include an effect of the stiffness recovery once an opened crack was closed and loaded in compression. The damage parameter was therefore ω-dependent and defined as

$$D(\omega) = \begin{cases} \max\left\{1 - \frac{\sigma}{E\varepsilon}, D^{\omega^+}_{\max}\right\} & \text{for} \quad \omega \geq 0 \\ \max\left\{1 - \frac{\sigma}{E\varepsilon}, D^{\omega^-}_{\max}\right\} & \text{for} \quad \omega < 0, \end{cases} \tag{4.18}$$

where $D^{\omega^+}_{\max}$ and $D^{\omega^-}_{\max}$ is highest damage reached in the loading history when the strut was loaded in mixed mode tension or compression, respectively. Figure

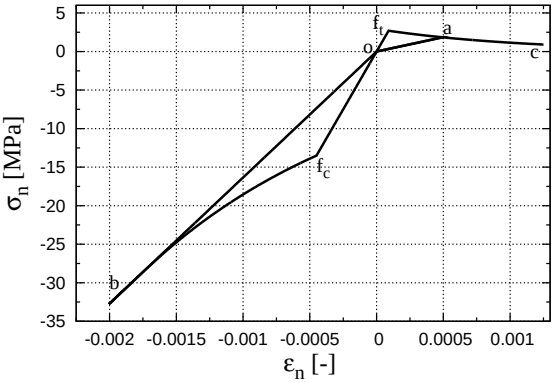

Figure 4.3: Behavior of a strut with the stiffness recovery in compression. The strut is loaded in tension ($o - f_t - a$), then unloaded to o, then loaded by compression ($0 - f_c - b$), then unloaded to o and finally loaded in tension again ($o - a - c$)

.

4.1 Solution strategies

In the previous Section, the behavior of a single strut was described. Global behavior of a structure or specimen is obtained from solution of discretized equations of equilibrium that can be written as

$$\mathsf{f}_{int}(\mathsf{d}) = \mathsf{f}_{ext}, \tag{4.19}$$

where $\mathsf{f}_{int}(\mathsf{d})$ is the internal force vector obtained by localization of f^{ij} corresponding to all struts in the model, d is the vector collecting the nodal displacements[1] of all nodes and f_{ext} is the external force vector collecting the load acting on the structure. Assume that the external force vector is independent on the nodal displacements. In the case of linear elasticity, the internal force vector can be directly expressed as

$$\mathsf{f}_{int}(\mathsf{d}) = \mathsf{K}\mathsf{d}, \tag{4.20}$$

where K is the global stiffness matrix of the model. Substituting Eq. (to Eq. (the global response of the model can be directly[2] computed as

$$\mathsf{d} = \mathsf{K}^{-1}\mathsf{f}_{ext}. \tag{4.21}$$

For a nonlinear material response, the internal force vector becomes a nonlinear function of the nodal displacements d. In the previous Equation, the global stiffness matrix, K, becomes a function of the nodal displacement as well and

$$\mathsf{d} = \mathsf{K}^{-1}(\mathsf{d})\mathsf{f}_{ext}. \tag{4.22}$$

Such an Equation can not be solved directly. Therefore, the concept of linearization is applied.

4.1.1 Linearization

Suppose that $\mathsf{f}_{int}(\overline{\mathsf{d}})$ is the vector of internal forces generated by nodal displacements $\overline{\mathsf{d}}$. The internal forces in the vicinity of $\overline{\mathsf{d}}$ can be expanded into Taylor series leading to

$$\mathsf{f}_{int}(\overline{\mathsf{d}} + \Delta\mathsf{d}) = \mathsf{f}_{int}(\overline{\mathsf{d}}) + \frac{\partial \mathsf{f}_{int}}{\partial \mathsf{d}}\Big|_{\mathsf{d}=\overline{\mathsf{d}}}\Delta\mathsf{d} + \dots. \tag{4.23}$$

For a small displacement increment, $\Delta\mathsf{d}$, the nonlinear terms represented by dots can be neglected and we obtain a linear approximation of the internal forces

$$\mathsf{f}_{int}(\overline{\mathsf{d}} + \Delta\mathsf{d}) \approx \mathsf{f}_{int}(\overline{\mathsf{d}}) + \mathsf{K}(\overline{\mathsf{d}})\Delta\mathsf{d} \tag{4.24}$$

in which $\mathsf{K}(\overline{\mathsf{d}})$ is the global tangent stiffness matrix of the model.

Having defined the linearized relationships, an incremental-iterative solution can be formulated to solve Eq. (. Usually, the external load is applied in several incremental steps and in every step, the structural response is computed from equilibrium equations, Eq. (. The step-size of the global load-adding loop can be controlled by several ways. Two control techniques, the direct displacement control and the indirect displacement control technique were implemented.

[1] Term displacements stands both for displacements and rotations.

[2] Conjugate gradients solver is used in the current implementation of the model.

4.1.2 Direct displacement control

The nodal displacements, d, can be divided into two parts $\{\mathsf{d}\} = \{\mathsf{d}_1, \mathsf{d}_2\}^{\mathrm{T}}$; d_1 corresponds to the internal DOFs which are unknown and d_2 collects DOFs with prescribed values. Accordingly, the vector of internal and external forces can be divided into $\{\mathsf{f}_{\mathsf{int}}\} = \{\mathsf{d}_{\mathsf{int},1}, \mathsf{d}_{\mathsf{int},2}\}^{\mathrm{T}}$ and $\{\mathsf{f}_{\mathsf{ext}}\} = \{\mathsf{f}_{\mathsf{ext},1}, \mathsf{f}_{\mathsf{ext},2}\}^{\mathrm{T}}$, respectively. External forces $\mathsf{f}_{ext,1}$ are prescribed and for simplicity equal to zero. External forces $\mathsf{f}_{ext,2}$ collects reactions at nodes with the prescribed nodal displacements d_2. The equilibrium equations are partitioned as

$$\mathsf{f}_{int,1}(\mathsf{d}_1, \mathsf{d}_2) = \mathsf{o} \tag{4.25}$$

$$\mathsf{f}_{int,2}(\mathsf{d}_1, \mathsf{d}_2) = \mathsf{f}_{ext,2}. \tag{4.26}$$

For the prescribed d_2, d_1 can be obtained by solving Eq. (. Substituting (to Eq. (, the reactions are computed. As already said, the system is solved in incremental steps and the structural response is tracked. Let $\mathsf{d}_1^{(n-1)}$ and $\mathsf{d}_2^{(n-1)}$ be solutions of Eqs. (and (in a step number $(n-1)$. Eq. (can be linearized as

$$\mathsf{f}_{int,1}^{(n-1)} + \mathsf{K}_{11}^{(n-1)} \Delta \mathsf{d}_1^{(n,1)} + \mathsf{K}_{12}^{(n-1)} \Delta \mathsf{d}_2^{(n,1)} = \mathsf{o}, \tag{4.27}$$

where $\mathsf{K}_{11} = \partial \mathsf{f}_{int,1} / \partial \mathsf{d}_1$ ands $\mathsf{K}_{12} = \partial \mathsf{f}_{int,1} / \partial \mathsf{d}_2$ are blocks of the global tangent stiffness matrix

$$\mathsf{K} \equiv \frac{\partial \mathsf{f}_{int}}{\partial \mathsf{d}} = \begin{bmatrix} \frac{\partial \mathsf{f}_{int,1}}{\partial \mathsf{d}_1} & \frac{\partial \mathsf{f}_{int,1}}{\partial \mathsf{d}_2} \\ \frac{\partial \mathsf{f}_{int,2}}{\partial \mathsf{d}_1} & \frac{\partial \mathsf{f}_{int,2}}{\partial \mathsf{d}_2} \end{bmatrix} = \begin{bmatrix} \mathsf{K}_{11} & \mathsf{K}_{12} \\ \mathsf{K}_{21} & \mathsf{K}_{22}. \end{bmatrix} \tag{4.28}$$

The increment $\Delta \mathsf{d}_2^{(n,1)}$ is prescribed and $\Delta \mathsf{d}_1^{(n,1)}$ is obtained by solving Eq. (. The approximation of the displacement $\mathsf{d}_1^{(n)} = \mathsf{d}_1^{(n-1)} + \Delta \mathsf{d}_1^{(n,1)}$ is constructed and Eq. (can be linearized around $(\mathsf{d}_1^{(n)}, \mathsf{d}_2^{(n)})$. This leads to the modifications of the global tangent stiffness matrix and to new corrections $\Delta \mathsf{d}_1^{(n,k)}$. The procedure is repeated until the convergence criteria are satisfied.

4.1.3 Arc length method - indirect displacement control

For the proportional loading, the external load can be expressed as $\mathsf{f}_{ext} = \lambda \overline{\mathsf{f}}$, where $\overline{\mathsf{f}}$ is a reference load vector and λ is a load parameter. Assume a converged displacements $\mathsf{d}^{(n-1)}$ and the corresponding load parameter $\lambda^{(n-1)}$. In the next step, n, a combination of $\mathsf{d}^{(n)}$ and $\lambda^{(n-1)}$ satisfying

$$\mathsf{f}_{int}(\mathsf{d}^{(n)}) = \lambda^{(n)} \overline{\mathsf{f}} \tag{4.29}$$

are to be found. The load parameter, $\lambda^{(n)}$, is an additional unknown. Therefore, an additional equation controlling a length of the step is required. In the

case of the indirect displacement control, the equation yields

$$\mathsf{c}^{\mathrm{T}}\Delta\mathsf{d} = \overline{\Delta l}, \tag{4.30}$$

where c is a column vector prescribing a projection of the displacement vector onto the direction given by c and $\overline{\Delta l}$ is the step size. The choice of the c needs to be such that $\mathsf{c}^{\mathrm{T}}\Delta\mathsf{d}$ is increasing all the time. Linearized equations of equilibrium in $i-th$ iteration of step n read then

$$\mathsf{K}^{(n,i-1)}\delta\mathsf{d}^{(n,i)} = \lambda^{(n,i-1)}\overline{\mathsf{f}} - \mathsf{f}_{int}^{(n,i-1)} + \delta\lambda^{(n,i)}\overline{\mathsf{f}}, \tag{4.31}$$

where $\delta\mathsf{d}^{(n,i)}$ is the unknown displacement correction and $\delta\lambda^{(n,i)}$ is the unknown correction of the load parameter. The Eq. (can be split into two separated equations

$$\mathsf{K}^{(n,i-1)}\delta\mathsf{d}_0 = \lambda^{(n,i-1)}\overline{\mathsf{f}} - \mathsf{f}_{int}^{(n,i-1)}\mathsf{K}^{(n,i-1)}\delta\mathsf{d}_f = \delta\lambda^{(n,i)}\overline{\mathsf{f}} \tag{4.32}$$

and the unknown displacement correction, $\delta\mathsf{d}^{(n,i)}$, can be expressed as

$$\delta\mathsf{d}^{(n,i)} = \delta\mathsf{d}_0 + \delta\lambda^{(n,i)}\delta\mathsf{d}_f. \tag{4.33}$$

Substituting Eq. (into Eq. (, the correction of the load parameter can be expressed as

$$\delta\lambda^{(n,i)} = \frac{\overline{\Delta l} - \mathsf{c}^{\mathrm{T}}\Delta\mathsf{d}^{(n,i-1)} - \mathsf{c}^{\mathrm{T}}\delta\mathsf{d}_0}{\mathsf{c}^{\mathrm{T}}\delta\mathsf{d}_f}. \tag{4.34}$$

Adaptive step length (Crisfield 1984, Bittnar & Šejnoha 1992) was introduced to accelerate or damp the analysis. The step length in the current step, $\overline{\Delta l}$, was computed as

$$\overline{\Delta l} = \overline{\Delta l}_{prev}\sqrt{\frac{N_{it,opt}}{N_{it,prev}}}, \tag{4.35}$$

where $\overline{\Delta l}_{prev}$ stands the step length in the previous step, $N_{it,prev}$ is the number of iterations needed to fulfill the convergence criteria in the previous step and $N_{it,opt}$ is a parameter describing the optimal number of iterations in which the convergence criteria should be fulfilled. The effect of the damping and acceleration of the analysis is demonstrated in Figure

After initial step with elastic solution found in one iteration, the step length in the second step is $\sqrt{N_{it,opt}}$-times bigger. Close to the peak load the analysis is damped due to higher number of iterations needed for convergence (localization of the main crack) while at the last stages the increase of the step length is visible again.

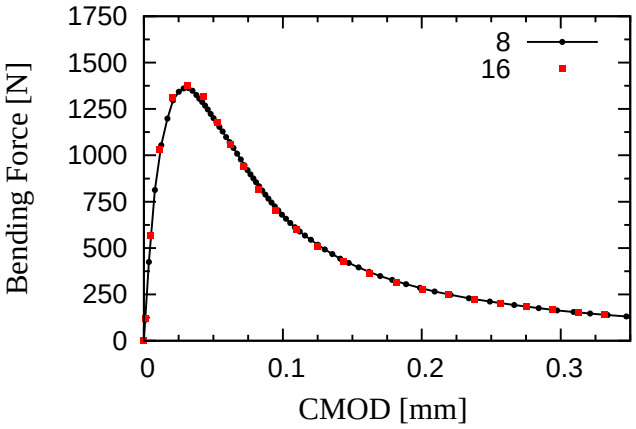

Figure 4.4: Effect of variable arc length for different different choices of $N_{it,opt}$ on a simulation of TPBT.

Similar accelerating and damping technique was implemented for the direct displacement control as well. The increment of the prescribed displacement, $\Delta \mathsf{d}_2^{(n,1)}$ in Eq. (, was computed as:

$$\Delta \mathsf{d}_2^{(n,1)} = \overline{\Delta l} \Delta \mathsf{d}_2, \tag{4.36}$$

where $\overline{\Delta \mathsf{d}_2}$ is the reference displacement increment and $\overline{\Delta l}$ is computed from Eq. (.

4.1.4 Governing parameters of the nonlinear problem solution - convergence analysis

In the $i-th$ step of the linearized solution, the solution of Eq.(was accepted when $\gamma^i \leq \gamma_{con}$, where

$$\gamma^i = \frac{W_{un}}{W_{in}} \tag{4.37}$$

$$W_{un} = |\mathsf{d}|^{\mathrm{T}} |\mathsf{f}_{un}| \tag{4.38}$$

$$W_{in} = |\mathsf{d}|^{\mathrm{T}} |\mathsf{f}_{int}| \tag{4.39}$$

$$\mathsf{f}_{un} = \mathsf{f}_{int} - \mathsf{f}_{ext}. \tag{4.40}$$

The absolute values $|\{\mathsf{x}\}| = \{|\mathsf{x}_1|, |\mathsf{x}_2|, \ldots\}^{\mathrm{T}}$ and γ_{con} is the prescribed tolerance. In order to identify the influence of the choice of the tolerance, γ_{con}, a convergence analysis was performed. Seven simulations with the ratios from

$\gamma_{con} = 1 \times 10^{-1}$ to $\gamma_{con} = 1 \times 10^{-4}$ were run for the TPBT of Aalborg basis concrete described in Paper IV. Results are shown in Figure

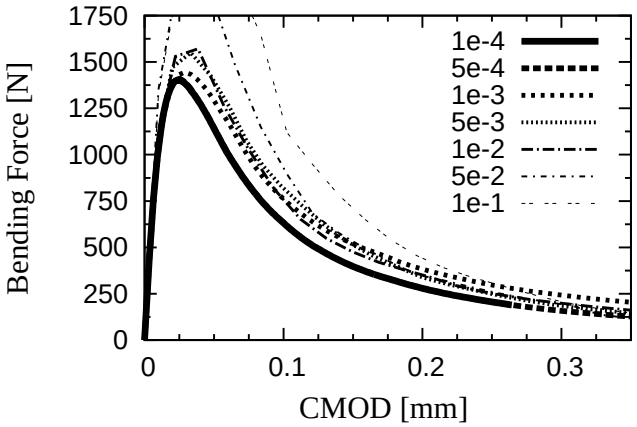

Figure 4.5: Convergence analysis of the TPBT.

4.2 Model enrichments

4.2.1 Matrix nodes

In the original implementation of the model, centers of aggregates are taken as the nodes of the finite element discretization and the contact is assumed to be placed in the middle of the ligament between the aggregates. Under such an assumption, the crack is forced to propagate only in regions with the biggest distances to aggregates which is in a contradiction with experimental observations where cracks tend to propagate "around" aggregates as well as with the assumption of the ITZ being the weakest part in the mesostructure. Assuming that the cracking takes place in the middle between the aggregates only also creates an exaggerated roughness of the crack path. In order to improve the behavior of the model, additional artificial nodes, *matrix nodes*, were placed in the inter-particle volume resulting in a more natural crack propagation (see Figure

The described enrichment results in a more realistic crack propagation with a reduced roughness of the crack path and only the roughness resulting from mesostructural geometry is preserved as is illustrated by Figure

Reducing the crack path roughness and increasing the number of contacts in the model leads to changes is the predicted response which is then dependent on

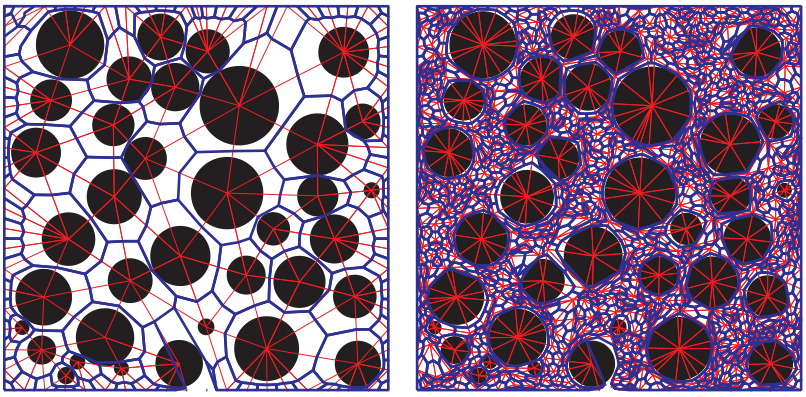

Figure 4.6: 2D scheme of the effect of the additional matrix nodes on the number of contacts.

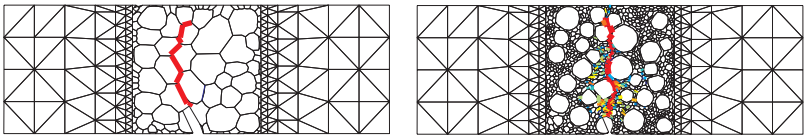

Figure 4.7: 2D scheme of the effect of the additional matrix nodes on the crack roughness in mode-I fracture propagation in a TPBT.

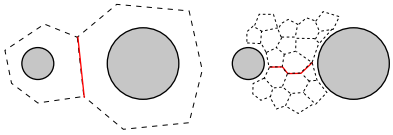

Figure 4.8: Scheme of a radial crack propagation in the enriched model.

the amount of the matrix nodes added. A convergence analysis was performed to quantify these effects. A reference mesostructure was generated and then the matrix nodes were added in 5 steps. In every step, $\frac{1}{4}N_{agg}$ of matrix nodes were added, where N_{agg} is the amount of proper aggregates generated according to Eq. (. The response does not change significantly anymore after $\frac{3}{4}N_{agg}$ matrix nodes were added (see Figure

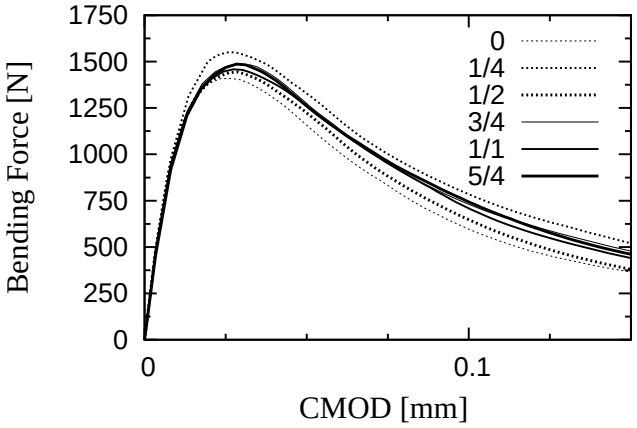

Figure 4.9: Convergence analysis with respect to the addition of the matrix nodes.

4.2.2 Effect of the ITZ

The elastic normal stiffness of the contact, E, corresponds to the averaged stiffness of materials laying between two nodes of the strut, see Eq. (. Since the diameter of the smallest aggregate simulated by authors in the original work was 4.75 mm, it was possible to neglect the effect of the ITZ. However, in an application where the diameter of the smallest simulated aggregate is comparable with the thickness of the ITZ, it is necessary to include the effect of ITZ on the stiffness of the contact. The average stiffness of the materials between two nodes can be approximated by the serial coupling and

$$E_{ITZ} = l/(l_a/E_a + l_m/E_m + l_{ITZ}/E_{ITZ}), \tag{4.41}$$

where E_a, E_m and E_{ITZ} are Young's moduli of aggregates, matrix and ITZ, respectively. Length l_a corresponds to segments of the strut laying inside particles, l_{ITZ} corresponds to two times ITZ thickness and $l_m = l - l_a - l_{ITZ}$ denotes the remaining part of the strut belonging to the matrix.

Figure

4.3 Implementation

This Section describes solutions and algorithms used for some of the major challenges found during the numerical implementation of the model.

The two dimensional version of the model was implemented in Matlab with satisfactory performance. However, when the model was extended into three

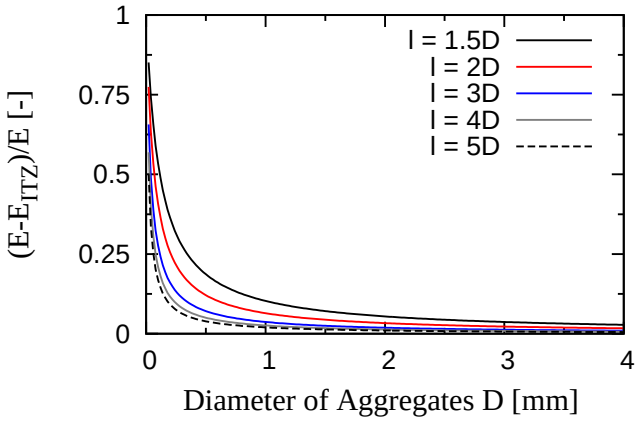

Figure 4.10: Effect of the ITZ on the stiffness of the strut for varying aggregates diameter and length of the strut.

dimensions, the computational time increased for orders of magnitude and become unacceptable. Therefore the model was implemented in C++ and several modifications improving the performance were done.

4.3.1 Model building

During the particle generation phase, the newly created particle was checked for overlapping with all previously generated particles in the 2D implementation of the model. In three dimensions, however, such a simple approach resulted in a very poor performance. The performance was improved using a grid overlay algorithm. A three dimensional grid storing IDs of particles presented in or overlapping with a cell of the grid was created. Then, the newly created particle was checked for overlapping only with the particles belonging to cells overlapping with the new particle and the cells stored the ID of the new particle.

In the model building phase, the most of the computational time was spent by the detection of edges of tetrahedrons and by linking of the struts created from edges with the tetrahedrons. It was necessary to detect every edge of tetrahedrons presented, create a strut from the edge and make sure that there is one and only one strut at the given edge. Further, it was necessary to know to which tetrahedrons does the edge belongs to and vice versa. The original straightforward implementation was following:

```
for (all tetrahedrons)
     for (all edges of the tetrahedron)
          for (all struts created so far)
```

```
                if (edge not yet represented by strut)
                     make new strut
                end if
           end for
     end for
end for

for (all struts)
     for (all tetrahedrons)
          if (strut and tetrahedron share 2 vertexes)
               strut saves id of the tetrahedron
               tetrahedron saves id the of strut
          end if
     end for
end for
```

New implementation was following:

```
create a map mapping combinations of vertexes with yet unknown id of strut
for (all tetrahedrons)
     for (all combinations of vertexes of the tetrahedron)
          if (id in the map for the given combination of vertexes is empty)
               make new strut
               save id of the new strut in the map
          end if
          strut at the map at the given combination saves id of the tetrahedron
     end for
end for

for (all struts)
     for (all tetrahedrons ids saved by the strut)
          tetrahedron saves id of strut
     end for
end for
```

Such a modification resulted in a significant improvement of the computational time reducing the model building phase from tens of minutes to tens of seconds for the same (complex) mesostructure.

4.3.2 Sparse matrix algebra and solver

As already mentioned in the introductory part of this Section, poor performance of the Matlab built-in sparse matrix algebra package was the main reason for the C++ implementation of the particle model. Several sparse matrix packages available on the Internet were implemented and compared. Regrettably, none of them fitted the needs of the program and author's programming skills. Some of the packages showed great performance, but creation and especially modification of matrices during computation necessary e.g. during updating of the global stiffness matrix was cumbersome and required e.g. copying of the matrix to the memory which ruined the performance. Some packages provided straightforward and simple access to the matrix and its elements and their modification, but did not performed much better compared to the Matlab implementation. Finally, a sparse matrix algebra package developed by Cyrille Dunant from LMX, EPFL (Dunant 2009) was implemented. The package provided simple access to the elements of the matrix and satisfactory performance.

Systems of equations were solved by conjugate gradients solver with diagonal preconditioning of the matrix of coefficients, see (Rektorys & a spol. 1981).

4.3.3 Parts of specimens outside of the FPZ

In the two dimensional implementation of the particle model, the material outside the vicinity of the FPZ was modeled using linear finite elements. To preserve the same number of DOFs per node, the triangular elements with drilling degrees of freedom (Felippa 2003) were implemented, see Figure

In three dimensions, however, the implementation of similar approach would require a significant amount of coding. Therefore a different approach was utilized. The bulk material was modeled using the particle model as well, but the minimal diameter of the aggregate generated as well as the spacing of the nodes on the edges of the specimen were reduced. The struts created outside of the FPZ were treated as linear elastic without any strength limits. Figure

4.4 Applications of the particle model

In this Section, applications of the introduced particle models demonstrating the advantages and disadvantages of the approach are presented. The particle model is used for simulation of experiments with complex stress distributions, e.g. a non-proportional mixed-mode experiment, in Section

However, the major application of the particle model - upscaling of fracture properties and prediction of the strength of cementitious materials - is discussed

in Chapter

4.4.1 Simulation of complex experiments

Most of the complexity of the mechanical behavior of concrete on macro-scale results from its heterogeneous mesostructure. When the concrete is modeled under the assumption of homogeneity, this complexity has to be included in constitutive laws which makes them complex, with many parameters and thus difficult to be determined experimentally. Since the heterogeneous geometry is already captured by the heterogeneous models, simple material laws with straightforward physical meaning can be used instead.

Paper III presents a comparison of the particle model and the lattice model (Eliáš 2009) for simulation of non-proportional mixed-mode crack growth in concrete.

Simulations of the mode I experiments (TPBT) and of cylinders loaded in compression presented in Paper IV are another demonstration of the robustness of the particle model. Material properties of the model were measured on mortar samples and inserted into the particle model of concrete for the TPBT and compression tests. The predictions matched favorably the experimental records. Details can be found in Paper IV.

4.4.2 Intrinsic variability and size effect

The process of meso-structure generating described in Section

Comparison of 2D and 3D particle model

Initially, the effect of the random placing of aggregates was studied using the 2D implementation of the particle model. 10 simulations of the TPBT described in Section

From Figure

In the case of the three dimensional model, the effect of the initial crack branching is smeared through the thickness of the specimen and the simulations are therefore more objective. Application of the three dimensional particle model to simulate the intrinsic variability and the size effect in the TPBT simulations is discussed in Section

Size effect

The ability of the particle model to simulate the size effect was investigated using the 3D implementation. Sets of simulation of the TPBT, see Appendix

Figure

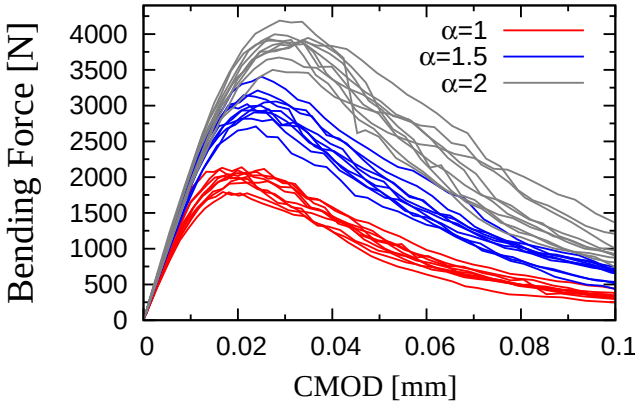

Figure 4.11: Effect of the random aggregates placement on the response of the TPBT for different sizes of the specimen simulated using the 2D particle model.

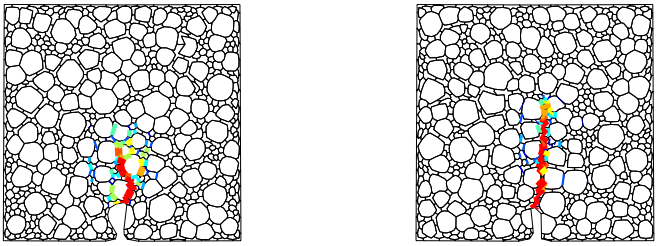

a) b

Figure 4.12: Two types of the initial crack propagation in 2D particle model: crack branching leading to higher peak load, a), and a single crack formed in the matrix, b).

4.4.3 Effect of aggregates volume fraction

The effect of the volume fraction of aggregates on the simulated response of the TPBT was investigated. The material properties of the mortar containing aggregates up to 2 mm, see Paper IV for details about material parameters identification and underlying assumptions, are summarized in Table

The increased amount off aggregates results in the higher peak load. The higher peak load is caused by the increased width of the fracture process zone and increased roughness of the main crack path resulting in promoted bridging and increased amount of the dissipated energy. The right hand sides of Figures

Model parameter	Abbreviation [unit]	value
Young's modulus of aggregates	E_a [GPa]	80
Young's modulus of matrix	E_m [GPa]	28.3
Young's modulus of ITZ	E_{ITZ} [GPa]	10
Thickness of ITZ	l_{ITZ} [mm]	0.043
Coupling parameters	α [-]	0.25
Uniaxial meso-tensile strength	f_t [MPa]	3.93
Uniaxial meso-shear strength	f_s [MPa]	$3f_t$
Mode-I meso-fracture energy	G_t [J/m^2] 66.7	
Mode-II meso-fracture energy	G_t [J/m^2]	$12.5G_t$
Friction coefficient	μ [-]	0.2
Uniaxial meso-compressive strength	f_c [MPa]	1000

Table 4.1: Material parameters used for the case studies with the particle model. Values of remaining parameters of the material model not relevant for the mixed-mode crack propagation which are not listed in the table were taken from (Cusatis et al. 2003).

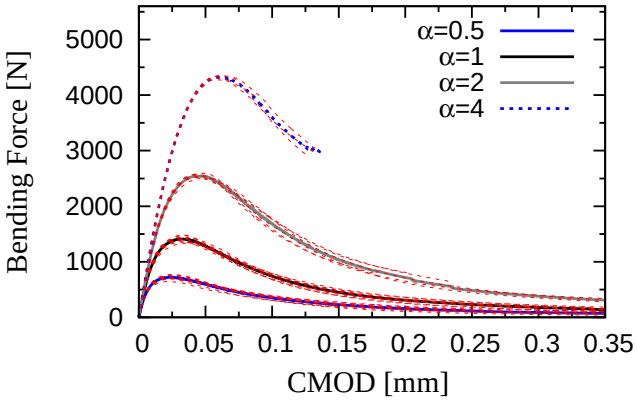

Figure 4.13: Size effect: simulations of TPBTs with similar geometries but different sizes.

4.4.4 Numerical comparison of mode-I fracture tests

Section

Application of the hinge model-based inverse analysis described in Section

TPBT described in Appendix

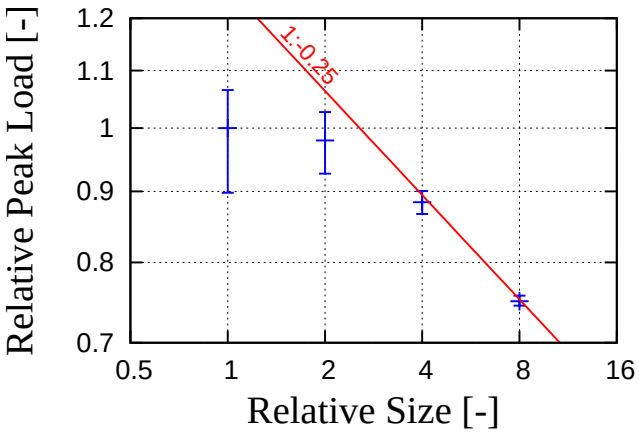

Figure 4.14: Size effect: normalized peak load and scatter of the peak load for different sizes of TPBT.

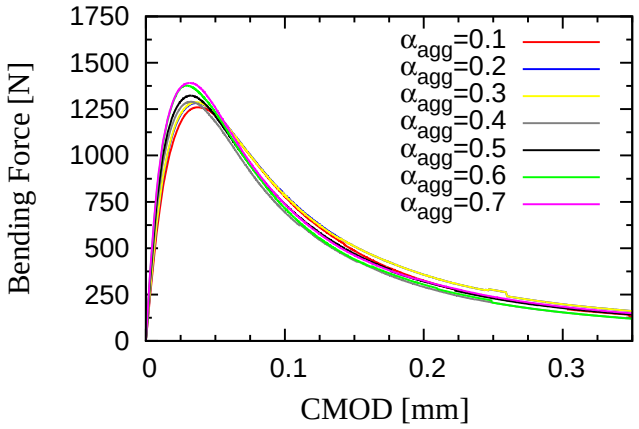

Figure 4.15: Effect of aggregate volume fraction on the simulated response of the TPBT.

Extraction of traction-separation law from particle model simulation

During the simulation of an experiment with the particle model, it is possible to determine the shape of the TSL. The shape, based on Hillerborg's assumptions, see Chapter

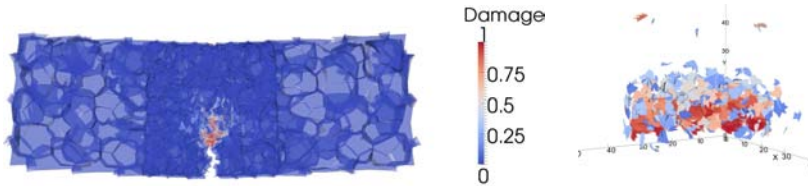

Figure 4.16: Crack pattern at the peak load for $\alpha_{agg} = 0.6$ and the cracked contacts of cells with damage > 0.1.

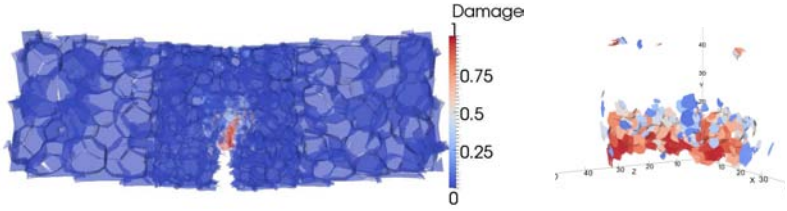

Figure 4.17: Crack pattern at the peak load for $\alpha_{agg} = 0.1$ and the cracked contacts of cells with damage > 0.1.

Results and discussion

Figure

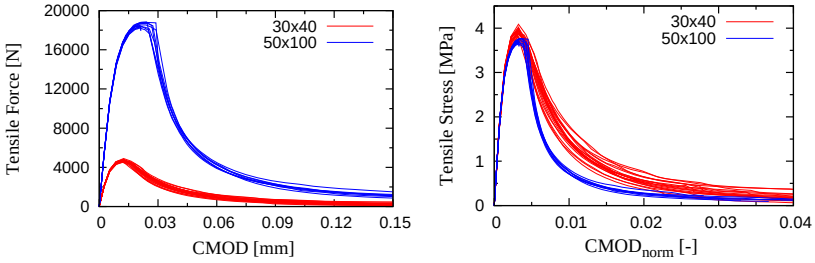

Figure 4.18: Simulations of UTTs, a), and their normalizations with respect to size, b).

In the case of TPBT simulations, Figures

Simulations of the WST, see Figures

Figures

The hinge-model based inverse analysis, or any analysis assuming that the cracking takes place at the plane between the notch tip and the support, can

Material	Test	E [GPa]	f_t [MPa]	G_f [J/m^2]
Concrete AW	TPBT	38.7	3.54	159.2
	WST	36.1	3.47	171.6
Concrete AB	TPBT	37.1	3.97	136.5
	WST	26.6	3.29	194.8
Mortar AW	TPBT	27.2	4.15	75.06
	WST	22.7	2.50	116.3
Mortar AB	TPBT	27.8	5.11	66.65
	WST	23.0	2.52	77.83
Micro-mortar AW	TPBT	31.1	4.23	51.46
	WST	20.0	2.16	84.86
Micro-mortar AB	TPBT	29.1	4.23	48.68
	WST	24.5	2.32	49.80

Table 4.2: Comparison of material properties identified by the hinge model-based inverse analysis from TPBT and WST.

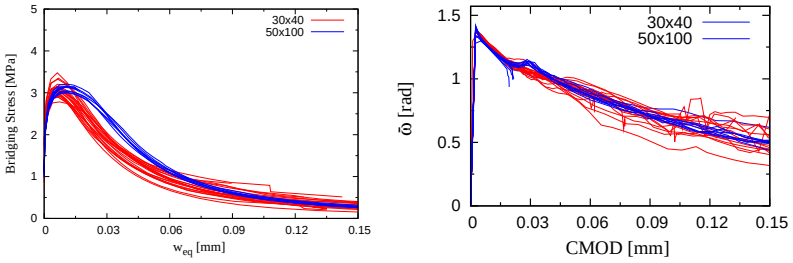

a) b)

Figure 4.19: Traction-separation law computed in the particle model simulation, a), and the average direction of the crack propagation at the mesoscale, b), for uniaxial tensile test simulations.

not model neither the cracking above the notch tip, neither the mixed-mode cracking in the mesostructure of the material out of the plane. However, the energy dissipated in these zones influences the experimental record that is used as the input for the inverse analysis and fitted. The higher values of fracture energies and lower values of tensile strengths listed in Table

Finally, Figure

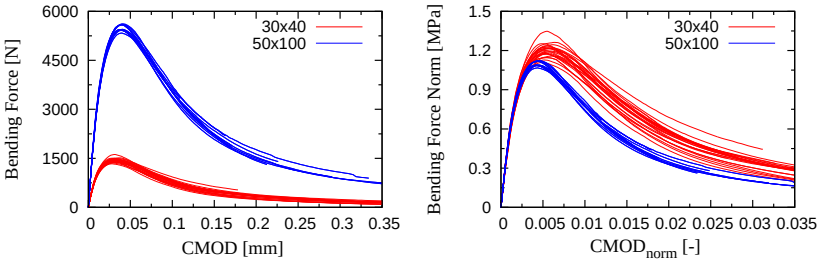

Figure 4.20: Simulations of TPBTs, a), and their normalizations with respect to size, b).

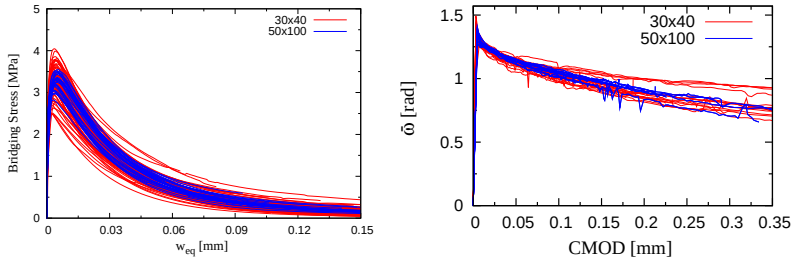

Figure 4.21: Traction-separation law computed in the particle model simulation, a), and the average direction of the crack propagation at the mesoscale, b), for TPBT simulations.

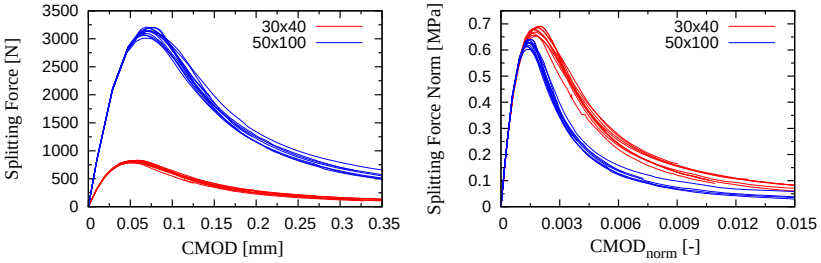

Figure 4.22: Simulations of WSTs, a), and their normalizations with respect to size, b).

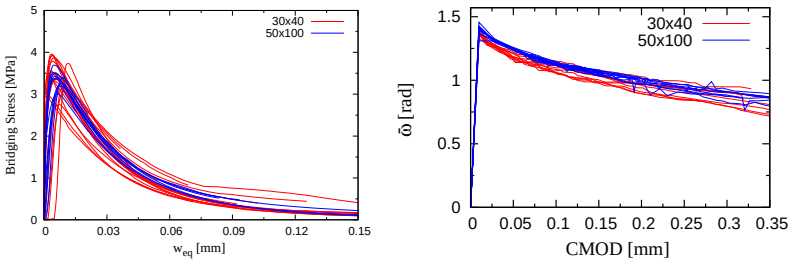

a) b)

Figure 4.23: Traction-separation law computed in the particle model simulation, a), and the average direction of the crack propagation at the mesoscale, b), for WST simulations.

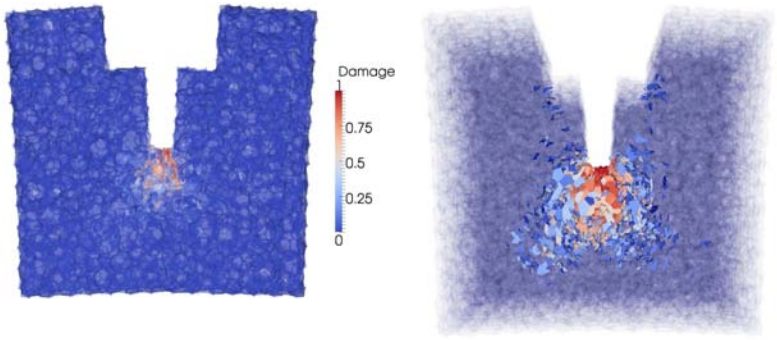

a) b)

Figure 4.24: Crack pattern at the peak load in the WST on ≈ 10 mm slice containing the from face of th specimen, a), and all cracked contacts of cells viewed from the front face, b).

Figure 4.25: Experimentally observed curved crack propagation caused by the mixed-mode crack propagation in the WST.

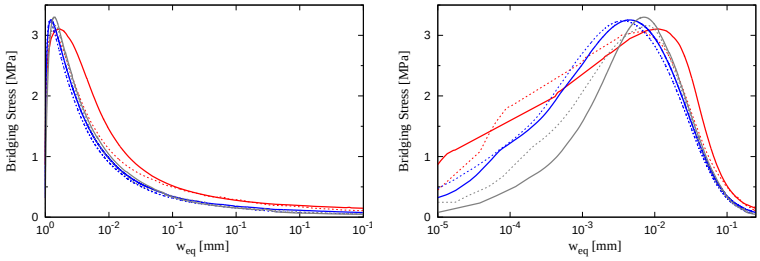

a) b)

Figure 4.26: Comparison of averaged traction-separation laws computed in the particle model simulations of UTT, TPBT and WST, a), and the same with logarithmic x-axis to emphasize the difference in the initial slope, b).

Chapter 5

Upscaling of Fracture Properties

Reliable prediction of behavior of complex materials such as concrete based on easily obtainable input data and a known geometry is very challenging from the numerical point of view. At the same time, however, it is one of the most desirable things in cement and concrete industry. Especially nowadays, when the cement is becoming more and more complex due to the intensive use of the SCMs, a strong need of tools for predictions of mechanical properties of materials made from such cements exists. Such a tool needs to address three main subjects to be successful: a) acquisition of input material parameters of the material models used; b) sufficiently accurate representation of the complex geometry and c) establishment of numerical and material models capable of simulating the desired processes in the given geometry. In this Section, two frameworks based on the particle model described in Chapter

5.1 Upscaling from meso to macro level: Cementitious materials containing aggregates

This Section is a condensation of Paper IV which provides all details.

The particle model discussed in Chapter

Material properties of the fictitious crack model were identified by the approach described in Paper I and in Section

As elaborated previously in Chapters

Both the response of the TPBT and CC specimens were simulated with the particle model on concrete and mortar level. In order to understand the importance of the identified parameters on the simulated response in the TPBT and

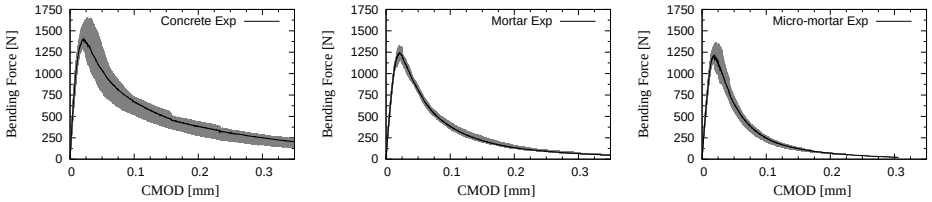

Figure 5.1: Experimental results of the TPBT for concrete a), mortar b) and micro-mortar c). The solid lines show average from six records while the shaded areas show experimental scatter

Material	E [GPa]	f_t [MPa]	G_f [J/m^2]
Concrete	38.8	3.42	137
Mortar	28.3	3.93	66.7
Micro-mortar	27.9	4.05	47.8

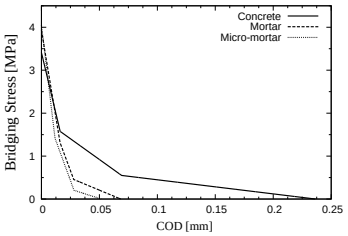

Figure 5.2: Material properties and shapes of traction separation laws of the investigated materials identified by the hinge model.

to evaluate the importance of the remaining parameters, a sensitivity analysis was performed for the mortar to concrete upscaling. All the identified material parameters together with shear strength, mode-II fracture energy and α were randomly generated with uniform distribution in the interval of ± 25 % from the reference value. The geometry and material properties not important for the global mode-I fracture process were kept constant. Pearson's correlation coefficients were evaluated as functions of CMOD for the relevant material parameters. The correlation coefficient, $\rho_{M,CMOD}$, of the material property M for given CMOD was computed as (Bittnar & Šejnoha 1992)

$$\rho_{M,CMOD} = \frac{n\sum_{i=1}^{n} m_i P_{i,CMOD} - \sum_{i=1}^{n} m_i \sum_{i=1}^{n} P_{i,CMOD}}{\sqrt{n\sum_{i=1}^{n} m_i^2 - \left(\sum_{i=1}^{n} m_i\right)^2}\sqrt{n\sum_{i=1}^{n} P_{i,CMOD}^2 - \left(\sum_{i=1}^{n} P_{i,CMOD}\right)^2}},$$

where n is the number of sampling computations, m_i is the value of the parameter M in the $i-th$ sampling computation and $P_{i,CMOD}$ is the value of bending force interpolated for given CMOD from the $i-th$ computation. Correlation

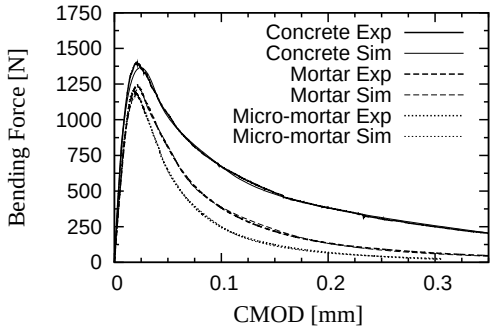

Figure 5.3: Comparison of the averaged experimental records with their simulations using the hinge model and the identified material parameters listed in Figure

coefficients for the relevant parameters are plotted in Figure

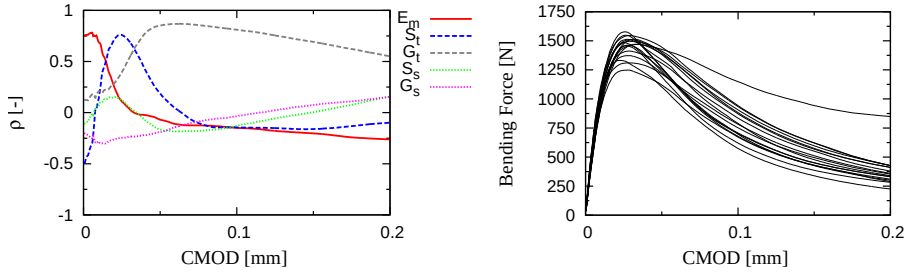

a) b)

Figure 5.4: Pearson's correlation parameter for important material parameters in the TPBT a) and the set of sampling computations b).

Not enough data on the shear strength and mode-II fracture energy of mortars can be found in literature. Significant effort has been put into investigation of the mode-II properties of concrete, however, a literature survey yields highly scattered data. Comparisons of ratios between mode-I and mode-II fracture energies done in (Neto, et al. 2004) addresses ratios from $G_{f,II}/G_{f,I} \approx 25$ (Reinhardt, et al. 1997) to less than 10 (Täljsten 1994). Therefore, additional CC experiments were performed and simulated. Contrary to simulating mode-I crack propagation in the TPBT, when simulating the crack propagation typical for the CC, increasing S_s and G_s both have an positive effect on the global response which makes the CC experiment suitable for the identification

of the shear parameters through fitting of the CC model.

In the CC experiments, the specimens were placed directly between the loading platens without any friction modifying devices. Thus, in the particle model of the CC, all displacements were set to zero on the bottom surface and the upper surface was allowed to move in the load direction only. Rotations at the boundary were kept unconstrained. A parametric study varying S_s/S_t

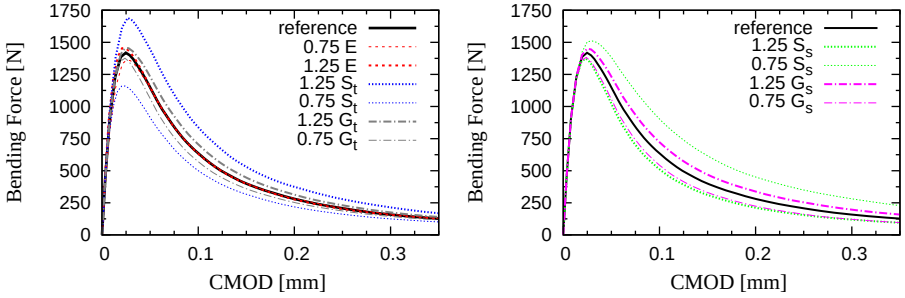

Figure 5.5: Effect of variation of ±25 % of the identified a) and fitted b) material parameters on the global response of the TPBT.

and G_s/G_t was performed to identified the proper combination of the shear parameters. The geometry as well as the remaining parameters were kept constant. Figure

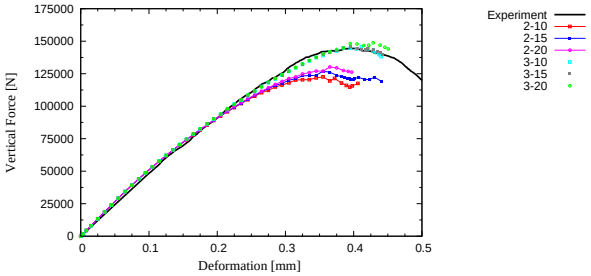

Figure 5.6: Sensitivity of the CC simulation to S_s and G_s. The first number in legend is S_s/S_t while the second denotes G_s/G_t.

Table

Finally, the material properties summarized in Table

The following conclusions can be drawn:

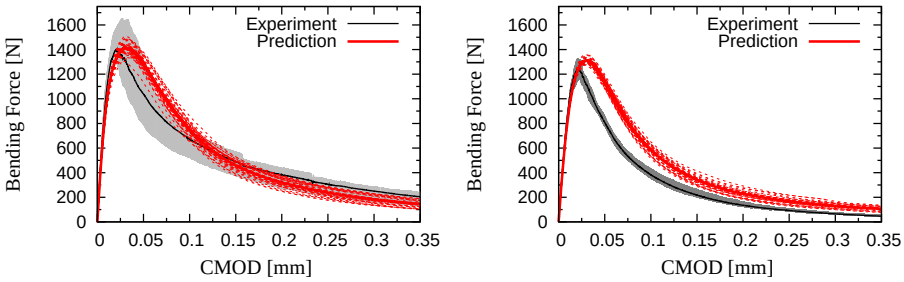

Figure 5.7: Comparison of the prediction with the experimental records of TPBT for a) mortar to concrete upscaling and b) micro-mortar to mortar upscaling. Dashed lines show different simulations with randomly generated mesostructures.

- The particle model with the measured material properties provides predictions of crack propagation in the TPBT matching favorably the experimental records and at the same time provides fitted responses of the CC tests.
- The predictions show a more ductile response compared to the experimental records, presumably due to the missing explicit incorporation of the ITZ in the model[1]. Nevertheless, incorporation of the aforementioned features into the model would significantly increase number of material parameters of the model and hence would make the presented framework much more complicated especially from the experimental point of view.
- Shear strength and mode-II energy on the meso-level play important roles in the advanced stages of the crack propagation. Their direct identification, however, is not possible neither from TPBT nor CC tests with the matrix and were therefore fitted.
- Fracture propagation in the uniaxial compression of concrete and mortar is initially mode-I and later a mixed-mode crack propagation dominated process on the mesoscale. Therefore, the same set of material properties as in the case of TPBT prediction was successfully used for predicting the CC response up to the peak load.
- The particle model in the applied form is not suitable for simulation of the softening part of the CC experiments since it can not describe correctly creation of new contacts and mutual shearing of heavily damaged parts

[1] Assuming that the strength of aggregates is significantly higher compared to the strength of matrix and ITZ

contributing to the load bearing capacity of the material.

Further details are provided in Paper IV.

Model parameter	Abbreviation [unit]	Mortar	Concrete	Source / Note
Young's modulus of aggregates	E_a [GPa]	80	80	from (Li, et al. 1999, Nadeau 2003)
Young's modulus of matrix	E_m [GPa]	27.9	28.3	identified by HM
Young's modulus of ITZ	E_{ITZ} [GPa]	10	10	from (Li et al. 1999, Nadeau 2003)
Thickness of ITZ	l_{ITZ} [mm]	0.043	0.043	from (Nadeau 2003)
Coupling parameters	α [-]	0.25	0.25	from (Cusatis et al. 2003)
Uniaxial meso-tensile strength	S_t [MPa]	4.05	3.93	identified by HM
Uniaxial meso-shear strength	S_s [MPa]	$3S_t$	$3S_t$	fitted from CC
Mode-I meso-fracture energy	G_t [J/m^2]	47.8	66.7	identified by HM
Mode-II meso-fracture energy	G_t [J/m^2]	$12.5G_t$	$12.5G_t$	fitted from CC
Friction coefficient	μ [-]	0.2	0.2	from (Cusatis et al. 2003)
Uniaxial meso-compressive strength	S_c [MPa]	1000	1000	=deactivated

Table 5.1: Material parameters used for the upscaling. Values of remaining parameters of the material model not relevant for the mixed-mode crack propagation which are not listed in the table were taken from (Cusatis et al. 2003).

5.2 Upscaling from nano to micro level: Pure cement paste

5.2.1 In-situ observation of the crack propagation in pure cement pastes

Initial attempts to observe the crack propagation in cement pastes in situ date back several decades (Mindess & Diamond 1980, Mindess & Diamond 1982, Kjellsen & Jennings 1996).

Creep of the material during loading resulting in damage propagation even under constant deformation, heterogeneity of the material making the crack tracking difficult and formation of additional cracks due to drying in the observation chambers of SEM or ESEM are the major obstacles that have to be challenged during the experiments.

In the present work, the crack propagation during the TPBT on notched specimens was observed in the ESEM (model EVO 60 manufactured by Carl Zeiss). The dimensions of the specimens, the detailed description of the test setup as well as of the materials used can be found in Appendix

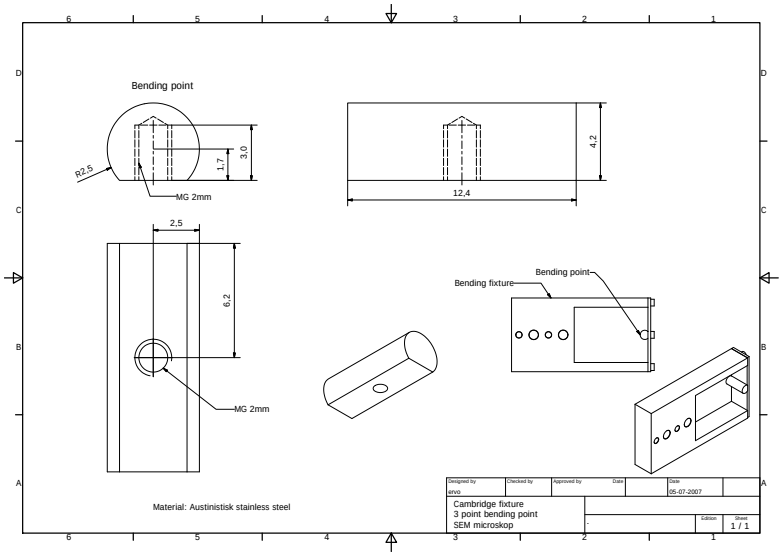

Figure 5.8: Scheme and dimensions of the TPBT loading stage used for the ESEM crack growth observation experiments.

Figures

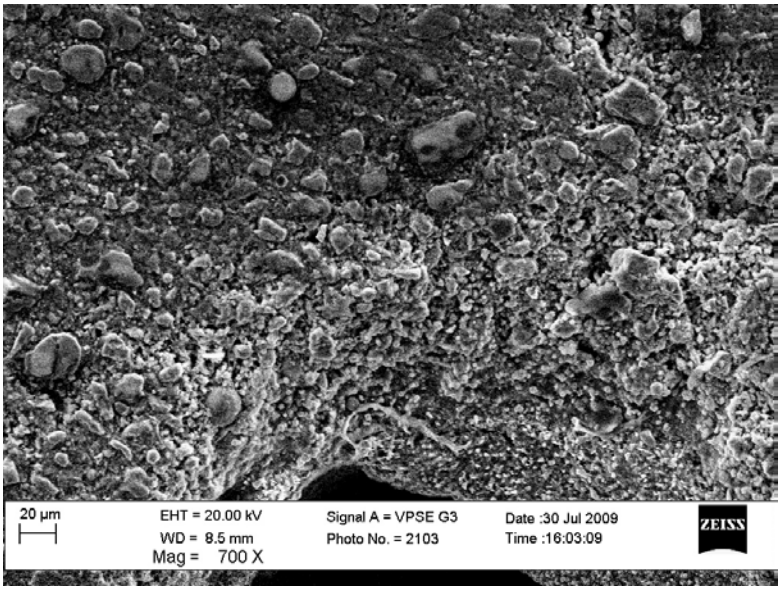

a) Load level ≈ 0.083 maximal load.

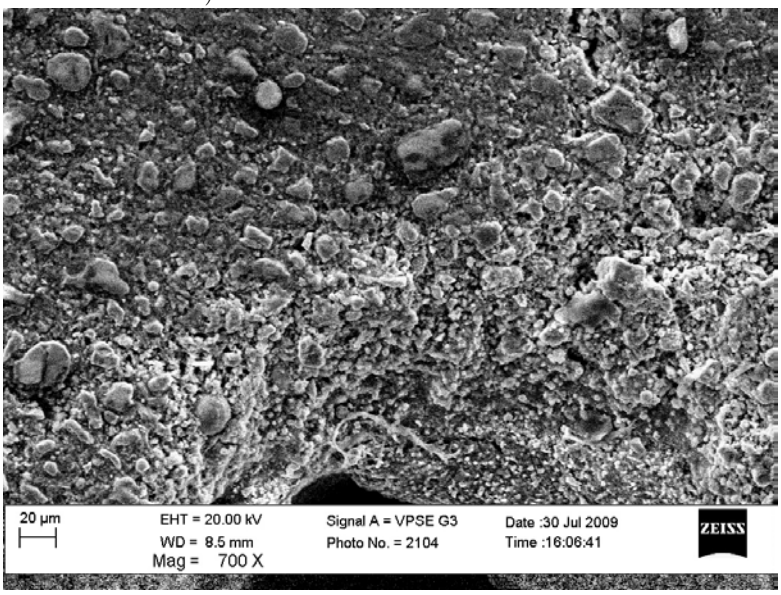

b) Load level ≈ 0.28 maximal load.

Figure 5.9: ESEM images of formation of the main crack at the zone close to the notch tip in the TPBT on pure cement paste.

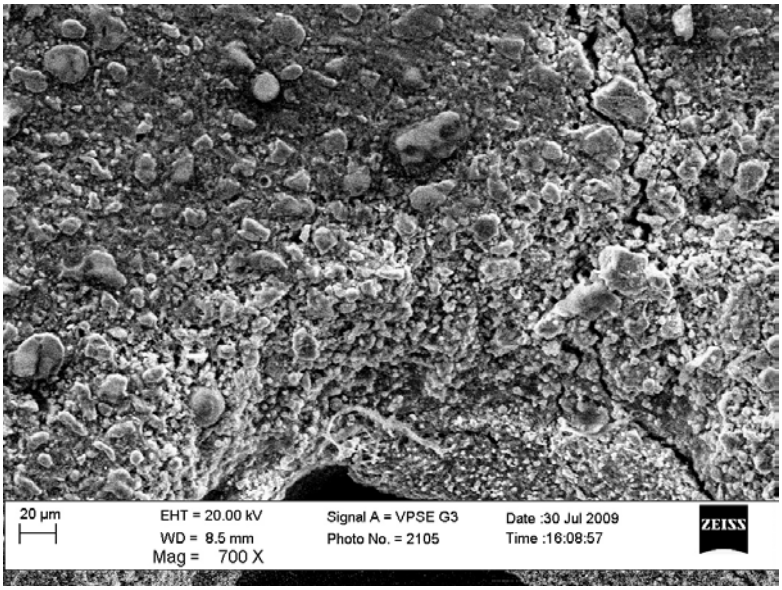

a) Load level ≈ 0.44 maximal load.

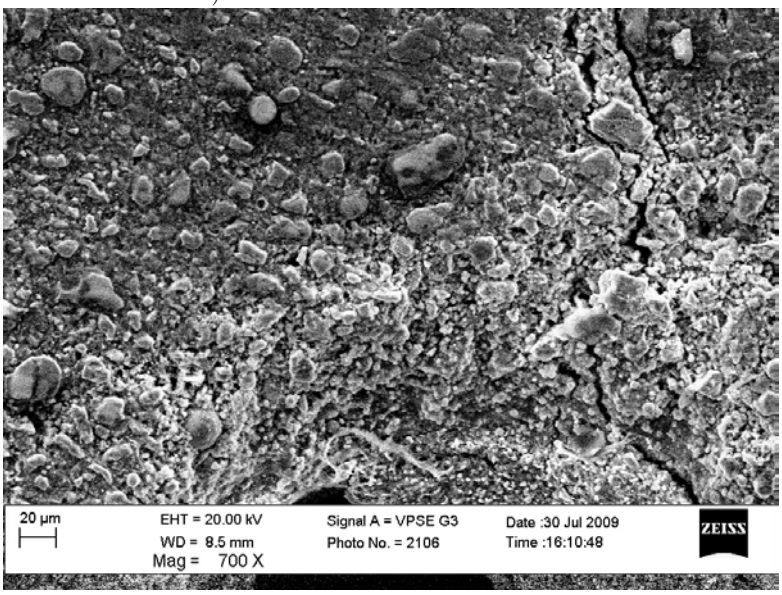

Load level ≈ 0.55 maximal load.

Figure 5.10: ESEM images of formation of the main crack at the zone close to the notch tip in the TPBT on pure cement paste.

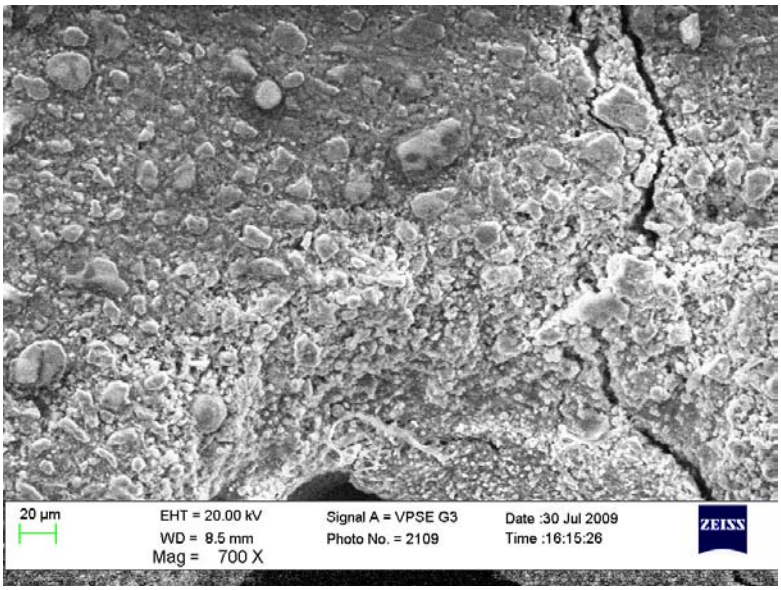

Load level ≈ 0.86 maximal load.

Figure 5.11: ESEM image of formation of the main crack at the zone close to the notch tip in the TPBT on pure cement paste.

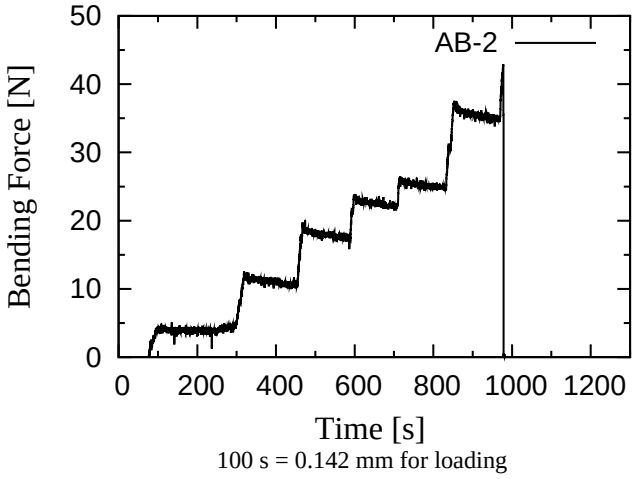

Figure 5.12: Loading history corresponding to Figures

The second set of images, Figures

After the in-situ observations of the crack propagation, fractured surfaces of the specimens were investigated. Figure

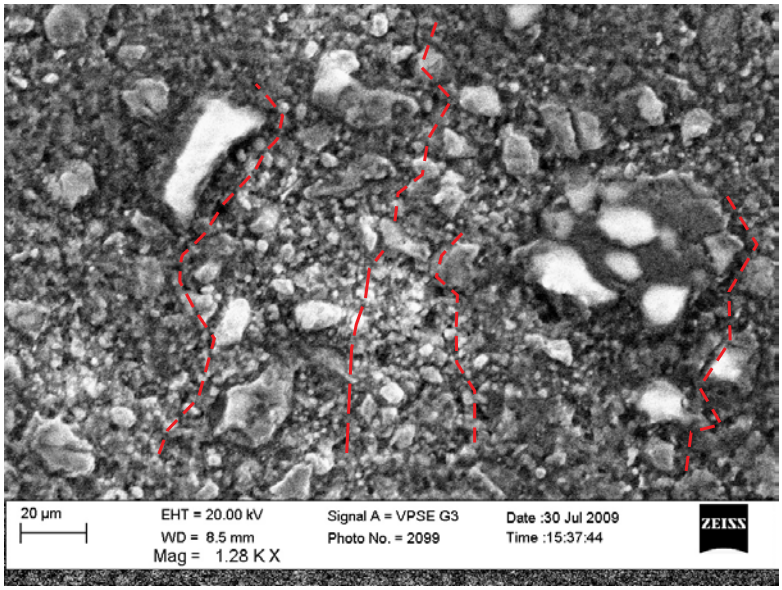

a)

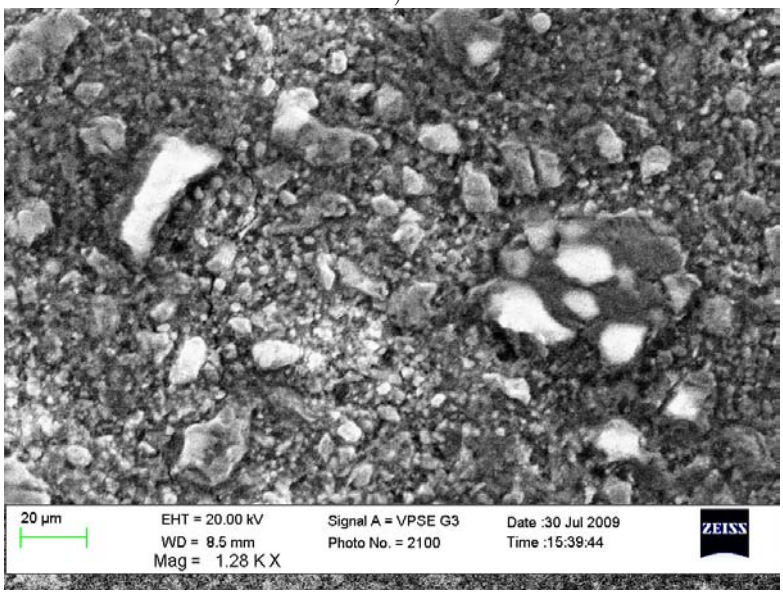

b)

Figure 5.13: ESEM images of formation of micro-cracks, a), and formation of the main crack, b), in the pure cement paste loaded in the TPBT.

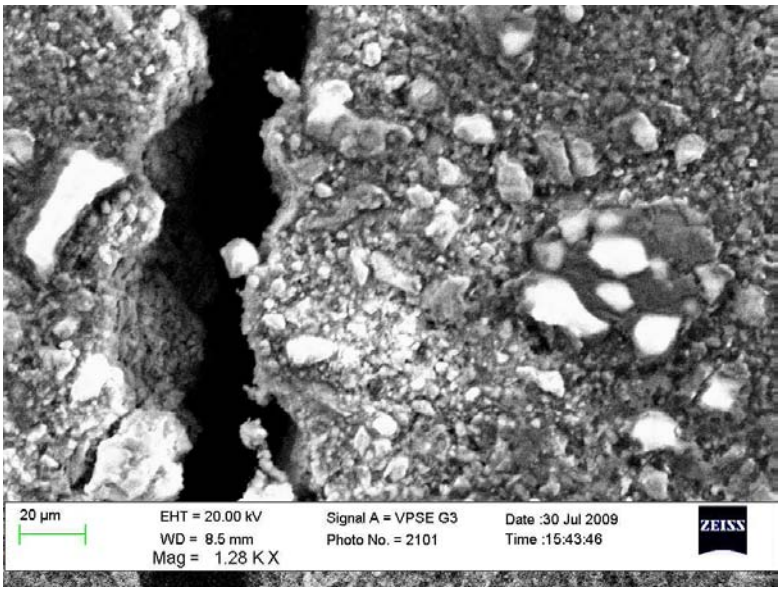

Figure 5.14: ESEM image of the final crack pattern found in the pure cement paste loaded in the TPBT.

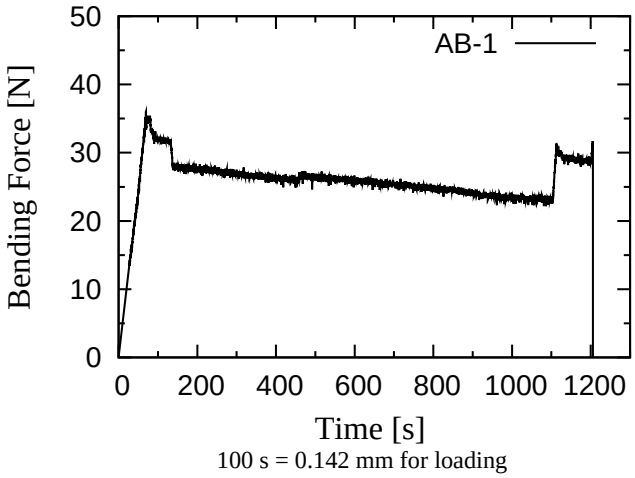

Figure 5.15: Loading history corresponding to Figures

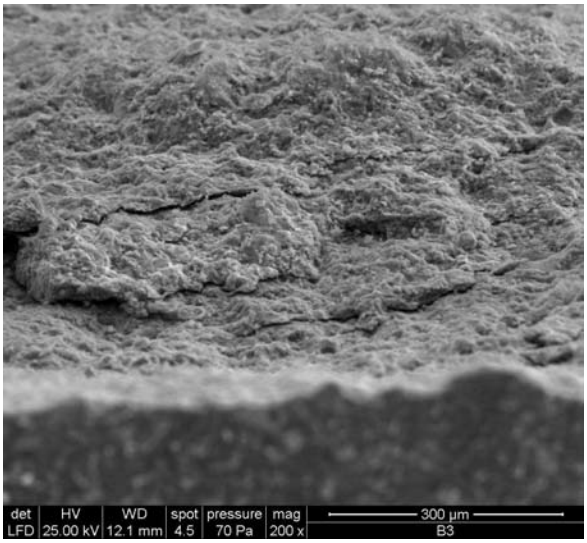

a)

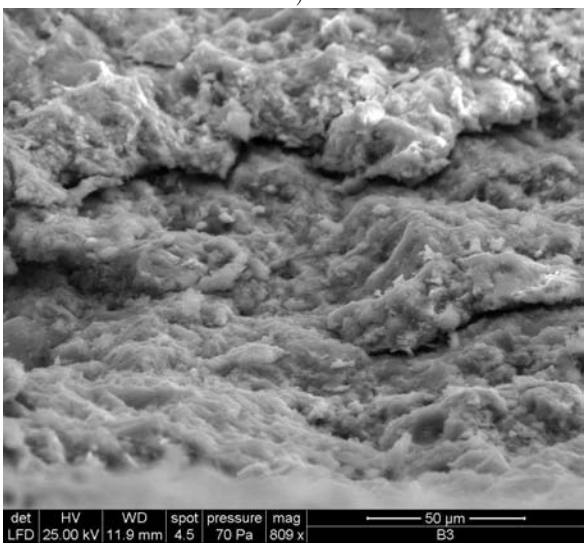

b)

Figure 5.16: ESEM images the crack after the test: a) crack branching and tortuosity from the side view (the front side of the specimen with the main crack running from left to right hand size is visible at the bottom) and magnified view of the same, b).

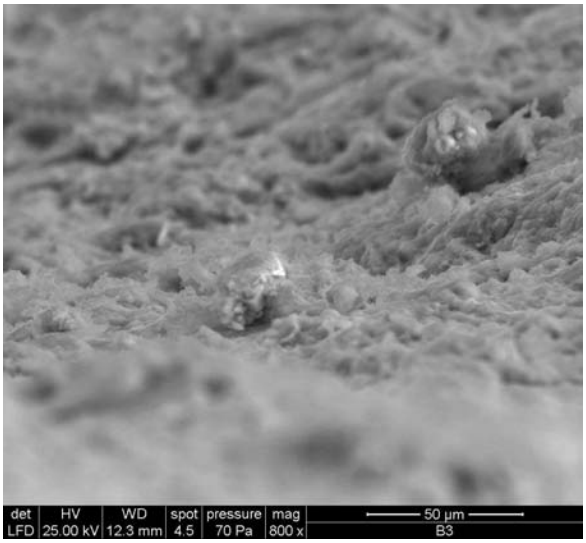

a)

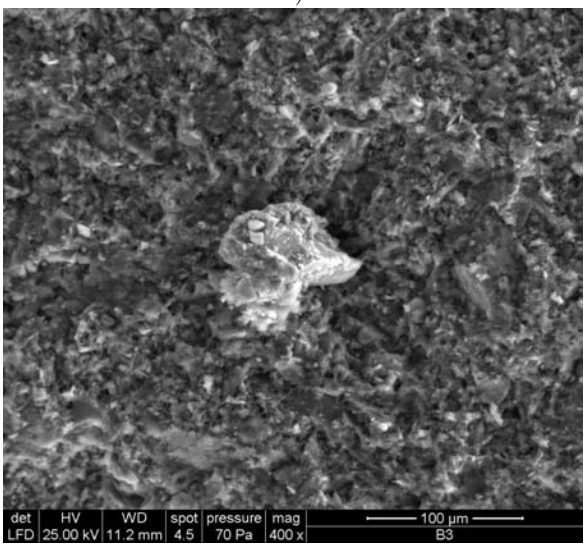

b)

Figure 5.17: ESEM images the crack after the test: a) particles bridging the crack viewed from the front side of the specimen and a particle bridging the crack viewed from the perpendicular direction to the main crack in b).

From these observations, two main conclusions can be drawn:

1. At the investigated scale, the cement paste does not exhibit the perfectly brittle behavior. Comparing Figures

5.2.2 Prediction of strength of cement pastes

This Section is a condensation of Paper V which provides all details.
Several approaches for estimation of the strength of multiphase materials can be found. When the microstructure is relatively simple (such as matrix-pore inclusions in case of, for example, reinforced concrete or polycrystals in metals), a homogenization based on the definition of Linear Comparison Composite (LCC) (Castaneda 1996, Castaneda 2002) or methods based on the second order moment estimate of stress and strains in each phase of the heterogeneous material (Dormieux, et al. 2006, L. Dormieux 2002) can be used. In both cases, the non-linear constitutive laws of various phases are linearized in such a way that the traditional elastic homogenization schemes can be applied. The correct capturing of the average strain and stress field in each phase is the main problem in mean-field homogenization schemes. The problem becomes even more pronounced for complex microstructures such as the cement paste where stress localization is hard to capture. Still, a formulation with quadratic stress average assuming von Mises yield condition was successfully applied to cement paste assuming acircular (needle-type) geometry of hydration products (Pichler, et al. 2008). It should be noted, however, that authors were not looking for a solution of the variational problem but for loss of linearity based on the second order estimates. The same results can be potentially achieved by solving the linear elastic problem with FEM of FFT (Moulinec & Suquet 1998) methods, thus giving physically similar but more precise estimates thanks to considering explicitly the actual microstructure.
In order to incorporate the information about the real microstructure of cement paste, a discretization of digital images with the variational formulation of the lower bound of the strength with Drucker-Prager yield criterion was done in (Ganneau, et al. 2007). This formulation is similar to the formulation mentioned above with the difference that an estimation of stress and strain in each phase are not needed. Instead, the discretization of the microstructure in a way similar to FEM leads, as a result, to a nonlinear programming problem.
All aforementioned methods are based on the yield limit theory and perfect plasticity and just basically approach the same problem from different sides. However, in-situ observations of the crack propagation in the cement paste loaded in compression (Mindess & Diamond 1982) showed that cracks

parallel to the loading direction are formed in the specimen prior the peak load is reached. Therefore, it can be expected that the localized tensile failure of the C-S-H and other phases in the microstructure will be as important as the yielding of the C-S-H. The importance of the localized failure will be even more pronounced in the cement paste subjected to tension. Therefore the particle model introduced in Chapter
In the presented study, the mean-field strength homogenization approach used in (Pichler et al. 2008), approaches based on the solution of linear-elastic problems with FEM and FFT and a modified particle model based on (Cusatis et al. 2003) are utilized to predict the tensile and compressive strength of three cement pastes. Critical aspects of each method are identified, discussed and compared with other methods.
Three different microstructures were considered: the first was scanned[2], and the other two are simulated using CemHyd3D(Bentz 2000) hydration model for two different types of cements. The first microstructure was a X-ray microtomography image, see (Bentz, et al. 2002) for details, of cement paste with W/C of 0.3 made from "cement 133" according to the orginal work hydrated for 7 days (see `http://visiblecem.nist.gov/cement` for all the details). The cement is labeled as NIST Cem in the rest of this work. This particular microstructure was chosen due to its hydration time which is being comparable with other microstructures generated using CemHyd3D (Bentz 2000). The first generated cement was Aalborg White cement, labeled as Cem A in the rest of the work, and the second one an OPC labeled as Cem C.
In order to avoid fitting of phase properties, nanoindentation was considered to provide mechanical properties of the main hydration product - C-S-H - in cement paste (Constantinides & Ulm 2007) from which LD-C-S-H and HD-C-S-H properties can be obtained among others. For the sake of comparison of results obtained from modeled microstructures (Cem A and C modeled in CemHyd3D) with the scanned one (NIST Cem), where only three phases were distinguished - porosity, hydrates and unhydrated clinker. Separation thresholds were set according to recommendations from (Bentz et al. 2002). Elastic properties of C-S-H were set to 25.55 GPa in all calculations (average values from (Šmilauer 2005, Constantinides & Ulm 2007)) and Poisson's ratio was set to 0.24. In addition, in the case of the modeled microstructures (Cem A and Cem C), the elastic properties of the other phases were taken from (Šmilauer 2005). The C-S-H was considered to be the only phase allowed to yield/crack. Regarding the strength/yield properties of C-S-H, the only experimentally

[2] `http://visiblecem.nist.gov/cement`

available strength parameter is hardness $H = P_{max}/A_c$, where P_{max} is the maximum load during the indentation and A_c is the contact area. Using different hypothesis regarding the yield surface of C-S-H, different scaling relationships relating H to the yield surface properties can be obtained. For $J2$ plasticity with $f_{y,J2} << E$ (which is the case of cementitious materials) this scaling relationship reads $f_{y,J2} = H/2.8$ (Cheng & Cheng 2004).

Phase	E [GPa]	ν [-]	$f_{y,J2}$ [GPa]	H [GPa]
Porosity	0.001	0.4999	Inf	Inf
Clinker	135.0	0.3	Inf	Inf
Hydrates	25.5	0.24	0.214	0.6

Table 5.2: Assumed material properties of the cement paste phases.

The mean-field strength homogenization approach is described in detail in (Pichler et al. 2008) as well as in Paper V. The description of the FFT can be found ibidem. Descriptions of the FEM and the particle model follows.

The FEM was applied in a very straightforward and simple way. The voxel representation of the microstructure obtained from the hydration model or the X-ray photomicrography was directly discretized using 8 node linear brick elements. The model was then loaded with mixed boundary conditions - DOFs in the loaded direction were prescribed on the two opposite faces (0 at one side and a nonzero displacement on the other size). At one of the corner nodes at the first face, all DOFs were set to zero to avoid a rigid body motion. Remaining DOFs of the model were kept unconstrained. Three types of analyses were performed: 1) Full nonlinear plastic analysis of the scanned microstructure (NIST Cem) computed in Abaqus and used as a benchmark solution for the comparison with the particle model. 2) A simple linear analysis to find the loss of linearity and effective elastic properties of the microstructures loaded in tension and compression, respectively, used for comparison with FFT and with $J2$ homogenized ellipsoidal yield criterion. 3) Linear computations on the level of individual struts of the particle model.

Particle models for simulation of the fracture propagation in concrete are based on the assumption that all the cracking and possibly other nonlinear phenomena take place in the matrix phase, e.i. mortar in the case of concrete, between the particles, i.e. aggregates. This assumption allows significantly simplified formulations of kinematics compared to the classical FEA and volumes with a large number of particles can be modeled with a reasonable computational time and memory requirements. The assumptions made for concrete can be extended to the case of the cement paste

since most of the plastic yielding and cracking takes place in hydrates and the unhydrated clinkers can be viewed as aggregates.
In the presented study, the model of Cusatis (Cusatis et al. 2003) was chosen as the base. The unhydrated clinkers were approximated by spherical particles conserving the volume of clinkers and the positions of centers of gravity. Then the volume was tessellated according to the procedure described in (Cusatis et al. 2003, Cusatis et al. 2006, Cusatis & Cedolin 2007). In contrary to the case of mortar or concrete where the matrix phase can be considered as a homogeneous material, the properties of the matrix phase, or rather of the interparticle volume, differ significantly for individual contacts in the cement paste microstructure. The increased heterogeneity of the material is the result of the hydration which is, in terms of positioning of hydration products, essentially a random process. Therefore, the simple averaging of the elastic stiffnesses along the struts as well as concept of one set of material properties used in the case of concrete have to be abandoned and every strut has to be treated separately.
After the discretization of the microstructure by the struts, the diameters of the particles were set to zero. The entire volume between two nodes was homogenize using the FFT and FEM for every strut (loss of linearity was used as a strength estimation in all cases). The internodal volume was discretized by voxels aligned with the orientation of the strut and homogenized using the FFT and FEM. Effective Young's modulus, Poisson's ratio, tensile (f_t), shear (f_s) and compressive (f_c) strengths of the internodal volumes were obtained and assigned to the strut discretizing the connection. Since the internodal volume was small (typically ≈ 100 voxels), it was assumed that the loss of linearity should approximate reasonably well the yield limit of the strut. In cases where there were not any C-S-H voxels in the internodal volume, struts were assumed to be elastic without any strength limits. The comparison of the homogenization based on the FEM and FFT is shown in the following Section.
The material model proposed in the original particle model (Cusatis et al. 2003) was utilized and modified. The material behaved elastically until the elastic boundary depending on the tensile, shear and compressive strength is reached. Then a nonlinear behavior is applied. In the presented implementation, the response was considered elasto-brittle for $\omega > \omega_0$, see (and Figure
The Particle Model with the FEM-based homogenization of the internodal volume ($PM-FEM$) and the ellipsoidal yield condition, see Paper V, was used to simulate a uniaxial compression test on cubical microstructures cut from the NIST tomography data with size of edges equal to 60 μm (RVE_{60}). The microstructure was chosen in the way that it did not contain any large

unhydrated grains that would bridge the entire microstructure, see Figure

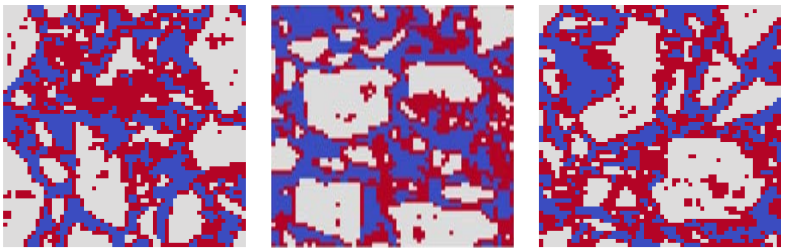

Figure 5.18: Microstructure of 60×60×60 μm used for initial comparison of the methods - three mutually orthogonal cut planes going through the center of the microstructure.

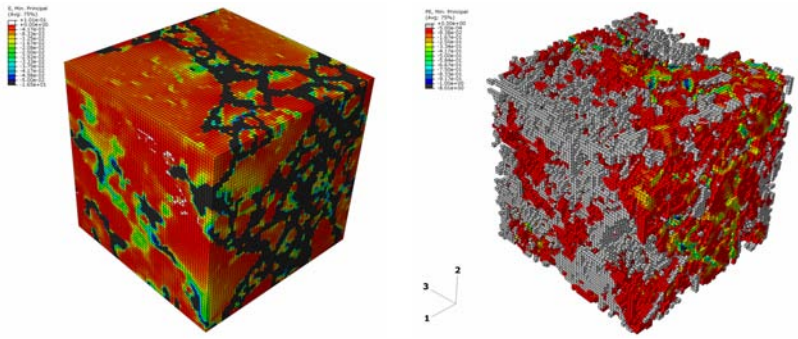

a) b)

Figure 5.19: Elastic stain in all phases, a), and plastic strain in C-S-H after the last step of the full non-linear FEM analysis in Abaqus for RVE_{60}. The microstructure was loaded in direction 1.

Further, the particle model with the FEM-based homogenization of the internodal volume and the ellipsoidal and $J2$ yield conditions was used to study an effect of the size of the microstructure on the stress-strain response in uniaxial compression and tension, respectively. Brittle cracking of contacts was considered. Two sizes of the microstructure were considered: the already introduced RVE_{60} and 150 μm microstructure, RVE_{150}. Comparison of the stress-strain curves for the two sizes is plotted in Figure All the introduced methods were compared on the small NIST Cem microstructure RVE_{60}. In the case of Self-Consistent (SC) scheme, see Pa-

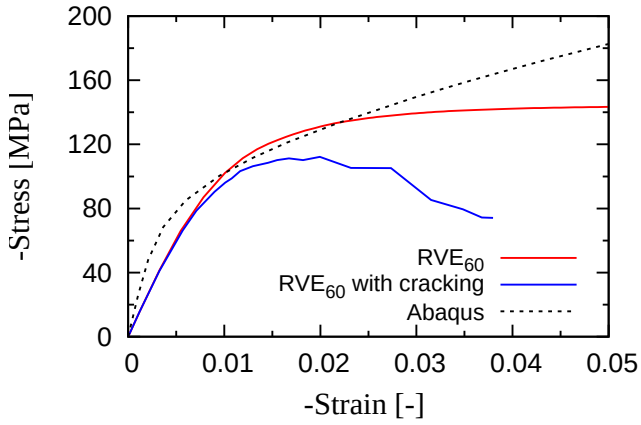

Figure 5.20: Comparison of stress-strain curves predicted by the particle model with and without cracking and the stress-strain curve from the full nonlinear FEM analysis in Abaqus.

per V, the $J2$ plasticity was assumed while the other methods also considered ellipsoidal yield condition. The FEM and FFT were used to find the loss of linearity which was assumed to be the strength. The particle model included the cracking of contact in tension and the strengths corresponds to the peak loads in Figure

As can be seen from the Table, the scatter of the predicted elastic and strength properties is large. Young's modulus predicted by the $PM - FEM$ is significantly lower compared to the other methods. This is due the utilized volume tessellation. The tessellation is based on centers of gravity (Cusatis et al. 2003) and therefore cannot simulate the elastic loading exactly, as is the case of models based on Voronoi tessellation (Eliáš 2009). The difference in Young's modulus between FFT and FEM is caused by the different boundary conditions assumed by the methods. The FEM models was loaded by mixed boundary conditions, while the FFT model was loaded by periodic boundary conditions which should, in general, give the best results (Šmilauer 2005). The SC method does not consider the actual arrangement of phases which leads to the overestimation of Young's modulus.

Comparison of strength properties is more difficult. FFT and FEM were used to find the loss of linearity only, which is far from the maximum capacity of the material (compare values from Table

The PM simulation combining the yielding and cracking of C-S-H predicted

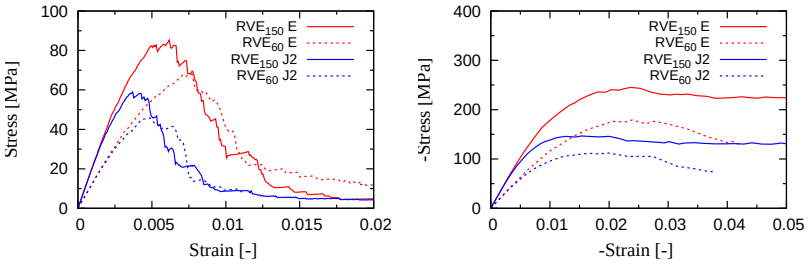

a) b)

Figure 5.21: Simulations of the uniaxial tensile test, a), and the uniaxial compressive test, b), on the NIST cement microstructure of 60 and 150 μm assuming $J2$ and ellipsoidal yield condition, respectively.

not only values of tensile and compressive strength, but provided the entire responses in terms of stress-strain curves, see Figure
The numerically predicted microstructures of Cem A and Cem C at three different ages - after 1, 7 and 28 days of hydration - were studied using the PM. The goal of this study was to investigate whether the approximate particle model can model the difference between the two cements observed experimentally (see Appendix

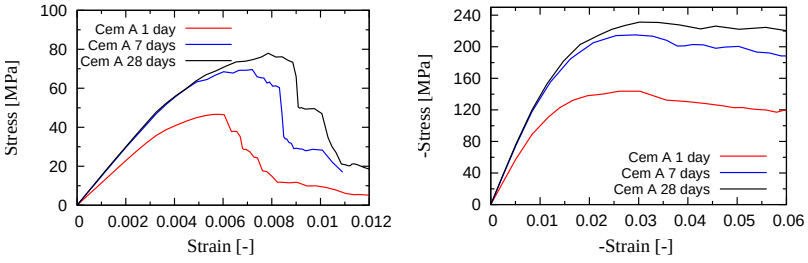

a) b)

Figure 5.22: Simulations of the uniaxial tensile test, a), and the uniaxial compressive test, b), on Cem A microstructures.

The effect of hydration on the elastic and strength properties on the level of individual struts was already discussed. The improvement of the properties of struts is reflected by the change of predicted behavior of microstructures. The longer the hydration the higher tensile and compressive strength. Further, it can be seen for both cements that responses in 7 and 28 days are

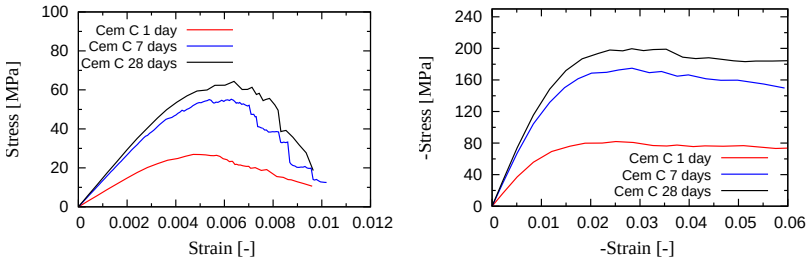

a) b)

Figure 5.23: Simulations of the uniaxial tensile test, a), and the uniaxial compressive test, b), on Cem C microstructures.

significantly less ductile compared to responses after 1 day.
In the presented study, the mean-field strength homogenization approach used in (Pichler et al. 2008), approaches based on the solution of linear-elastic problems with FEM and FFT and a modified particle model based on (Cusatis et al. 2003) were utilized to predict the tensile and compressive strength of three cement pastes. Three different microstructures were considered: the first was scanned[3], and the other two are simulated using CemHyd3D (Bentz 2000) hydration model for two different types of cements. Two material models of C-S-H in compression were used for every model - $J2$ plasticity and the elliptical yield condition resulting from the porous nature of the C-S-H. Both material models assumed perfectly brittle behavior in mixed-mode tension.
The following conclusions can be drawn:

- Responses of the scanned and modeled microstructures are qualitatively identical.
- Methods based on the loss of linearity (FEM and FFT and the mean-field strength homogenization approach (SC)) give inconsistent results and can not be used for reliable predictions:
  - SC does not reflect the actual microstructure and significantly overestimates strengths compared to FFT and FEM.
  - FFT and FEM reflect the microstructure, however, the loss of linearity is significantly dependent on the discretization and is not a good approximation of the strength.
- Particle model with FEM-based homogenization of the internodal volume without cracking provides results matching favorably the full non-

[3] http://visiblecem.nist.gov/cement

linear FEM solution with significantly reduced computational time.

- Cracking of the C-S-H plays an important role in the compressive test and contributes significantly to the difference between the compressive and tensile strengths.
- Size of the RVE is an important parameter influencing significantly the strength.
- The type of the yield condition changes the responses only in the quantitative way while qualitatively the influence is not important. However, both investigated yield conditions overestimates peak strengths significantly for the considered material parameters.

Method	Young's Modulus [GPa]	Compressive Strength [MPa]	Tensile Strength [MPa]
SC_{J2}	23.117	128.721	128.721
FFT_{J2}	17.278	11.591	11.591
FEM_{J2}	19.629	18.244	18.244
$PM - FEM_{J2}$	12.973	112.156	45.828
FFT_E	17.278	28.026	21.818
FEM_E	19.629	31.480	24.003
$PM - FEM_E$	12.973	179.157	67.960

Table 5.3: Comparison of elastic and nonelastic properties of the RVE predicted by the investigated methods. Subscripts denote the yield condition assumed.

Chapter 6

Conclusions

The effect of heterogeneities in cementitious materials on the fracture propagation was studied on two material scales - cementitious materials with aggregates and pure cement paste. Objectives of the thesis were following:

- Critical review of the models for fracture propagation in heterogeneous materials on the scale of concrete and mortar with respect to their practical applicability (measuring of material properties, possibility to simulate real-sized specimens etc.)
- Development and verification of a framework for prediction of crack propagation in concrete and mortar involving work ranging from experimental work and material parameters identification to the simulations of fracture propagation in real-sized specimens.
- Verification of the developed framework against experimental data.
- Obtaining understanding of the basic nature of cracking processes in cement paste, extension of the developed framework to the scale of cement paste and predicting the compressive and tensile limit of the cement paste based on its microstructure and measured properties of phases.

In this Chapter, the proposed frameworks are summarized and conclusions are drawn.

6.1 Cementitious materials with aggregates

The proposed framework consists of three main parts:

- Experiments
- Identification of material properties
- Modeling

6.1.1 Experiments

Three types of experiments for determination of the mode-I fracture properties based on the assumptions of the fictitious crack method were compared - wedge splitting test, three point bending test and uniaxial tensile test (only numerically). The inverse analysis of the experimental records revealed significant discrepancies between material properties identified from the three point bending test and the wedge splitting test. Therefore the tests were simulated using the enriched particle model together with the uniaxial tensile test. Two sizes of specimens were simulated for each test to eliminate the effect of size. From the comparison of the traction-separation laws computed from the simulations and from the observation of the crack propagation in the model, the following conclusions were drawn:

- In the case of the uniaxial tensile test, the energy dissipated through microcracking outside of the plane of the notch depends significantly on the size of the specimen and is responsible for the difference in the computed traction-separation laws despite the relatively deep notches.
- Significant amount of energy dissipated in the wedge splitting specimen outside of the expected fracture process zone (above the tip of the notch) and due to a mixed-mode loading ahead of the main crack is responsible for significant difference in the computed traction separation laws as well as for the discrepancies observed in the identified material properties.
- In the three point bending test, the energy is dissipated in the expected fracture process zone and the computed traction-separation laws were consistent between the two sizes despite significant size effect observed at the global responses.

Due to the aforementioned reasons, the three point bending test was chosen as the main experiment for the identification of the material properties for simulations as well as for their verification.

6.1.2 Identification of material properties

The semi-analytical method for mode-I fracture propagation is based on the hinge model for specimens loaded with a combination of the bending moment and the normal force. The advantage is that it provides a closed-form analytical solution for the Crack Opening Displacement (COD) for a given load of the hinge, assuming linear elastic material behavior with a multi-linear traction-separation law. The hinge model is based on the assumption that the presence of the crack changes the stress and the strain field only locally while the rest of the structure remains unaffected. Using

the closed-form formula instead of the FE discretization is reflected by the reduction of the computational costs.

Even though the hinge model is capable of providing a closed-form analytical solution for any piece-wise linear TSL, derivation of an analytical solution for a more than bi-linear TSL and its implementation would be very complicated. Therefore a semi-analytical approach, with iterative neutral axis position assessment is employed. This modification allows us to involve both multi-linear traction-separation lawa as well as the multi-linear elastic behavior of the undamaged material in the computation with only a tiny increase in the computation costs in the global iterative scheme. The hinge model is suitable for simulation of mode-I fracture test where the crack cross-section is loaded by a combination of bending and normal load.

The traditionally used bi-linear traction separation law can be substituted by a tri-linear or quad-linear law increasing accuracy of simulation while still keeping the optimization well constrained and solutions unique. Further, it is verified that the identified parameters can be used as the input for FEA providing results matching favorably the experimental record used for the identification. The identified material parameters are thus independent on the model used for the identification.

However, even though the hinge-model is a very efficient model with very low computational demands (one simulation takes roughly 10 seconds), the entire inverse analysis procedure can still be time consuming. The reason is that, especially for cases when high precision and dense point spacing are desired, a huge number of iterations is needed to fulfill the convergence criteria and the entire inverse analysis can easily take several hours. The time needed to perform the hinge model-based inverse analysis is very sensitive to the initial estimation of the material parameters, especially the shape of the traction-separation law is important. The initial estimation of the shape of the traction-separation law of the investigated material is constructed in the following way: Young's modulus and tensile strength are guessed and the back analysis is run and the traction-separation law is found and smoothen. Starting from such an initial estimation reduces the number of global iterations needed to fulfill the convergence criteria in the hinge model-based inverse analysis is reduced with only negligible increase in the computational costs (back analysis and the fitting of the traction-separation law takes ≈ 2 seconds while 1 global iteration in the hinge model-based inverse analysis takes ≈ 5 minutes for the considered density of points).

6.1.3 Model for fracture propagation

Three different types of models capable of simulating the fracture propagation in a heterogeneous material were considered. Their advantages and disadvantages are summarized in the following overview:

Continuum Mechanics approach Section

Since the main focus of the research undertaken was put on the upscaling of the fracture properties from one material scale to another, the particle model was chosen because of its low computational demands allowing the experimental scale separation. Particle model of Cusatis (Cusatis et al. 2003, Cusatis et al. 2006, Cusatis & Cedolin 2007) was taken as the underlying model. The particle model was extended to include the effect of interfacial transition zone on the elastic properties to be able to simulate a broader range of aggregates diameters with satisfactory accuracy. Further, the particle model was enriched with matrix nodes - additional zero-diameter particles reducing the artificial roughness of the crack path and thus making the crack path more realistic.

6.1.4 Verification of the framework

Three types of cementitious materials - concrete, mortar and micromortar - were prepared and tested in three point bending test and in compressive test on cylinders. Material properties of the fictitious crack model were identified by inverse analysis providing elastic stiffness, uniaxial tensile strength, macroscopical mode-I energy and the shape of the traction-separation law of the materials. The remaining material parameters of the material model used in the particle model need to be estimated or possibly identified from additional experiments. In the presented framework, shear properties of the material were fitted in a such a way that the particle model simulation of a compressive test matched favorably the experimental record.

The particle model with the identified material properties was used to predict the response of the investigated materials in the three point bending tests. The following conclusions can be drawn:

- The particle model with the measured material properties provides predictions of crack propagation in three point bending test and compressive test matching favorably the experimental records.
- However, the predictions show more ductile response compared to the experimental records due to missing explicit incorporation of the ITZ in the model and due to missing localization limiters. Nevertheless, incorporation of the aforementioned features into the model

would significantly increase number of material parameters of the model and hence would make the presented framework much more complicated especially from the experimental point of view.

- Shear strength and mode-II energy on the meso-level play important role in advanced stages of the crack propagation. Their direct identification, however, is not possible neither from three point bending tests nor compressive tests and were therefore fitted.
- Fracture propagation in the uniaxial compression of concrete and mortar is initially mode-I and later mixed-mode crack propagation dominated process on the mesoscale. Therefore, the same set of material properties as in the case of three point bending test prediction was successfully used for predicting of the compressive test response up to the peak load.
- The particle model in the applied form is not suitable for simulation of the softening part of the compressive test experiments since it can not describe correctly creation of new contacts and mutual shearing of heavily damaged parts contributing to the load bearing capacity.

6.2 Pure cement paste

The crack propagation during the TPBT on notched specimens was observed in the ESEM. From these observations, two main conclusions can be drawn:

(a) At the investigated scale, the cement paste does not exhibit purely brittle behavior but shows intensive propagation of cracks in mode-I even before the peak load in mode-I is reached.

(b) The observed fracture mechanisms are qualitatively very similar to those observed in the case of mortars and concrete. The formation of the main crack is preceded by intensive micro-cracking and the stiff cement phases provide the bridging. The width of the zone with micro-cracking is in order of ≈ 100 μm and the roughness of the crack is in order of tens of μm.

Thus, the particle model used in Paper IV for the prediction of behavior of concrete and mortar based on material properties measured on mortar and micro-mortar, respectively, is presumably applicable also for the case of cement phase.

In contrary to the case of mortar or concrete where the matrix phase can be considered as a homogeneous material, the properties of the matrix phase, or rather of the interparticle volume, differ significantly for individual contacts in the cement paste microstructure. The increased

heterogeneity of the material is the result of the hydration which is, in terms of positioning of hydration products, essentially a random process. Therefore, the simple averaging of the elastic stiffnesses along the struts as well as concept of one set of material properties used in the case of concrete have to be abandoned and every strut has to be treated separately.
After the discretization of the microstructure by the struts, the diameters of the particles were set to zero. The entire volume between two nodes was homogenize using the finite element method for every strut (loss of linearity was used as a strength estimation in all cases). The material model applied in the case of mortar and concrete was modified in the following way: the response was considered elasto-brittle for a contact loaded in tension or in mixed-mode and perfectly plastic for case of the mixed-mode with dominating compression.
Material properties of cement phases identified from nanoindentation experiments were considered. Elastic modulus was computed from the unloading slope while the strength properties were computed from hardness. Two types of the yield conditions were compared: classical $J2$ plasticity and the elliptical yield surface obtained from upscaling of the building blocks of C-S-H.

6.2.1 Verification

The modified particle model with the material properties obtained from nanoindentation was used to simulate compressive and tensile tests of three types of microstructures - X-ray microtomography image of an ordinary portland cement paste with water/cement ratio of 0.3 hydrated for 7 days, microstructures of a white cement and an ordinary portland cement with water/cement ratio of 0.4 modeled in the hydration model (microstructures after 1, 7 and 28 days of hydration). The following conclusions can be drawn:

- Responses of the scanned and modeled microstructures are qualitatively identical.
- Particle model with FEM homogenization of the internodal volume without cracking provides simulations of compression without cracking matching favorably the nonlinear FEM solution with significantly reduced computational time.
- Cracking of the C-S-H plays and important role in the compressive test and contributes significantly to the difference between the compressive and tensile strengths.
- Size of the RVE is an important parameter influencing significantly

the strength.

- The type of the yield condition changes the responses only in the quantitative way while qualitatively the difference is not important.
- The proposed framework predicts correctly differences in strengths between different types of cements observed experimentally as well as the effect of hydration on strength.

Appendix A

Experiments

This Appendix does not present any coherent stand-alone Section. Rather, this Appendix collects detailed descriptions of all experimental procedures, records and materials referenced at various parts of this thesis and in the attached papers.

A.1 Experiments for upscaling of fracture properties

A.1.1 Materials

Cementitious materials of four different materials scales - concrete, mortar, micro-mortar and pure cement paste - were prepared. The materials differed in the size of the largest aggregates used, in the W/C and volume fractions of aggregates. The concrete contained aggregates up to 8 mm, mortar up to 2 mm, micro-mortar up to 0.8 mm and cement paste was without any aggregates. Washed sea gravel and sand were used. Two different binders were used for preparation of concrete, mortar and micro-mortar. The first set of specimens was prepared from Aalborg White cement (Cem A) and the second set was prepared using Aalborg Basis ordinary portland cement. One additional type of binder - Cem C - was added for the case of the pure cement paste and the smallest specimens made from micro-mortar. The W/C varied between 0.47 in the case of concrete and 0.4 in the case of pure cement paste. The differences were assumed to compensate the effect of the increased volume of the ITZ changing the effective W/C in the bulk material.
The PSD characterizing the aggregates is shown in Figure
Figure

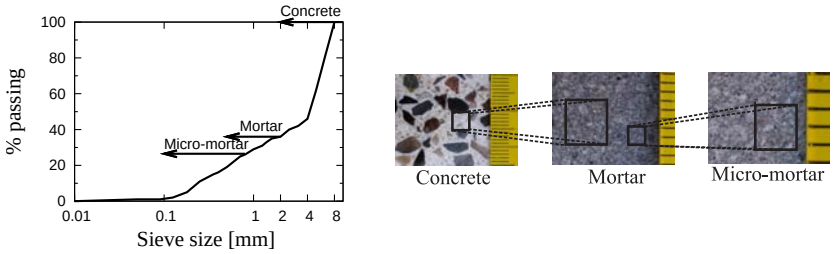

a) b)

Figure A.1: a) Particle Size Distribution characterizing investigated materials and b) graphical illustration of the up-scaling.

Characterization of binders

Two types of cement binders, Cem A and Cem C, were used for preparation of pure cement pastes for mechanical testing and their hydration was modeled in Paper V. Tables

Sieve diameter D_i [mm]	volume fraction passing f_i [%]
10.0	100
8.00	100
6.30	81
5.00	62
4.0	46
3.15	42
2.80	41
2.50	40
2.00	36
1.60	35
1.40	33
1.25	31
1.00	29
0.800	26
0.710	25
0.500	19
0.400	16
0.355	15
0.250	11
0.180	5
0.125	2
0.0900	1
0.0630	1
0.0500	1
0.0100	0

Table A.1: Characterization of the PSD curve used in the experiments for upscaling of fracture properties

Material	d_{min} [mm]	d_{max} [mm]	α_{agg} [-]	W/C [-]
Concrete	0.01	8.0	0.65	0.47
Mortar	0.01	2	0.40	0.44
Micro-mortar	0.01	0.8	0.32	0.43
Paste	-	-	-	0.4

Table A.2: Detail description of investigated materials: $\mathrm{d_{min}}$ and d_{max} refer to minimal and maximal sizes of aggregates used, respectively; α_{agg} denotes volume fraction of aggregates in the fresh mix and W/C is the water to cement ratio.

Content [%]	Cem A	Cem C
C_3S	67.1	62.3
C_2S	23.6	18.4
C_4AF	0.00	7.1
C_3A	3.5	6.0
C	0.8	0
MgO	0.2	0.7
Sulfate	4.2	5.1
$CaCO_3$	0.6	0.5

Table A.3: Chemical composition of the investigated cements measured by Rietveld analysis.

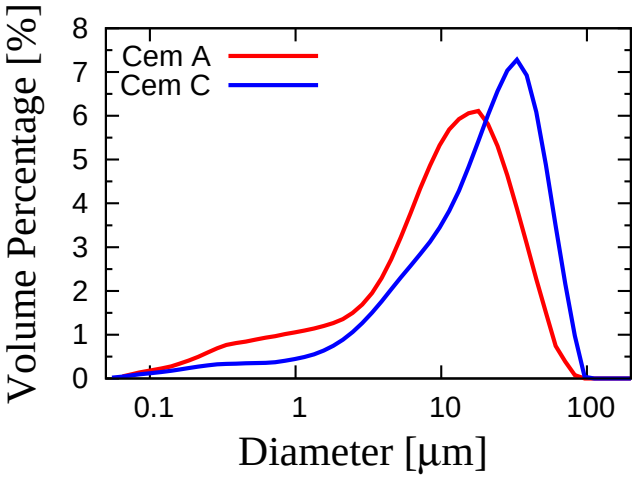

a)

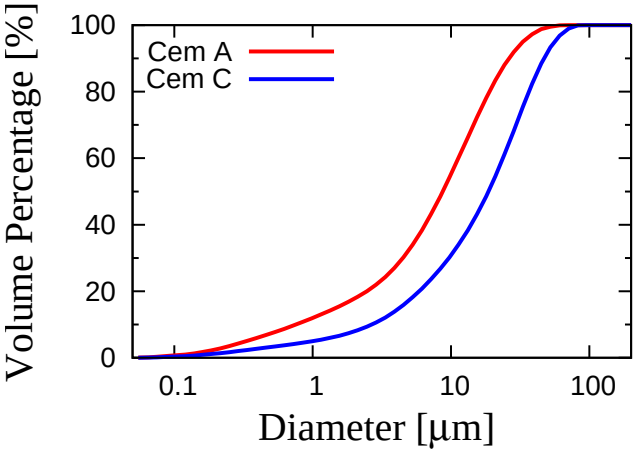

b)

Figure A.2: Particle size distribution curves, a), and cumulative particle size distribution curves, b), for Cem A and Cem C.

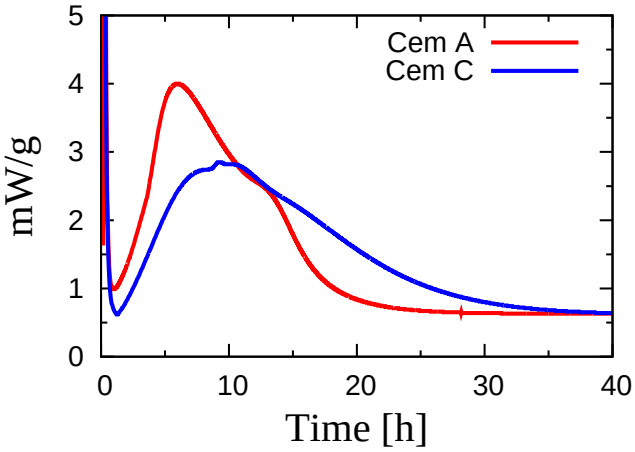

Figure A.3: Calorimetric record of heat of hydration of Cem A and Cem C prepared according to Section

A.1.2 Mixing and curing

The materials with aggregates were mixed in a rotary drum mixer not allowing continuous adding of water. Thus the mixing water was added in two steps: 10% of water was added and mixed with aggregates for 1 minute; then the binder was added and the mixing continued for 1 minute; the rest of water was added and mixed for another 2 minutes. The samples were cast immediately after the mixing. The concrete samples were vibrated using a vibration table. The samples made from mortar and micro-mortar were compacted manually with several impacts, since there was a danger of the separation of phases when the machine vibration would be used. After the casting, samples were stored in laboratory conditions (approximately 20°C) overnight covered with a plastic foil. The samples were demolded after approximately 24 hours and were moved to a warm water bath (50°C) where were kept for another seven days. Then notches were cut and the samples were kept in the laboratory conditions until the testing took place (approximately 3 months).

Mixing of pure cement pastes

The specimens made from pure cement paste as well as the specimens made from the micro-mortar used in the TPBT in the ESEM were prepared according to the mixing procedure shown in Figures
After the mixing, samples were casted immediately. The material was compacted manually with several impacts, since there was a danger of the separation of phases when the machine vibration would be used. After casting, samples were stored in laboratory conditions (approximately 20°C) overnight covered with a plastic foil. The samples were demolded after approximately 24 hours and were moved to a warm water bath (50°C) where were kept for another seven days. The notches were casted.

Procedure for mixing for cement pastes

Purpose
Mixing of cement paste in batches of approximately 120 cm^3.

Equipment
- Mixer equipped with a paddle, see Figure 1 and 2. Such mixer may be obtained from IKA – Weke GMBH & CO.KG (www.ika.net);
- Paddle, diameter of 44.5 mm. This paddle is custom made at EPFL; contact Emmanuel Galluci;
- Scale (accuracy 0.01 g.)
- Plastic containers with lid for weighing and mixing, see Figure 3:
  - Binder: conical cylindrical cup approx. diameter 54 mm at bottom and 75 mm at top and 100 mm high;
  - Water: e.g. conical cylindrical cup approx. diameter 60 mm at bottom and 70 mm at top and 60 mm high;

  Such cups may be obtained from Semadeni (www.semadeni.com);
- Moulds (size and amounts depends on your purpose);
- Room of ambient temperature.

Possible additional equipment
- A powder mixer for blending of powder; capacity 0.5 litres, maximum speed of rotation 60 rpm (adjustable), e.g. a TURBULA model T2 F shaker mixer from Glen Mills Inc. (www.glenmills.com), see Figure 4. The powder mixer container is set into three-dimensional movement that exposes the product to always changing, rhythmically pulsing motion.
- If the control of the mixer is analog an instrument to check the rotational speed of the paste mixer; e.g. JAQUET type DMR 903.

Figure 1: Paste mixer (LABORTECHNIK RW 20.n)

Figure 2: Custom made paddle

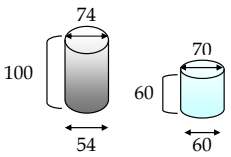

Figure 3: Containers for weighing and mixing, dimensions in (mm)

Figure 4: Powder mixer (TURBULA shaker-mixer)

Prepared by VK for Core project 4: Reactivity of blended cements with SCM
Revised by VK, MCA and MGE March 8, 2007, Revised MCA and MGE October 11, 2007
\\Server1\grupper\MC-RTN_NanoCem\Materials and procedures\Procedures\MCRTN_CP4_ProcedureMixing_Rev_071011.doc

Figure A.4: Mixing procedure for pure cement paste, part 1.

Materials
- Cement
- Distilled water (20°C)
- Possible supplementary materials
- Possible chemical admixtures
- Saturated calcium hydroxide for possible saturated curing

Mix proportions are given in Table 1. The size of container and paddle for mixing is suitable for pastes from 160 g powder. The mix proportions are based on a constant volume water to volume binder ratio and w/c=0.4 of the paste with cement A. The need for use of superplasticizer when mixing pastes with silica fume is to be discussed with Elkem and Sika.

Procedure
Blending of binders
Either use a powder blender
1. Weighed out the cement and the supplementary cementitious materials in amounts to fit the volume of the powder mixer.
2. Blend the binders in the TURBULA shaker-mixer for minimum 5 hours
3. Weighed out the exact amount of binders

or blend binders in "binder container"
4. Weighed out the exact amounts of cement and the supplementary cementitious materials in the "binder container" and blend by shaking the container with two 15-20 mm glass balls in for 5 min.

Mixing
5. Adjust the rotational speed of the mixer to 500 rpm (if analog check rotational speed)
6. Add the water to the cement and immediately after mix the paste at a rotational speed of 500 rpm for 3 minutes.
7. Stop the mixing for 2 minutes, and cover the paste during this period. If analog check rotational speed adjust the rotational speed of the mixer to 2000 rpm
8. Mix at a rotational speed of 2000 rpm for 2 minutes.

Casting
Cast your samples, ensure proper compaction.

Curing
Either sealed curing
9. Close the flask with the paste and put on the date and time when the hydration cement paste started. Keep sealed to restrict evaporation and ingress of CO_2.

or saturated curing
10. The samples should not dry at any time). Add a few drops of saturated calcium hydroxide right after casting and add additional saturated calcium hydroxide to keep the sample saturated (minimum the amount which will be imbibed (sucked in) due to 6 ml/100 g cement and 18g/100 silica fume). The sample size should be limited to ensure transport of water to the center of the sample; i.e. high samples should be de-moulded and kept submerged in saturated calcium hydroxide in a slightly larger container. Keep sealed to restrict evaporation and ingress of CO_2.

Figure A.5: Mixing procedure for pure cement paste, part 2.

A.1.3 Test setups

This Section briefly describes the experimental setups used.

Three point bending test

TPBTs were performed on prismatic specimens, see Figure

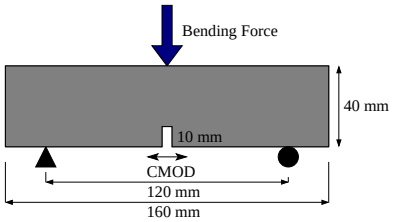

Figure A.6: Scheme of the three point bending test setup and specimen.

Wedge splitting test

Dimensions of the WST specimens according to the nomenclature introduced in Figure

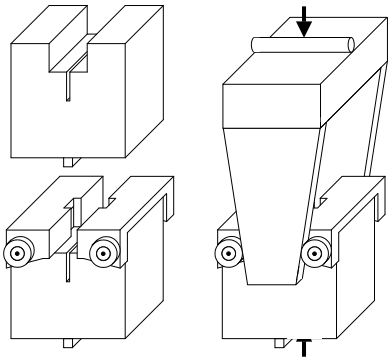

Figure A.7: Scheme of the wedge splitting test setup.

Compression test on cylinders

The compression experiments were performed on cylinders with diameter of 60 mm and height of 120 mm before grinding, see Figure

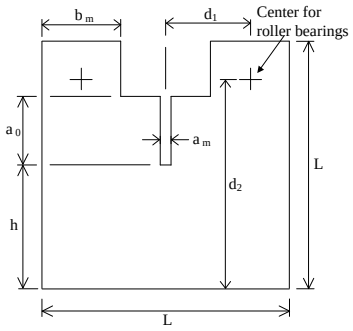

(a)

Figure A.8: Scheme of the wedge splitting test specimen. Dimensions are summarized in Table

	L	h	a_0	a_m	b_m	d_1	d_2
mm	100	50.0	28.0	4.5	35.0	39.5	85.4

Table A.4: Dimensions of the wedge splitting test specimen. The nomenclature is introduced in Figure

Three point bending test in ESEM

The specimens for the TPBT in the chamber of the ESEM were of the identical shape as the specimens for the TPBT shown in Figure
The speed of the screw-driven mechanism imposing the load was 0.142 mm per 100 s (source: calibration by a technician in Riso). However, such a speed yielded underestimated values of slopes of the records. For example, initial slopes of records in Figure

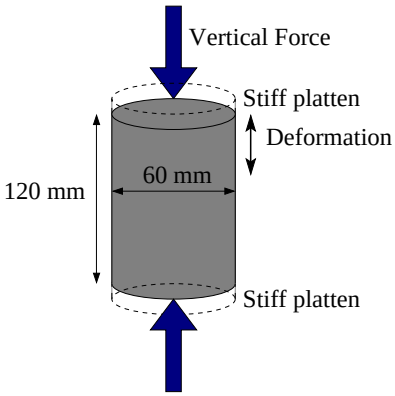

Figure A.9: Scheme of the test setup for compression on cylinders and specimen dimensions.

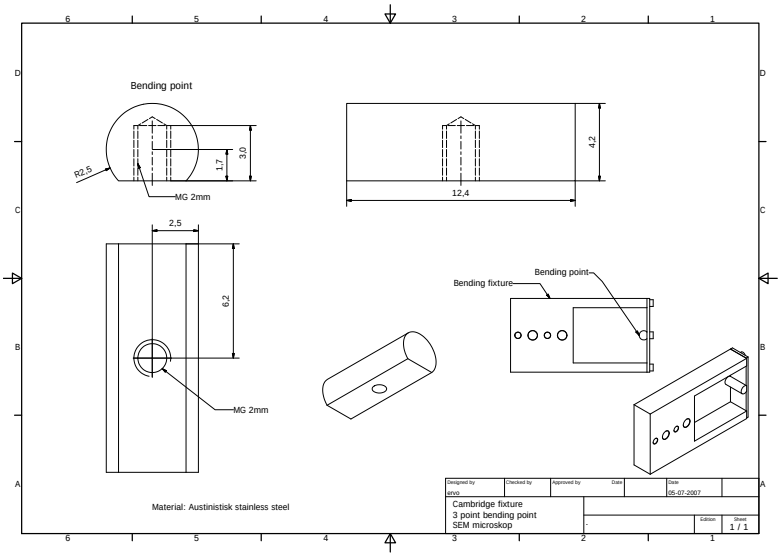

Figure A.10: Scheme of the TPBT setup used in ESEM.

A.1.4 Data filtering and manipulation

For certain applications such as the inverse analysis based on the semi-analytical hinge model described in Section
In cases when more than one specimen of the material were tested in the same test, records were averaged in the following way:

- the initial parts of all records were cut off and extrapolated, records were shifted to the origin;
- the largest deformation measured was discretized into several (thousands) equidistantly placed points;
- for every point, loads corresponding to the point were obtained by the linear interpolation of the records;
- for every point, the average load was computed by summing the interpolated values divided by number of records with maximal measured deformation greater than the deformation corresponding to the point.

The averaging is schematically shown in Figure

A.1.5 Results

In the main part of the thesis, only the averaged experimental record and possibly extreme values are shown. For sake of complexity, all experimental records are listed in this Section.

Three point bending tests results

Three types of material - concrete, mortar and micro-mortar described in Section
Six specimens were tested per every material. However, in some cases only five records are plotted. In such cases, one of the experiments went wrong and the record was excluded.

Wedge splitting tests results

Three types of material - concrete, mortar and micro-mortar described in Section
Five specimens were tested per every material. However, in some cases only four records are plotted. In such cases, one of the experiments went wrong and the record was excluded.

Compression on cylinders - tests results

Three types of material - concrete, mortar and micro-mortar described in Section
Three specimens were tested in the case of concrete and two specimens for other materials.

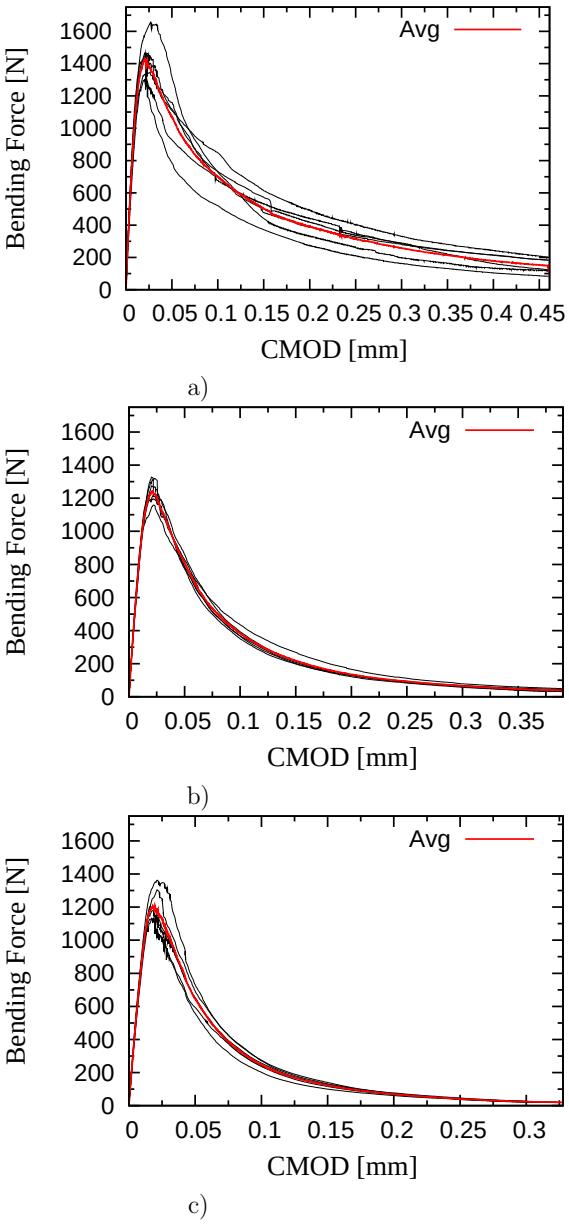

Figure A.11: Results of three point bending test for a) concrete, b) mortar and c) micro-mortar. Aalborg Basis cement was used as the binder.

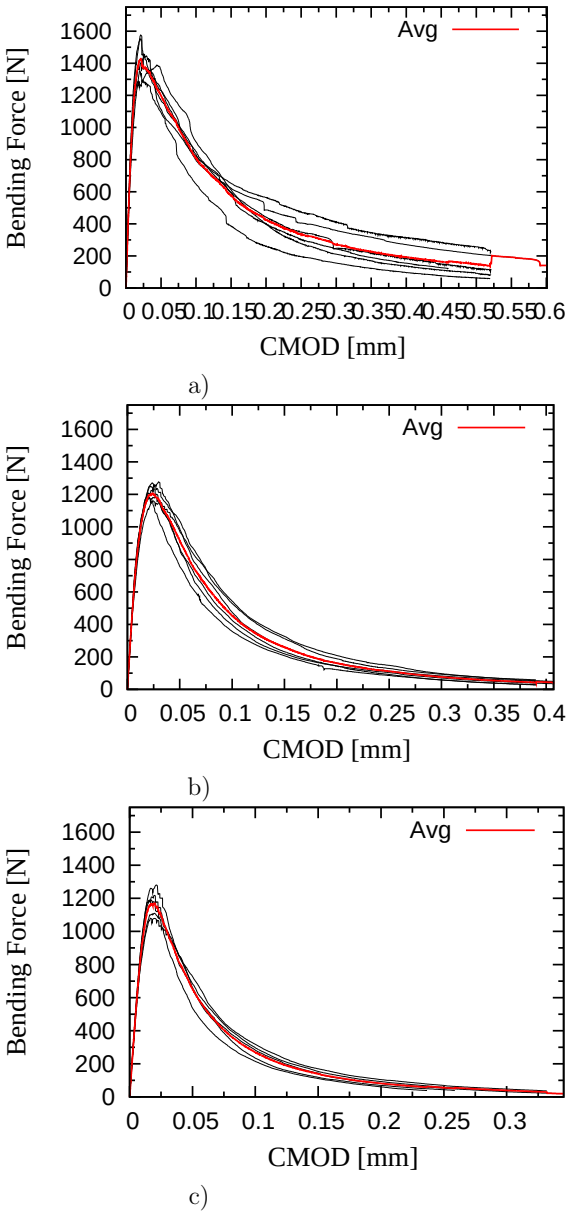

Figure A.12: Results of three point bending test for a) concrete, b) mortar and c) micro-mortar. Aalborg White cement (Cem A) was used as the binder.

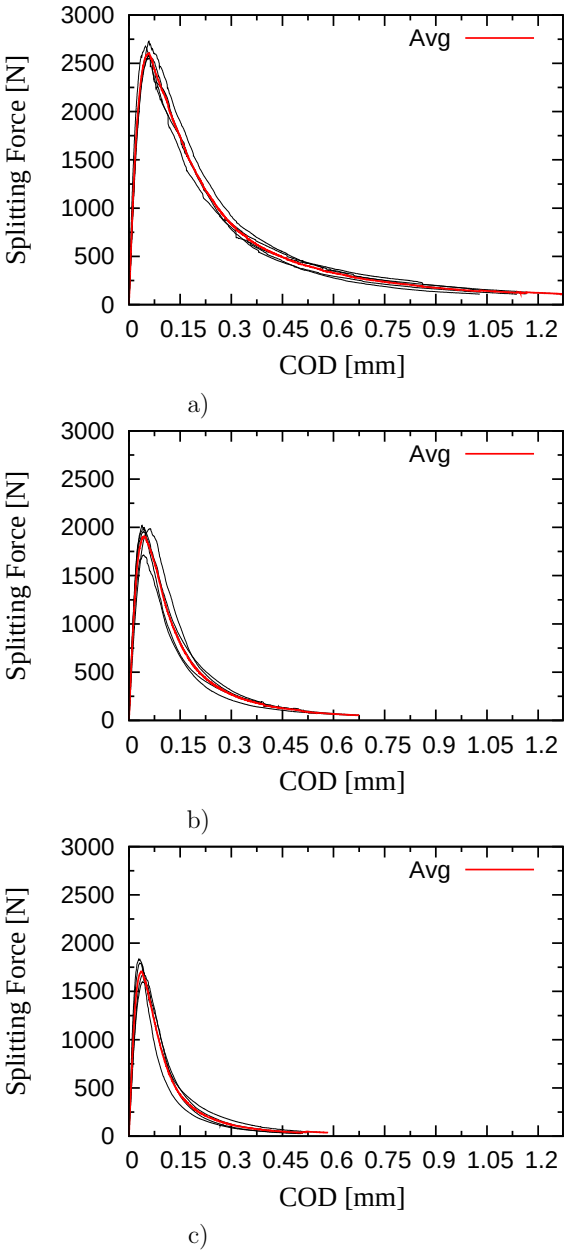

Figure A.13: Results of wedge splitting test for a) concrete, b) mortar and c) micro-mortar. Aalborg Basis cement was used as the binder.

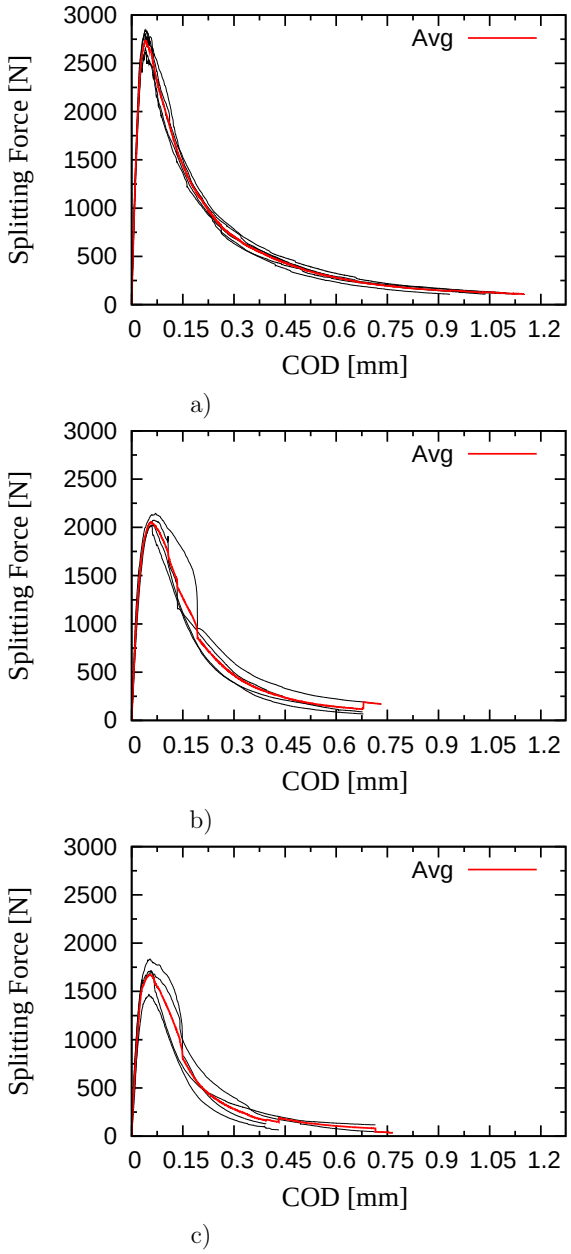

Figure A.14: Results of wedge splitting test for a) concrete, b) mortar and c) micro-mortar. Aalborg White cement (Cem A) was used as the binder.

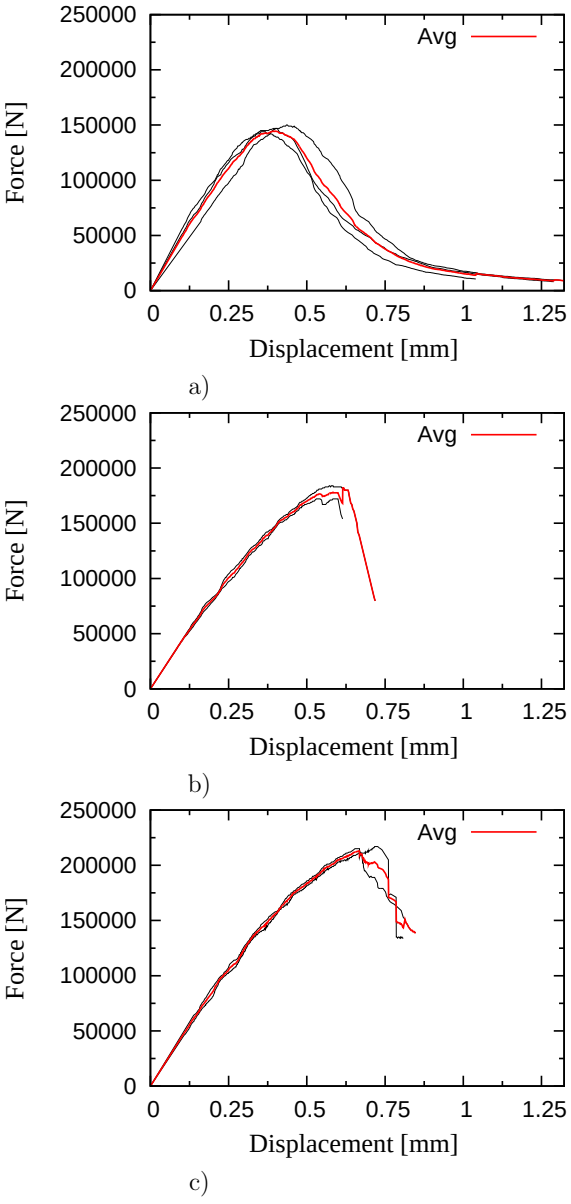

Figure A.15: Results of compressive tests on cylinders for a) concrete, b) mortar and c) micro-mortar. Aalborg Basis cement (Cem A) was used as the binder.

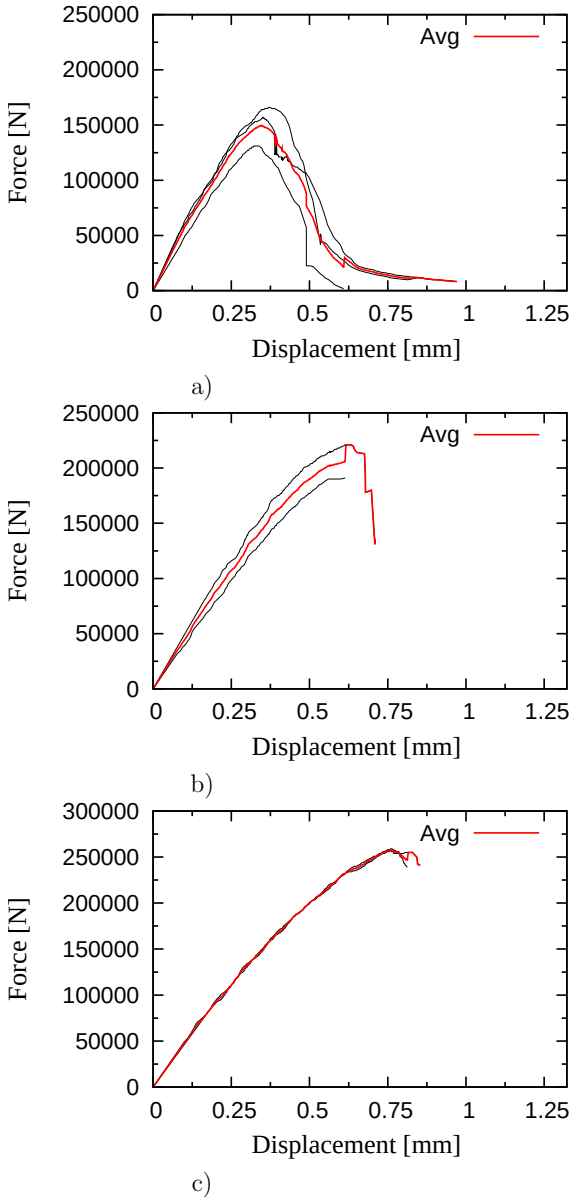

Figure A.16: Results of compressive tests on cylinders for a) concrete, b) mortar and c) micro-mortar. Aalborg White cement (Cem A) was used as the binder.

Three point bending test in ESEM - tests results

Two types of cement pastes, see Sections

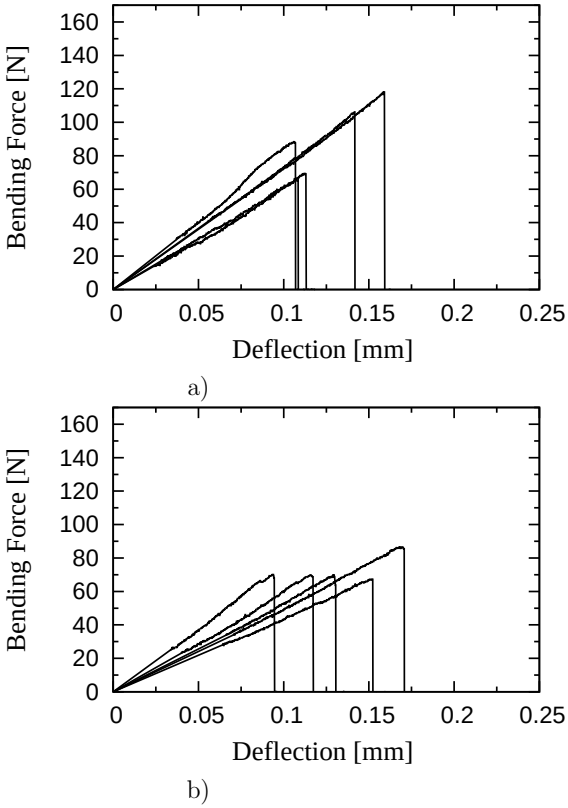

Figure A.17: Results of TPBT in ESME for a) Aalborg White cement paste (Cem A) and b) Cem C cement paste.

Two types of micro-mortars, see Sections

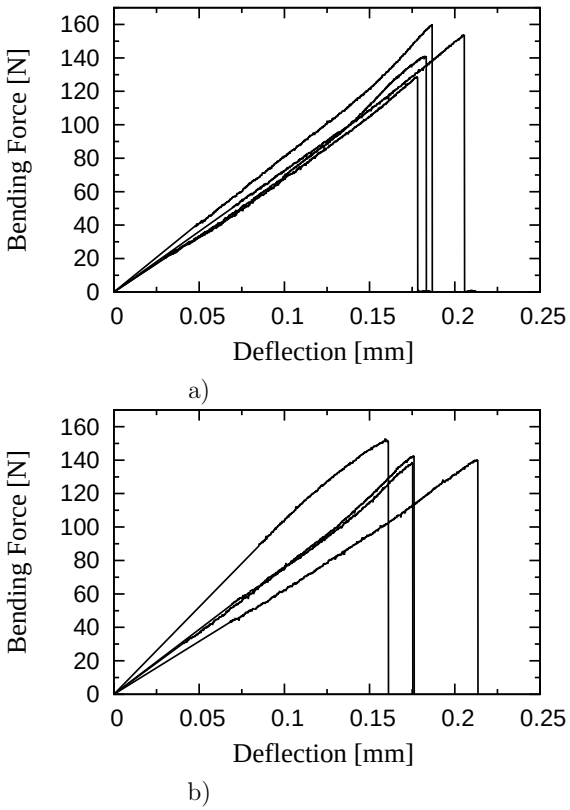

Figure A.18: Results of TPBT in ESME for a) Aalborg White (Cem A) and b) Cem C micro-mortar.

Bibliography

H. Abdalla & B. Karihaloo (2003). 'Determination of size-independent specific fracture energy of concrete from three-point bend and wedge splitting tests'. *Magazine of Concrete Research* **55**(2):133–141.

J. Aboudi (1991). *Mechanics of composite materials : A unified micromechanical approach*, vol. 29 of *Studies in Applied Mechanics*. Elsevier.

M. D. Adley & M. H. Sadd (1992). 'Continuum models for materials with lattice-like microstructure'. *Computers & Structures* **43**(1):13 – 18.

M. Alexander (1993). 'Two experimental techniques for studying the effects of the interfacial zone between cement paste and rock'. *Cement and Concrete Research* **23**(3):567 – 575.

M. J. Aquino, et al. (1995). 'Mechanical properties of the aggregate and cement interface'. *Advanced Cement Based Materials* **2**(6):211 – 223.

G. I. Barenblatt (1959). 'On equilibrium cracks forming during brittle gracture (in Russian)'. *Prikladnaya Matematika i Mekhanika (PMM)* **23**:434–444. Originally published in Russian, 1957, see e.g. (Karihaloo 1995).

G. I. Barenblatt (1962). 'The mathematical theory of equilibrium cracks in brittle fracture'. *Advances in Applied Mechanics* **7**:55–129. Originally published in Russian, 1957, see e.g. (Karihaloo 1995).

Z. P. Bažant (1976). 'Instability ductility and size effect in strain-softening concrete'. *ACSE J. Engng Mech* **102**:331–344.

Z. P. Bažant & L. Cedolin (1979). 'Blunt crack band propagation in finite element analysis'. *ACSE J. Engng Mech* **105**:297–325.

Z. P. Bažant & B. H. Oh (1983). 'Crack Band Theory for Fracture of Concrete'. *Materials and Structures* **16**:155–157.

Z. P. Bazant (2002). 'Concrete fracture models: testing and practice'. *Engineering Fracture Mechanics* **69**(2):165 – 205.

T. Belytschko & T. Black (1999). 'Elastic Crack growth in finite elements with minimal remeshing'. *International Journal for Numerical Methods in Engineering* (45):601–620.

S. Bishnoi (2008). *Vector modelling of hydrating cement microstructure and kinetics.* Ph.D. thesis, EPFL, Programme doctoral Sciences et Gnie des matriaux, IMX Institut des matriaux, Lausanne, Switzerland.

Z. Bittnar & J. Šejnoha (1992). *Numercické metody mechaniky [2].* Vydavatelství ČVUT. in Czech.

J. E. Bolander & S. Saito (1998). 'Fracture analyses using spring networks with random geometry'. *Engineering Fracture Mechanics* **61**(5-6):569 – 591.

A. Caballero, et al. (2006). '3D meso-structural analysis of concrete specimens under uniaxial tension'. *Computer Methods in Applied Mechanics and Engineering* **195**(52):7182 – 7195. Computational Modelling of Concrete.

A. Caballero, et al. (2008). 'Consistent tangent formulation for 3D interface modeling of cracking/fracture in quasi-brittle materials'. *Computer Methods in Applied Mechanics and Engineering* **197**(33-40):2804 – 2822.

A. Carpinteri (1989). 'Cusp catastrophe interpretation of fracture instability'. *Journal of the Mechanics and Physics of Solids* **37**(5):567–582.

P. Casanova (1995). *Béton renforcés de fibres métaliques : du matériau à la strucure.* Ph.D. thesis, ENPC.

M. Crisfield (1984). 'Accelerating and damping the modified Newton-Raphson method'. *Computers and Structures* **18**(3):395 – 407.

G. Cusatis, et al. (2003). 'Confinement-Shear Lattice Model for Concrete Damage in Tension and Compression: I. Theory'. *Journal of Engineering Mechanics* .

G. Cusatis, et al. (2006). 'Confinement-shear lattice CSL model for fracture propagation in concrete'. *Computer Methods in Applied Mechanics and Engineering* **195**(52):7154 – 7171. Computational Modelling of Concrete.

G. Cusatis & L. Cedolin (2007). 'Two-scale study of concrete fracturing behavior'. *Engineering Fracture Mechanics* **74**(1-2):3 – 17. Fracture of Concrete Materials and Structures.

K. Duan, et al. (2003). 'Thickness effect on fracture energy of cementitious materials'. *Cement and Concrete Research* **33**(4):499 – 507.

D. S. Dugdale (1960). 'Yielding of Steel Sheets Containing Slits'. *Journal of the Mechanics and Physics of Solids* **8**:100–104.

C. Dunant (2009). *Alkali-silica-reaction in Swiss concrete dams*. Ph.D. thesis, EPFL.

J. Eliáš (2009). *Discrete Simulation of Fracture Process in Disordered Materials*. Ph.D. thesis, Brno University of Technology, Faculty of Civil Engineering.

J. Eliáš & P. Frantík (2009). 'Limitations of sequentially linear solution procedure'. In *International Conferenco of Fracture*, Ottawa, Ontario, Canada. In print.

M. Elices, et al. (2002). 'The cohesive zone model: advantages, limitations and challenges'. *Engineering Fracture Mechanics* **69**(2):137 – 163.

A. Elsharief, et al. (2003). 'Influence of aggregate size, water cement ratio and age on the microstructure of the interfacial transition zone'. *Cement and Concrete Research* **33**(11):1837 – 1849.

L. D. Enochson & R. K. Otnes (1969). *Programming and analysis for digital time series data*. Shock and Vibration Information Center, volume 3 of the shock and vibration monograph series edn.

C. A. Felippa (2003). 'A study of optimal membrane triangles with drilling freedoms'. *Computer Methods in Applied Mechanics and Engineering* **192**(16-18):2125 – 2168.

A. A. Griffith (1920). 'The Phenomena of Rupture and Flow in Solids'. *Philosophical transactions of the Royal Society of London, Series A, Physical sciences and engineering* **221**:163–198.

S. Hentz, et al. (2004). 'Discrete element modelling of concrete submitted to dynamic loading at high strain rates'. *Computers & Structures* **82**(29-30):2509 – 2524.

A. Hillerborg, et al. (1976). 'Analysis of crack formation and crack growth in concrete by means of fracture mechanics and finite elements'. *Cement Concrete Research* **6**:773–782.

K. Hossain & M. Lachemi (2007). 'Strength, durability and microstructural aspects of high performance volcanic ash concrete'. *Cement and Concrete Research* **37**(5):759 – 766.

X. Hu & K. Duan (2004). 'Influence of fracture process zone height on fracture energy of concrete'. *Cement and Concrete Research* **34**(8):1321 – 1330.

X.-Z. Hu & Y.-W. Mai (1992). 'Cracks bridging analysis for alumina ceramics undermonotonic and cyclic loading'. *Journal of the American Ceramic Society* **75**:848–853.

A. E. Idiart, et al. (2009). 'Computational modeling of external sulfate attack in concrete at the meso-level'. In *X International Conference on Computational Plasticity*, Barcelona,Spain.

A. E. Idiart, et al. (2007). 'H-M mesostructural analysis of the effect of aggregates on the drying shrinkage microcraking of concrete'. In *IX International Conference on Computational Plasticity*, Barcelona,Spain.

G. R. Irwin (1957). 'Analysis of Stresses and strains near the End of a Crack Traversing a Plate'. *Journal of Applied Mechanics* **24**:361–364.

J. G. J. Planas & M. Elices (1999). 'Size effect and inverse analysis in concrete fracture'. *International journal of fracture* **95**:367–378.

J. S. Jacobsen, et al. (2009). 'Private communication. To be published'.

J. S. Jacobsen, et al. (to be published). 'Measurement and Characterization of Mixed Mode Fracture in Concrete'. In *Framcos 7*.

M. Jirásek (1998). 'Nonlocal models for damage and fracture: Comparison of approaches'. *International Journal of Solids and Structures* **35**(31-32):4133 – 4145.

M. Jirásek (2006a). 'Advanced course on Modeling of Localized Inelastic Deformation'. Lecture notes.

M. Jirásek (2006b). *Modeling of Localized Inelastic Deformation*. Lecture notes.

B. L. Karihaloo (1995). *Fracture Mechanics & Structural Concrete*. Concrete Design and Construction Series. Longman Scientific & Technical, Essex, England.

B. L. Karihaloo, et al. (2003). 'Lattice modelling of the failure of particle composites'. *Engineering Fracture Mechanics* **70**(17):2385 – 2406.

A. K.Gupta & H. Akbar (1984). 'Cracking in Reinforced Concrete Analysis'. *Journal of Structural Engineering* **110**:1735–1746.

R. P. Khatri, et al. (1995). 'Effect of different supplementary cementitious materials on mechanical properties of high performance concrete'. *Cement and Concrete Research* **25**(1):209 – 220.

Y. Kitsutaka (1997). 'Fracture parameters by polylinear tension-softening analysis'. *Journal of Engineering Mechanics* **123**(5):444–450.

K. O. Kjellsen & H. M. Jennings (1996). 'Observations of microcracking in cement paste upon drying and rewetting by environmental

scanning electron microscopy'. *Advanced Cement Based Materials* **3**(1):14 – 19.

S. H. Kwon, et al. (2008). 'Effect of specimen size on fracture energy and softening curve of concrete: Part II. Inverse analysis and softening curve'. *Cement and Concrete Research* **38**(8-9):1061 – 1069.

G. Li, et al. (1999). 'Effective Young's modulus estimation of concrete'. *Cement and Concrete Research* **29**(9):1455 – 1462.

H. N. Linsbauer & E. K. Tschegg (1986). 'Fracture energy determination of concrete with cube shaped specimens (in german)'. *Zement und Beton* **31**:38–40.

H.-K. Man & J. G. van Mier (2008). 'Influence of particle density on 3D size effects in the fracture of (numerical) concrete'. *Mechanics of Materials* **40**(6):470 – 486.

S. Mindess & S. Diamond (1980). 'A preliminary SEM study of crack propagation in mortar'. *Cement and Concrete Research* **10**(4):509 – 519.

S. Mindess & S. Diamond (1982). 'A device for direct observation of cracking of cement paste or mortar under compressive loading within a scanning electron microscope'. *Cement and Concrete Research* **12**(5):569 – 576.

J. Mougaard, et al. (2010). 'A partly and fully cracked triangular XFEM element for modeling cohesive fracture'. *International Journal For Numerical Methods in Engineering* Submitted 2010.

J. C. Nadeau (2003). 'A multiscale model for effective moduli of concrete incorporating ITZ water-cement ratio gradients, aggregate size distributions, and entrapped voids'. *Cement and Concrete Research* **33**(1):103 – 113.

P. Neto, et al. (2004). 'The influence of mode II fracture on concrete strengthened with CFRP'. *Computers and Structures* **82**(17-19):1495 – 1502. Computational Mechanics in Portugal.

J. F. Olesen (2001). 'Fictitious Crack Propagation in Fiber-Reinforced Concrete Beams'. *Journal of Engineering Mechanics* **127**(3):272–280.

L. Østergaard (2003). *Early-Age Fracture Mechanics and Cracking of Concrete. Experiments and Modelling. To be published.* Ph.D. thesis, Department of Civil Engineering, Technical University of Denmark, Lyngby, Denmark.

L. Østergaard, et al. (2002). 'Interpretation and Inverse Analysis of the Wedge Splitting Test'. In *Fracture Mechanics Beyond 2000*, vol. II, pp. 593–600. EMAS Publications, Sheffield, UK.

T. C. Powers & T. L. Brownyards (1948). 'Studies of the physical properties of hardened cement paste'. Bulletin 22, Research Laboratories of the Portland Cement Association, Chicago.

N. S. Que (2003). *Identification of cohesive crack fracture paramaters using mathematical programming*. Ph.D. thesis, School of Civil and Enviromental Engineering, The University of New South Wales, Sydney, Australia.

A. A. Ramezanianpour & V. M. Malhotra (1995). 'Effect of curing on the compressive strength, resistance to chloride-ion penetration and porosity of concretes incorporating slag, fly ash or silica fume'. *Cement and Concrete Composites* **17**(2):125 – 133.

H. W. Reinhardt, et al. (1997). 'Shear of structural concrete members and pure mode II testing'. *Advanced Cement Based Materials* **5**(3-4):75 – 85.

K. Rektorys & a spol. (1981). *Pvrehled užité matematiky*. SNTL Nakladatelství technické literatury, Praha. in Czech.

P. E. Roelfstra & F. H. Wittmann (1986). 'Numerical method to link strain softening with failure of concrete'. In *Fracture Toughness and Fracture Energy of Concrete*, pp. 163–175. Elsevier.

J. G. Rots, et al. (2008). 'Robust modeling of RC structures by "event-by-event" startegy'. *Engineering Fracture Mechanics* **75**:590–614.

E. Schlangen & J. van Mier (1992). 'Experimental and numerical analysis of micromechanisms of fracture of cement-based composites'. *Cement and Concrete Composites* **14**(2):105 – 118. Special Issue on Micromechanics of Failure in Cementitious Composites.

J. Skoček & H. Stang (2008). 'Inverse analysis of the wedge-splitting test'. *Engineering Fracture Mechanics* **75**(10):3173 – 3188.

H. Stang, et al. (2007). 'On the application of cohesive crack modeling in cementitious materials'. *Materials and Structures* **40**(4):365–374.

H. Tada, et al. (1985). *The Stress Analysis of Cracks Handbook*. Paris Productions Incorporated, 226 Woodbourne Dr., St. Louis, Missouri, USA.

B. Täljsten (1994). *Plate bondingstrengthening of existing previous termconcretenext term structures with epoxy bonded plates of steel or fibre reinforced plastics*. Ph.D. thesis, Lulea University of Technology.

W. A. Tasong, et al. (1998). 'Aggregate-cement paste interface. ii: influence of aggregate physical properties'. *Cement and Concrete Research* **28**(10):1453 – 1465.

H. Toutanji, et al. (2004). 'Effect of supplementary cementitious materials on the compressive strength and durability of short-term cured concrete'. *Cement and Concrete Research* **34**(2):311 – 319.

Y. Uchida & B. I. G. Barr (1998). 'Tension softening curves of concrete determined from different test specimen geometries'. In *Fracture Mechanics of Concrete Structures*, pp. 387–398. Aedificatio Publishers, Freiburg, Germany 17–30.

J. Ulfkjær, et al. (1995). 'Analytical model for fictitious crack propagation in concrete beams'. *Journal of Engineering Mechanics* **121**(1):7–15.

J. P. Ulfkjær & R. Brincker (1993). 'Indirect determination of the σ-w relation of HSC through three-point bending'. In *Fracture and Damage of Concrete and Rock - FCDR-2*, pp. 135–144. E & FN Spon.

J. F. Unger, et al. (2007). 'Modelling of cohesive crack growth in concrete structures with the extended finite element method'. *Computer Methods in Applied Mechanics and Engineering* **196**(41-44):4087 – 4100.

J. G. M. van Mier & M. R. A. van Vliet (2002). 'Uniaxial Tension Test for the Determination of Fracture Parameters of Concrete: State of the Art'. *Engineering Fracture Mechanics* **69**:235–247.

V. Šmilauer (2005). *Elastic properties of hydrating cement paste determined from hydratation models*. Ph.D. thesis, Czech Technical University in Prague, Faculty of Civil Engineering, Czech Technical University in Prague, Prague, Czech Republic.

R. Walter & J. F. Olesen (2008). 'Cohesive mixed mode fracture modelling and experiments'. *Engineering Fracture Mechanics* **75**(18):5163 – 5176.

G. Wang, et al. (2008). 'Particle modeling of dynamic fracture simulations of a 2D polymeric material (nylon-6,6) subject to the impact of a rigid indenter'. *Computational Materials Science* **44**(2):449 – 463.

F. Wittmann, et al. (1990). 'Size effect on fracture energy of concrete'. *Engineering Fracture Mechanics* **35**(1-3):107 – 115. Special Issue Fracture and Damage of Concrete and Rock.

Q. Xiao & B. Karihaloo (2007). 'An overview of a hybrid crack element and determination of its complete displacement field'. *Engineering Fracture Mechanics* **74**(7):1107 – 1117. Fracture of Materials: Moving Forwards.

D. Xie & A. M. Waas (2006). 'Discrete cohesive zone model for mixed-mode fracture using finite element analysis'. *Engineering Fracture Mechanics* **73**(13):1783 – 1796.

Z. Zhao, et al. (2008). 'Effect of specimen size on fracture energy and softening curve of concrete: Part I. Experiments and fracture energy'. *Cement and Concrete Research* **38**(8-9):1049 – 1060.

R. Zimbelmann (1985). 'A contribution to the problem of cement-aggregate bond'. *Cement and Concrete Research* **15**(5):801 – 808.

A. Zubelewicz & Z. P. Bazant (1987). 'Interface Element Modeling of Fracture in Aggregate Composites'. *Journal of Engineering Mechanics* **113**(11):1619–1630.

List of Figures

List of Tables

List of Abbreviations

AB	Aalborg Basis cement
AW	Aalborg White cement
BCM	Bridged Crack Model
CC	Cylinder Compression
CMOD	Crack Mouth Opening Displacement
COD	Crack Opening Displacement
CZM	Conhezive Zone Models
DOF	Degree Of Freedom
ESEM	Environmental Scanning Electron Microscope
FCM	Fictitious Crack Model
FE	Finite Element
FEA	Finite Element Analysis
FEM	Finite Element Method
FFT	Fast Fourier Transform
FPZ	Fracture Process Zone
ITZ	Interfacial Transition Zone
LCC	Linear Comparision Composite
LEFM	Linear Elastic Fracture Mechanics
OPC	Ordinary Portland Cement
PSD	Particle Size Distribution
RVE	Representative Volume Element
SCM	Supplementary Cementitious Materials
TSL	Traction-Separation Law
TPBT	Three Point Bending Test
UTT	Uniaxial Tensile Test
W/C	Water to Cement ratio
WST	Wedge Splitting Test
XFEM	eXtended Finite Element Method

Part II

Appended Papers

Paper I Inverse analysis of the wedge splitting test Published in: *Engineering Fracture Mechanics*

Paper II Application of optical deformation analysis system on wedge splitting test and its inverse analysis Published in: *Material and Structures*

Paper III Discrete modeling of mixed-mode crack growth in concrete - Extended version of "Discrete modeling of mixed-mode crack growth in concrete" from *The Proceedings of the First International Conference on Computational Technologies in Concrete Structures (CTCS'09)*

Paper IV Upscaling of fracture properties - discrete modeling Submitted to: *Cement and Concrete Research*

Paper V From microstructure to strength of cement paste - critical aspects - Draft; will be submitted to: *Cement and Concrete Research*

Paper I

Inverse analysis of the wedge-splitting test

Jan Skoček and Henrik Stang
Published in: *Engineering Fracture Mechanics*

Inverse analysis of the wedge-splitting test

Jan Skoček[*,†] and Henrik Stang[*]

[*]Department of Civil Engineering, Technical University of Denmark
(DTU Byg), 2800 Kgs. Lyngby, Denmark
[†] e-mail: jas@byg.dtu.dk

Published in: *Engineering Fracture Mechanics*

Abstract

The amount of information which it is possible to retrieve from the wedge-splitting test is investigated. Inverse analysis is undertaken based on the analytical hinge model for various multi-linear softening curves. This showed that the commonly used bi-linear softening curve can be replaced by an up to quad-linear curve, which is reflected by increased accuracy of the test simulation. Furthermore it was demonstrated that the next refinement of the softening curve leads to convergence problems due to problems with local minima. Finally, the semi-analytically obtained results are verified using FEM simulations.

A.1 Introduction

In recent years, crack initiation and propagation in quasi-brittle materials such as concrete and other cement-based materials has usually been modelled using the cohesive crack model. This model, unlike linear elastic fracture mechanics, also considers energy dissipation in the so-called fracture process zone. According to the original works of Barenblatt (Barenblatt 1962) and Dugdale (Dugdale 1960), crack faces are allowed to transfer certain tractions, which correspond nicely to the bridging mechanisms observable in heterogeneous materials. The most often used nonlinear fracture model for concrete, Hillerborgs fictitious crack model (Hillerborg et al. 1976), is derived from the cohesive crack model for cases where the energy dissipated at the crack tip is negligible compared to the energy dissipated in the fracture process zone.
The stress intensity factor at the crack tip is then equal to zero, crack faces close smoothly, and the fracture process is governed by the relationship between the magnitude of transferred stress and the crack opening. This model is quite simple and provides a reasonable estimation of the crack propagation in quasi-brittle materials. On the other

hand, determination of the stress-crack opening relationship, or softening curve, presents significant difficulties even for pure mode-I loading conditions.

The most straightforward approach is to perform a tensile test. With its direct interpretation, a tensile test can provide the softening curve for the tested material right away. However, this is only true for very well-controlled tests performed with a testing machine with no eccentricity on a perfect sample. Unfortunately, tensile tests are very sensitive to eccentricities in applied loads and the rotational boundary conditions of the specimen. There is also the danger that multiple cracking will occur due to the non-homogeneity of the investigated material. All of these influences can introduce significant error into measurements and make the results obtained unusable. This topic has been widely discussed, e.g. in the work of van Mier and van Vliet (van Mier & van Vliet 2002) and further by Østergaard (Østergaard 2003).

The second option for softening curve estimation is an indirect determination, usually using the three-point bending test setup. The load-mid span deflection relationship, from which the softening curve can be extracted, is usually measured in this test. However, the three-point bending test also needs to be performed under well-controlled conditions. Due to the large amount of elastic energy stored in the specimen, snap-back can occur during loading. And the influence of specimens own weight is significant and cannot be ignored, especially in the case of early-aged concretes and mortars. Another test setup for indirect determination of the softening curve is the Wedge-Splitting Test (WST). The WST setup is shown in Figure

After test data has been recorded, inverse analysis needs to be performed to establish material properties. The inverse analysis consists of three main parts: (1) data obtained from laboratory or in-situ tests, (2) simulation of the test using the parameters to be determined, and (3) a optimization process to minimize a suitable norm for discrepancies between the test data and the corresponding data obtained from the simulation. Many approaches for the obtaining of fracture properties have been developed in recent decades. These approaches can, generally speaking, be divided into two main groups. The first group involves inverse analyses that determine the following point on the softening curve by minimization of the discrepancy between the computed value at following point and the corresponding measured point on the load-displacement curve. Figure

In the second group, inverse analysis advances in different way. Once the softening curve type, e.g. power law or bi-linear curve, has been de-

fined, a global optimization process, involving several measured points takes place. This global optimization can be done in two basic ways: either one optimization process involving the determination of all variables at once or a sequence of sub-optimizations determining selected variables one after the other. As shown in Østergaard's work (Østergaard 2003), this second type of inverse analysis provides higher robustness due to a lower risk of reaching local minima.

One of the methods from this second type of inverse analysis, which requires knowledge of some of the parameter values, is the compliance technique pioneered by Hu and Mai (Hu & Mai 1992). Knowledge of the uniaxial tensile strength is required for this method, and the parameters describing the power softening law can then be determined. Roelfstra and Wittmann (Roelfstra & Wittmann 1986) developed finite element based inverse analysis with prescribed bi-linear softening. The bilinear softening curve seems to provide sufficiently accurate results for a wide range of materials, such as concrete, fibre-reinforced concrete, cement mortar or rock, and is therefore widely used. For more detailed information about types of inverse analyses applicable for determination of the softening curve, see the work of Que (Que 2003), where this topic is discussed in detail.

The bi-linear softening curve is usually used to approximate the softening behaviour of cementitious materials. It could be expected that refinement of the softening curve by using a greater number of lines would be reflected in the improved accuracy of the WST test simulation. On the other hand, the inverse analysis might become unstable because the amount of information we are trying to determine is too great. The amount of information which can be extracted from a single WST has never been investigated, and that was the motivation for the investigation described in this paper.

The purpose of this paper is to investigate the possibility and reliability of extending the inverse analysis to more than bi-linear softening curves. The goal is to determine the maximal possible number of lines in the softening curve that we can obtain and to check if this refinement is reflected in increased accuracy in the experiment simulation. For this task, the semi-analytical approach is used as the background for the inverse analysis of the WST. The inverse analysis introduced is capable of estimating both elastic and fracture properties from a single WST as will be shown below.

A.2 Inverse analysis of the WST

This paper focuses on the inverse analysis of the WST coming out of Østergaard's approach, see (Østergaard 2003). The method is based on the hinge model developed Ulfkjær et al. (Ulfkjær et al. 1995) and improved by Olesen (Olesen 2001) for elements loaded with a combination of the bending moment and the normal force. The advantage of the original hinge model is that it can provide a closed-form analytical solution for the COD for a given load of the hinge, assuming linear elastic material behaviour with a multi-linear softening curve. The hinge model is based on the assumption that the presence of the crack changes the stress and the strain field only locally, and the rest of the structure remains unaffected. This is reflected in a reduction in the computational cost since only part of the structure is calculated using a closed-form solution instead of expensive FEM or XFEM simulations. Even though this hinge model is capable of providing a closed-form analytical solution for any piece-wise linear softening curve, derivation of an analytical solution for a more than bi-linear softening curve and its implementation as code would be very complicated. Therefore a semi-analytical approach, with iterative neutral axis position assessment is employed in this work. This modification allows us to involve both the multi-linear softening curve and the multi-linear elastic behaviour of undamaged material in the computation with only a tiny increase in the computation costs in the global iterative scheme.

A.2.1 The hinge model

The purpose of this section is to summarize the hinge model described by Olesen (Olesen 2001) and to present its extension for general multi-linear softening curve. The crack propagation is modelled as the incremental layer of spring elements within the rigid element boundary allowed to rotate and translate to ensure compatibility with the bulk of the structures modelled with classical elastic theory, see Figure
The $CMOD_{WST}$, here defined as the opening of the specimen at the line of loading, depends on three different contributions. The first contribution, δ_e, is caused by the elastic deformation of the specimen. The second one is the opening due to the presence of the crack, δ_w. Finally, the third contribution is due to the geometrical amplification, which arises from the fact that there is a certain distance from the crack mouth located at h, to the line where $CMOD_{obs}$ is measured located at point b. This contribution, δ_g, is caused by the rotation of

the crack faces. Thus, $CMOD_{WST}$, is given by:

$$CMOD_{WST} = \delta_e + \delta_w + \delta_g \ . \tag{A.1}$$

For evaluation of the first term in Eq. (the formula found in Tada et al. (Tada et al. 1985) can be used. The elastic deformation is expressed there as

$$\delta_e = \frac{P_{SP}}{Et} v_2 \ ,$$

where t stands for the thickness of the specimen and v_2 is a function of the ratio between the length of the initial notch and the distance from the loading line to the bottom of the specimen. In this case, the ratio is given by $x = 1 - h/b$ and

$$v_2 = \frac{x}{(1-x)^2}(38.2 - 55.4x + 33.0x^2) \ .$$

In Tadas formula, only opening due to the horizontal splitting force is considered. This simplification, however, does not lead to any significant error in particular since in the cracked phase, the contribution of δ_e is negligible in comparison with δ_w. In the elastic phase, the error introduced can be also ignored, as shown in (Østergaard 2003).
The second term in Eq. (, δ_w, can be directly evaluated according to (Olesen 2001) at point $y = h$. The last term, δ_g, as derived in (Østergaard 2003), is defined as

$$\delta_g = 2(b-h)\left(\frac{\delta_w}{2d} - \frac{\phi^{el}}{1-\beta_i}\right) \ ,$$

where ϕ^{el} is the maximal elastic angular deformation of the hinge and β_i is a dimensionless parameter defined by

$$\beta_i = \frac{f_t a_i s}{E}. \tag{A.2}$$

The solution fulfilling Eqs. (cannot be obtained in closed form even for the analytical hinge model and an optimization process needs to be performed. The goal is to find such force P which minimizes Eqs. (. The optimization process evaluates the following cycle, until Eqs. (are satisfied:

(a) update values of P and ϕ in accordance with the simplex search method (Matlab R2006a[1] optimization tool is used);

[1] www.mathworks.com

(b) find neutral axis position y_0 from condition of equilibrium

$$\int_0^h \sigma(y)\,\mathrm{d}y - P = 0\ ;$$

(c) compute the bending moment transferred by the hinge as

$$M_{hinge} = \int_0^h \sigma(y)(y - y_0)\,\mathrm{d}y\ ;$$

(d) evaluate Eqs. (.

A.2.2 The inverse analysis

The shape of the softening curve is given a priori by defining the number of the lines in the softening curve and the corresponding values of a_i and b_i are then searched. There is no need for additional experimentally obtained data since E and f_t can be identified too. The inverse analysis presented here is a generalization of the inverse analysis used in (Østergaard 2003) for more than bi-linear softening curves. The inverse analyses computation consists of three steps that are repeated until convergence criteria are reached. The first step presents the computation of Young's modulus E. For this purpose, only those data corresponding to the elastic loading, are used. Since this part of working diagram is governed by the E only, its determination is very fast and reliable. Once Young's modulus is found, the tensile strength f_t and the first descending branch of the softening curve a_1 are searched. Further, $N-1$ searchings are carried out to find a_i and b_i, where $i = 2, \cdots, N$. The entire process can be written into the following scheme:

```
while (convergence is not achieved)
```

$$\min_{E} \sum_{j=1}^{K^{el}} \|P_{j,obs} - P_{j,hinge}\|$$

$$\min_{f_t,a_1} \sum_{j=1}^{K} \|P_{j,obs} - P_{j,hinge}\|$$

```
for i=2:N
```

$$\min_{a_i,b_i} \sum_{j=1}^{K} \|P_{j,obs} - P_{j,hinge}\|$$

```
check convergence
```

The above step-by-step inverse analysis has several advantages. The main one is in the fact that individual inner optimizations have no problem with the local minima, as shown in (Østergaard 2003), which

is not necessarily the case for global optimization of all variables in one minimization step (Ulfkjær & Brincker 1993).. This allows the use of simpler and more efficient searching algorithms which, of course, is reflected in the lower computational cost of the proposed process.
Since each measurement can be affected by errors, it is impossible to fit the model exactly to the measurements. This means that the choice of the appropriate robust norm of $\|P_{obs} - P_{hinge}\|$ plays a significant role. The goal of such a norm is to eliminate the influence of noise and outliers in the measurements, which does not happen in the commonly used norm

$$L_2 = \frac{(P_{obs} - P_{hinge})^2}{2}$$

which emphasizes the influence of the outliers. That is why the $L_1 - L_2$ norm was chosen for our purpose:

$$L_1 - L_2 = \|P_{obs} - P_{hinge}\| = \sqrt{1 + \frac{(P_{obs} - P_{hinge})^2}{2}} - 1 \ .$$

This norm behaves like the L_2 for small $|P_{obs} - P_{hinge}|$, whereas for greater differences (the case of the outliers) it behaves like the $L_1 = |P_{obs} - P_{hinge}|$, see Figure
Note that the observations on the load-CMOD curve must be placed equidistantly with regard to the arc length in the normalized coordinate system in order to arrive at as precise results as possible. This is due to the fact that no part of the load-CMOD curve should be weighted higher than any other part. The equidistantly placed observations are obtained by linear interpolation of the measured data.

A.3 Determination of the optimal number of DOFs in the softening curve

Measurements for CEM II based high-performance concrete with silica fume and fly ash performed and described by Østergaard in his thesis (Østergaard 2003) were used as the experimental data. The mixture properties and the curing conditions are described in details ibidem. The specimen dimensions, see
The main goal of the present paper was to find the optimal number of DOFs in the softening curve. The idea was to change the number of lines in the determined multi-linear softening curve, N, and check whether the accuracy of the simulation of the WST using the determined softening curve improved or not. At the same time, the

robustness of the proposed algorithm was investigated. For this latter investigation, two sets of the initial estimations were considered. The first one consisted in changing the "shape" of the initial softening curve, see Figure
Since both the accuracy of computed results and reasonable computational costs need to be considered, the convergence criterion was set to 1% and the distance of the points generated by the arc length method in the normalized coordinate system was set to 0.01.
The first set of initial estimations was created in the following way. First, the softening curves with both equidistantly placed b_i and w_i, see Figure
Afterwards, the inverse analysis for the second set of the initial softening curves for $N = 2 \cdots 5$ was performed. Again, four initial starting estimations were used for each value of N. In this case, the shape of the initial softening curve remained constant with both b_i and w_i equidistantly placed, Figure
In Figures

A.4 FEM verification

In order to verify the results obtained, the WST was simulated using standard FE software DIANA Release 9.1[2] which support the multi-linear softening curve. The WST specimen was modelled in 2D, since, as demonstrated in (Østergaard et al. 2002), the 2D model is fully capable of representing the WST. Figure

A.5 Conclusion

This paper fills gaps in present knowledge of the inverse analysis of the WST. In particular it addresses the question about the amount of information that can be retrieved from the WST using inverse analysis. The robustness of the inverse analysis algorithm proposed by Østergaard (Østergaard 2003) was investigated for increasing numbers of lines in the multi-linear softening curve. It was shown that the algorithm is robust enough to be able to determine the parameters of softening curves consisting of up to four lines. When simulation for $N = 2, 3$ and 4 are compared, it is clear that the most widely used bi-linear softening curve can be replaced by the tri- or even the quad-linear curve with advantage, decreasing the total discrepancy between

[2] www2.tnodiana.com

the experiment and its simulation. For For $N = 5$ problems with local minima occurred and the algorithm was not able to reach convergence criteria. The sensitivity of the inverse analysis to variations in the initial estimations was investigated for two groups of these variations. Firstly, the shapes of the initial softening curves were changed and after that the initial values of the uniaxial tensile strength and of the critical crack opening were changed for a fixed shape. It was shown that inverse analysis is much more sensitive to initial values of the uniaxial tensile strength and the critical crack opening. The initial shape of the softening curve does not play a very important role if the initial approximations for uniaxial tensile strength and critical crack opening are accurate. It was also shown that the WST is capable of providing both elastic and fracture properties with high reliability and the hinge model is a useful tool for its simulation with only minimal computational costs. When the obtained material parameters were directly used for the material model in the FEM simulation, the predicted data compared favourably with the measured ones.

A.6 Acknowledgments

The authors are grateful to the European Community under the Marie Curie Research Training Network MRTN-CT-2005-019283 "Fundamental understanding of cementitious materials for improved chemical physical and aesthetic performance" (`http://www.nanocem.org/MC-RTN/`) for the full support of Jan Skoček.

Bibliography

G. I. Barenblatt (1962). 'The mathematical theory of equilibrium cracks in brittle fracture'. *Advances in Applied Mechanics* **7**:55–129. Originally published in Russian, 1957, see e.g. (Karihaloo 1995).

D. S. Dugdale (1960). 'Yielding of Steel Sheets Containing Slits'. *Journal of the Mechanics and Physics of Solids* **8**:100–104.

A. Hillerborg, et al. (1976). 'Analysis of crack formation and crack growth in concrete by means of fracture mechanics and finite elements'. *Cement Concrete Research* **6**:773–782.

X.-Z. Hu & Y.-W. Mai (1992). 'Cracks bridging analysis for alumina ceramics undermonotonic and cyclic loading'. *Journal of the American Ceramic Society* **75**:848–853.

J. G. J. Planas & M. Elices (1999). 'Size effect and inverse analysis in concrete fracture'. *International journal of fracture* **95**:367–378.

Y. Kitsutaka (1997). 'Fracture parameters by polylinear tension-softening analysis'. *Journal of Engineering Mechanics* **123**(5):444–450.

H. N. Linsbauer & E. K. Tschegg (1986). 'Fracture energy determination of concrete with cube shaped specimens (in german)'. *Zement und Beton* **31**:38–40.

J. F. Olesen (2001). 'Fictitious Crack Propagation in Fiber-Reinforced Concrete Beams'. *Journal of Engineering Mechanics* **127**(3):272–280.

L. Østergaard (2003). *Early-Age Fracture Mechanics and Cracking of Concrete. Experiments and Modelling. To be published.* Ph.D. thesis, Department of Civil Engineering, Technical University of Denmark, Lyngby, Denmark.

L. Østergaard, et al. (2002). 'Interpretation and Inverse Analysis of the Wedge Splitting Test'. In *Fracture Mechanics Beyond 2000*, vol. II, pp. 593–600. EMAS Publications, Sheffield, UK.

N. S. Que (2003). *Identification of cohesive crack fracture paramaters using mathematical programming.* Ph.D. thesis, School of Civil and

Enviromental Engineering, The University of New South Wales, Sydney, Australia.

P. E. Roelfstra & F. H. Wittmann (1986). 'Numerical method to link strain softening with failure of concrete'. In *Fracture Toughness and Fracture Energy of Concrete*, pp. 163–175. Elsevier.

H. Tada, et al. (1985). *The Stress Analysis of Cracks Handbook*. Paris Productions Incorporated, 226 Woodbourne Dr., St. Louis, Missouri, USA.

Y. Uchida & B. I. G. Barr (1998). 'Tension softening curves of concrete determined from different test specimen geometries'. In *Fracture Mechanics of Concrete Structures*, pp. 387–398. Aedificatio Publishers, Freiburg, Germany 17–30.

J. Ulfkjær, et al. (1995). 'Analytical model for fictitious crack propagation in concrete beams'. *Journal of Engineering Mechanics* **121**(1):7–15.

J. P. Ulfkjær & R. Brincker (1993). 'Indirect determination of the σ-w relation of HSC through three-point bending'. In *Fracture and Damage of Concrete and Rock - FCDR-2*, pp. 135–144. E & FN Spon.

J. G. M. van Mier & M. R. A. van Vliet (2002). 'Uniaxial Tension Test for the Determination of Fracture Parameters of Concrete: State of the Art'. *Engineering Fracture Mechanics* **69**:235–247.

Paper II

Application of optical deformation analysis system on wedge splitting test and its inverse analysis

Jan Skoček and Henrik Stang
Published in: *Materials and Structures*

Application of optical deformation analysis system on wedge splitting test and its inverse analysis

Jan Skoček*,† and Henrik Stang*

*Department of Civil Engineering, Technical University of Denmark (DTU Byg), 2800 Kgs. Lyngby, Denmark
† e-mail: jas@byg.dtu.dk

Submitted to: *Materials and structures*

Abstract

An alternative approach of fracture tests evaluation based on optical measurements of displacements is investigated in this paper. The non-linear hinge model based inverse analysis outgoing from the optically measured crack mouth opening displacements is introduced for the wedge splitting test. Results of the inverse analysis are compared with traditional inverse analysis based on clip gauge data. Then the optically measured crack profile and crack tip position are compared with predictions done by the non-linear hinge model and a finite element analysis. It is shown that the inverse analysis based on the optically measured data can provide material parameters of the fictitious crack model matching favorably those obtained by classical inverse analysis based on the clip gauge data. Further advantages of using of the optical deformation analysis lie in identification of such effects as aggregates bridging and crack branching. These effects would remain hidden if the crack profile is simulated by a model based on the fictitious crack model.

A.1 Introduction

Post-peak behavior of quasi-brittle materials such as concrete and mortar are often modeled using Hillerborg's fictitious crack model (Hillerborg et al. 1976) which introduces a relation between crack opening and the magnitude of the stress transfered by the crack, the so-called cohesive law, traction-separation law or softening curve. For determination of the traction-separation law of a given material, load versus displacement curves recorded during crack propagation in experiments with standard test specimens are often taken as starting point. Data interpretation typically takes the form of inverse analysis, see e.g. (Skoček &

Stang 2008) where different types of inverse analysis and corresponding material parameters are presented and discussed. Typically, the displacement of a single point or the displacement difference between two points is measured by a Linear Variable Displacement Transducer (LVDT) or a clip gauge attached to the specimen. However, this approach of displacement measurement has several limitations. First of all, the point where the displacement measurement takes place needs to be specified a priory. Secondly, as the fracture process is investigated on still smaller and smaller scale, sensors also need to be smaller. In certain cases, e.g. for experiments carried out in the chamber of an Environmental Scanning Electron Microscope (ESEM), the space is highly constraining and the transducer can not be used without shielding the specimen. The measurement of the complete crack propagation in terms of crack opening profile and crack tip position is clearly much more attractive than the single point measurement. Hence, optical measurement of the displacement presents a promising possibility avoiding the aforementioned disadvantages.

Optical measurement systems are typically capable of measuring displacements on the surface of the whole specimen or the part of the specimen where the cracking is supposed to occur. Specific points where the displacement is measured are defined after the test in data post processing. In principle, the only limitation in the number of points where displacement is recorded is the resolution of the digital imaging device and a virtually continuous displacement field can be obtained. The post processing is similar for experiments on all scales and the same software can be used for specimens differing for several orders of magnitude in size. Since any digital image sequence can be used as the input for the post processing, the approach is suitable for evaluation of displacement fields in specimens loaded in an chamber of an ESEM .

The disadvantage of this approach lies in its restrictions to surface deformations only. This implies that this approach is suitable only for cases where cracking can be considered uniform across the thickness of the specimen. This is fortunately the case for most of commonly used mode I fracture tests and an implicit assumption of Hillerborg's fictitious crack model. The assumption was verified e.g. in (Østergaard et al. 2002) where two- and three-dimensional analyses of the Wedge Splitting Test (WST) were compared.

The optical measurement of the deformation and crack propagation in a specimen during a fracture test can be used in two basic ways. The displacements of similar points that would be measured with a clip

gauge can be recorded and these records used in the same way as data from a transducer. Optical measurements, however, open up other, new possibilities of fracture process analysis. Instead of measuring the deformation in discrete points a displacement field can be recorded and continuous features such as the crack profile evolution or crack tip position can be measured. Measurement of such processes traditionally presents significant difficulties. The crack profile is traditionally obtained by impregnation techniques which however is unable to provide its evolution during loading for a single specimen due to its destructivity. The approximate crack tip position can be determined by acoustic emission which provides good three dimensional estimation of the dissipated energy. However, the crack profile and dissipation free opening of the crack cannot be characterized by such a technique. When optical deformation analysis is employed, the evolution of crack tip position and crack profile can be easily measured.

In this paper, a framework developed for inverse analysis of the WST based on optically acquired data is presented. First of all, extensions of the inverse analysis described in (Skoček & Stang 2008) supporting crack profile data is introduced. The extended inverse analysis is applied to data from the WST of ordinary concrete. The identified parameters of the fictitious crack model are then compared to those obtained by inverse analysis based on global response measured by clip gauge. The parameters are subsequently used as input parameters for simulations of the test by the Finite Element (FE) model and the non-linear semi-analytical hinge model (Ulfkjær et al. 1995, Olesen 2001, Østergaard 2003, Skoček & Stang 2008). Crack profiles and crack tip positions are computed and compared with those measured by the optical deformation analysis system. It is shown that the inverse analysis based on the optical measurement can provide material parameters of the fictitious crack model matching favorably those obtained by classical inverse analysis based on the clip gauge data. It is demonstrated that further advantages of using the optical deformation analysis lie in discovering of such effects as aggregates bridging and crack branching. These effects would remain hidden if the deformation would be measured by the clip gauge and the experiment simulated by the fictitious crack model. The ability of the non-linear hinge model and cohesive finite elements model to represent the crack profile and the crack tip position is investigated. It is found that the finite elements model performs better in the pre-peak regime whereas the hinge-model performs better in later stages of the crack propagation. None of these models, however, are capable of modeling the aforementioned effects identified

by the optical deformation analysis.

A.2 Material

The material used was a typical concrete with a well-graded coarse aggregates, naturally rounded, with size between 4 and 8 mm (1103 kg/m^3 of concrete). A washed sea sand 0-4 mm was used as finer aggregates (766 kg/m^3 of concrete). Aalborg white cement was used as a binder with water to cement ratio equal to 0.5. Ordinary tap water was used for the mixing process. After casting, the samples were stored in 20°C and covered with a plastic foil overnight. They were demolded after 24 hours and placed in an environmental chamber at 20°C and 85% relative humidity for six days. The samples were stored at 50 % relative humidity and 20°C for about a year before the test was performed.

A.3 Test setup

The WST was originally developed by Linsbauer and Tschegg (Linsbauer & Tschegg 1986) to determine specific fracture energy, G_F, of the investigated material. However, when applying a suitable model, the WST can provide information describing the softening in terms of the traction-separation law. The test setup is shown in Figure

A.4 Evaluation of the WST

As mentioned in the introductory part, measuring crack propagation during the fracture process is a complex and challenging task, especially if continuous data for a single specimen is needed. Optical deformation analysis is capable of providing such data. In our study, a system for optical 3D deformation analysis, Aramis 2M[3], was used. The data postprocessing software provided with Aramis investigates the correlation between stereo images of subsequent loading steps and computes relative displacements of characteristic points on the basis of which the 2D strain tensor can be calculated and, if calibrated, also to a displacement field in defined units can be constructed. The crack profile, the Crack Opening Displacement (COD) and the crack tip position can be evaluated for each load step. Thus a set of load versus COD curves can be constructed and used as input for the inverse analysis. Based on the manufacturer's specification, the theoretical resolution

[3] `http://www.gom.com`

of 1×10^{-5} times the image dimension (or 2 μm for the configuration used here) is possible for this equipment. Following previous results obtained with the same equipment (Pease, et al. 2006), an accuracy of ± 5 μm is expected.

A.4.1 Image analysis

Since, as discussed in the introductory part, the optical deformation analysis can provide information on the surface displacement only, the crack opening was measured between pairs of points equidistantly placed along the height of the WST specimen (see Figure
Two types of the inverse analysis were performed. The first one estimated material parameters by fitting the load vs. optically measured crack profile curve (load vs. COD curves for points with varying coordinate y) and the latter by fitting the load vs. CMOD measured by the clip gauge curve.
Following our previous results (Skoček & Stang 2008), the number of lines in the traction-separation law, N, was set to 3. Thus, the traction-separation law, $\sigma_w(w)$ has form

$$\sigma_w(w) = g(w) f_t,$$

where w stands for crack opening and f_t denotes uniaxial tensile strength. The function $g(w)$ is for the 3-linear traction-separation law defined as

$$g(w) = b_i - a_i w \ ; \quad w_{(i-1)} < w < w_i; \quad i = 1, 2, 3$$

where w_i corresponds to the intersection of i-th and $i+1$-th line and has the form $w_i = \frac{b_i - b_{i+1}}{a_i - a_{1+1}}$ for $i = 1, 2$ and $w_3 = w_c = \frac{b_3}{a_3}$. It means that 7 parameters (Young's modulus E, tensile strength f_t, $a_{1,2,3}$ and $b_{2,3}$) were identified in the inverse analysis. Parameter b_1 was not identified since $b_1 = 1$.
To be able to use COD measured by the optical deformation analysis system, the original inverse analysis had to be modified. Originally, the CMOD was measured by a clip gauge at the level of the load application point and the computed CMOD consisted of three contributions - the elastic deformation of the specimen, the opening due to the cracking and deformation caused by a certain distance between real crack mouth and the level of clip gauge measurement. Using the optical deformation analysis approach the COD is measured directly and hence the geometrical amplification of the deformation equals to zero. Finally, the COD computed at point y has form

$$COD_{hinge}(y) = \delta_e(y) + \delta_w(y), \tag{A.1}$$

	E[MPa]	f_t[MPa]	G_f[Jm^{-2}]	w_c[mm]
Clip-gauge	21680	1.3988	111.64	0.89964
Optical	21680	1.3307	108.30	0.60938

Table A.6: Comparison of material parameters obtained by the clip gauge date and optical data inverse analysis of the WST. Note that Young's modulus was not identified by the optical data based inverse analysis.

where $\delta_e(y)$ denotes the elastic deformation at point y and $\delta_w(y)$ denotes the true crack opening at point y. For evaluation of the first term in Eq. (, a simple linear relation can be used with $\delta_e(y) = \sigma(y)d/E$, where $\sigma(y)$ is elastic stress for uncracked material and bridging stress for cracked material, E stands for Young's modulus and d for the horizontal distance between the points, where the COD was measured by the optical device (see Figure

The norm of error reflecting the discrepancy between measured and computed load-crack opening curves had to be modified as well. Originally, the norm was set for one load vs. CMOD curve only. Now, since a crack profile is of interest, the global $L_1 - L_2$ norm of error has a form

$$L_1 - L_2 = \sum_{j=1}^{K} \frac{1}{M_j} \sum_{i=1}^{M_j} \left(\sqrt{1+\frac{(P_o^i(y_j)-P_h^i(y_j))^2}{2}} - 1 \right), \tag{A.2}$$

where K is number of curves describing the crack profile, M_j is number of uniformly placed points on $j-th$ curve, $P_o^i(y_j)$ is recorded splitting force and finally $P_h^i(y_j)$ is the splitting force computed by the hinge model. Such a norm ensures that every point on every curve is weighted equally. Since values of elastic deformation were very small compared to the noise in the optical measurement, Young's modulus was not identified and the value obtained from the inverse analysis based on the clip gauge data was used in this inverse analysis. The remaining parts of the algorithm are the same as described in (Skoček & Stang 2008). For the present study, three load vs. COD curves at $y = 50$ mm, $y = 41.8$ mm and $y = 29.4$ mm were chosen, thus $K = 3$. Figure

The resulting optimal material parameters computed by the inverse analysis of the optically acquired data were compared to those computed from global clip gauge data. Table

It can be seen that the inverse analysis based on the optical data provides very similar material parameters and that the traction-separation law, like the traditional one, results in favorable match of measured and computed splitting force vs. CMOD curve.

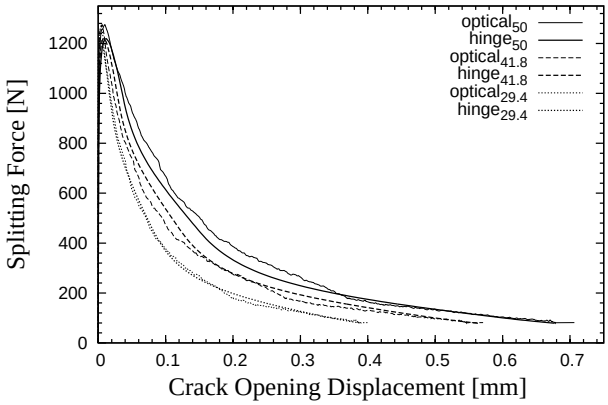

Figure 1: Comparison of optically measured and computed load vs. COD curves. Subscripts denote vertical position y of points.

A.5 Simulation of crack propagation

In the previous Section it was demonstrated that the optically determined deformation can be used instead of the traditional clip gauge determined deformation as the input for the inverse analysis. In this Section, the ability of the applied non-linear hinge model and the more general cohesive elements based Finite Elements Analysis (FEA) to simulate the crack profile and the crack tip position evolution during fracture process is investigated.

The hinge model allows for an analytical determination of the crack tip position as well as the crack profile after the angular deformation of the hinge is determined by an iterative procedure, see (Skoček & Stang 2008, Olesen 2001) for all details. The determination of the crack profile as well as of the crack tip position is then straightforward: the COD in each point where the tensile strength was reached during load history was recorded to describe the crack profile. The first point (from bottom of the specimen) where the stress reached the tensile strength of the material was recorded as the crack tip position for each load step.

In the FEA, the crack pattern was modeled using interface cohesive elements with the prescribed tri-linear softening behavior obtained from the non-linear hinge model-based inverse analysis based on the optical data. The WST specimen was modeled in 2D, since, as demonstrated

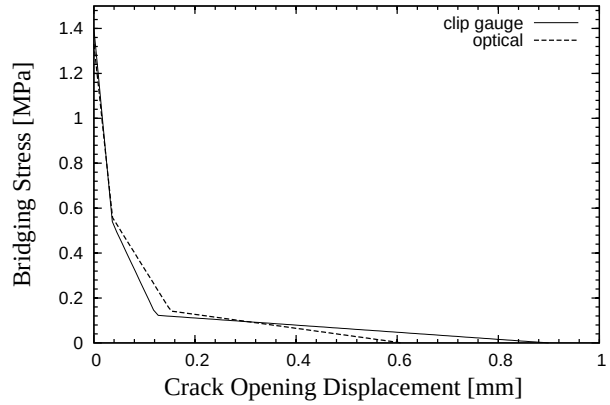

a)

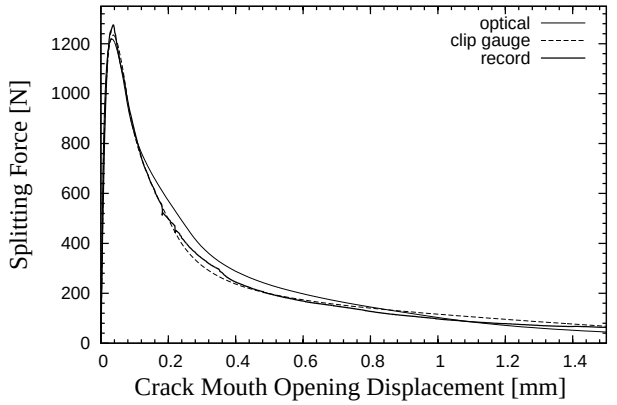

b)

Figure 2: Comparison of identified traction-separation laws a) and simulation of splitting force vs. CMOD curves based on the identified material parameters b).

in (Østergaard et al. 2002), the 2D model is fully capable of representing the WST. Figure

As already mentioned, the measured crack profile was obtained from the deformation measured between discrete pairs of points as shown in Figure

The crack tip position evolution during loading was the task in the last study (see Figure

A.6 Conclusions

An alternative approach to data collection for the inverse analysis of the wedge splitting test was introduced. The crack opening displacement was measured by an optical deformation analysis system, Aramis, and the inverse analysis was modified to be able to use such data as input. It was shown that material parameters of the fictitious crack model can be determined using the optically determined data with similar accuracy compared to the traditional approach using a clip gauge for data collecting. The Young's modulus cannot be determined by the presented approach due to too small values of elastic deformations measured.

Advantages of using the optical deformation analysis system during fracture mechanical tests were discussed. Crack profiles can be measured during fracture propagation. However, measuring and analysis of small deformations is complicated due to inhomogeneity of the strain field and due to noise. Consequently the crack tip position needs to be extrapolated from the measurements. Phenomena such as an aggregate bridging effect or crack branching can be qualified and quantified.

Further, the ability of the nonlinear hinge model and finite element analysis based on interface cohesive elements to simulate crack profiles and crack tip position was investigated. It was found that though both models provide similar overall response in the term of the load vs. CMOD curve. Crack profiles and especially crack tip position differs considerably. Therefore, special care needs to be taken if processes sensitive to crack tip position, e.g. transport processes in cracked media, are concerned.

A.7 Acknowledgements

The authors are grateful to the European Community under the Marie Curie Research Training Network MRTN-CT-2005-019283 "Fundamental understanding of cementitious materials for improved chemical physical and aesthetic performance" (`http://www.nanocem.org/MC-RTN/`) for the full support of Jan Skoček.

We would like to express our special thanks to Bradley J. Pease for his help with the optical deformation analysis system.

Bibliography

A. Caballero, et al. (2006). '3D meso-structural analysis of concrete specimens under uniaxial tension'. *Computer Methods in Applied Mechanics and Engineering* **195**(52):7182 – 7195. Computational Modelling of Concrete.

G. Cusatis & L. Cedolin (2007). 'Two-scale study of concrete fracturing behavior'. *Engineering Fracture Mechanics* **74**(1-2):3 – 17. Fracture of Concrete Materials and Structures.

A. Hillerborg, et al. (1976). 'Analysis of crack formation and crack growth in concrete by means of fracture mechanics and finite elements'. *Cement Concrete Research* **6**:773–782.

H. S. J. Skoček (2008). 'Inverse analysis of the wedge splitting test'. *Submitted to Engineering Fracture Mechanics* .

H. N. Linsbauer & E. K. Tschegg (1986). 'Fracture energy determination of concrete with cube shaped specimens (in german)'. *Zement und Beton* **31**:38–40.

H.-K. Man & J. G. van Mier (2008). 'Influence of particle density on 3D size effects in the fracture of (numerical) concrete'. *Mechanics of Materials* **40**(6):470 – 486.

J. F. Olesen (2001). 'Fictitious Crack Propagation in Fiber-Reinforced Concrete Beams'. *Journal of Engineering Mechanics* **127**(3):272–280.

L. Østergaard (2003). *Early-Age Fracture Mechanics and Cracking of Concrete. Experiments and Modelling. To be published.* Ph.D. thesis, Department of Civil Engineering, Technical University of Denmark, Lyngby, Denmark.

L. Østergaard, et al. (2002). 'Interpretation and Inverse Analysis of the Wedge Splitting Test'. In *Fracture Mechanics Beyond 2000*, vol. II, pp. 593–600. EMAS Publications, Sheffield, UK.

J. Ulfkjær, et al. (1995). 'Analytical model for fictitious crack propagation in concrete beams'. *Journal of Engineering Mechanics* **121**(1):7–15.

B.J. Pease, et al. (2006). 'Photogrammetric Assessment of Flexure Induced Cracking of Reinforced Concrete Beams under Service Loads'. *Proceedings of the 2nd International RILEM Symposium, Advances in Concrete through Science and Engineering*, Québec City, Canada, September 2006.

Paper III

Discrete modeling of mixed-mode crack growth in concrete

Jan Skoček, Jan Eliáš and Henrik Stang

Extended version of "Discrete modeling of mixed-mode crack growth in concrete" from *The Proceedings of the First International Conference on Computational Technologies in Concrete Structures (CTCS'09)*

Discrete modeling of mixed-mode crack growth in concrete

Jan Skoček[*,†], Jan Eliáš[‡] and Henrik Stang[*]

[*] Department of Civil Engineering, Technical University of Denmark (DTU Byg), 2800 Kgs. Lyngby, Denmark
[†] e-mail: jas@byg.dtu.dk
[‡] Brno University of Technology, Faculty of Civil Engineering, Institute of Structural Mechanics, Veveø 331/95, 602 00 Brno, Czech Republic, +420 5411 7116, elias.j@fce.vutbr.cz

Extended version of "Discrete modeling of mixed-mode crack growth in concrete" from *The Proceedings of the First International Conference on Computational Technologies in Concrete Structures (CTCS'09)*

Abstract

In the framework of cohesive crack models and finite element modeling, simulations of the mixed-mode crack propagation in concrete presents a challenging task both from the numerical point of view and in the view of definition of material laws. In contrary to mode I propagation, mixed-mode crack patterns are much more complex and can not be predicted a priory. Therefore, remeshing techniques or XFEM implementation need to be employed, resulting in increased computational demands, especially in 3D. Beyond the mode I traction separation law, a mode II traction separation law referring shear opening to a bridging shear stress needs to be defined. Moreover, a law projecting mode I and II laws into a general direction of the crack opening has to be defined. A description of the shear dilatancy caused by the roughness of the real crack is a further material law required. Determination of the material parameters presents a complicated process since most of them can not be measured directly but needs to be identified using an inverse analysis. On the other hand, discrete models leaving the assumption of homogeneity of the material and moving to simpler material laws on a lower material scale can be an attractive choice with results comparable to the traditional aforementioned approach.

In the presented study, two discrete models based on different assumptions are applied to simulation of mixed-mode fracture tests of laboratory scale specimens under varying loading. The first

model belongs to lattice models discretizing the material into three types of lattice elements - aggregate, matrix and interfacial transition zone. The elements behave elasto-brittle with the elastic limit dependent on the direction of straining. The second model belongs to the group of particle models. Contacts between particles are defined and discretized by nonlinear struts. The models are used to simulate a non-proportional mixed-mode test. The specimen is loaded in mode I opening up to the peak load and then sheared/opened under 45°. Despite the different assumptions, both models are capable of predicting correctly trends and mechanisms observed in the experiments and help with understanding of the observed fracture process and with an explanation of instabilities observed during experiments.

A.1 Introduction

Simulation of the fracture process in heterogeneous quasi-brittle materials such as concrete or mortar presents a challenging task. Several models for realistic simulations of a global response of the material in mode I experiments were proposed, for example the most widely spread Hillerborg's fictitious crack model (Hillerborg et al. 1976). Such models assume homogeneous and elastic effective material properties for the bulk behavior and averaged relationships between the crack width and bridging stresses. Utilization of such models is well established and the models are available in many commercial codes. The identification of material parameters, especially for mode I fracture, has been also widely investigated, e.g. (Skoček & Stang 2008).

These models, however, have several limitations resulting from their assumptions. Such models can not simulate effects on scales similar to the size of heterogeneities of the material such as micro-cracking prior to the formation of the main crack, crack branching or aggregates bridging. The mixed-mode fracture propagation is a challenging task as well and complicated material laws introducing mode I and mode II coupling, shear dilatancy, sensitivity to confining stresses etc. are needed.

Several models going beyond the assumption of homogeneity of the material on one side and capable to simulate global behavior of real-sized concrete specimens on the other side were proposed. Since the heterogeneous microstructure is already captured by these models, simpler material laws can be used and the models are more robust and allow simulations of complex loadings with a single model. Since it is gener-

ally not possible to model behavior of every single particle and bond in the material, some simplifications have to be done. Two main trends can be found in literature.
The first one builds on a simplified geometry, e.g. by considering only the biggest aggregates, and on a detailed description of the behavior of all phases and their connections. As an example, the approach of Carol's group (Caballero et al. 2006) is based on a classical 3D finite element method with non-linear interfaces between aggregates-mortar and mortar-mortar connections. The advantage of such an approach lies in its accuracy resulting from using well established continuous finite elements method. The disadvantage rises from its computational demands allowing considering only very limited number of aggregates (64 in the case of (Caballero et al. 2006)). The material parameters identification presents a further complication. Material parameters describing elastic, as well as non-elastic, behavior are needed for all phases and contacts. The execution and interpretation of direct experiments is extremely difficult on this scale and identification of the parameters from a larger scale experiment is difficult as well.
The second trend builds on a simplification of material models as well as on the simplified abstract geometry. Lattice models, see e.g. work of van Mier's group (Man & van Mier 2008), belong to the latter group. The grain structure of the actual material is usually modeled by three phases - aggregates, matrix and Interfacial Transition Zone (ITZ) - and discretized using simple beams or truss elements, see Figure
The model of Cusatis (Cusatis et al. 2003) which assumes geometrical simplifications and complex material laws using effective properties of the material represents a compromise between the two approaches described above. In this model, mesostructure of concrete is described by two phases - aggregates and matrix - and discretized by struts connecting centers of the aggregates (see Figure
In the presented study, two discrete models, elasto-brittle lattice-type model and Cusatis-type particle model, are compared with the biaxial fracture mechanical testing. Basic assumptions of the models are briefly introduced in Section

A.2 Experiments

Specimens made from ordinary concrete described in

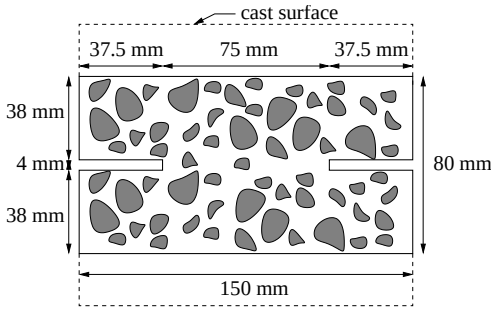

Figure 1: Dimensions of the mixed-mode specimens. Thickness is 75 mm.

A.2.1 Test setup

The specimens were loaded in the biaxial loading machine closely described in (Østergaard, et al. 2007). The experiment was performed under displacement control where Crack Mouth Opening Displacements (CMODs) measured in vertical (labeled as y-direction in Figure

A.2.2 Material

The specimens were made from ordinary concrete with Aalborg Basis portland cement used as binder. Washed sea sand and gravel were used as aggregates. Table

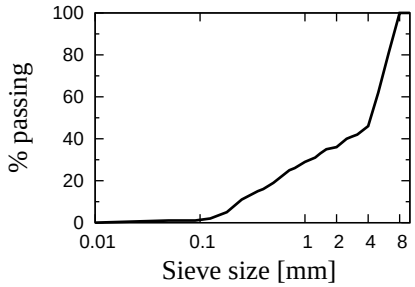

Figure 2: Particle size distribution of aggregates.

Specimens were casted and kept in laboratory conditions for 24 hours. Then they were moved to 50° C water bath where they were kept for

seven days. After removal from the water bath the specimens were cut from the beam and kept in the laboratory conditions until the testing took place.

A.3 Brief description of adopted discrete models

A.3.1 Creation of numerical concrete

The first part of the modeling, a creation of the idealized microstructure of the investigated material, is the same for both models. Initially, an idealized geometry of the material was created. Spherical particles were generated in the specimen according to given PSD which is given as a set of pairs - diameters D_i and volume fractions, f_i, of aggregates passing the sieve with diameter D_i (see Figure
Further discretization of the numerical concrete as well as material models and solution strategies are model-dependent and are briefly introduced in Sections
The mesoscopical damage-like constitutive model is formulated in terms of effective stress, σ, effective strain, ε and coupling strain, ω. The effective stress is computed by

$$\sigma = \sqrt{\sigma_{\mathrm{N}}^2 + \frac{\sigma_{\mathrm{T}}^2}{\alpha}} \quad \text{where} \quad \sigma_{\mathrm{T}} = \sqrt{\sigma_{\mathrm{L}}^2 + \sigma_{\mathrm{M}}^2},$$

where σ_{N} is the stress perpendicular to the contact plane and σ_{L} and σ_{M} denote two mutually perpendicular stresses at the plane of the contact.
Accordingly, the effective strain can be expressed as

$$\varepsilon = \sqrt{\varepsilon_{\mathrm{N}}^2 + \alpha\varepsilon_{\mathrm{T}}^2} \quad \text{with} \quad \varepsilon_{\mathrm{T}} = \sqrt{\varepsilon_{\mathrm{L}}^2 + \varepsilon_{\mathrm{M}}^2}.$$

The coupling strain, ω, reflecting direction of the loading of the strut, is expressed as

$$\tan\omega = \frac{\varepsilon_{\mathrm{N}}}{\sqrt{\alpha}\varepsilon_{\mathrm{T}}}.$$

See (Cusatis et al. 2003) for all the details. The effective stress, σ, needs to satisfy inequality $0 \leq \sigma \leq \sigma_b(\varepsilon, \omega)$, where the effective stress boundary, $\sigma_b(\varepsilon, \omega)$, can be expressed as

$$\sigma_b(\varepsilon, \omega) = \sigma_{b,0}(\omega)\exp\left[\frac{K(\omega)}{\sigma_{b,0}(\omega)}\left\langle\chi(\varepsilon, \omega) - \varepsilon_0(\omega)\right\rangle\right], \tag{A.1}$$

where $\langle\bullet\rangle = \max\{0, \bullet\}$. Function $\sigma_{b,0}(\omega)$ is the initial boundary of the elastic domain, see Figure

The factor $K(\omega)$ accounts for strain softening of the material and depends on fracture energies in mode-I, G_t, and mode-II, G_s, and on the direction of straining, ω. The factor $\langle \chi(\varepsilon, \omega) - \varepsilon_0(\omega) \rangle$ accounts for the irreversibly of the damage. Details can be found in (Cusatis, et al. 2003a, Cusatis, et al. 2003b).
The originally proposed material model is more complex and beyond the mixed-mode fracture propagation in the mesostructure reflecting strain hardening in compression as well as effects of confining stresses/strains. However, in the investigated experiments, the majority of the energy is dissipated for loadings with $\omega > \omega_0$, where ω_0 is the loading direction where $\sigma_{b,01}(\omega) = \sigma_{b,02}(\omega)$ in Figure

A.3.2 Lattice model

In contrast to the first particle approach, the second modeling strategy is based on a mesh that is independent on the grain layout. The lattice is generated from a set of random nuclei and concrete mesoscale structure is projected onto this discretization (Figure
In order to minimize the influence of the mesh structure on the crack direction, the lattice of irregular geometry is chosen. The discretization strategy is taken from (Bolander, et al. 2000). The nuclei are placed into the domain with a mutual distance restriction. Cells obtained by Voronoi tessellation serve as ideally rigid bodies. Concept of rigid-body-spring network published in (Kawai 1978) was originally applied on Voronoi facets in (Bolander & Saito 1998). The neighboring facets are connected by set of zero length springs (normal, shear, and rotational) in the middle of the common facet boundary. All the springs are elasto-brittle, and their elastic properties are derived according to behavior of the underlying continuum. The benefit that arises from Voronoi tessellation is the elastically uniform structure, see (Bolander, et al. 1999).
The solution procedure is step-by-step linear. In every step, elastic solution is calculated, the most loaded spring set is found, and the step solution is scaled so that the critical spring reaches the failure criterion. The material characteristics of the springs then are reduced. This classical, simple strategy is suitable only for proportional loading paths.
Non-proportional loadings require a more sophisticated solution algorithm. Convenient modification of classical strategy is published in (DeJong, et al. 2008). Here, another enhancement proposed in (Eliáš 2009) is used. After a rupture of a spring set, the stresses and nodal

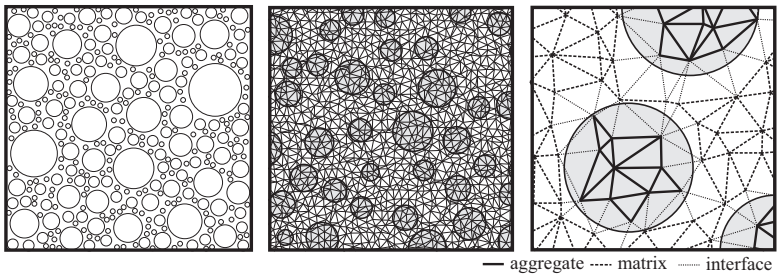

Figure 4: (a) computer generated grain layout; (b) layout projected onto the lattice; (c) zoom in on the mesostructure .

displacements are not released. The structure is loaded by the forces that were transferred by the broken spring set. Obviously, other spring sets can break during this stress redistribution. Therefore, the loading forces from broken spring set are scaled in the same way as the main load. When some bond reaches its failure criterion during the stress redistribution, the bond is removed and loading forces are updated. This redistribution process continues until the equilibrium is reached, i.e. the loading vector is zero. The next step keeps stresses from previous step and sums them together with a stress increment caused by an increase of the main load. The strategy is step-by-step linear. It can be compared with a dynamic model with infinite damping.

Many failure criteria of lattice elements were proposed and published. The modified criteria of (Bolander & Saito 1998) was found to be the most convenient. Adopted failure surfaces are shown in Figure

Aggregates interlocking and curvature of a crack cause shear resistance of an existing tensile crack. In order to mimic this resistance, the material model had to adopt stiffness recovery of broken spring connections which come to negative normal strains. Only a stiffness of the normal spring is recovered, because conditions for recovering shear and rotational springs are ill-defined. The recovery of the stiffness must not lead to any change of the stress state in the spring. This is possible only when the extension of the normal spring is zero. Recovering the shear or the rotational stiffnesses when the tangential or rotational springs extensions are zero lacks any physical meaning.

The elasto-brittle model is generally mesh dependent. The mesh structure influences primarily the direction of the crack propagation, while the mesh density has a strong influence on the strength of lattice structure. Both kinds of the mesh dependency are significantly reduced by

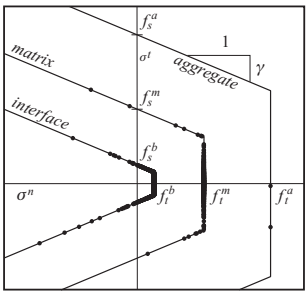

Figure 5: Present fracture criteria. Solid circles show stress state when elements were broken.

		interface	matrix	aggregates	
tensile strength	f_t	4.4	17.6	35.2	MPa
shear strength	f_s	6.6	26.4	52.8	MPa
Poisson's ratio	ν	0.2	0.2	0.2	
elastic modulus	E	30	30	105	GPa
net size			0.8		mm

Table A.7: Material parameters of the lattice model used in simulations.

tensile strength	f_t	2.0	MPa
mode I fracture energy	G_t	20	J/m^2
shear strength	f_s	6.0	MPa
mode II fracture energy	G_s	250	J/m^2
coupling parameter	α	0.8	-
elastic modulus of aggregates	E_a	90	GPa
elastic modulus of matrix	E_m	30	GPa

Table A.8: Material parameters of the particle model used in simulations.

the applied incorporating of the aggregate structure. The grain layout outweighs the directional bias and brings some internal length of the material.

A.4 Results and discussion

Two discrete models, nonlinear particle model and elasto-brittle lattice model described in Section
Figure
The simulations have, however, shown the major challenge in the experimental setup. As can be seen from Figure

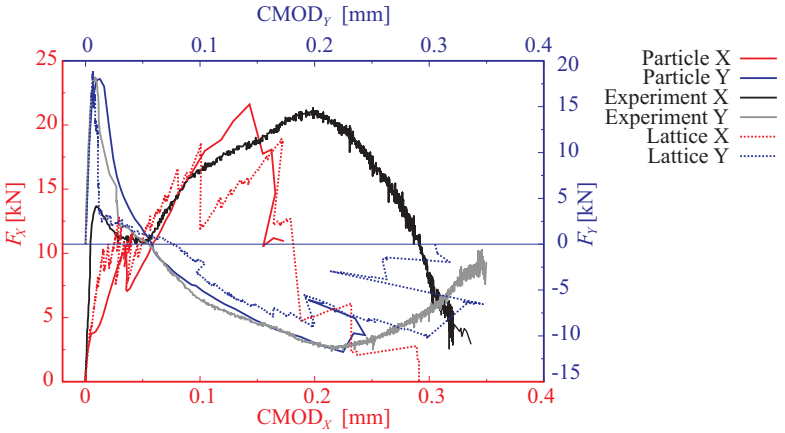

Figure 6: Computed force-CMOD curves in comparison with experimentally measured data. The simulated responses were computed as the average from the two CMODs corresponding to left and right notches in Figure

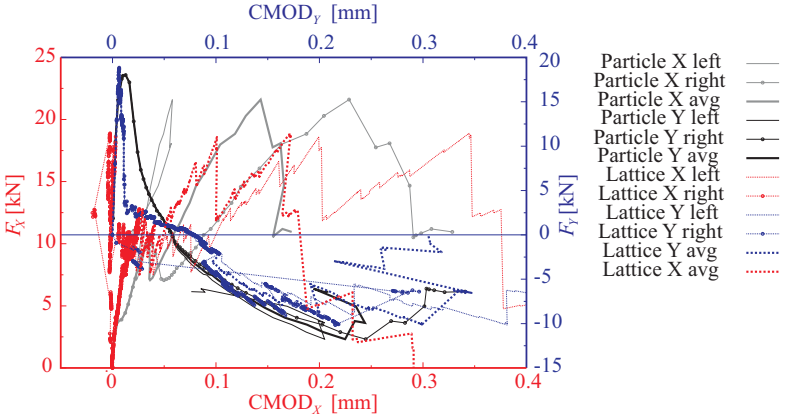

Figure 7: Computed force-CMOD curves plotted separately for left and right side of the specimen. The average response is predicted with experiments in Figure

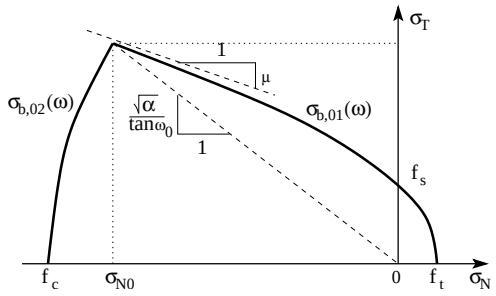

Figure 3: Initial boundary of the elastic domain of the material model.

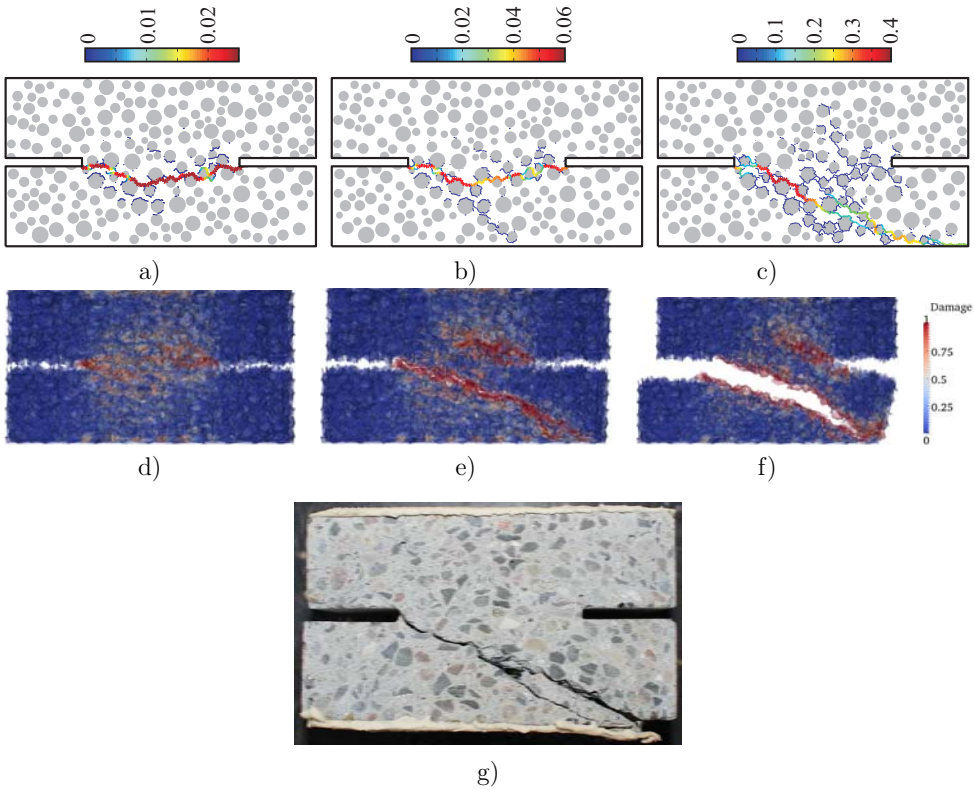

Figure 8: Comparison of the simulated and measured crack patterns. The first row shows prediction of the crack openings by the lattice model at a) the end of tensile load (machine vertical deformation 0.025 mm), b) the closing of the main crack in vertical direction when $F_y \approx 0$ kN and c) at the peak of the shear force. Colors and widths of lines indicate openings of cracks in millimeters. The middle row shows damage and opening simulated by the particle model at the same stages. These plots are 10 mm wide cuts of the specimen containing the front face. Deformations are magnified 50x. Figure g) shows the final crack pattern after complete destroying of the specimen.

A.5 Acknowledgements

The authors would like to express thanks to Jonas S. Jacobsen for the experimental part of the work.
The authors are grateful to the European Community under the Marie Curie Research Training Network MRTN-CT-2005-019283 "Fundamental understanding of cementitious materials for improved chemical physical and aesthetic performance" (`http://www.nanocem.org/MC-RTN/`) for the full support of Jan Skoček.
The second author acknowledges financial support of the Grant Agency of the Czech Republic, project No. 103/07/0760.

Bibliography

J. E. Bolander, et al. (2000). 'Structural Concrete Analysis Using Rigid-Body-Spring Networks'. *Computer-Aided Civil and Infrastructure Engineering* **15**:120–133.

J. E. Bolander & S. Saito (1998). 'Fracture analyses using spring networks with random geometry'. *Engineering Fracture Mechanics* **61**:569–591.

J. E. Bolander, et al. (1999). 'Stress analysis using elastically homogeneous rigid-body-spring networks'. *Journal of Structural Mechanics and Earthquake Engineering* **633**:25–32.

A. Caballero, et al. (2006). '3D meso-structural analysis of concrete specimens under uniaxial tension'. *Computer Methods in Applied Mechanics and Engineering* **195**(52):7182 – 7195. Computational Modelling of Concrete.

G. Cusatis, et al. (2003a). 'Confinement-Shear Lattice Model for Concrete Damage in Tension and Compression: I. Theory'. *Journal of Engineering Mechanics* **129**(12):1439–1448.

G. Cusatis, et al. (2003b). 'Confinement-Shear Lattice Model for Concrete Damage in Tension and Compression: II. Computation and Validation'. *Journal of Engineering Mechanics* **129**(12):1449–1458.

G. Cusatis, et al. (2003c). 'Confinement-Shear Lattice Model for Concrete Damage in Tension and Compression: I. Theory'. *Journal of Engineering Mechanics* .

M. J. DeJong, et al. (2008). 'Sequentially linear analysis of fracture under non-proportional loading'. *Engineering Fracture Mechanics* **75**:5042–5056.

J. Eliáš (2009). *Discrete simulation of fracture processes of disordered materials*. Ph.D. thesis, Brno University of Technology, Faculty of Civil Engineering.

A. Hillerborg, et al. (1976). 'Analysis of crack formation and crack growth in concrete by means of fracture mechanics and finite elements'. *Cement Concrete Research* **6**:773–782.

J. S. Jacobsen, et al. (2009). 'Private communication. To be published'.

T. Kawai (1978). 'New discrete models and their application to seismic response analysis of structures'. *Nuclear Engineering and Design* **48**:207–229.

H.-K. Man & J. G. van Mier (2008). 'Influence of particle density on 3D size effects in the fracture of (numerical) concrete'. *Mechanics of Materials* **40**(6):470 – 486.

L. Østergaard, et al. (2007). 'Biaxial Testing Machine for Mixed Mode Cracking of Concrete'. In *Fracture Mechanics of Concrete and Concrete Structures : New Trends in Fracture Mechanics of Concrete*, pp. 263–270. The Netherlands.

J. Skoček & H. Stang (2008). 'Inverse analysis of the wedge-splitting test'. *Engineering Fracture Mechanics* **75**:3173–3188.

Paper IV

Upscaling of fracture properties - discrete modeling

Jan Skoček and Henrik Stang
Submitted to: *Cement and Concrete Research*

Upscaling of fracture properties - discrete modeling

Jan Skoček[*,†] and Henrik Stang[*]

[*]Department of Civil Engineering, Technical University of Denmark
(DTU Byg), 2800 Kgs. Lyngby, Denmark
[†] e-mail: jas@byg.dtu.dk

Submitted to: *Cement and Concrete Research*

Abstract

Mechanical behavior of structures made from cementitious materials has been successfully modeled using non-linear fracture mechanics in recent decades. On the structural scale, an assumption of homogeneity of the material is valid and well established theories can be applied. However, if focus is put on phenomena of a similar scale as is the characteristic size of inhomogeneities of the material (e.g. crack branching in concrete meso-structure, surface cracking due to expansion reactions, up-scaling or down-scaling of fracture properties), a model which reflects the heterogeneous nature of the material needs to be applied. In the presented work, a non-linear particle model is used to predict up-scaling of fracture properties. Fracture energy, elastic stiffness and tensile strength of an ordinary portland cement paste and mortar are identified from three point bending test experiments using a simulation based on the fictitious crack model and the assumption of homogeneity of the material. These properties are then, together with the particle size distribution of aggregates, used to predict fracture properties and behavior of a mortar and micro-concrete (aggregates up to 8 cm in diameter) using the non-linear particle model.

A.1 Introduction

Simulation of the fracture process in heterogeneous quasi-brittle materials such as concrete or mortar presents a challenging task. Several models for realistic simulations of a global response of the material in mode-I experiments were proposed, for example the most widely spread Hillerborg's fictitious crack model (Hillerborg et al. 1976). Such models assume homogeneous and elastic effective material properties for the bulk behavior and averaged relationships between the crack width and bridging stresses. Utilization of such models is well established and

the models are available in many commercial numerical computer codes for structural analysis. The identification of material parameters, especially for mode-I fracture, has been also widely investigated (Skoček & Stang 2008).

Such models, however, have several limitations resulting from their assumptions. Models base on the averaged elastic and non-elastic properties can not simulate effects on scales similar to the size of heterogeneities of the material such as micro-cracking prior to the formation of the main crack, crack branching or aggregates bridging. Similarly, if simulations of complex loadings are of interest, for example non-proportional mixed-mode experiments, complicated material laws introducing mode-I and mode-II coupling, shear dilatancy and related sensitivity to confining stresses etc. are needed. These parameters, however, often lack sound physical background and are used as fitting parameters.

Several models going beyond the assumption of homogeneity of the material and at the same time capable of simulating global behavior of real-sized concrete specimens have been proposed. Since the heterogeneous microstructure responsible for most of the complexity of the concrete behavior is already captured by such models, simpler material laws can be used and the models are more robust. In contrary to the models assuming homogeneous material, the heterogeneous models are capable of providing more reliable information about processes on the scale similar to the scale of heterogeneities. This can be used with advantages in up-scaling of the fracture propagation. Down-scaling, i.e. focusing on the meso-scale processes in a global simulation can lead to the better estimation of the local crack propagation which is of a special importance for coupled transport-mechanical models where the crack widths predicted by a homogeneous model will be overestimated compared to a heterogeneous model capable of predicting the crack branching and microcracking. Up-scaling, i.e. bringing a known information from the meso-level to the global level is another application of the heterogeneous models that can not be solved using the homogeneous models. Since it is generally not possible to model behavior of every single particle and bond in the material, some simplifications have to be introduced. Two main trends can be found in literature.

The first builds on a simplified geometry, e.g. by considering only the biggest aggregates, and on a detailed description of the behavior of all phases and their connections. As an example, the approach of Carol et al. (Caballero et al. 2006, Caballero et al. 2008) is based on the classical 3D finite element method with non-linear interfaces be-

tween aggregates-mortar and mortar-mortar connections. The advantage of such an approach lies in its accuracy resulting from utilization of well established framework of the finite element method with common types of elements and material laws. The disadvantages arise from computational demands of such an approach allowing consideration of only a very limited number of aggregates (64 in the case of (Caballero et al. 2006)).

The second trend builds on a simplification of material models as well as on the simplified abstract geometry. Lattice models, see e.g. work of van Mier's group (Man & van Mier 2008) or (Eliáš 2009), belong to the latter group. The geometry of the actual material is usually modeled by three phases - aggregates, matrix and the Interfacial Transition Zone (ITZ) - and discretized using simple beams or truss elements. The material models are usually elastic-brittle or elastic step-wise brittle. With such an approach, much finer aggregates can be considerer in the simulation compared to the model based on the continuous representation of material. Due to step-wise elasto-brittle behavior of the elements, the solution of the non-linear problem of damage and crack propagation breaks into a sequence of linear problems.

Both aforementioned approaches share one common disadvantage. Since the aggregates, mortar and ITZ are modeled explicitly, it is necessary to determine their material properties, which is extremely difficult especially in the case of the ITZ since the ITZ properties are highly sensitive to the type and size of aggregates used (Tasong et al. 1998, Elsharief et al. 2003, Aquino et al. 1995, Zimbelmann 1985, Alexander 1993), age (Elsharief et al. 2003), binder (Elsharief et al. 2003, Aquino et al. 1995, Zimbelmann 1985) and the test used for the identification (Aquino et al. 1995, Zimbelmann 1985, Alexander 1993).

The model of Cusatis (Cusatis et al. 2003), which assumes geometrical simplifications and complex material laws using effective properties of the material on mesoscale, represents a compromise between the two approaches described above. In this model, the mesostructure of concrete is described by two phases - aggregates and matrix - and discretized by struts connecting centers of the aggregates. Each strut has a nonlinear stress-strain relationship in tension, shear and compression, but the strut is treated as a homogeneous, effective material. Such an approach allows considering a relatively large number of aggregates in the simulation. This makes an effective separation of scales possible and the model is therefore suitable for the up-scaling or down-scaling of fracture processes. The material laws are formulated in effective properties which makes their identification simpler compared to the

two afore mentioned cases. However, the ITZ is not modeled explicitly which could have an effect on the global response of certain systems. From applications of the models for the simulation of fracture propagation in the heterogeneous materials it is, however, not clear to what extent the material properties used by the models can be measured independently. The purpose of this study is thus the investigating of a possibility of predicting of the crack propagation in heterogeneous materials (concrete and mortar) based on measured material parameters. It the present study, a modified model of Cusatis (Cusatis et al. 2003) is used for up-scaling of fracture properties from the scale of cement paste with very fine aggregates (up to 0.8 mm) to the scale of concrete. The material properties on the mesoscale are identified from experiments. These are then, together with the idealized mesostructure of the material, based on the measured Particle Size Distribution curve (PSD), used as an input for the particle model to predict the response of the material in a mode-I fracture test on the global level. The work is organized in the following way. After the introduction, composition and preparation of the investigated materials on different scales are described in Section

A.2 Materials

Cementitious materials of three different materials scales - concrete, mortar and micro-mortar - were prepared. The materials differed in the size of the largest aggregates used, d_max and in the Water to Cement ratio (W/C). The concrete contained aggregates up to 8 mm, mortar up to 2 mm and micro-mortar up to 0.8 mm. Washed sea gravel and sand were used. Ordinary portland cement was used as the binder. The W/C varied between 0.47 in the case of concrete and 0.43 in the case of micro-mortar. The differences were introduced to compensate for the effect of the increased volume of ITZ changing the effective W/C in the bulk material. The Particle Size Distribution curve (PSD) characterizing the materials is shown in Figure

Material	d_{min} [mm]	d_{max} [mm]	α_{agg} [-]	W/C [-]
Concrete	0.01	8.0	0.65	0.47
Mortar	0.01	2	0.40	0.44
Micro-mortar	0.01	0.8	0.32	0.43

Table A.10: Detail description of investigated materials.

The materials were mixed in a rotary drum mixer not allowing contin-

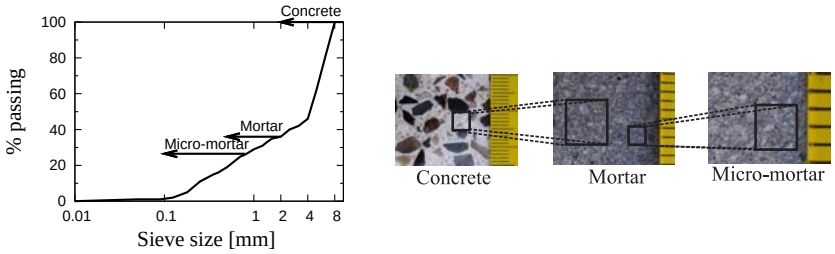

a) b)

Figure 1: a) Particle Size Distribution characterizing investigated materials and b) graphical illustration of the up-scaling.

uous adding of water. Thus the mixing water was added in two steps: 10% of water was added and mixed with aggregates for 1 minute; then the binder was added and the mixing continued for 1 minute; the rest of water was added and mixed for another 2 minutes. The samples were cast immediately after mixing. The concrete samples were vibrated using a vibration table. The samples made from mortar and micro-mortar were compacted manually by bouncing the mold gently 4-5 times against a flat surface since there was a danger of separation of phases when using the machine vibration. After casting, samples were stored in laboratory conditions (approximately 20°C) overnight covered with a plastic foil. The samples were demolded after approximately 24 hours and were moved to a warm water bath (50°C) where they were kept for another seven days. Finally, notches were cut and the samples were kept in the laboratory conditions until the testing took place (approximately 3 months).

A.3 Experiments

Six Three Points Bending Tests (TPBT) and two tests on Cylinders in uniaxial Compression (CC) were performed for every material. The specimens were identical for all materials and their geometries, dimensions and test setups are depicted in Figure

The CC experiments were controlled by displacement control with rate of 0.6 mm/min. The cross head was equipped with a hinge assuring a uniform load at the upper surfaces. The displacement was measured

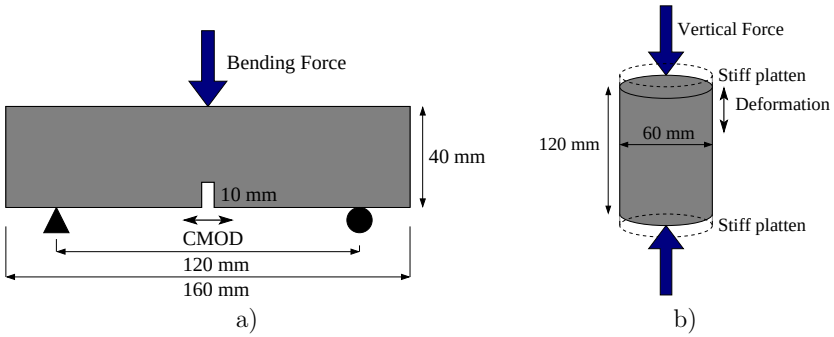

Figure 2: Geometry and dimensions of a) TPBT and b) CC specimens. Out of plane thickness of TPBT specimens was 40 mm.

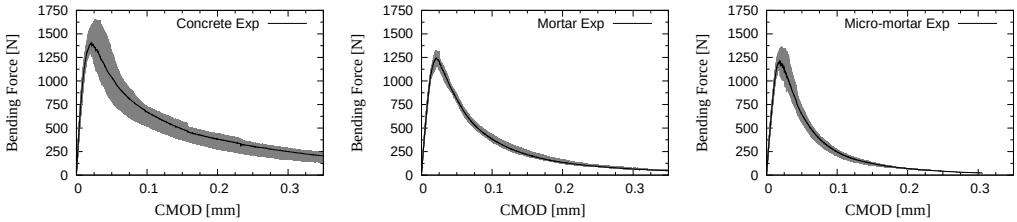

Figure 3: Experimental results of the TPBT for concrete a), mortar b) and micro-mortar c). The solid lines show average from six records while the shaded areas show experimental scatter

as the average of 3 LVDTs to eliminate the rotations of the cross head during the experiment. The upper and bottom surfaces of cylinders were grind to assure parallel and planar surfaces. Stiff loading platens were used. Averaged experimental records are plotted in Figure

A.4 Interpretation of the TPBT experiments based on the assumption of homogeneity

In order to identify material parameters of the investigated materials, a semi-analytical model based on assumptions of the classical beam theory and material homogeneity - the so-called Hinge Model (HM) - was used. The hinge model is described in (Ulfkjær et al. 1995, Olesen 2001). The model assumes that the mode-I fracture process

zone in a quasi-brittle material can be modeled using a simple beam element with linear strain distribution for the undamaged section and a set of infinitesimally small springs governed by a multi-linear Traction Separation Law (TSL) for the cracked section. The internal forces and deformation of the cross-section can be analytically expressed once the angular deformation of the beam element is determined. Such a tool can therefore be effectively used for simulations of simple fracture experiments such as the TPBT and if an error minimizing algorithm is introduced, the hinge model can be used as an effective tool for the identification of the material properties, see (Østergaard 2003, Skoček & Stang 2008). Young's modulus, tensile strength, fracture energy and the shape of the TSL can be identified using such an approach. Tri-linear TSL was used in this study. The algorithm used as well as other details of the identification can be found in (Skoček & Stang 2008). Figure

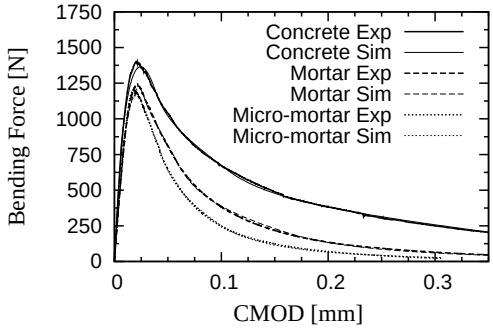

Figure 4: Comparison of the averaged experimental records with their simulations using the hinge model and the identified material parameters listed in Figure

A.5 Multi-scale modeling of experiments

In this study, a particle model based on the work of Cusatis (Cusatis et al. 2003a, Cusatis et al. 2003b, Cusatis, et al. 2006, Cusatis & Cedolin 2007) is used to predict the behavior of cementitious materials based on knowledge of its composition (PSD and volume fraction of aggregates) and material properties of its constituents.

Material	E [GPa]	f_t [MPa]	G_f [J/m^2]
Concrete	38.8	3.42	137
Mortar	28.3	3.93	66.7
Micro-mortar	27.9	4.05	47.8

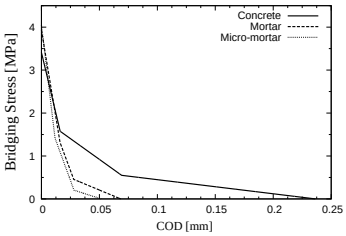

Figure 5: Material properties and shapes of traction separation laws of the investigated materials identified by the hinge model.

A.5.1 Particle model

Initially, an idealized geometry of the material was created. Spherical particles were generated in the specimen according to the PSD which is given as a set of pairs - diameters D_i and volume fractions, f_i, of aggregates passing the sieve with diameter D_i (see Figure
The geometrical discretization of the idealized geometry as well as the material model were taken from (Cusatis & Cedolin 2007). The following paragraphs briefly describe the most important aspects of the model necessary for understanding of the presented application and stress the improvements done. Readers are referred to the original works for full explanations.
The adopted particle model lumps the behavior of the modeled material into a contact between two cells containing always one and only one particle. The cells are created based on tessellation of the mesostructure and determines geometrical properties - position and area - of the contacts. The contacts are created and discretized in the following way. First, the idealized geometry is triangulated using 3D Delaunay triangulation of particles centers (second image of Figure
The elastic normal stiffness of the contact, E, corresponds to the averaged stiffness of materials laying between two nodes of the strut. Since the diameter of the smallest aggregate simulated by authors in the original work was 4.75 mm, it was possible to neglect the effect of the ITZ. However, in the present study the diameter of the smallest simulated aggregate is 0.8 mm which is only one order of magnitude larger than the thickness of the ITZ (Nadeau 2003), it is necessary to include the effect of ITZ on the stiffness of the contact. The average stiffness of the materials between two nodes can be approximated by the serial coupling and $E = l/(l_a/E_a + l_m/E_m + l_{ITZ}/E_{ITZ})$, where E_a, E_m and E_{ITZ} are Young's moduli of aggregates, matrix and ITZ, respectively.

Length l_a corresponds to segments of the strut laying inside particles, l_{ITZ} corresponds to two times ITZ thickness and $l_m = l - l_a - l_{ITZ}$ denotes the remaining part of the strut belonging to the matrix. The elastic shear stiffness, E_{T}, can be expressed as a fraction of the normal stiffness, $E_{\mathrm{T}} = \alpha E$, where α is a coupling parameter controlling the Poisson's ratio.

The mesoscopical damage-like constitutive model is formulated in terms of effective stress, σ, effective strain, ε and coupling strain, ω. The effective stress is computed by

$$\sigma = \sqrt{\sigma_{\mathrm{N}}^2 + \frac{\sigma_{\mathrm{T}}^2}{\alpha}} \quad \text{where} \quad \sigma_{\mathrm{T}} = \sqrt{\sigma_{\mathrm{L}}^2 + \sigma_{\mathrm{M}}^2},$$

where σ_{N} is the stress perpendicular to the contact plane and σ_{L} and σ_{M} denote two mutually perpendicular stresses at the plane of the contact.

Accordingly the effective strain can be expressed as

$$\varepsilon = \sqrt{\varepsilon_{\mathrm{N}}^2 + \alpha\varepsilon_{\mathrm{T}}^2} \quad \text{with} \quad \varepsilon_{\mathrm{T}} = \sqrt{\varepsilon_{\mathrm{L}}^2 + \varepsilon_{\mathrm{M}}^2}.$$

The coupling strain, ω, reflecting direction of the loading of the strut, is expressed as

$$\tan\omega = \frac{\varepsilon_{\mathrm{N}}}{\sqrt{\alpha}\varepsilon_{\mathrm{T}}}.$$

See (Cusatis et al. 2003) for all the details. The effective stress, σ, needs to satisfy inequality $0 \leq \sigma \leq \sigma_b(\varepsilon, \omega)$, where the effective stress boundary, $\sigma_b(\varepsilon, \omega)$, can be expressed as

$$\sigma_b(\varepsilon, \omega) = \sigma_{b,0}(\omega)\exp\left[\frac{K(\omega)}{\sigma_{b,0}(\omega)}\left\langle\chi(\varepsilon, \omega) - \varepsilon_0(\omega)\right\rangle\right], \tag{A.1}$$

where $\langle\bullet\rangle = \max\{0, \bullet\}$. Function $\sigma_{b,0}(\omega)$ is the initial boundary of the elastic domain, see Figure

The factor $K(\omega)$ accounts for strain softening of the material and depends on fracture energies in mode-I, G_t, and mode-II, G_s, and on the direction of straining, ω. The factor $\langle\chi(\varepsilon, \omega) - \varepsilon_0(\omega)\rangle$ accounts for the irreversibly of the damage. Details can be found in (Cusatis et al. 2003a, Cusatis et al. 2003b).

The originally proposed material model is more complex and beyond the mixed-mode fracture propagation in the mesostructure reflecting strain hardening in compression as well as effects of confining stresses/strains. However, in the investigated experiments, the majority of the energy is dissipated for loadings with $\omega > \omega_0$, where ω_0 is the loading direction where $\sigma_{b,01}(\omega) = \sigma_{b,02}(\omega)$ in Figure

A.5.1.1 Convergence analysis and matrix nodes

The global equations of equilibrium were solved using incremental linearized analysis governed by the indirect displacement control technique described e.g. in (Jirásek 2006) with adaptive step length (Crisfield 1984, Bittnar & Šejnoha 1992). The ratio between the work of unbalanced forces and the work of internal forces was used as the convergence criterion for every step. In order to identify the influence of the choice of the convergence criterion, a convergence analysis was performed. Seven simulations with the ratios between the work of unbalanced forces and work of internal forces between 10^{-1} and 10^{-4} were run. The material properties from Table
In the original implementation of the model, centers of aggregates are taken as the nodes of the finite element discretization and the contact is assumed to be placed in the middle of ligament between the aggregates. Under such an assumption, the crack is forced to propagate only in regions with the biggest distances to aggregates which is in contradiction to experimental observations where cracks tend to propagate "around" aggregates as well as to the assumption of the ITZ being the weakest part in the mesostructure. Assuming that the cracking takes place in the middle between the aggregates only also creates an exaggerated roughness of the crack path. In order to improve the behavior of the model, additional artificial nodes with zero diameter, *matrix nodes*, were placed in the inter-particle volume resulting in a crack propagation more consistent with experimental observations (see Figure

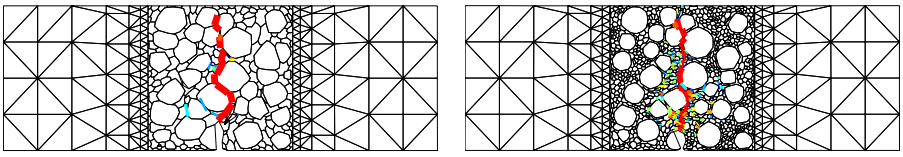

a) b)

Figure 7: Comparison of the crack roughness in 2D simulation of TPBT for case with a) 100 and b) with 800 matrix nodes.

The described enrichment results in a more realistic crack propagation with a reduced roughness of the crack path and only the roughness resulting from mesostructural geometry is preserved as is illustrated by Figure

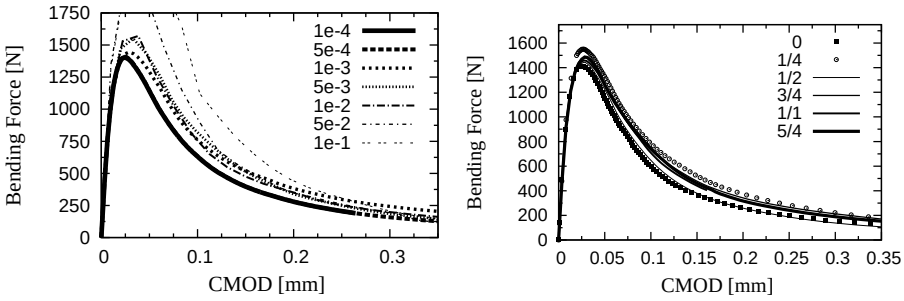

Figure 8: Convergence analysis with respect to a) relative work of unbalanced forces as the convergence criterion in the linearized steps and b) addition of matrix nodes.

A.5.2 Input parameters

Mode-I fracture propagation on the global scale presents a very complex problem once zoomed down to meso-scale. The mesoscopical model requires a large number of material parameters of which some are not easily obtained. Generally, due to computational demands, simple models, usually based on the assumption of homogeneity of the material, are often used for material parameter identification. This, however, reduces the number of parameters which can be identified from an experiments. The identification procedure based on the semi-analytical hinge model was introduced in Section

Based on the results in (Li et al. 1999, Nadeau 2003), Young's modulus of aggregates E_a, and ITZ, E_{ITZ}, were set to 80 GPa and 10 GPa, respectively. The thickness of the ITZ, l_{ITZ}, was fixed to 0.043 mm (Nadeau 2003). The coupling parameter was set to $\alpha = 0.25$ as proposed by authors of the original model. Young's modulus of matrix, E_m, tensile strength, S_t, and mode-I fracture energy, G_t, were directly identified by the HM-based inverse analysis of the experiments performed on the pure matrix.

Both the response of the TPBT and CC specimens were simulated with the particle model. In order to identify the importance of the identified parameters on the simulated response in the TPBT and to evaluate the importance of the remaining parameters, a sensitivity analysis was performed for the mortar to concrete upscaling. All the identified material parameters together with shear strength, mode-II fracture energy and α were randomly generated with uniform distribution in

the interval of ±25 % from the reference value. The geometry and the assumed material properties as well as other properties not important for the global mode-I fracture process were kept constant. Pearson's correlation coefficients as a function of CMOD were evaluated for the relevant material parameters. The correlation coefficient, $\rho_{M,CMOD}$, of the material property M for given CMOD was computed as (Bittnar & Šejnoha 1992)

$$\rho_{M,CMOD} = \frac{n\sum_{i=1}^{n} m_i P_{i,CMOD} - \sum_{i=1}^{n} m_i \sum_{i=1}^{n} P_{i,CMOD}}{\sqrt{n\sum_{i=1}^{n} m_i^2 - \left(\sum_{i=1}^{n} m_i\right)^2}\sqrt{n\sum_{i=1}^{n} P_{i,CMOD}^2 - \left(\sum_{i=1}^{n} P_{i,CMOD}\right)^2}},$$

where n is the number of sampling computations, m_i is the value of the parameter M in the $i-th$ sampling computation and $P_{i,CMOD}$ is the value of bending force interpolated for given CMOD from the $i-th$ computation. Correlation coefficients for the relevant parameters are plotted in Figure

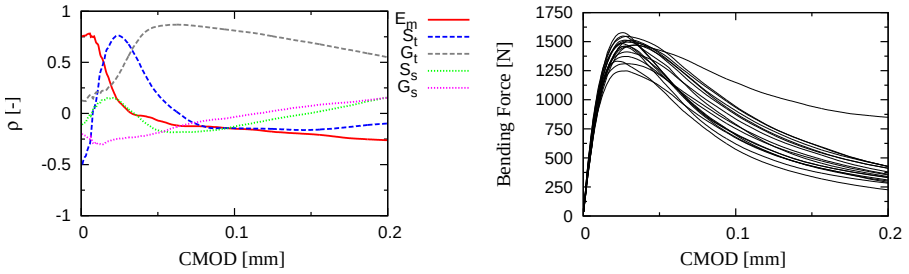

a) b)

Figure 9: Pearson's correlation parameter for important material parameters in the TPBT a) and the set of sampling computations b).

Not enough data on the shear strength and mode-II fracture energy of mortars can be found in literature. Significant effort has been put into investigation of the mode-II properties of concrete, however, a literature survey yields highly scattered data. Comparisons of ratios between mode-I and mode-II fracture energies done in (Neto et al. 2004) addresses ratios from $G_{f,II}/G_{f,I} \approx 25$ (Reinhardt et al. 1997) to less than 10 (Täljsten 1994). Therefore, additional CC experiments were performed. In contrast to the mode-I crack propagation in the TPBT, the crack propagation typical for the CC is characterized by

the fact that increasing S_s and G_s both have an positive effect on the global response which makes the CC experiment suitable for the identification of the shear parameters using the CC model.
In the CC experiments, the specimens were placed directly between the loading platens without any friction modifying devices. Thus, in the particle model of the CC, all displacements were set to zero on the bottom surface and the upper surface was allowed to move in the load direction only. Rotations were kept unconstrained. A parametric

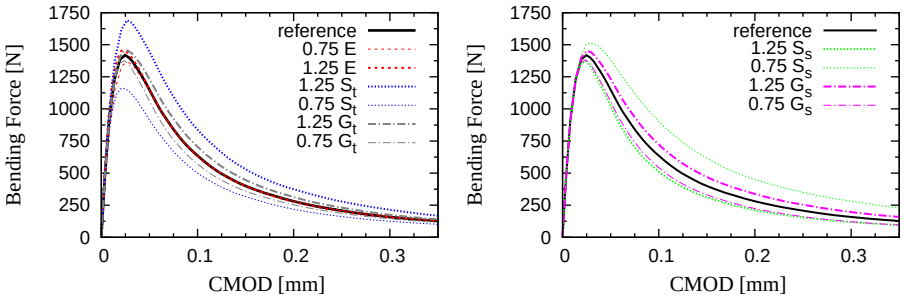

Figure 10: Effect of variation of ±25 % of the identified a) and fitted b) material parameters on the global response of the TPBT.

study varying S_s/S_t and G_s/G_t was performed on mortar to concrete upscaling to identify the proper combination of the shear parameters. The geometry as well as the remaining parameters were kept constant. Figure

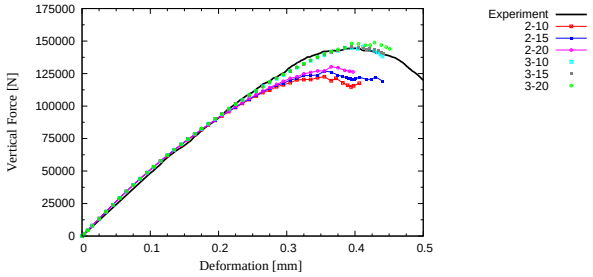

Figure 11: Sensitivity of the CC simulation to S_s and G_s. The first number in legend is S_s/S_t while the second denotes G_s/G_t.

Table

A.5.3 Results and discussion

The goal of the presented study is to investigate the possibility of predicting the fracture propagation in mode-I in heterogeneous materials on the basis of, primarily, measured material properties and known idealized geometry. TPBTs of mortar and concrete specimens were simulated using the particle model described in Section
Figure
Due to the random geometry of the numerical concrete and mortar, the particle model is suitable for the prediction and explanation of the scatter seen in the experimental data. As is visible from the presented results, trends in the measured scatter can be predicted correctly, see Figure
Even though the specimens crack in global mode-I fracture propagation, shear and crack sliding play an important role at the mesoscale. This topic was already partly discussed in Section

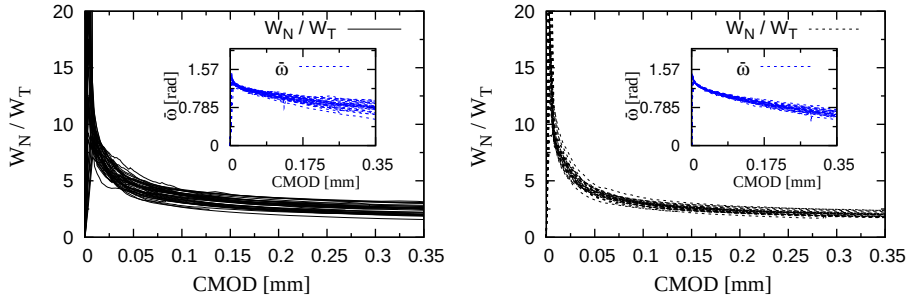

Figure 12: Evolution of the ratio between energies dissipated in local shearing and normal opening, W_N/W_T, and energetically averaged direction of crack propagation, $\bar{\omega}$ in the predictions of TPBT for a) mortar to concrete upscaling and b) micro-mortar to mortar upscaling.

Figure
In the case of mortar to concrete upscaling, the predictions of CC experiments shown in Figure

A.6 Conclusions

The possibility of simulating the fracture propagation in heterogeneous materials on the basis of a material model with primary input parame-

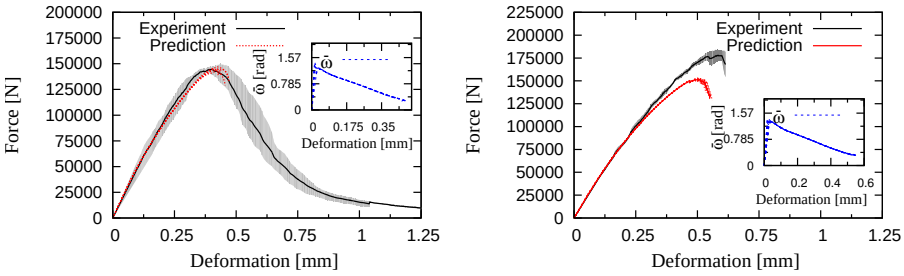

Figure 13: Comparison of the prediction with the experimental records of CC tests for a) mortar to concrete upscaling and b) micro-mortar to mortar upscaling. Dashed lines show different simulations with randomly generated geometries.

ters that can be easily measured was investigated. The particle model introduced in (Cusatis et al. 2003a, Cusatis et al. 2003b) was chosen because it works with effective parameters and provides computationally effective tool allowing suitable scale separation in experiments. The original particle model was enriched with matrix nodes for more realistic crack path simulation and with the effect of the ITZ in the elastic regime, see Section

A.7 Acknowledgments

The authors are grateful to the European Community under the Marie Curie Research Training Network MCRTN-CT-2005-019283 "Fundamental understanding of cementitious materials for improved chemical physical and aesthetic performance" (`http://www.nanocem.org/MC-RTN`) for the full support of Jan Skoček.

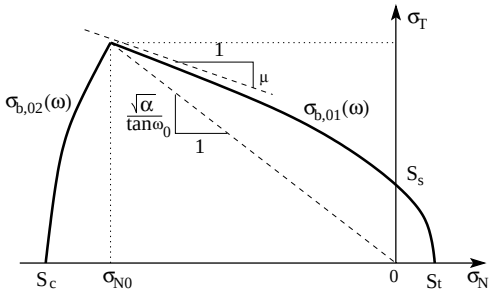

Figure 6: Initial boundary of the elastic domain of the material model.

Model parameter	Abbreviation [unit]	Mortar	Concrete	Source / Note
Young's modulus of aggregates	E_a [GPa]	80	80	from (Li et al. 1999, Nadeau 2003)
Young's modulus of matrix	E_m [GPa]	27.9	28.3	identified by HM
Young's modulus of ITZ	E_{ITZ} [GPa]	10	10	from (Li et al. 1999, Nadeau 2003)
Thickness of ITZ	l_{ITZ} [mm]	0.043	0.043	from (Nadeau 2003)
Coupling parameters	α [-]	0.25	0.25	from (Cusatis et al. 2003)
Uniaxial meso-tensile strength	S_t [MPa]	4.05	3.93	identified by HM
Uniaxial meso-shear strength	S_s [MPa]	$3S_t$	$3S_t$	fitted from CC
Mode-I meso-fracture energy	G_t [J/m^2]	47.8	66.7	identified by HM
Mode-II meso-fracture energy	G_t [J/m^2]	$12.5G_t$	$12.5G_t$	fitted from CC
Friction coefficient	μ [-]	0.2	0.2	from (Cusatis et al. 2003)
Uniaxial meso-compressive strength	S_c [MPa]	1000	1000	=deactivated

Table A.11: Material parameters used for the upscaling. Values of remaining parameters of the material model not relevant for the mixed-mode crack propagation which are not listed in the table were taken from (Cusatis et al. 2003).

Bibliography

M. Alexander (1993). 'Two experimental techniques for studying the effects of the interfacial zone between cement paste and rock'. *Cement and Concrete Research* **23**(3):567 – 575.

M. J. Aquino, et al. (1995). 'Mechanical properties of the aggregate and cement interface'. *Advanced Cement Based Materials* **2**(6):211 – 223.

Z. Bittnar & J. Šejnoha (1992). *Numercické metody mechaniky [2].* Vydavatelství ČVUT. in Czech.

A. Caballero, et al. (2006). '3D meso-structural analysis of concrete specimens under uniaxial tension'. *Computer Methods in Applied Mechanics and Engineering* **195**(52):7182 – 7195. Computational Modelling of Concrete.

A. Caballero, et al. (2008). 'Consistent tangent formulation for 3D interface modeling of cracking/fracture in quasi-brittle materials'. *Computer Methods in Applied Mechanics and Engineering* **197**(33-40):2804 – 2822.

M. Crisfield (1984). 'Accelerating and damping the modified Newton-Raphson method'. *Computers and Structures* **18**(3):395 – 407.

G. Cusatis, et al. (2003a). 'Confinement-Shear Lattice Model for Concrete Damage in Tension and Compression: I. Theory'. *Journal of Engineering Mechanics* **129**(12):1439–1448.

G. Cusatis, et al. (2003b). 'Confinement-Shear Lattice Model for Concrete Damage in Tension and Compression: II. Computation and Validation'. *Journal of Engineering Mechanics* **129**(12):1449–1458.

G. Cusatis, et al. (2006). 'Confinement-shear lattice CSL model for fracture propagation in concrete'. *Computer Methods in Applied Mechanics and Engineering* **195**:7154–7171.

G. Cusatis, et al. (2003c). 'Confinement-Shear Lattice Model for Concrete Damage in Tension and Compression: I. Theory'. *Journal of Engineering Mechanics* .

G. Cusatis & L. Cedolin (2007). 'Two-scale study of concrete fracturing behavior'. *Egineering Fracture Mechanics* **74**:3–17.

J. Eliáš (2009). *Discrete simulation of fracture processes of disordered materials*. Ph.D. thesis, Brno University of Technology, Faculty of Civil Engineering.

A. Elsharief, et al. (2003). 'Influence of aggregate size, water cement ratio and age on the microstructure of the interfacial transition zone'. *Cement and Concrete Research* **33**(11):1837 – 1849.

A. Hillerborg, et al. (1976). 'Analysis of crack formation and crack growth in concrete by means of fracture mechanics and finite elements'. *Cement Concrete Research* **6**:773–782.

M. Jirásek (2006). 'Advanced course on Modeling of Localized Inelastic Deformation'. Lecture notes.

G. Li, et al. (1999). 'Effective Young's modulus estimation of concrete'. *Cement and Concrete Research* **29**(9):1455 – 1462.

H.-K. Man & J. G. van Mier (2008). 'Influence of particle density on 3D size effects in the fracture of (numerical) concrete'. *Mechanics of Materials* **40**(6):470 – 486.

J. C. Nadeau (2003). 'A multiscale model for effective moduli of concrete incorporating ITZ water-cement ratio gradients, aggregate size distributions, and entrapped voids'. *Cement and Concrete Research* **33**(1):103 – 113.

P. Neto, et al. (2004). 'The influence of mode II fracture on concrete strengthened with CFRP'. *Computers and Structures* **82**(17-19):1495 – 1502. Computational Mechanics in Portugal.

J. F. Olesen (2001). 'Fictitious Crack Propagation in Fiber-Reinforced Concrete Beams'. *Journal of Engineering Mechanics* **127**(3):272–280.

L. Østergaard (2003). *Early-Age Fracture Mechanics and Cracking of Concrete. Experiments and Modelling*. Ph.D. thesis, Department of Civil Engineering, Technical University of Denmark, Lyngby, Denmark.

H. W. Reinhardt, et al. (1997). 'Shear of structural concrete members and pure mode II testing'. *Advanced Cement Based Materials* **5**(3-4):75 – 85.

J. Skoček & H. Stang (Submitted in 2009). 'Application of optical deformation analysis system on wedge splitting test and its inverse analysis'. *Materials and Structures Journal* .

J. Skoček & H. Stang (2008). 'Inverse analysis of the wedge-splitting test'. *Engineering Fracture Mechanics* **75**(10):3173 – 3188.

B. Täljsten (1994). *Plate bondingstrengthening of existing previous termconcretenext term structures with epoxy bonded plates of steel or fibre reinforced plastics.* Ph.D. thesis, Lulea University of Technology.

W. A. Tasong, et al. (1998). 'Aggregate-cement paste interface. ii: influence of aggregate physical properties'. *Cement and Concrete Research* **28**(10):1453 – 1465.

J. Ulfkjær, et al. (1995). 'Analytical model for fictitious crack propagation in concrete beams'. *Journal of Engineering Mechanics* **121**(1):7–15.

R. Zimbelmann (1985). 'A contribution to the problem of cement-aggregate bond'. *Cement and Concrete Research* **15**(5):801 – 808.

Paper V

From microstructure to strength of cement paste - critical aspects

Jan Skoček and Denis Davydov

Draft; will be submitted to: *Cement and Concrete Research*

From microstructure to strength of cement paste - critical aspects

Jan Skoček* and and Denis Davydov†

*Department of Civil Engineering, Technical University of Denmark (DTU Byg), 2800 Kgs. Lyngby, Denmark
e-mail: jas@byg.dtu.dk
† Faculty of Civil Engineering, Czech Technical University, Department of Mechanics, Thákurova 7, 166 29 Prague 6, Czech Republic
e-mail: denis.davydov@fsv.cvut.cz

Draft; will be submitted to: *Cement and Concrete Research*

Abstract

In the case of the ordinary Portland cement paste, a simple relationship linking the strength of the cement paste with its porosity was proposed and widely used for a long time. However, in today's blended cements, systems with higher porosity and higher strength at the same time are often found. Thus, the arrangement of the phases in the RVE plays an important role and the simple relationship can not be used anymore. It is well understood that the modeling of microstructures of such systems and models linking microstructures with mechanical properties are necessary for the strength prediction. In the presented study, the mean-field strength homogenization approach, approaches based on numerical solutions of linear-elastic problems and a modified particle model for concrete are utilized to predict the tensile and compressive strength of measured and modeled microstructures. Critical aspects of every method are identified, discussed and compared with other methods. It is verified that analytical methods based on the second order stress estimates do not reflect the actual microstructure and significantly overestimate strengths compared to results from the numerical methods. Further, it is verified and quantified that the perfectly brittle strength estimate differs significantly from the strengths obtained from particle model for cement microstructures and thus only nonlinear material models and nonlinear simulations can provide satisfactory results. The modified particle model provides a robust modeling tool with results

matching favorable results of a full nonlinear finite element analysis with a significantly reduced computational costs. Further, the effect of cracking of the C-S-H is investigated using the particle model.

A.1 Introduction

In the case of the Ordinary Portland Cement (OPC) paste, a simple relationship linking the strength of the cement paste with its porosity was proposed and widely used (Powers & Brownyards 1948) for a long time. However, in today's blended cements, systems with higher porosity and higher strength at the same time are often found. Thus, the arrangement of the phases in the RVE plays an important role and the simple relationship can not be used anymore. It is well understood that the modeling of microstructures of such systems and models linking microstructures with mechanical properties are necessary for the strength prediction.

Several approaches for estimation of the strength of multiphase materials can be found. When the microstructure is relatively simple (such as matrix-pore inclusions in case of, for example, reinforced concrete or poly-crystals in metals), a homogenization based on the definition of Linear Comparison Composite (LCC) (Castaneda 1996, Castaneda 2002) or methods based on the second order moment estimate of stress and strains in each phase of the heterogeneous material (Dormieux et al. 2006, L. Dormieux 2002) can be used. In both cases, the nonlinear constitutive laws of various phases are linearized in such a way that the traditional elastic homogenization schemes can be applied. These approaches are formulated as variational problems which are aimed to find the dissipation capacity of the heterogeneous material. In other words, the collapse occurs when the limit of the maximum plastic dissipation is reached. The main problem in analytical homogenization methods is that the secant stiffness tensor is not uniform in each phase. It can be approached either by defining a reference state for each phase based on the first or second order moment or by introducing the LCC with a-priory unknown properties. The correct capturing of the average strain and stress field per phase is the main problem in the mean-field homogenization schemes. The problem becomes even more pronounced for complex microstructures such as the cement paste where the stress localization is hard to capture. Still, the formulation with quadratic stress average for von Mises yield condition was successfully applied to cement paste assuming acircular (needle-

type) geometry of hydration products (Pichler et al. 2008). It should be noted that authors were not solving the variational problem but assuming perfectly brittle behavior based on the second order estimates. The same results can be potentially achieved by solving the linear elastic problem with Finite Element Method (FEM) of Fast Fourier Transform (FFT) (Moulinec & Suquet 1998), thus giving physically similar but more precise estimates thanks to considering explicitly the actual microstructure. Never the less, the authors obtained satisfactory agreement between the prediction of the analytical model and experimental results for an early age strength-evolution of cement pastes mixed at different Water-Cement ratios (W/C). However, the deviatoric yield limit for the main hydration product - C-S-H - was not obtained experimentally (e.g. from nanoindentation) but was fitted, resulting in a value about 20 MPa (Pichler et al. 2008). Yet, results of nanoindentation clearly shows a hardness value of C-S-H in the range 0.5-1.5 GPa (Sorelli, et al. 2008, Constantinides & Ulm 2007) which can be recalculated into the yield limit assuming von Mises ($J2$) plasticity dividing by 2.8 (Cheng & Cheng 2004, Vandamme & Ulm 2008). This estimate leads to one order of magnitude higher value of $J2$ strength than the strength used in (Pichler et al. 2008).

In order to incorporate the information about the real microstructural of cement paste, a discretization of digital images with the variational formulation of the lower bound (statically admissible stress fields) with Drucker-Prager yield criterion was done in (Ganneau et al. 2007). This formulation is similar to the mentioned above with the difference that an estimation of stress and strain in each phase are not needed thank to the discretization of the microstructure in a way similar to the FEM leading, as a result, to a nonlinear programming problem. It is interesting to note that the cohesion of C-S-H equal to 120 MPa was used (Ganneau et al. 2007). It led to a meaningful homogenized strength of about 10-20 MPa and on the other hand agrees with nanoindentation experiments. Therefore, the question of possibility of application of the mean field strength homogenization schemes to the cement paste complex microstructure naturally arises. The answer to this question is one of the aims of the presented paper. Let us note that none of the above mentioned method considers interface strength criteria.

All aforementioned methods are based on the yield limit theory and perfect plasticity and just approach the problem from different sides. However, in-situ observations of the crack propagation in the cement paste loaded in compression (Mindess & Diamond 1982) showed that

cracks parallel to the loading direction are formed in the specimen prior the peak load is reached. Therefore, it can be expected that the localized tensile failure of the C-S-H and other phases in the microstructure will be as important as the yielding of the C-S-H. The importance of the localized failure will be even more pronounced in the cement paste subjected to tension. Therefore a particle model similar to the model used for simulations of the fracture process in concrete (Cusatis et al. 2003) was modified for the cement paste and heterogeneous matrix in the presented study. Such an approximative model is suitable for handling complex heterogeneous materials and can combine the yielding with the localized failure of the C-S-H with reasonable computational costs.

In the presented study, the mean-field strength homogenization approach used in (Pichler et al. 2008), approaches based on the solution of linear-elastic problems with the FEM and FFT and a modified particle model based on (Cusatis et al. 2003) are utilized to predict the tensile and compressive strength of three cement pastes: first was measured[4], and the other two are simulated using CemHyd3D (Bentz 2000) hydration model for two different types of cements. Critical aspects of every method are identified, discussed and compared with other methods.

Authors are aware of the existence of more advanced numerical models for strength predictions of heterogeneous materials, see e.g. (Ganneau et al. 2007, Pichler et al. 2008, Pierard 2006), and of very simplified approaches and strong assumptions used in certain places of this study. However, the main goal of this study is to critically review available approaches considering same hypothesis, discuss their robustness and efficiency and identify the missing gaps in knowledge necessary for practical application of the approaches. The more advanced models not considered in the comparison share the most important assumptions with some of the methods and the main findings are therefore valid for them as well, as discussed in Conclusions.

The outline of the paper is the following: Section

A.2 Investigated materials and microstructures

Seven different cement microstructures were studied. The first one was X-ray microtomography image, see (Bentz et al. 2002) for details, of cement paste with W/C of 0.3 made from cement 133 hydrating for 7

[4] `http://visiblecem.nist.gov/cement`

days (see `http://visiblecem.nist.gov/cement` for all the details). The cement is labeled as NIST Cem in the rest of this work. This particular microstructure was chosen due to its longest hydration time which is comparable with other microstructures. Focusing initially on performance at later ages only allows us to use simpler models since effects of the artificial connectivity in the model and related problems with the resolution of the input play significantly smaller role compared to the early age performance, see (Chamrová 2010).
The remaining microstructures were generated using CemHyd3D (Bentz 2000). The first generated cement was Aalborg White cement, labeled as Cem A in the rest of the work, and the second one an OPC labeled as Cem C. Microstructures were generated after 1, 7 and 28 days of hydration. Composition of the cements can be found in Table

Content [%]	Cem A	Cem C
C_3S	67.1	62.3
C_2S	23.6	18.4
C_4AF	0.00	7.1
C_3A	3.5	6.0
C	0.8	0
MgO	0.2	0.7
Sulfate	4.2	5.1
$CaCO_3$	0.6	0.5

Table A.12: Chemical composition of the investigated cements measured by Rietveld analysis.

A.2.1 Material properties of cement phases

In order to avoid any fitting of phase properties, the nanoindentation was considered as the source of mechanical properties of the main hydration product - the C-S-H (Constantinides & Ulm 2007). From the nanoindentation, LD-C-S-H and HD-C-S-H properties can be obtained among others. For the sake of comparison of results obtained from modeled microstructures (Cem A and C modeled in CemHyd3D) with the measured one (NIST Cem), where only three phases were distinguished - porosity, hydrates and unhydrated clinker (separation thresholds were set according to recommendations from (Bentz et al. 2002)), elastic properties of the C-S-H were set to 25.55 GPa in all calculations (average values from (Šmilauer 2005, Constantinides & Ulm 2007)) and Poisson's ratio was set to 0.24. In addition, in the case of the mod-

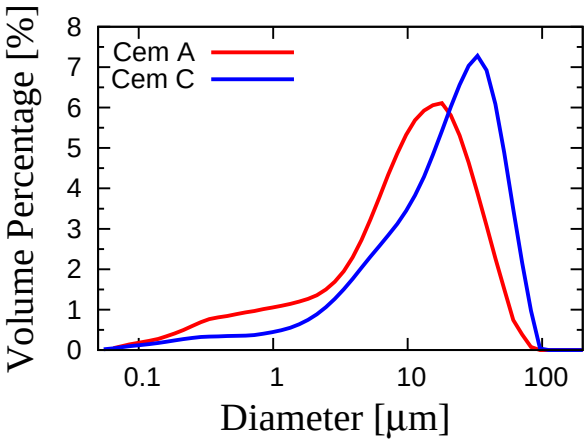

a)

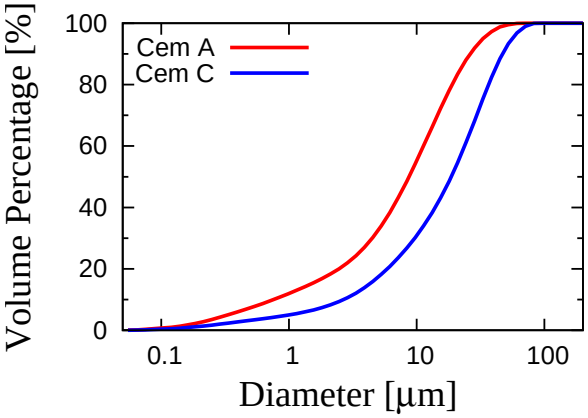

b)

Figure 1: Particle size distribution curves, a), and cumulative particle size distribution curves, b), for Cem A and Cem C.

eled microstructures (Cem A and Cem C), the elastic properties of the other phases were used from (Šmilauer 2005). The C-S-H was considered to be the only phase allowed to yield/crack. Regarding the strength/yield properties of the C-S-H, the only experimentally available strength parameter is hardness $H = P_{max}/A_c$, where P_{max} is the maximum load during the indentation and A_c is the contact

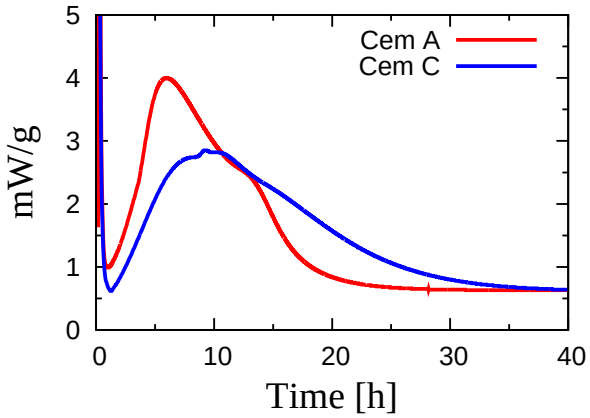

Figure 2: Calorimetric record of heat of hydration of Cem A and Cem C cement pastes.

area. Using different hypothesis regarding the yield surface of the C-S-H, different scaling relationships relating H to the yield surface properties can be obtained. For $J2$ plasticity with $f_{y,J2} << E$ (which is the case of cementitious materials) this scaling relationship reads $f_{y,J2} = H/2.8$ (Cheng & Cheng 2004).

Phase	E [GPa]	ν [-]	$f_{y,J2}$ [GPa]	H [GPa]
Porosity	0.001	0.4999	Inf	Inf
Clinker	135.0	0.3	Inf	Inf
Hydrates	25.5	0.24	0.214	0.6

Table A.13: Assumed material properties of the cement paste phases.

Yet, we would like to use more physically motivated yield surface. Current understanding of the C-S-H microstructure is that it is a porous medium (Jennings, et al. 2007, Allen, et al. 2007, Constantinides & Ulm 2004, Constantinides & Ulm 2007). In (Vandamme & Ulm 2008), the author assumed Drucker-Prager yield behavior for the C-S-H building blocks, then homogenized it to the level of nanoindentation experiment and developed scaling relationships for such a case. The resulting yield surface represents an elliptical yield criterion. Such a description was used for both types of C-S-H and also for all hydrates in the case of experimentally obtained microstructure. This choice corresponds to the weakest link and therefore is a safe estimate. Additional details regarding strength homogenization used for the C-S-H are presented

in Section
Material properties of the phases are summarized in Table

A.3 Utilized methods

A.3.1 Mean field elasticity homogenization

A brief description of the mean field elastic homogenization approach needed for the plastic homogenization is presented in the following part.
Consider a Representative Volume Element (RVE) of an elastic heterogeneous material composed of n phases with the volume fractions f_γ, such that $\sum_\gamma f_\gamma = 1$. The RVE is subjected on its boundary, denoted ∂V, to a displacement condition of the Hashin-type:

$$\partial V : \boldsymbol{u}(\boldsymbol{x}) = \mathbf{E} \cdot \boldsymbol{x} \,, \tag{A.1}$$

where $\boldsymbol{u}(\boldsymbol{x})$ is a microscopic displacement field, $\boldsymbol{x}$ denotes a position vector at the microscopic scale and $\mathbf{E}$ is a macroscopic strain related to the microscopic strain $\boldsymbol{\varepsilon}(\boldsymbol{x})$ by the volume averaging relation:

$$\mathbf{E} = < \boldsymbol{\varepsilon}(\boldsymbol{x}) >_V = \frac{1}{V} \int_V \boldsymbol{\varepsilon}(\boldsymbol{x}) \mathrm{d}V = \sum_\gamma f_\gamma \boldsymbol{\varepsilon}_\gamma \,, \tag{A.2}$$

where $\boldsymbol{\varepsilon}_\gamma$ is strain averaged over the phase. Analogously, the microscopic stress and the macroscopic stress are related by the volume averaging relation:

$$\boldsymbol{\Sigma} = < \boldsymbol{\sigma}(\boldsymbol{x}) >_V \ . \tag{A.3}$$

To connect the macroscopic strain, $\mathbf{E}$, with the microscopic strain, $\boldsymbol{\varepsilon}$, the linear strain localization condition is postulated for each phase γ:

$$\varepsilon_\gamma = \mathbb{A}_\gamma : \mathbf{E} \tag{A.4a}$$

$$\langle \mathbb{A} \rangle_V = \sum_\gamma f_\gamma \mathbb{A}_\gamma = \mathbb{I} \,, \tag{A.4b}$$

where $\mathbb{A}$ is a fourth-order localization or concentration tensor which depends on the morphology, elastic properties and fractions of the phases. Considering the linear elastic constitutive law for each microscopic phase, $\boldsymbol{\sigma} = \mathbb{C} : \boldsymbol{\varepsilon}$, together with strain localization condition (

$$\boldsymbol{\Sigma} = \langle \boldsymbol{\sigma} \rangle_V = \langle \mathbb{C} : \boldsymbol{\varepsilon} \rangle_V = \langle \mathbb{C} : \mathbb{A} \rangle_V : \mathbf{E} = (\sum_\gamma f_\gamma \mathbb{C}_\gamma : \mathbb{A}_\gamma) : \mathbf{E} = \mathbb{C}_{\mathrm{hom}} : \mathbf{E} \tag{A.5}$$

with f_r-volume fraction of phase, $\mathbb{C}_\gamma$ - stiffness tensor of the phases, $\mathbb{C}_{\text{hom}}$ - homogenized stiffness:

$$\mathbb{C}_{\text{hom}} = \sum_\gamma f_\gamma \mathbb{C}_\gamma : \mathbb{A}_\gamma. \tag{A.6}$$

The average strains of each phase are set equal to the strains in a single ellipsoidal inclusion with stiffness $\mathbb{C}_\gamma$ embedded in an infinite matrix of stiffness $\mathbb{C}_m$, subjected to the fictitious (uniform) strains $\mathbf{E}^\infty$ at infinity. This problem was analytically solved by Eshelby (J.D. 1957, J.D. 1959). The average strains of the inclusion is given by the formula:

$$\boldsymbol{\varepsilon_\gamma} = [\mathbb{I} + \mathbb{P}_\gamma^m : (\mathbb{C}_\gamma - \mathbb{C}_m)]^{-1} : \mathbf{E}^{\boldsymbol{\infty}} \,, \tag{A.7}$$

where $\mathbb{P}_\gamma^m$ is the fourth-order Hill tensor characterizing the interaction between the inclusion and the infinite matrix. Integral and closed-from solutions for $\mathbb{P}_\gamma^m$ are available for a number of inclusion shapes and symmetries of the elasticity tensor. $\mathbb{P}_\gamma^m$ can be written in the following form:

$$\mathbb{P}_\gamma^m = \mathbb{S}_\gamma^m : \mathbb{C}_m^{-1} \,, \tag{A.8}$$

where $\mathbb{S}_\gamma^m$ - is the Eshelby tensor of phase γ, which depends on $\mathbb{C}_m$, the geometry and the orientation of phase γ. For the phase, chosen to be matrix with respect to the others phases $\mathbb{C}_\gamma = \mathbb{C}_m$ and (

$$\boldsymbol{\varepsilon_\mathbf{m}} = \mathbf{E}^{\boldsymbol{\infty}} \,. \tag{A.9}$$

The strains $\mathbf{E}^{\boldsymbol{\infty}}$, prescribed at infinity of the matrix surrounding a single phase, must be related appropriately to the macroscopic strains $\mathbf{E}$, imposed as uniform boundary condition onto the RVE.
If the phases are sufficiently far apart from each other (dilute concentration), $\mathbf{E}^{\boldsymbol{\infty}}$ can be approximated as

$$\mathbf{E}^{\boldsymbol{\infty}} = \mathbf{E} \,. \tag{A.10}$$

Using (

$$\mathbb{A}_\gamma^{(D)} = [\mathbb{I} + \mathbb{P}_\gamma^m : (\mathbb{C}_\gamma - \mathbb{C}_m)]^{-1} \,. \tag{A.11}$$

Inserting (
In the case of the non-dilute concentration of the phases the interactions have to be considered. The simplest consideration of the phases

interactions is to define the fictitious remote strain $\mathbf{E}^{\infty}$ such that the strain average rule (

$$\mathbf{E} =< [\mathbb{I} + \mathbb{P}^m_\gamma : (\mathbb{C}_\gamma - \mathbb{C}_m)]^{-1} >_V : \mathbf{E}^{\infty} \, . \tag{A.12}$$

Back-substitution of (

$$\mathbb{A}^{(MT)}_\gamma = [\mathbb{I} + \mathbb{P}^m_\gamma : (\mathbb{C}_\gamma - \mathbb{C}_m)]^{-1} :< [\mathbb{I} + \mathbb{P}^m_\alpha : (\mathbb{C}_\alpha - \mathbb{C}_m)]^{-1} >^{-1}_V \, . \tag{A.13}$$

Insertion of (
For the Self-Consistent (SC) scheme the reference medium is chosen to be homogenized, i.e. $\mathbb{C}_m \equiv \mathbb{C}_{\rm hom}$. This leads to the self-consistent formulation of localization tensor:

$$\mathbb{A}^{(SC)}_\gamma = [\mathbb{I} + \mathbb{P}^{hom}_\gamma : (\mathbb{C}_\gamma - \mathbb{C}_{hom})]^{-1} :< [\mathbb{I} + \mathbb{P}^{hom}_\alpha : (\mathbb{C}_\alpha - \mathbb{C}_{hom})]^{-1} >^{-1}_V \, . \tag{A.14}$$

Using (
The most common case is to consider phases to be isotropic and inclusions to be spherical. The first assumption leads to

$$\begin{aligned} \mathbb{C}_\gamma &= 3K_\gamma \mathbb{J} + 2G_\gamma \mathbb{K} \\ \mathbb{C}_{\rm hom} &= 3K_{\rm hom} \mathbb{J} + 2G_{\rm hom} \mathbb{K} \end{aligned} \tag{A.15}$$

where K_γ, G_γ are bulk and shear moduli of the phase γ. $J_{ijkl} = \frac{1}{3}\delta_{ij}\delta_{kl}$, $\mathbb{K} = \mathbb{I} - \mathbb{J}$. The second assumption of spherical inclusion implies the following form of the Eshelby tensor $\mathbb{S}^m_\gamma$:

$$\mathbb{S}^m_\gamma = \alpha_m \mathbb{J} + \beta_m \mathbb{K} \, , \tag{A.16}$$

where

$$\alpha_m = \frac{3K_m}{3K_m + 4G_m} \, , \beta_m = \frac{6(K_m + 2G_m)}{5(3K_m + 4G_m)} \, , \tag{A.17}$$

where K_m, G_m are bulk and shear moduli of the reference medium. Substituting (

$$K_{hom} = \sum_\gamma f_\gamma K_\gamma [1 + \frac{\alpha_m}{K_m}(K_\gamma - K_m)]^{-1} < [1 + \frac{\alpha_m}{K_m}(K_\alpha - K_m)]^{-1} >^{-1}_V \tag{A.18a}$$

$$G_{hom} = \sum_\gamma f_\gamma G_\gamma [1 + \frac{\beta_m}{G_m}(G_\gamma - G_m)]^{-1} < [1 + \frac{\beta_m}{G_m}(G_\alpha - G_m)]^{-1} >^{-1}_V \tag{A.18b}$$

In case of Mori-Tanaka homogenization, K_m and G_m are known in advance and are chosen to be the properties of one of the phases. Whereas for the Self-Consistent scheme, $K_m \equiv K_{hom}$ and $G_m \equiv G_{hom}$, this lead to the solution of system of two nonlinear equations:

$$K_{hom} = \sum_r f_\gamma K_\gamma [1 + \frac{\alpha_{hom}}{K_{hom}}(K_\gamma - K_{hom})]^{-1} < [1 + \frac{\alpha_{hom}}{K_{hom}}(K_\alpha - K_{hom})]^{-1} \quad \forall \quad \text{(A.19a)}$$

$$G_{hom} = \sum_r f_\gamma G_\gamma [1 + \frac{\beta_{hom}}{G_{hom}}(G_\gamma - G_{hom})]^{-1} < [1 + \frac{\beta_{hom}}{G_{hom}}(G_\alpha - G_{hom})]^{-1} \quad \forall \quad \text{(A.19b)}$$

For material, consisting of two phases, close form solution of Eq. (is available.

A.3.2 Mean field strength homogenization

A.3.2.1 Formulation

The goal is to obtain a macroscopic strength domain of a heterogeneous material knowing microscopic strength domains of each phase in the material and certain information on the microstructure. The presented description follows (Dormieux et al. 2006).
Limit analysis aims to find the maximum load $\boldsymbol{\Sigma}$, which corresponds to the plastic collapse of the heterogeneous material, that is a state at which an ability to dissipate applied load is exhausted. The behavior of each phase at plastic collapse is assumed to follow the principle of maximum dissipation:

$$\boldsymbol{\sigma} = \frac{\partial \pi_\gamma(\mathbf{d})}{\partial \mathbf{d}} \,, \tag{A.20}$$

where $\mathbf{d}$ is strain rate and π_γ is the maximum dissipation capacity (support function) of phase γ:

$$\pi_\gamma = \sup_{\boldsymbol{\sigma}^* \in G_\gamma} \boldsymbol{\sigma}^* : \mathbf{d} \,. \tag{A.21}$$

The strength domain of each phase G_γ is considered to be convex. The *RVE* of the considered microstructure is then loaded by a homogeneous

strain rate, which is described by the following system of equations:

$$\begin{aligned}
\boldsymbol{\nabla}\cdot\boldsymbol{\sigma} &= \mathbf{0} && \text{in } V && \text{(A.22a)}\\
\boldsymbol{\sigma} &= \tfrac{\partial \pi_\gamma(\mathbf{d})}{\partial \mathbf{d}} && \text{in } V_\gamma && \text{(A.22b)}\\
\mathbf{d} &= \tfrac{1}{2}(\boldsymbol{\nabla}\boldsymbol{v} + \boldsymbol{v}\boldsymbol{\nabla}) && \text{in } V && \text{(A.22c)}\\
\boldsymbol{v} &= \mathbf{D}\cdot\boldsymbol{x} && \text{on } \partial V && \text{(A.22d)}
\end{aligned}$$

From the convexity of strength domains G_γ, the maximum dissipation capacity of the system reads:

$$\Pi^{hom}(\mathbf{D}) \equiv \sup_{\boldsymbol{\Sigma}\in G^{hom}} \boldsymbol{\Sigma}:\mathbf{D} = \inf_{\mathbf{d}\in K(\mathbf{D})} \pi(\mathbf{d}(\boldsymbol{v}),\boldsymbol{x})\,, \tag{A.23}$$

where

$$K(\mathbf{D}) = \{\boldsymbol{v}(\boldsymbol{x}) \;\mid\; \boldsymbol{v}(\boldsymbol{x}) = \mathbf{D}\cdot\boldsymbol{x} \quad on \;\; \partial V\} \tag{A.24}$$

is the set of kinematically admissible strain rate. The relationship between macroscopic stress at plastic collapse, $\boldsymbol{\Sigma}$, and the macroscopic strain rate, $\mathbf{D}$, is

$$\boldsymbol{\Sigma} = \frac{\partial \Pi^{hom}}{\partial \mathbf{D}}\,. \tag{A.25}$$

A.3.2.2 Effective Strain Rate approach

The aim is to estimate the solution of the system Eq. (. Mean field elastic linear homogenization theories cannot be applied straight away due to nonlinearity of the Eq. (. There are different ways of approaching this problem. One of them is to introduce the Effective Strain Rate into Eq. ((Dormieux et al. 2006, Carioua, et al. 2008). Assuming that the maximum dissipation capacity of a phase depends only on the first and second invariants of strain yields:

$$\pi_\gamma(\mathbf{d}) = \pi_\gamma(I_1', J_2')\,, \tag{A.26}$$

with

$$\begin{aligned}
\mathbf{d} &= \frac{1}{3} I_1' \mathbf{I} + \boldsymbol{\delta} && \text{(A.27a)}\\
I_1' &= \mathrm{tr}(\mathbf{d}) && \text{(A.27b)}\\
J_2' &= \frac{1}{2}\boldsymbol{\delta}:\boldsymbol{\delta} && \text{(A.27c)}\\
& && \text{(A.27d)}
\end{aligned}$$

Eq. (leads to:

$$\boldsymbol{\sigma} = \frac{\partial \pi_\gamma}{\partial I_1'}\mathbf{I} + \frac{\partial \pi_\gamma}{\partial J_2'}\boldsymbol{\delta} \equiv \mathbb{C}^\gamma : \mathbf{d} \tag{A.28}$$

with

$$k^\gamma = \frac{1}{I_1'}\frac{\partial \pi_i}{\partial I_1'} \tag{A.29a}$$

$$2\mu^\gamma = \frac{\partial \pi_i}{\partial J_2'} \tag{A.29b}$$

$$\tag{A.29c}$$

The last equation clearly shows the nonlinearity in the 'secant' stiffness tensor which is overcome by introducing the effective strain rate:

$$\boldsymbol{\sigma} = \mathbb{C}^\gamma(\boldsymbol{x}) : \mathbf{d} \approx \mathbb{C}^\gamma_{appr}(\mathbf{d}^\gamma) : \mathbf{d}\,, \tag{A.30}$$

where $\mathbf{d}^\gamma$ is a suitably chosen strain rate measure for phase γ. The simplest choice is an average (first moment) of the strain rate over phase γ:

$$\mathbf{d}^\gamma = \overline{\mathbf{d}(\boldsymbol{x})}^\gamma\,. \tag{A.31}$$

Second-order moments proved to be a much better choice for the strength homogenization:

$$\sqrt{J_2'^r} = \sqrt{\frac{1}{2}\overline{\boldsymbol{\delta} : \boldsymbol{\delta}}^\gamma}\,. \tag{A.32}$$

Thus, the following steps are part of the effective strain rate secant homogenization technique:

(a) Eq. (reduces the originally nonlinear problem to the standard problem of heterogeneous elasticity, thus all the machinery of Eshelby homogenization is applicable.

(b) It is necessary to choose a reference strain rate, $\mathbf{d}^\mathbf{r}$, to be used in the linearization and then develop it as a function of macro strain rate $\mathbf{d}^\gamma = \mathbf{d}^\gamma(\mathbf{D})$. This is done in the framework of linear elasticity.

(c) Solving the nonlinearity of the problem: $\boldsymbol{\Sigma} = \mathbb{C}^{hom}(\mathbf{D}) : \mathbf{D}$ is the final step.

A.3.2.3 Second-order momentum for a reference strain rate

As mentioned before, the second order moment are better choices as reference strain rates. Let us now develop this estimation for phase γ,

present in microstructure. By definition:

$$d_d^\gamma = \sqrt{\overline{\boldsymbol{\delta} : \boldsymbol{\delta}}^\gamma} \tag{A.33}$$

$$d_v^\gamma = \sqrt{\overline{d_v^2}^\gamma}\,, \tag{A.34}$$

where $d_v = \mathrm{tr}(\mathbf{d})$. The macroscopic strain rate energy density is

$$W = \frac{1}{2}\mathbf{D} : \mathbb{C}^{hom} : \mathbf{D} \tag{A.35}$$

Assuming isotropic elastic material, it is expressed as

$$W = \frac{1}{2}K^{hom}D_v^2 + G^{hom}\boldsymbol{\Delta} : \boldsymbol{\Delta}\,. \tag{A.36}$$

Similarly, the strain rate energy density of phase γ reads

$$w_\alpha = f_\alpha(\frac{1}{2}k^\alpha d_v^2 + g^\alpha \boldsymbol{\delta} : \boldsymbol{\delta})\,, \tag{A.37}$$

where f_α is volume fraction of phase α. It is obvious that

$$W = \sum_\alpha w_\alpha\,. \tag{A.38}$$

Now, let us develop the derivatives of Eq. (with respect to k^γ and g^γ considering that the local strain rate field of phase α is a function of k^α and g^α:

$$\frac{1}{2}\frac{\partial K^{hom}}{\partial g^\gamma}D_v^2 + \frac{\partial G^{hom}}{\partial g^\gamma}\boldsymbol{\Delta} : \boldsymbol{\Delta} = f_\gamma\left(\overline{\boldsymbol{\delta} : \boldsymbol{\delta}}^\gamma + \overline{\boldsymbol{\sigma} : \frac{\partial \mathbf{d}}{\partial g^\gamma}}^\gamma\right) \tag{A.39a}$$

$$\frac{1}{2}\frac{\partial K^{hom}}{\partial k^\gamma}D_v^2 + \frac{\partial G^{hom}}{\partial k^\gamma}\boldsymbol{\Delta} : \boldsymbol{\Delta} = f_\gamma\left(\overline{d_v^2}^\gamma + \overline{\boldsymbol{\sigma} : \frac{\partial \mathbf{d}}{\partial k^\gamma}}^\gamma\right) \tag{A.39b}$$

The first terms after the equality signs are exactly squares of second-order moments (Eq. (, Eq. ()), and the last terms equal zero. So, these equations can be rewritten as

$$\frac{1}{2}\frac{\partial K^{hom}}{\partial g^\gamma}D_v^2 + \frac{\partial G^{hom}}{\partial g^\gamma}\boldsymbol{\Delta} : \boldsymbol{\Delta} = f_\gamma(d_d^\gamma)^2 \tag{A.40a}$$

$$\frac{1}{2}\frac{\partial K^{hom}}{\partial k^\gamma}D_v^2 + \frac{\partial G^{hom}}{\partial k^\gamma}\boldsymbol{\Delta} : \boldsymbol{\Delta} = f_\gamma(d_v^\gamma)^2\,. \tag{A.40b}$$

A.3.2.4 Perfectly Brittle Behavior

Considering each phase to be perfectly brittle, previously obtained results can be used to approximate the yield limit of the composite by the stress level, at which at least one phase reaches its yield surface. Eq. (are (second-order) estimations of strain rate in each phase and therefore can be directly used in yield functions of each phase to find when the yielding will start. Let us show it on the example of $J2$ plasticity.

The quadratic deviatoric stress average σ_d^γ is defined by analogy to Eq. (and is related to d_d^γ by $\sigma_d^\gamma = 2g^\gamma d_d^\gamma$. Using Eq. (this leads to:

$$\sigma_d^\gamma = \frac{2\ g_\gamma}{\sqrt{f_\gamma}} \left[\frac{1}{2} \frac{\partial K^{hom}}{\partial g^\gamma} (D_v)^2 + \frac{\partial G^{hom}}{\partial g^\gamma} \boldsymbol{\Delta} : \boldsymbol{\Delta} \right]^{\frac{1}{2}} . \tag{A.41}$$

Now, let us consider that RVE is subjected to uniaxial tension $\boldsymbol{\Sigma} = -\Sigma_{11} e_1 e_1$ where e_i are the base vectors. $\Sigma_v = -\Sigma_{11}$ and $\Sigma_d = \sqrt{2/3}\Sigma_{11}$. The macroscopic stresses and strains are related by

$$\Sigma_v = 3K^{hom} E_v \tag{A.42a}$$
$$\Sigma_d = 2G^{hom} E_d \,. \tag{A.42b}$$

Eq. (holds both for strain rate $\mathbf{D}$ and $\mathbf{E}$, therefore using Eq. (in it leads to:

$$\sigma_d^\gamma = \frac{2\ g_\gamma}{\sqrt{f_\gamma}} \left[\frac{1}{2} \frac{\partial K^{hom}}{\partial g^\gamma} (\frac{1}{3K^{hom}})^2 \Sigma_{11}^2 + \frac{2}{3} \frac{\partial G^{hom}}{\partial g^\gamma} (\frac{1}{2G^{hom}})^2 \Sigma_{11}^2 \right]^{\frac{1}{2}} , \tag{A.43}$$

which can be rewritten as:

$$\sigma_d^\gamma = \Sigma_{11} \frac{2\ g_\gamma}{\sqrt{f_\gamma}} \left(-\frac{1}{18} \frac{\partial 1/K^{hom}}{\partial g^\gamma} - \frac{\partial 1/G^{hom}}{\partial g^\gamma} \frac{1}{6} \right)^{\frac{1}{2}} . \tag{A.44}$$

The obtained equation can be directly used in J_2 yield limit function for each phase γ in order to calculate the critical load Σ_{11}^γ at which yield limit is reached. Thus, using perfect brittle assumption, the strength at the level of RVE is

$$\Sigma = \min(\Sigma_{11}^\gamma) \tag{A.45}$$

This approach was used in (Pichler et al. 2008) for prediction of cement paste strength from volume fractions of its constituents.

A.3.2.5 LCC Homogenization method

The limitation of the Effective Strain Rate approach is the necessity of choosing the particular averaging measure. In order to overcome it, the concept of Linear Comparison Composite (LCC) was introduced (Castaneda 1996, Castaneda 2002). The principle is similar: approximation of a non-linear behavior by a linear one, but the main difference is that parameters of the linear behavior are fictitious and are variables of the problem. These parameters are then suitably chosen in order to find the lowest upper bound of the dissipation energy of a homogeneous material. In our description of this method, we will follow (Vandamme & Ulm 2008).

Let us consider a fictitious comparison composite in which the behavior of each phase is given by

$$\boldsymbol{\sigma} = \mathbb{C}_\gamma : \mathbf{d} + \boldsymbol{\tau_\gamma} \,. \tag{A.46}$$

The strain rate energy of such composite material

$$w_0(\boldsymbol{x}, \mathbf{d}) = \sum_\gamma \chi_\gamma(\boldsymbol{x}) w_\gamma(\mathbf{d}) \tag{A.47a}$$

$$w_\gamma(\mathbf{d}) = \frac{1}{2}\mathbf{d} : \mathbb{C}_\gamma : \mathbf{d} + \tau_\gamma : \mathbf{d} \,, \tag{A.47b}$$

where $\chi_\gamma(\boldsymbol{x})$ are indicator functions, such that $\chi_\gamma(\boldsymbol{x}) = 1$ if $\boldsymbol{x}$ is in phase i, and 0 otherwise. Considering $w_0 = \pi + w_0 - \pi$, the following estimate can be obtained

$$\inf_{\boldsymbol{v}\in K(\mathbf{D})} \overline{w_0(\boldsymbol{x}, \mathbf{d}(\boldsymbol{v}))} \geq \inf_{\boldsymbol{v}\in K(\mathbf{D})} \overline{\pi(\boldsymbol{x}, \mathbf{d}(\boldsymbol{v}))} + \inf_{\boldsymbol{v}\in K(\mathbf{D})} \overline{w_0(\boldsymbol{x}, \mathbf{d}(\boldsymbol{v})) - \pi(\boldsymbol{x}, \mathbf{d}(\boldsymbol{v}))}. \tag{A.48}$$

The first term is the macroscopic strain rate energy $W_0(\mathbf{D})$ of the LCC:

$$W_0(\mathbf{D}) = \inf_{\boldsymbol{v}\in K(\mathbf{D})} \overline{w_0(\boldsymbol{x}, \mathbf{d}(\boldsymbol{v}))} \,. \tag{A.49}$$

The second is $\Pi^{hom}(\mathbf{D})$ and the last one, multiplied by -1, can be overestimated by:

$$\begin{aligned} &- \inf_{\boldsymbol{v}\in K(\mathbf{D})} \overline{w_0(\boldsymbol{x}, \mathbf{d}(\boldsymbol{v})) - \pi(\boldsymbol{x}, \mathbf{d}(\boldsymbol{v}))} = \\ &\sup_{\boldsymbol{v}\in K(\mathbf{D})} \overline{\pi(\boldsymbol{x}, \mathbf{d}(\boldsymbol{v})) - w_0(\boldsymbol{x}, \mathbf{d}(\boldsymbol{v}))} \leq \sum_\gamma f_\gamma \nu_\gamma \,, \end{aligned} \tag{A.50}$$

where

$$\nu_\gamma = -\sup_{\mathbf{d}} \overline{\pi(\mathbf{d}) - w_\gamma(\mathbf{d})} \tag{A.51}$$

is a constant in each phase of the volume fraction f_γ. As a result, the following upper bound for Π^{hom} is obtained:

$$\Pi^{hom}(\mathbf{D}) \leq W_0(\mathbf{D}) + \sum_\gamma f_\gamma \nu_\gamma \,. \tag{A.52}$$

Our aim is to find the elastic parameters of a fictitious LCC that will lead to the lowest possible estimate of Π^{hom}, that is infimum of the right hand side of Eq. (. Since infimum and supremum can be replaced by stationary points, this new estimate is

$$\widetilde{\Pi^{hom}}(\mathbf{D}) = \mathrm{stat}_{\mathbb{C}_\gamma,\tau_\gamma}\left(W_0(\mathbf{D}) + \sum_\gamma f_\gamma \nu_\gamma\right) \tag{A.53}$$

$$\nu_\gamma = \mathrm{stat}_{\mathbf{d}}\left(\pi(\mathbf{d}) - w_\gamma(\mathbf{d})\right) \tag{A.54}$$

Thus, the main steps in the LCC homogenization method are:

(a) From linear micromechanics, compute the macroscopic strain rate energy $W_0(\mathbf{D})$.

(b) For each phase, compute ν_i.

(c) Find stationary points of Eq. (and Eq. ((solve for $\mathbb{C}_i$ and τ_i). As a result, obtain the estimate of Π^{hom}.

Application of th LCC to a matrix-pore composite with Drucker-Prager yield surface leads to (Vandamme & Ulm 2008):

$$\left(\frac{\sigma_m - \Sigma_0^{hom}}{A^{hom}}\right)^2 + \left(\frac{\sigma_d}{\sqrt{2}B^{hom}}\right)^2 = 1 \tag{A.55}$$

with

$$\left(\frac{A^{hom}}{c_s}\right)^2 = \frac{\eta^2\mathcal{K}(\eta - \alpha_s^2\mathcal{K})}{(\eta - 2\alpha_s^2\mathcal{K})^2} \tag{A.56a}$$

$$\left(\frac{B^{hom}}{c_s}\right)^2 = \frac{\eta\mathcal{M}(\eta - \alpha_s^2\mathcal{K})}{\eta - 2\alpha_s^2\mathcal{K}} \tag{A.56b}$$

$$\frac{\Sigma_0^{hom}}{c_s} = -\frac{\eta\alpha_s\mathcal{K}}{\eta - 2\alpha_s^2\mathcal{K}} \tag{A.56c}$$

Depending on the sign of $\eta - 2\alpha_s^2\mathcal{K}$, the yield surface will be hyperbolic, parabolic or ellipsoidal:

$$\eta - 2\alpha_s^2\mathcal{K}(\frac{k_s}{g_s} = \frac{1}{\alpha_s^2}) \begin{cases} < 0 & \text{Elliptic Criterion} \\ = 0 & \text{Limit Parabola} \\ > 0 & \text{Hyperbolic Criterion} \end{cases} \tag{A.57}$$

where $\mathcal{K} = \mathcal{K}(\frac{1}{\alpha_s^2}, \eta)$ and $\mathcal{M} = \mathcal{M}(\frac{1}{\alpha_s^2}, \eta)$ are dimensionless functions from the solution of elastic homogenization problem Eq. (in case of solid-pore composite with solid properties k_s and g_s:

$$K^{hom} = g_s \mathcal{K}(\frac{k_s}{g_s}, \eta) \tag{A.58a}$$

$$G^{hom} = g_s \mathcal{M}(\frac{k_s}{g_s}, \eta) \tag{A.58b}$$

The following properties of the C-S-H building block were considered (Vandamme & Ulm 2008): $\alpha_s = 0.207$, $c_s = 0.392$; Porosity of $LD-$C-S-H was set to 0.31, which together with used α_s and c_s yields(Vandamme & Ulm 2008) indentation hardness $H = 0.5945GPa$, the latter is negligibly different from the one, considered before $H = 0.60$ for $J2$ plasticity and thus models are comparable. In (Jennings et al. 2007), $LD-$C-S-H porosity was reported to be 0.36, therefore our choice of this parameter is also meaningful. Homogenized plastic parameters are: $\left(A^{hom}/c_s\right)^2 = 1.0113$, $\left(B^{hom}/c_s\right)^2 = 0.3144$, $\left(\Sigma_0^{hom}/c_s\right) = -0.2799$. Comparison of used $J2$ and elliptical yield surfaces is present in Fig.

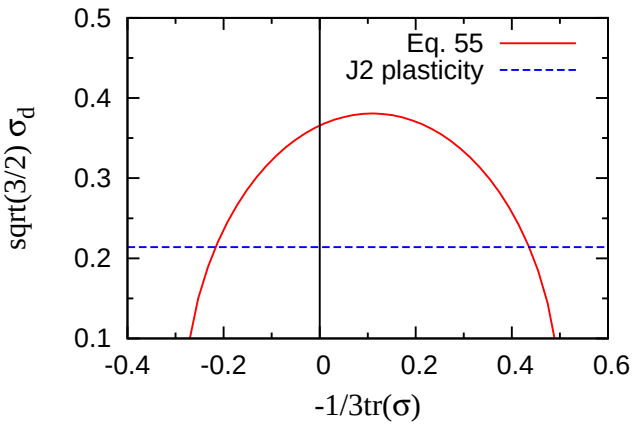

Figure 3: Comparison of the considered yield surfaces for C-S-H.

A.3.3 Fast Fourier Transform Homogenization method

A.3.3.1 Formulation

In this Section, the FFT algorithm for homogenization proposed in (Moulinec & Suquet 1998) is briefly summarized. This method is proposed in order to obtain local and overall responses of nonlinear composites. It is generally directly applied to 2D or 3D microstructures obtained from experimental techniques such as SEM/BSE images, 3D tomography, TEM and others. A general approach to incorporate detailed information on the microstructure (not just volume fractions) is to mesh it and calculate its response to particular loading using FEM. However, serious difficulties arise from meshing. The FFT method avoids difficulties due to meshing and can be used even in the case of nonlinear phase behavior. As an input it requires data sampled in a grid of regular spacing, which is the usual output of all digital image methods. FFT also does not require the formation of the tangent stiffness matrix and therefore consumes less memory and can be used for finer discretization.

Let us consider a RVE of an arbitrary complex heterogeneous medium composed of linear elastic phases. Extension to nonlinear behavior will be discussed later. We then consider periodic boundary conditions. The local strain field $\boldsymbol{\epsilon}(\boldsymbol{u}(\boldsymbol{x}))$ is split into its average $\mathbf{E}$ and fluctuation term $\boldsymbol{\epsilon}(\boldsymbol{u}^*(\boldsymbol{x}))$:

$$\boldsymbol{\epsilon}(\boldsymbol{u}(\boldsymbol{x})) = \boldsymbol{\epsilon}(\boldsymbol{u}^*(\boldsymbol{x})) + \mathbf{E} \tag{A.59}$$

or equivalently

$$\boldsymbol{u}(\boldsymbol{x}) = \boldsymbol{u}^*(\boldsymbol{x}) + \mathbf{E} \cdot \boldsymbol{x} \tag{A.60}$$

Periodic boundary conditions require the fluctuation term $\boldsymbol{u}^*$ to be periodic ($\boldsymbol{u}^* \sharp$) and traction $\boldsymbol{\sigma} \cdot \boldsymbol{x}$ to be anti-periodic ($\boldsymbol{\sigma} \cdot \boldsymbol{x} - \sharp$).

Before solving the heterogeneous problem, let us consider a homogeneous linear elastic medium with stiffness $\mathbb{C}$ subjected to a polarization field $\boldsymbol{\tau}(\boldsymbol{x})$:

$$\left\{ \begin{array}{lcll} \boldsymbol{\sigma}(\boldsymbol{x}) & = & \mathbb{C}^0 : \boldsymbol{\epsilon}(\boldsymbol{u}^*(\boldsymbol{x})) + \boldsymbol{\tau}(\boldsymbol{x}) & \forall \boldsymbol{x} \in V \\ \boldsymbol{\nabla} \cdot \boldsymbol{\sigma}(\boldsymbol{x}) & = & \mathbf{0} & \forall \boldsymbol{x} \in V \end{array} \right. \tag{A.61}$$

The solution of Eq. (can be expressed in real and Fourier spaces, respectively, by means of the periodic Green operator $\mathbb{G}^0(\mathbb{C}^0)$:

$$\boldsymbol{\epsilon}(\boldsymbol{u}^*) = -\mathbb{G}^0 * \boldsymbol{\tau} \qquad \forall \boldsymbol{x} \in V \tag{A.62}$$

where $(f * g)(\boldsymbol{x}) \equiv \int_{R^3} f(\boldsymbol{y}) g(\boldsymbol{x} - \boldsymbol{y}) \mathrm{d}\boldsymbol{y}$, or, in Fourier space,

$$\hat{\boldsymbol{\epsilon}}^*(\boldsymbol{\xi}) = -\hat{\mathbb{G}^0} : \hat{\boldsymbol{\tau}}(\boldsymbol{\xi}) \qquad \forall \boldsymbol{\xi} \neq 0, \qquad \hat{\boldsymbol{\epsilon}}^*(0) = 0 \tag{A.63}$$

Operator $\mathbb{G}^0$ is explicitly known in Fourier space, and when the reference material is isotropic (with Lame coefficients λ^0 and μ^0), it takes the form

$$\mathbb{G}^0_{ijkh}(\boldsymbol{\xi}) = \frac{1}{4\mu^0 \|\boldsymbol{\xi}\|^2}(\delta_{ki}\xi_h\xi_j+\delta_{hi}\xi_k\xi_j+\delta_{kj}\xi_h\xi_i+\delta_{hj}\xi_k\xi_i)-\frac{\lambda^0+\mu^0}{\mu^0(\lambda^0+2\mu^0)}\frac{\xi_i\xi_j\xi_k\xi_h}{\|\boldsymbol{\xi}\|^4} \tag{A.64}$$

Now, let us consider a heterogeneous elastic composite medium with the stiffness $\mathbb{C}(\boldsymbol{x})$ and macroscopic strain $\mathbf{E}$:

$$\begin{cases} \boldsymbol{\sigma}(\boldsymbol{x}) = \mathbb{C}(\boldsymbol{x}) : (\boldsymbol{\epsilon}(\boldsymbol{u}^*(\boldsymbol{x})) + \mathbf{E}) & \forall \boldsymbol{x} \in V \\ \boldsymbol{\nabla} \cdot \boldsymbol{\sigma}(\boldsymbol{x}) = 0 & \forall \boldsymbol{x} \in V \end{cases} \tag{A.65}$$

For now, we will consider $\mathbf{E}$ to be prescribed, however boundary conditions with prescribed stress can be considered as well. Let us introduce a reference homogeneous elastic material with $\mathbb{C}^0$ and polarization stress $\boldsymbol{\tau}(\boldsymbol{x})$, defined as

$$\boldsymbol{\tau}(\boldsymbol{x}) = \left(\mathbb{C}(\boldsymbol{x}) - \mathbb{C}^0\right) : \boldsymbol{\epsilon}(\boldsymbol{u}(\boldsymbol{x})) \tag{A.66}$$

Using this definition, Eq. (can be rewritten as

$$\begin{cases} \boldsymbol{\sigma}(\boldsymbol{x}) = \mathbb{C}^0 : \boldsymbol{\epsilon}(\boldsymbol{u}^*(\boldsymbol{x})) + \boldsymbol{\tau}(\boldsymbol{x}) + \mathbb{C}^0 : \mathbf{E} & \forall \boldsymbol{x} \in V \\ \boldsymbol{\nabla} \cdot \boldsymbol{\sigma}(\boldsymbol{x}) = 0 & \forall \boldsymbol{x} \in V \end{cases} \tag{A.67}$$

Comparing the obtained formulation with the auxiliary problem Eq. (, we notice that the definition of the stress differs in a constant term, yet this term obviously will not affect the solution of the equilibrium equation $\boldsymbol{\nabla} \cdot \boldsymbol{\sigma} = 0$ and so both problems have the same solution. Therefore, the solution of Eq. (reads

$$\boldsymbol{\epsilon} = -\mathbb{G}^0 * \boldsymbol{\tau} + \boldsymbol{\Sigma} \tag{A.68}$$

or, in Fourier space,

$$\hat{\boldsymbol{\epsilon}}(\boldsymbol{\xi}) = -\hat{\mathbb{G}^0}(\boldsymbol{\xi}) : \hat{\boldsymbol{\tau}}(\boldsymbol{\xi}) \quad \forall \boldsymbol{\xi} \neq 0, \qquad \hat{\boldsymbol{\epsilon}}(0) = \mathbf{E} \tag{A.69}$$

A.3.4 Algorithm

Before developing Eq. (into an algorithm, let us note that $\mathbb{G}^0 * (\mathbb{C}^0 : \boldsymbol{\epsilon}) = \boldsymbol{\epsilon}$. Thus, the algorithm reads:

(a) Initialize: $\boldsymbol{\epsilon}^0(x) = \mathbf{E}$, $\boldsymbol{\sigma}^0(x) = \mathbb{C} : \boldsymbol{\epsilon}^0(x)$.

(b) Compute (discrete) Fourier transform of stresses $\hat{\boldsymbol{\sigma}}$.

(c) Check equilibrium conditions in Fourier space.

(d) Update strain in Fourier space: $\hat{\boldsymbol{\epsilon}}(\boldsymbol{\xi}) - = \hat{\mathbb{G}^0}(\boldsymbol{\xi}) : \hat{\boldsymbol{\sigma}}(\boldsymbol{\xi})$ and $\hat{\boldsymbol{\epsilon}}(\mathbf{0}) = \mathbf{E}$ (follows from Eq. (and Eq. ().

(e) Compute Inverse (discrete) Fourier transform of total strains $\boldsymbol{\epsilon}$.

(f) Update stresses from strains: $\boldsymbol{\sigma}(\boldsymbol{x}) = \mathbb{C}(\boldsymbol{x}) : \boldsymbol{\epsilon}(\boldsymbol{x})$.

Equilibrium conditions can be easily rewritten in Fourier space and therefore the error serving to check convergence is

$$e = \frac{\left(\overline{\|\boldsymbol{\xi} \cdot \hat{\boldsymbol{\sigma}}\|^2}\right)^{1/2}}{\|\hat{\boldsymbol{\sigma}}(0)\|} \tag{A.70}$$

Discrete representation of the problem naturally arises from the regular voxel input from tomography, BSE or cement hydration models. Therefore, all unknowns are sampled on that grid ($N_1 \times N_2 \times N_3$). This discretization can be used in discrete Fast Fourier Transform (DFFT) packages ((Frigo & Johnson 2005)). Corresponding frequencies in Fourier space read for even and odd cases of N_j, respectively:

$$\xi_j = (-\frac{N_j}{2}+1)\frac{1}{T_j}, (-\frac{N_j}{2}+2)\frac{1}{T_j}, \ldots, -\frac{1}{T_j}, 0, \frac{1}{T_j}, \ldots, (\frac{N_j}{2}-1)\frac{1}{T_j}, \frac{N_j}{2}\frac{1}{T_j} \tag{A.71}$$

$$\xi_j = -\frac{N_j - 1}{2}\frac{1}{T_j}, \ldots, -\frac{1}{T_j}, 0, \frac{1}{T_j}, \ldots, \frac{N_j}{2}\frac{1}{T_j} \tag{A.72}$$

where T_j is a period of the unit cell in $j-$th direction.

Any plastic or visco-plastic behavior can be considered as well. The main difference will be only in the last step of the algorithm: calculation of total stresses from total strain at the current iteration. Of course, one should keep track of all internal variables and update them after equilibrium is reached.

Applying DFFT, the following should be noted. The discrete Fourier transform is exact when the image cut-off frequency f^c (i.e. the frequency above which the Fourier transform of the image vanishes identically) is less than half of the sampling frequency (Shannon's theorem):

$$f_j^c < \frac{1}{2}\frac{N_j}{T_j} \tag{A.73}$$

This condition is not met in general (e.g. a discontinuous field does not have a cut-off frequency). However, an increase of image sampling leads to an increase of cut-off frequency, as expected, and therefore

the solution of the discrete problem approaches the solution of the continuous one.
FFT homogenization method was proven to give remarkably good results (J.C. Michel 1999). Prescribing stress boundary conditions may lead to big displacements in one step, therefore the direction is usually prescribed and the amplitude is considered to be unknown (J.C. Michel 1999):

$$\boldsymbol{\Sigma}(t) = k(t)\boldsymbol{\Sigma}^0 \tag{A.74}$$

requiring that

$$\boldsymbol{\Sigma}^0 : \mathbf{E}(t) = t \tag{A.75}$$

The choice of a reference medium (Lame constants for $\mathbb{G}$) is of great importance. A common approach is to use the mean value among all phases.
It is well known that FFT homogenization method does not converge when the contrast between the phases is infinite (void or rigid inclusions) or when the nonlinear behavior of phases results in very different stiffness matrices (J.C. Michel 1999). In order to overcome this, several modified schemes were introduced (J.C. Michel 2001): The first one is an accelerated scheme for composites with high contrasts (the rate of convergence is proportional to the square root of the contrast). The second scheme, adequate for composites with infinite contrast, is based on an augmented Lagrangian method. The resulting saddle-point problem involves three steps: 1) solving a linear elastic problem with FFT; 2) solving non-linear problem at each individual voxel; 3) updating Lagrange multipliers. Comparison of all schemes can be found in (H. Moulinec 2003).

A.3.5 Finite Element Method

The FEM was applied in a very straightforward and simple way. The voxel representation of the microstructure obtained from the hydration model or the X-ray photomicrography was directly discretized using 8 node linear brick elements. The model was then loaded with mixed boundary conditions - DOFs in the loaded direction were prescribed on the two opposite faces (0 at one side and a nonzero displacement on the other size). At one of the corner nodes at the first face, all DOFs were set to zero to avoid a rigid body motion. Remaining DOFs of the model were kept unconstrained.
Three types of analyses were performed: 1) Full nonlinear plastic analysis of the measured microstructure (NIST Cem) with a reduced size

computed in Abaqus and used as a benchmark solution for the comparison with the particle model, see Section
In all the analyses, material properties from Table

A.3.6 Particle model for cement paste

Particle models for simulation of the fracture propagation in concrete are based on the assumption that all the cracking and possibly other non-linear phenomena take place in the matrix phase, e.i. mortar in the case of concrete, between the particles, i.e. aggregates. This assumption allows significantly simplified formulations of kinematics compared to the classical FEA and volumes with a large number of particles can be modeled with a reasonable computational time and memory requirements. The assumptions made for concrete can be extended to the case of the cement paste since most of the plastic yielding and cracking takes place in hydrates and the unhydrated clinkers can be viewed as aggregates.
In the presented study, the model of Cusatis (Cusatis et al. 2003) was chosen as the base. The unhydrated clinkers were approximated by spherical particles conserving the volumes of clinkers and the positions of centers of gravity. Then the volume was tessellated according to the procedure described in (Cusatis et al. 2003, Cusatis et al. 2006, Cusatis & Cedolin 2007).
In contrary to the case of mortar or concrete where the matrix phase can be considered as a homogeneous material, the properties of the matrix phase, or rather of the interparticle volume, differ significantly for individual contacts in the cement paste microstructure. The increased heterogeneity of the material is the result of the hydration which is, in the terms of positioning of some hydration products, essentially a random process. Therefore, the simple averaging of the elastic stiffnesses along the struts as well as concept of one set of material properties used in the case of concrete have to be abandoned and every strut has to be treated separately.
After the discretization of the microstructure by the struts, the diameters of the particles were set to zero. The entire volume between two nodes was homogenize using the FFT and FEM for every strut (perfectly brittle assumption was used as a strength estimation in all cases). The SC was not used for the homogenization of the microstructure on the struts level since it assumes the RVE. However, the investigated internodal volumes were too small and heterogeneous to be considered as RVEs. The internodal volume was discretized by voxels aligned

with the orientation of the strut. The size of the voxels is $l/round(l/s)$ in longitudinal and $\sqrt{A}/round(\sqrt{A}/s)$ in transversal direction. l is length of the strut, s is the size of the edge of voxels in the original microstructure and A is the projected area of the contact discretized by the strut. The same phase as is the one of the voxels in which the center of gravity of the newly formed voxel is located is then assigned to the new voxel. Then the obtained volume is homogenized using the FFT or FEM and effective Young's modulus, Poisson's ratio, tensile (f_t), shear (f_s) and compressive (f_c) strengths of the internodal volumes were obtained and assigned to the strut discretizing the connection. Since the internodal volume was small (typically ≈ 100 voxels), it was assumed that the strength, based on perfectly brittle assumption should approximate reasonably well the yield limit of the strut. In cases where there were not any C-S-H voxels in the internodal volume, struts were assumed to be elastic without any strength limits. The comparison of the homogenization based on the FEM and FFT is shown in the following Section.

A.3.6.1 Comparison of FFT and FEM on the level of struts

Figures
Figures
The elastic properties predicted by the FFT and FEM homogenizations are consistent. However, the strength predicted by the FFT homogenization is systematically lower compared to the strength predicted by the FEM homogenization. Probably, this is induced by the fact, that each strut is an arbitrary microstructure, which is not periodic. Therefore, the computed DFFT is not equal to the FFT and thus the whole homogenization algorithm converges to slightly biased stress fields. The latter leads to bias in perfectly brittle strength estimate.
The effect of hydration is visible especially comparing plots for 1 day with plots for 28 days. For both cements as well as for both methods, Young's moduli show shift to larger values and the scatter is smaller due to decreasing volumes of stiff clinker and weak porosity and increasing volume of hydrates. The strength experiences a similar trend that is more pronounced for the FEM homogenization because of the aforementioned reasons.
Figure

A.3.6.2 Simulation of global response

The material model proposed in the original particle model (Cusatis et al. 2003) was utilized and modified. The material behaves elastically until the elastic boundary depending on the tensile, shear and compressive strength is reached. Then a nonlinear behavior occurs. In the presented implementation, the response was considered elasto-brittle for $\omega > \omega_0$, see (Cusatis et al. 2003) for explanations and Figure
The particle model with the FEM-based homogenization of the internodal volume and the Eq. (yield condition was used to simulate a uniaxial compression test on cubical microstructures cut from the NIST tomography data with size of edges equal to 60 μm (RVE_{60}). The microstructure was chosen in the way that it did not contain any large unhydrated grains that would bridge the entire microstructure, see Figure
Further, the particle model with the FEM-based homogenization of the internodal volume and the Eq. (and $J2$ yield conditions was used to study an effect of the size of the microstructure on the stress-strain response in uniaxial compression and tension, respectively. The brittle cracking of contact was considered. Two sizes of the microstructure were considered: the already introduced RVE_{60} and 150 μm microstructure, RVE_{150}. Comparison of the stress-strain curves for the two sizes is plotted in Figure

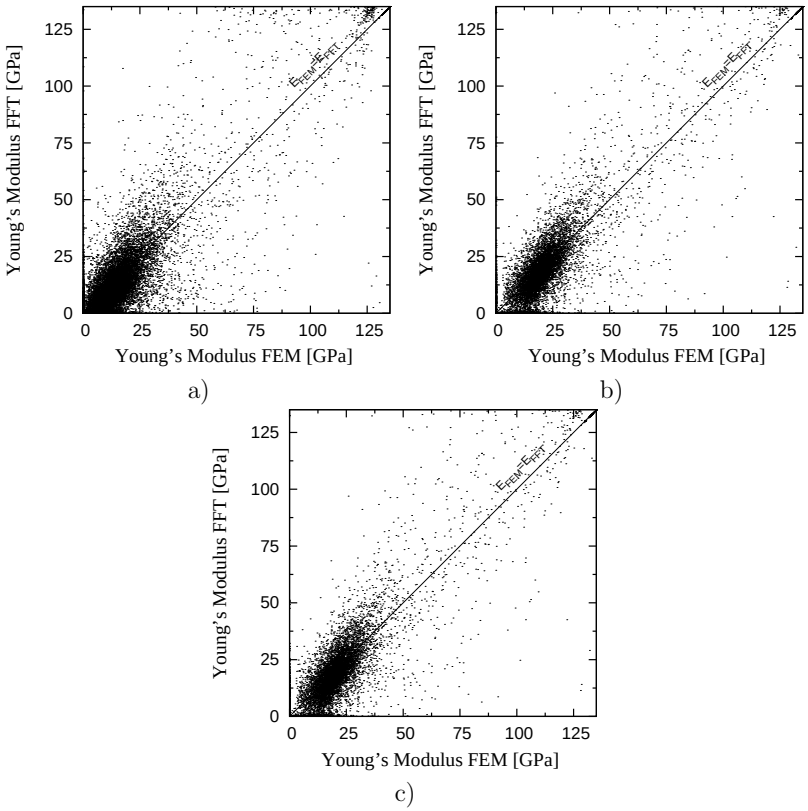

Figure 4: Comparison of the Young's moduli of the struts predicted by the FFT and FEM, respectively, for Cem A after 1, 7 and 28 days of hydration, respectively.

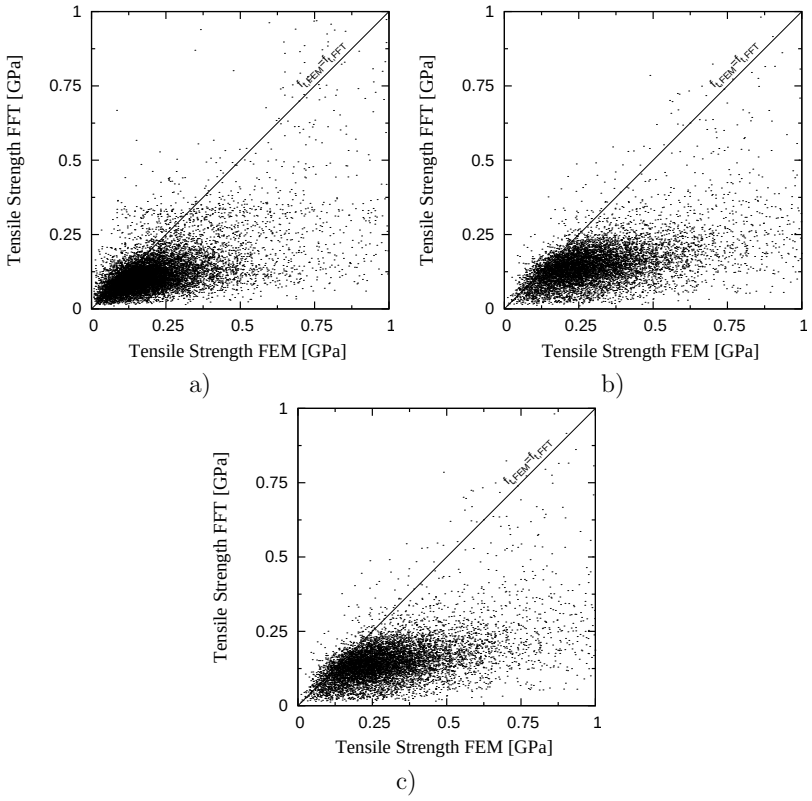

Figure 5: Comparison of the tensile strengths of the struts predicted by the FFT and FEM, respectively, for Cem A after 1, 7 and 28 days of hydration, respectively.

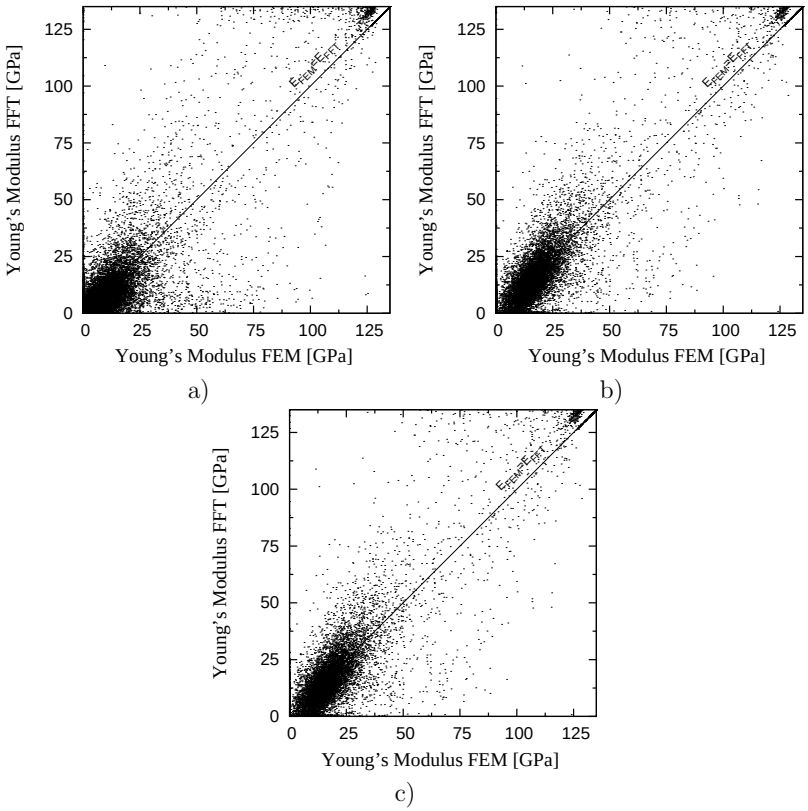

Figure 6: Comparison of the Young's moduli of the struts predicted by the FFT and FEM, respectively, for Cem C after 1, 7 and 28 days of hydration, respectively.

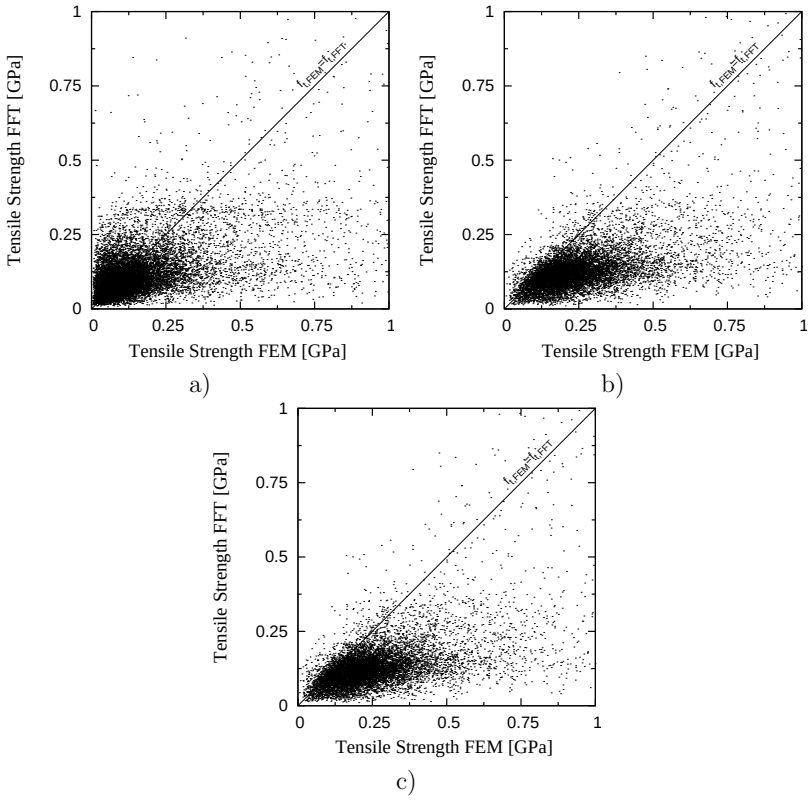

Figure 7: Comparison of the tensile strengths of the struts predicted by the FFT and FEM, respectively, for Cem C after 1, 7 and 28 days of hydration, respectively.

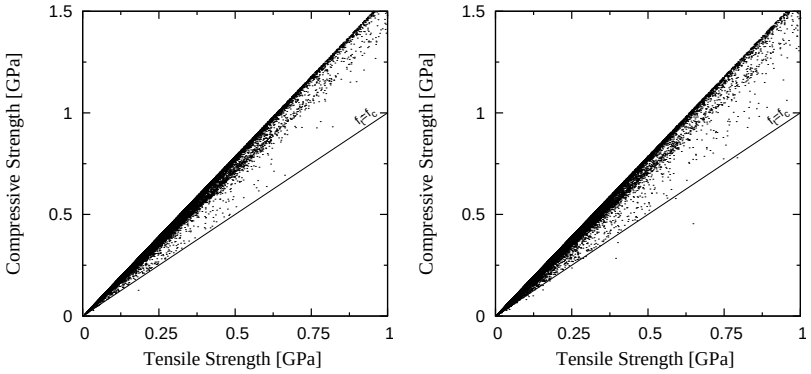

Figure 8: Comparison of tensile and compressive strengths of the struts for Cem A, a), and Cem C, b), considering the Eq. (yield criterion. $f_t = f_c$ for the $J2$ plasticity yield criterion.

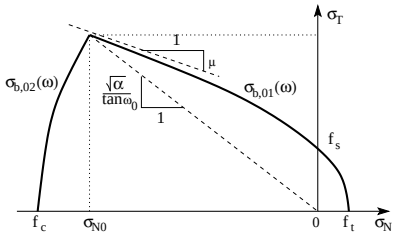

Figure 9: Material models of the struts: elastic domain. Brittle cracking occur when the domain is reached for $\omega > \omega_0$ and plastic yielding for $\omega < \omega_0$.

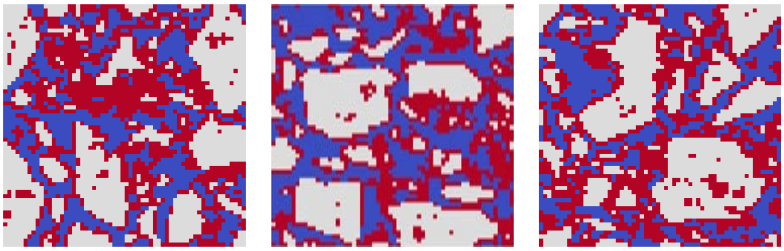

Figure 10: Microstructure of 60×60×60 μm used for initial comparison of the methods - three mutually orthogonal cut planes going through the center of the microstructure.

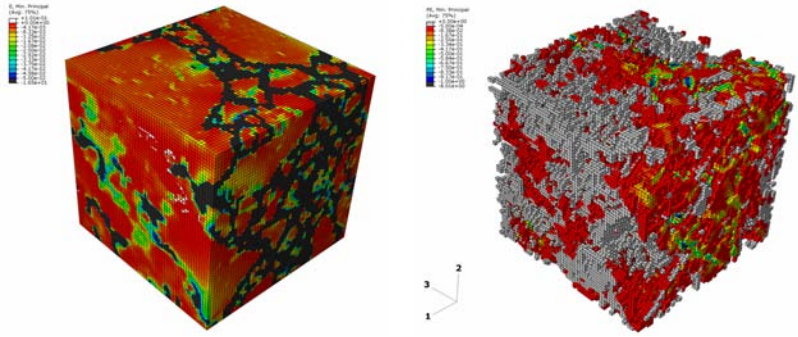

a) b)

Figure 11: Elastic stain in all phases, a), and plastic strain in C-S-H after the last step of the full non-linear FEM analysis in Abaqus for RVE_{60}. The microstructure was loaded in direction 1.

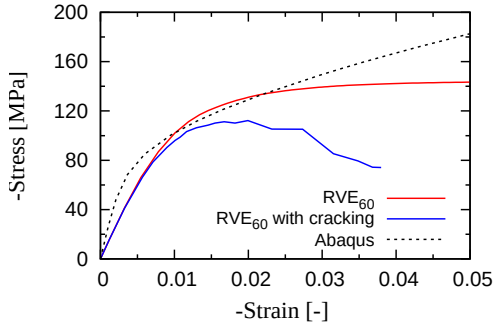

Figure 12: Comparison of stress-strain curves predicted by the particle model with and without cracking and the stress-strain curve from the full nonlinear FEM analysis in Abaqus.

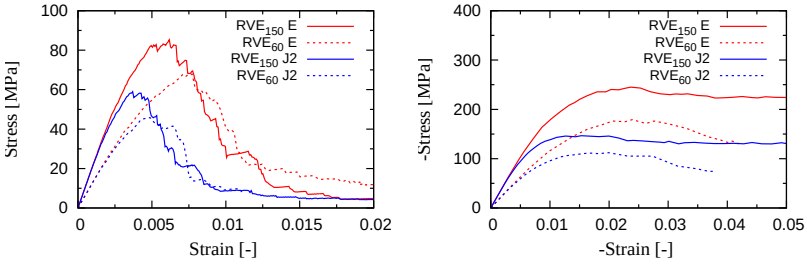

Figure 13: Simulations of the uniaxial tensile test, a), and the uniaxial compressive test, b), on the NIST cement microstructure of 60 and 150 μm assuming $J2$ and Eq. (yield condition, respectively.

A.4 Results and discussion

A.4.1 Comparison of methods on 60 μm RVE

Initially, all the introduced methods were compared on the example of the small NIST Cem microstructure RVE_{60}. In the case of SC, the $J2$ plasticity was assumed while the other methods also considered Eq. (yield condition. The FEM and FFT were used to find the strength based on perfectly brittle assumption. The particle model included the cracking of contact in tension and the strengths corresponds to the peak loads in Figure

As can be seen from the Table, the scatter of the predicted elastic and strength properties is large. Young's modulus predicted by the PM-FEM is significantly lower compared to the other methods. This is due the utilized volume tessellation. The tessellation is based on centers of gravity (Cusatis et al. 2003) and can not therefore simulate the elastic loading exactly, as is the case of models based on Voronoi tessellation (Eliáš 2009). The difference in Young's modulus between FFT and FEM is caused by the different boundary conditions assumed by the methods. The FEM models was loaded by mixed boundary conditions, see Section

Comparison of strength properties is more difficult. The FFT and FEM were used to find the strength based on perfectly brittle assumption. This estimate is far from the maximum capacity of the material (compare values from Table

The PM simulations combining the yielding and cracking of C-S-H predicted not only the values of tensile and compressive strength, but provided the entire responses in terms of stress-strain curves, see Figure

A.4.2 Modeled microstructures

Discussion at the end of Section

Figure

The effect of hydration on the elastic and strength properties on the level of individual struts was already discussed in Section

Tensile and compressive strengths in the case of particle model were obtained as the maximum loads in stress-strain curves (Figures

As it was already mentioned for the NIST microstructure, the particle model gives much higher values of compressive and tensile strengths compared to the FFT. This indeed means that the perfectly brittle assumption is too crude estimate of strengths. It is important to notice that the strengths, based on perfectly brittle assumption could sometimes lead to conceptually wrong results (consider results for Cem A

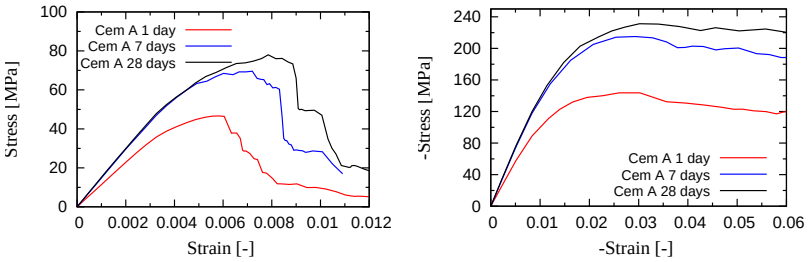

a) b)

Figure 14: Simulations of the uniaxial tensile test, a), and the uniaxial compressive test, b), on Cem A microstructures.

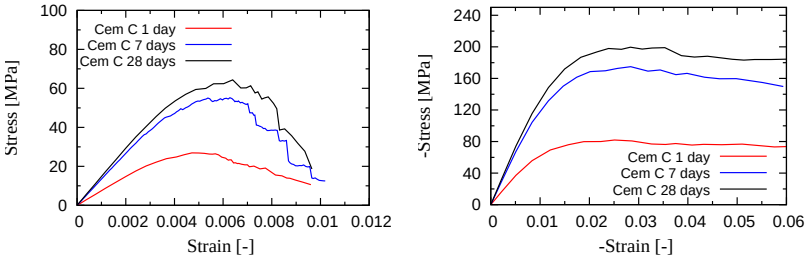

a) b)

Figure 15: Simulations of the uniaxial tensile test, a), and the uniaxial compressive test, b), on Cem C microstructures.

at 28 days, Figure

A.5 Conclusions

In the presented study, the mean-field strength homogenization approach used in (Pichler et al. 2008), approaches based on the solution of linear-elastic problems with FEM and FFT and a modified particle model based on (Cusatis et al. 2003) were utilized to predict the tensile and compressive strength of three cement pastes. Seven different microstructures were considered: first was measured (`http://visiblecem.nist.gov/cement`), and the other are simulated using CemHyd3D (Bentz 2000) hydration model for two different types of cements. Two material models of the C-S-H were used for every model - $J2$ plasticity and the elliptical yield condition resulting from

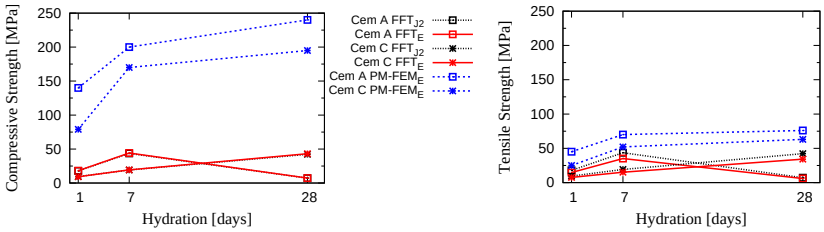

a) b)

Figure 16: Compressive, a), and tensile, b), strengths modeled with the particle model and and FFT for Cem A and Cem C 150 RVE_150 microstructures at different age.

the porous nature of the C-S-H.

The following conclusions can be drawn:

- Methods based on the perfect brittle assumption applied to heterogeneous stress field resulting from the FEM and FFT calculation or to the second order stress estimates give inconsistent results for considered microstructures and can not be used for reliable predictions:
  - Second order stress estimates do not reflect the actual microstructure and significantly overestimates strengths compared to results from FFT and FEM calculations.
  - FFT and FEM reflect the microstructure, however, the perfect brittle assumption is significantly dependent on the discretization and should not be used as a strength approximation of cement paste.
- Particle model with FEM homogenization of the internodal volume provides simulations of compression without cracking matching favorably the nonlinear FEM solution with significantly reduced computational time.
- Cracking of the C-S-H plays and important role in the compressive test and contributes significantly to the difference between the compressive and tensile strengths.
- Size of the microstructure is an important parameter influencing significantly the strength.
- The type of the yield condition changes the responses only in the quantitative way while qualitatively the difference is not pronounced.

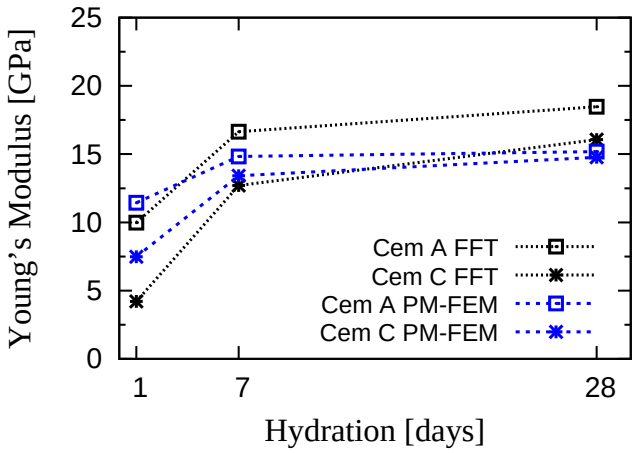

Figure 17: Elastic moduli calculated with FFT and PM for Cem A and Cem C microstructures at different age.

Method	Young's Modulus [GPa]	Compressive Strength [MPa]	Tensile Strength [MPa]
SC_{J2}	23.117	128.721	128.721
FFT_{J2}	17.278	11.591	11.591
FEM_{J2}	19.629	18.244	18.244
$PM-FEM_{J2}$	12.973	112.156	45.828
FFT_E	17.278	28.026	21.818
FEM_E	19.629	31.480	24.003
$PM-FEM_E$	12.973	179.157	67.960

Table A.14: Comparison of elastic and nonelastic properties of the RVE predicted by the investigated methods.

A.6 Acknowledgments

The authors are grateful to the European Community under the Marie Curie Research Training Network MCRTN-CT-2005-019283 "Fundamental understanding of cementitious materials for improved chemical physical and aesthetic performance" (`http://www.nanocem.org/MC-RTN/`) for the full support of Jan Skoček and Denis Davydov.
Further, the authors would like to acknowledge Jens Henrik Nielsen from Technical University of Denmark, Department of Civil Engineering, for his help with Abaqus simulations.

Bibliography

A. J. Allen, et al. (2007). 'Composition and density of nanoscale calcium-silicate-hydrate in cement'. *Nature materials* **6**:311–316.

D. Bentz (2000). 'CEMHYD3D:A Three-Dimensional Cement Hydration and Microstructure Developement Modeling Package. Version 2.0'. Report, Building and Fire Research Laboratory, National Institute of Standards and Technology, Gaithersburg, Mariland 20899.

D. Bentz, et al. (2002). 'The visible cement data set'. *Journal of Research of the National Institute of Standards and Technology* **107**(2):137–148.

S. Carioua, et al. (2008). 'Hardnesspacking density scaling relations for cohesive-frictional porous materials'. *Journal of the Mechanics and Physics of Solids* **56**(3):924–952.

P. P. Castaneda (1996). 'Exact second-order estimates for the effective mechanical properties of nonlinear composite materials'. *J. Mech. Phys. Solids* **44**(6):827–862.

P. P. Castaneda (2002). 'Second-order homogenization estimates for nonlinear composites incorporating field fluctuations: I - theory'. *J. Mech. Phys. Solids* **50**:737–757.

R. Chamrová (2010). *Modelling elastic properties of the hydrating cement paste from a vector microstructural model*. Ph.D. thesis, EPFL Lausanne.

Y.-T. Cheng & C.-M. Cheng (2004). 'Scaling, dimensional analysis, and indentation measurements'. *Materials Science and Engineering* **R 44**:91–149.

G. Constantinides & F.-J. Ulm (2004). 'The effect of two types of C-S-H on the elasticity of cement-based materials: Results from nanoindentation and micromechanical modeling'. *Cement and Concrete Research* **34**:67–80.

G. Constantinides & F.-J. Ulm (2007). 'The nanogranular nature of C-S-H'. *Journal of the Mechanics and Physics of Solids* **55**:64–90.

G. Cusatis, et al. (2003). 'Confinement-Shear Lattice Model for Concrete Damage in Tension and Compression: I. Theory'. *Journal of Engineering Mechanics* .

G. Cusatis, et al. (2006). 'Confinement-shear lattice CSL model for fracture propagation in concrete'. *Computer Methods in Applied Mechanics and Engineering* **195**(52):7154 – 7171. Computational Modelling of Concrete.

G. Cusatis & L. Cedolin (2007). 'Two-scale study of concrete fracturing behavior'. *Engineering Fracture Mechanics* **74**(1-2):3 – 17. Fracture of Concrete Materials and Structures.

L. Dormieux, et al. (2006). *Microporomechanics*. John Wiley & Sons, Ltd.

J. Eliáš (2009). *Discrete Simulation of Fracture Process in Disordered Materials*. Ph.D. thesis, Brno University of Technology, Faculty of Civil Engineering.

M. Frigo & S. G. Johnson (2005). 'The Design and Implementation of FFTW3'. *Proceedings of the IEEE* **93**(2):216–231. Special issue on "Program Generation, Optimization, and Platform Adaptation".

F. Ganneau, et al. (2007). 'An algorithm for computing the compressive strength of heterogeneous cohesive-frictional materials - Application to cement paste'. *Computers and Geotechnics* (34):254–266.

P. S. H. Moulinec (2003). 'Comparison of FFT-based methods for computing the response of composites with highly contrasted mechanical properties'. *Physica B* **338**:58–60.

P. J.C. Michel, H.Moulinec (1999). 'Effective properties of composite materials with periodic microstructure: a computational approach'. *Comput. Methods Appl. Mech. Engrg.* **172**:109–143.

P. J.C. Michel, H.Moulinec (2001). 'A computational scheme for linear and non-linear composites with arbitrary phase contrast'. *Int. J. Numer. Meth. Engng.* **52**:139–160.

E. J.D. (1957). 'The Determination of the Elastic Field of an Ellipsoidal Inclusion'. *Proceedings of Royal Society* **241**:376–396.

E. J.D. (1959). 'The Elastic Field Outside an Ellipsoidal Inclusion'. *Proceedings of Royal Society* **252**:561–569.

H. M. Jennings, et al. (2007). 'A multi-technique investigation of the nanoporosity of cement paste'. *Cement and Concrete Research* **37**:329–336.

D. K. L. Dormieux, A. Molinari (2002). 'Micromechanical approach to the behavior of poroelastic materials'. *J. Mech. Phys. Solids* **50**:2203–2231.

J. Michel, et al. (2007). 'Microscopic and macroscopic instabilities in finitely strained porous elastomers'. *Journal of the Mechanics and Physics of Solids* **55**:900–938.

S. Mindess & S. Diamond (1982). 'A device for direct observation of cracking of cement paste or mortar under compressive loading within a scanning electron microscope'. *Cement and Concrete Research* **12**(5):569 – 576.

H. Moulinec & P. Suquet (1998). 'Numerical method for computing the overall response of nonlinear composites with complex microstructure'. *Comput. Methods Appl. Mech. Engrg* (157):69–94.

B. Pichler, et al. (2008). 'Spherical and acicular representation of hydrates in a micromechanical model for cement paste: prediction of early-age elasticity and strength'. *Acta Mech. IN PRESS* .

O. Pierard (2006). *Micromechanics of inclusion-reinforced composites in elasto-plasticity and elasto-viscoplasticity: modeling and computation*. Ph.d. thesis, Universite Catholique de Louvain.

T. C. Powers & T. L. Brownyards (1948). 'Studies of the physical properties of hardened cement paste'. Bulletin 22, Research Laboratories of the Portland Cement Association, Chicago.

L. Sorelli, et al. (2008). 'The nano-mechanical signature of Ultra High Performance Concrete by statistical nanoindentation techniques'. *Cement and Concrete Research* **38**:1447–1456.

M. Vandamme & F.-J. Ulm (2008). *The nanogranular origin of concrete creep: A nonoindentation investigation of microstructure and fundamental properties of calcium-silicate-hydrates*. Ph.D. thesis, Massachusetts institute of technology.

V. Šmilauer (2005). *Elastic properties of hydrating cement paste determined from hydratation models*. Ph.D. thesis, Czech Technical University in Prague, Faculty of Civil Engineering, Czech Technical University in Prague, Prague, Czech Republic.

Mechanical behavior of structures made from cementitious materials has been successfully modeled using non-linear fracture mechanics in recent decades. On the structural scale, an assumption of homogeneity of the material is valid and well established theories can be applied. However, if focus is put on phenomena of a similar scale as is the characteristic size of inhomogeneities of the material, a model which refl ects the heterogeneous nature of the material needs to be applied.

A framework for prediction of strength of cementitious materials on various scale was developed and applied in this Thesis. The framework consists of an experimental part, an identi cation of material properties from the experiments and a modeling part based on an approximative discrete particle model taking into accout the heterogeneity of the material.

DTU Civil Engineering
Department of Civil Engineering
Technical University of Denmark

Brovej, Building 118
2800 Kgs. Lyngby
Telephone 45 25 17 00

www.byg.dtu.dk

ISBN: 9788778773111
ISSN: 1601-2917